Assessing Close Range Photogrammetric Approach to Evaluate Pavement Surface Condition

Prof. Saad Issa Sarsam
Department of Civil Engineering
College of Engineering-University of Baghdad
E-mail:saadisasarsam3@yahoo.com

Lect. Afrah Mekki Daham
Department of Surveying Engineering
College of Engineering-University of Baghdad
E-mail:afrah.daham@gmail.com

Assist. Lect. Amal Mahdi Ali
Department of Civil Engineering
College of Engineering-University of Baghdad
E-mail:amal.mahdi09@yahoo.com

ABSTRACT

The aim of this research is to adopt a close range photogrammetric approach to evaluate the pavement surface condition, and compare the results with visual measurements. This research is carried out on the road of Baghdad University campus in AL-Jaderiyiah for evaluating the scaling, surface texture for Portland cement concrete and rutting, surface texture for asphalt concrete pavement. Eighty five stereo images of pavement distresses were captured perpendicular to the surface using a DSLR camera. Photogrammetric process was carried out by using ERDAS IMAGINE V.8.4. The results were modeled by using a relationship between the photogrammetric and visual techniques and selected the highest coefficient of determination (R^2). The first technique is efficient in evaluating the rutting with (R^2) range between (0.985-0.997), (R^2) for the scaling range between(0.990–0.999),as compared to the visual evaluation. The macrotexture of the asphalt concrete with a high (R^2) range between (0.982-0.999) and (R^2) for the cement concrete pavement surface texture range between (0.980 - 0.998), as compared to the sand patch method.

Keywords: evaluation, pavement, photogrammetry, surface texture, visual.

إستخدام إسلوب المسح التصويري ذي المدى القريب لتقييم حالة سطح الرصفة

المدرس أفراح مكي دحام
قسم هندسة المساحة
كلية الهندسة، جامعة بغداد

الأستاذ سعد عيسى سرسم
قسم الهندسة المدنية
كلية الهندسة، جامعة بغداد

المدرس المساعد آمال مهدي علي
قسم الهندسة المدنية
كلية الهندسة، جامعة بغداد

الخلاصة

الهدف من البحث اعتماد تقنية المسح التصويري ذي المدى القريب لتقييم حالة الرصفة السطحية ومقارنة نتائجه بما يعادلها من التقييم البصري. تم تنفيذ هذا التطبيق على شبكة الطرق في حرم جامعة بغداد في منطقة الجادرية لتقييم حالة سطح الرصفة الكونكريتية والرصفة الأسفلتية مثل (سمك نسجة السطح، تدهور السطح، التخدد). ثم التقاط خمسة وثمانين زوج من الصور المجسمة العمودية لأنواع مختلفة من فشلات سطح الرصفة باستخدام كاميرا رقمية ، ثم أُجريت عملية المعالجة بأستخدام برنامج ERDAS IMAGINE V.8.4 . إن مقارنة النتائج بين تقنية المسح التصويري وتقنية الفحص البصري كانت من ناحية الحساب الكمي للفشلات و حساب شدة الضرر ثم نمذجتها بأستخدام اعلى قيمة لمعامل الترابط R^2. حيث إن تقنية المسح التصويري تعطي نتائج دقيقة لسطح الرصفة تتراوح اعلى قيمة لمعامل الترابط للتخدد R^2 مابين (0.985- 0.997). ومابين (0.990- 0.999)

لتدهور الرصفة الكونكريتية مقارنة بطريقة الفحص البصري. اما بالنسة لحالة نسجة سطح الرصفة الاسفلتية كانت R^2 تتراوح ما بين (0.982- 0.999) ، ولنسجة سطح الرصفة الكونكريتية كانت R^2 (0.980- 0.998) مقارنةً بالطريقة التقليدية sand patch.

الكلمات الرئيسية : تقييم ، الرصفة ، المسح التصويري ، نسجة السطح ، البصري.

1. INTRODUCTION

Distress is defined as a condition of pavement structure that reduces the ability of a pavement to provide a safe and comfortable ride to its users. A variety of pavement distress can occur due to different causes such as loads, environmental problems, and poor pavement maintenance management, **NDOR, 2002.**

The evaluation of pavement surface condition is considered as a first step in scheduling the pavement maintenance program and assessment of budget requirements. Many techniques have been established for such process, such as GIS, video imaging with image processing software and even visual examination. Close-range photogrammetry may be used as a research tool in civil engineering such as pavement evaluation monitoring. ERDAS IMAGINE software enables surface conditions to be represented as ortho-image. Close-range digital photogrammetry is seen as a possible approach in providing geometrical imaging for pavement distress studies without physically touching the surface being measured. The results obtained by this technique are compared with visual inspection, **Chai, 2005.**

2. MANUAL DATA COLLECTION

One of the common methods of obtaining pavement distress information is by visual inspection. The alternative approach is surveying the roads in a vehicle traveling. Manual assessment can be finished directly on the road or later in the office, **Ahmed** and **Haas, 2009.**

2.1 Visual Observation

Visual observation of pavement distress is the most common method for monitoring pavement surface condition. This has been traditionally performed by trained engineers who walk along the road to assess the distresses and produce report sheets. This technique is more dangerous and time-consuming. In addition, the accuracy and consistency of the data also depend on the experience of the inspectors who perform the survey, **Oh, 1998.**

2.2 Stereo Photogrammetric System

Image-collection technology is the systems record pavement surface images using a video camera or photographic camera mounted on a survey vehicle, **Ali , 2013.**

Photogrammetric evaluation is either done manually by capturing image and specially designed workstations while trained crews rate the recorded road surface or automatically by computer image processing software, **ACSIRO, 2009.**

3. EXPERIMENTAL WORK

An attempt to investigate the potential capabilities and flexibility technique of the measurement-based vertical stereovision system and ERDAS IMAGINE 8.4 software in quantification of pavement distresses is being performed and comparison of this technique with the visual method will be adopted.

4. PHOTOGRAMMETRIC PROCESS

The work flow process for collection of stereo images for system photogrammetric using is made up of five steps:

1. The Frame Design.
2. Calibration of Camera.
3. Measurements of Ground Control Points
4. Image Data Acquisition.
5. Photogrammetric Processing (ERDAS IMAGINE Software V.8.4).

4.1 The Frame Design

This frame was designed by fixing the height of photo exposure is (1m.), the desired focal length is (24mm), photo overlapping (60%) therefore, the base line become (37.5cm.). As shown in **Fig.1.**

4.2 Calibration of Camera.

Photogrammetric technique is performed by using DSLR camera (Canon EOS 600D).The camera calibration was done by Photo Modeler Program. The report of calibration camera is shown in **Table 1.**

4.3 Image Capture Stage

Within the study area, Eighty five stereo pair images of pavement distresses were captured perpendicular to the surface using Cannon EOS 600D with a resolution of 18 mega-pixels). A single stereo image was captured with 60% overlap setting. As shown in **Fig.2.**

4.4 Measurements of Ground Control Points

Photogrammetric field work began with creation of certain distribution of control points around the area of distress. As shown in the **Fig.3.** At least 3GCPs spread across each image were marked and measured with a Total Station device (TOPCON, GTS 235). Part of the coordinates of ground control points are illustrated in **Table 2.** GCPs referenced by to the tow points which measured by using Differential Global Position system (TOPCON Hiper- GR3). As shown in **Fig.4.** Coordinates of Bench Mark points are listed in **Table 3.**

4.5 Photogrammetric Processing

This process was carried out using ERDAS IMAGINE software version 8.4.

4.5.1 **Triangulation process**

Triangulation is performed to estimate the (X, Y, and Z) locations of tie points in stereo model and exterior orientation parameters (EOP) of images can be computed. The distribution of the ground control points, and other points in the adjusted stereo model was shown in **Fig.5.** The adjusted (EOP) that resultant from triangulation process are listed in **Table 4.**

4.5.2 **Creation ortho-images**

After performing triangulation with ERDAS IMAGINE software, ortho-images were created. Window measurement tool in orthorectified image that necessary to measure lengths, area and other distress condition. Orthorectified image is shown in **Fig.6.**

5. VISUAL INSPECTION APPROACH

Distress approach of Visual techniques was based on **USDOT-FHA, 2003 and NDOR, 2002** which performed by walking along the roadways, visually assessing the distress areas. The equipments were used represented by tape measure, ruler graduated in millimeters. **Fig.7** shows the pavement distress measured by using tape measures.

6. MEASUREMENT of SURFACE TEXTURE

The average macrotexture depth of asphalt concrete and cement concrete pavement surface determined using “sand patch” method ASTM E 965. **Fig.8** shows the sand patch test setup.

7. THE RESULT AND DISCUSSION

Results were modeled by using a mathematical relationship between the two techniques and selected the highest coefficient of determination (R^2). Pavement distresses divided into asphalt concrete and cement concrete pavement distresses.

A. Asphalt Concrete of Pavement Surface

A.1 Rutting

Table 5 shows the assessment of rutting area, depth and intensity using (photogrammetric and visual methods).**Fig.9** shows the correlation of results obtained by using both methods, it shows high correlation as indicated by high coefficient of determination R^2 = (0.997), (0.985), (0.996) for area, depth and intensity.

A.2 Macrotexture of asphalt concrete pavement

Table 6 shows the assessment of Macro texture area, depth and intensity using both testing methods (photogrammetric and sand patch MTD). **Fig.10** shows the correlation of results obtained by using both methods, it shows high correlation as indicated by high coefficient of determination R^2 = (0.999), (0.982), (0.999) for area, depth and intensity respectively. Such result is agreed with the work **Alshareef, 2011, China and James, 2012.**

B. Cement Concrete Pavement

B.1 Scaling

Table 7 shows the assessment of scaling area, depth and scaling intensity using both testing methods. **Fig.11** shows the correlation of results obtained by using both methods, it shows high correlation as indicated by high coefficient of determination R^2 = (0.999), (0.990), (0.998) for area, depth and intensity respectively.

B.2 Macrotexture of cement concrete pavement

Table 8 shows the assessment of Macrotexture area, depth and intensity using both testing methods (photogrammetric and sand patch MTD). **Fig.12** shows the correlation of results obtained by using both methods, it shows high correlation as indicated by high coefficient of determination R^2 = (0.998), (0.980), (0.998) for area, depth and intensity respectively.

8. CONCLUSIONS

The following conclusions have been made:-

1. Photogrammetric technique provides the ablity of accommodate more types of asphalt and concrete pavement surface distresses in the study area, especially, distress depth, and area by using a stereo vision technology.
2. Photogrammetric approach is efficient in evaluating the rutting with a high coefficient of determination ranged between (0.985 - 0.997) and the scaling with a high coefficient of determination ranged between (0.990 – 0.999), as compared to the traditional method of visual evaluation.
3. Photogrammetric approach is efficient in evaluating the macrotexture of the asphalt concrete with a high coefficient of determination ranged between (0.982 - 0.999) and cement concrete pavement surface with a high coefficient of determination ranged between (0.980 - 0.998), as compared to the traditional sand patch method.

REFERENCES

- ACSIRO, Australia´s Commonwealth Scientific and Industrial Research Organization, 2009, *Automated detection of road cracks* , http://www.csiro.au /solutions/psaa.html.

- Ahmed, M. F. and Haas, C. T., 2009, *The Potential of Low Cost Close Range Photogrammetry towards Unified Automatic Pavement Distress Surveying*, Proceedings of the Annual Waterloo Demographic Center Conference.

- Ali, A. M., 2013, *Assessing Close Range Photogrammetric Approach to Evaluate Pavement Surface Condition*, M.Sc. Thesis, Department of Surveying Engineering, University of Baghdad, Baghdad, Iraq.

- Alshareef, H. N., 2011, *Assessing Asphalt and Concrete Surface Texture in the Field*, M.Sc. Thesis, Department of Civil Engineering, the University of Baghdad, Baghdad, Iraq.

- ASTM, American Society for Testing and Materials, 2006 , *Road and Paving Materials.*

- Chai, L. T., 2005 , *Evaluation of Cracks and Disintegration Using Close Range Digital Photogrammetry and Image Processing Technique*, M.Sc. Thesis, Department of Civil Engineering, College of Engineering, University technology Malaysia.

- China, S. and James, D., 2012, *Comparison of Laser Based and Sand Patch Measurements of Pavement Surface Macrotexture* , DOI: 10.1061/ (ASCE) TE.1943-5436.0000315, American Society of Civil Engineers.

- ERDAS, Inc., 2003, *IMAGINE OrthoBASE User's Guide*, ERDAS IMAGINE V8.4, Printed in Georgia.

- NDOR, Nebraska Department of Roads, 2002, *Pavement maintenance manual*.

- Oh, H., 1998, *Image Processing Technique in Automated Pavement Evaluation System*, University of Connecticut: Ph.D. Dissertation.

- USDOT-FHA , **2003,** *Distress Identification Manual for the Long Term Pavement Performance Program*, FHWA-RD-03-031, US Department of transport.

NOMENCLATURE

R^2: coefficient of determination.
ω: rotation angle around the x axis.
ϕ: rotation angle around the y axis.
κ: rotation angle around the z axis.
DGPS: differential global position system
DSLR: digital single lenses reflex
Elev.: elevation
EOP: exterior orientation parameters
ERDAS: earth resources data analysis system
GCPs: ground control points
GIS: geographical information system
GR3: grade r3

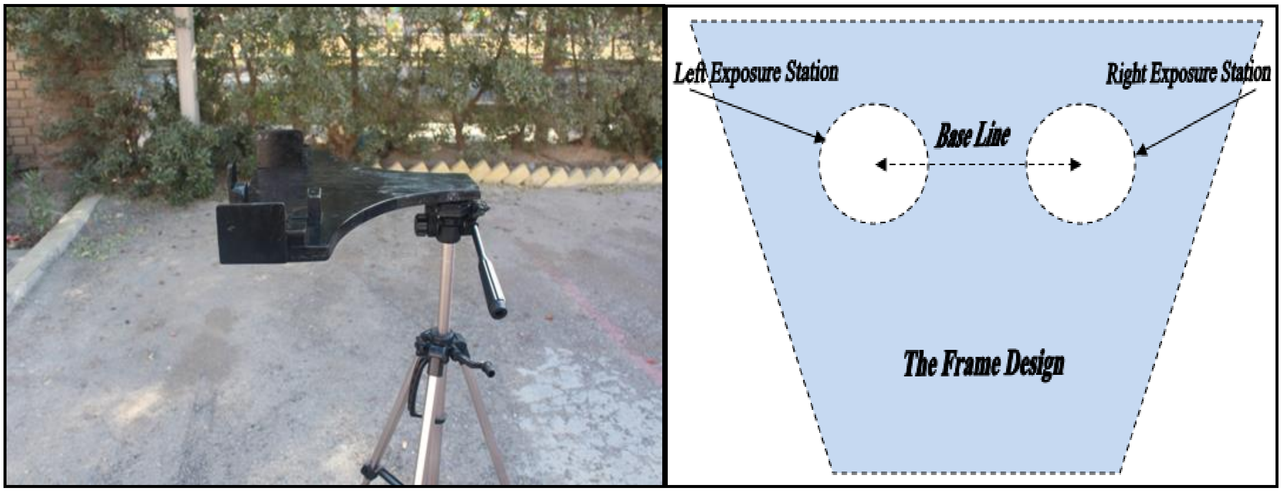

Figure 1. The designed frame and camera.

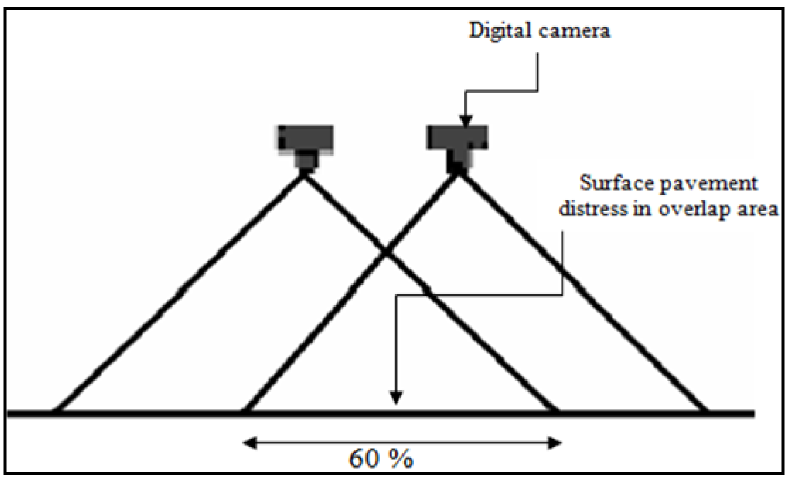

Figure 2. Stereo overlap image (60%).

Figure 3. Ground control point around distress area.

Figure 4. Sketch of two GPS points at the study area and DGPS device.

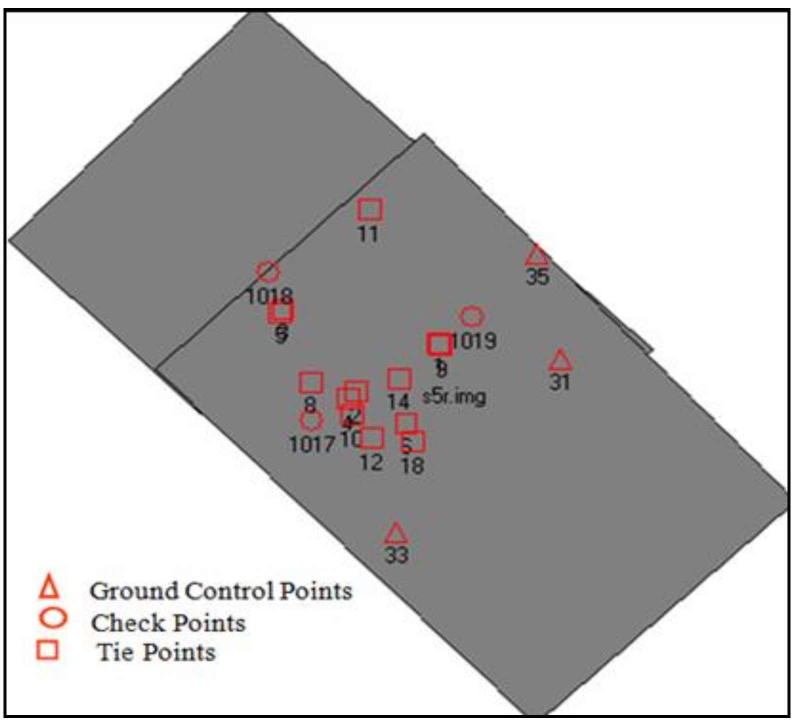

Figure 5. Distribution of ground control points, tie points and check points in the adjusted stereo model.

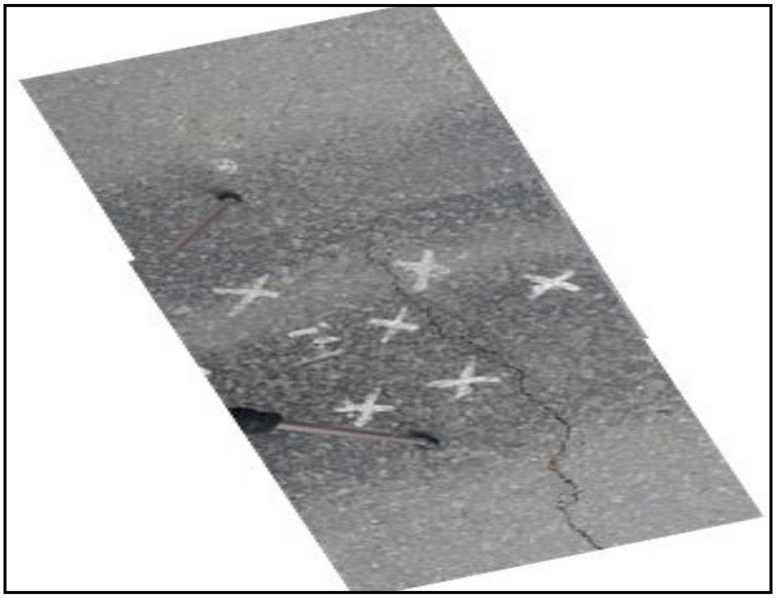

Figure 6. Orthorectified Image.

Figure 7. Visual inspection

Figure 8. Sand patch test.

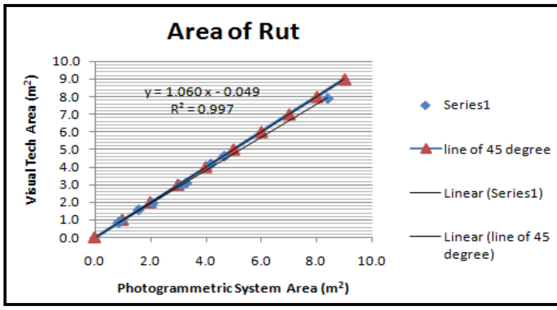

Correlation of photogrammetric rutting area with visual rutting area.

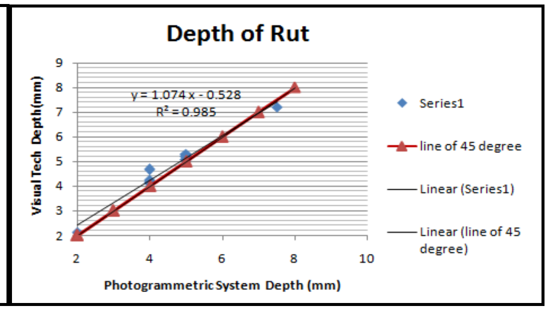

Correlation of photogrammetric rutting depth visual rutting depth.

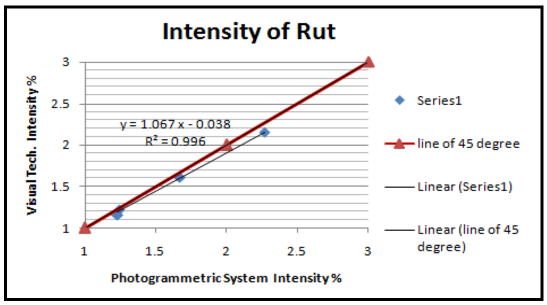

Correlation of photogrammetric rutting intensity with visual rutting intensity.

Figure 9. Correlation between two testing methods for evaluation of the rutting.

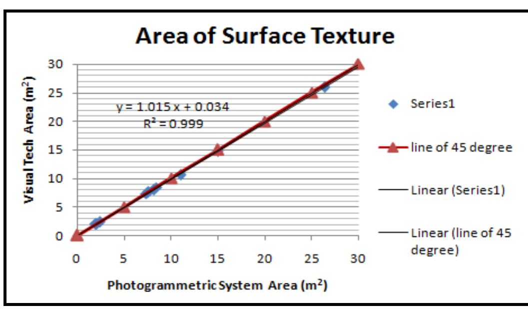

Correlation of photo. surface texture area with visual surface texture area.

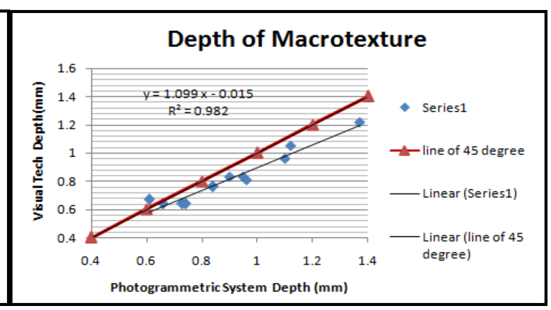

Correlation of photo. macrotexture depth with visual macrotexture depth

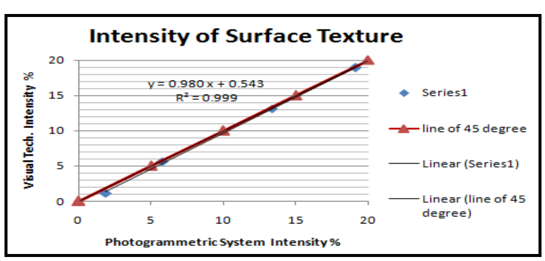

Correlation of photogrammetric surface texture area with visual surface texture area.

Figure10. Correlation between two testing methods for evaluation surface texture of asphalt concrete pavement.

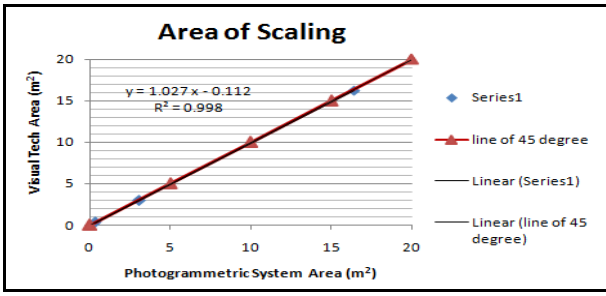

Correlation of photogrammetric scaling area with visual scaling area.

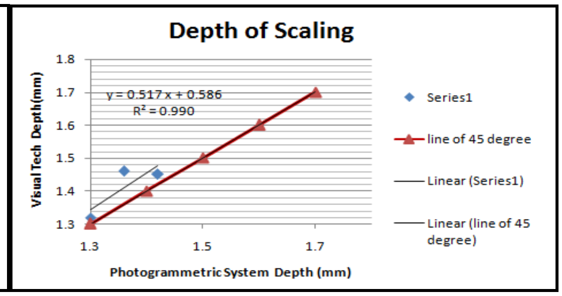

Correlation of photogrammetric scaling depth with visual scaling depth.

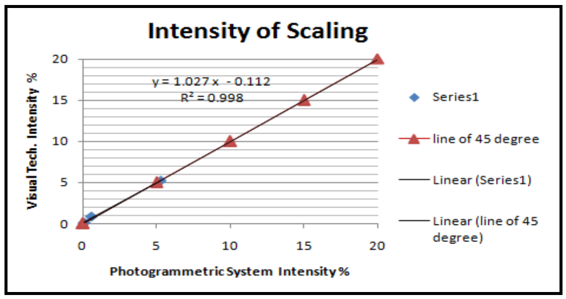

Correlation of photogrammetric scaling intensity with visual scaling intensity.

Figure11. Correlation between two testing methods for evaluation of scaling.

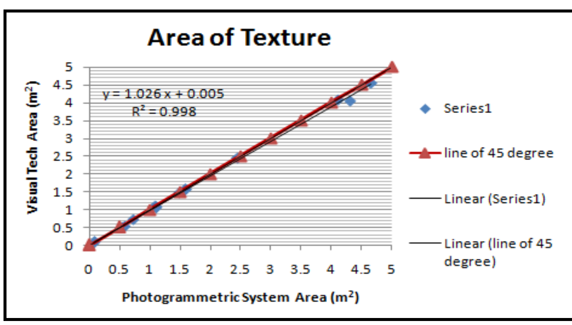

Correlation of photogrammetric macrotexture with visual area macrotexture area.

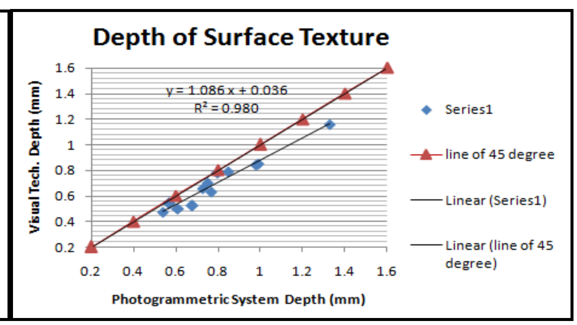

Correlation of photogrammetric macrotexture depth with visual macrotexture depth.

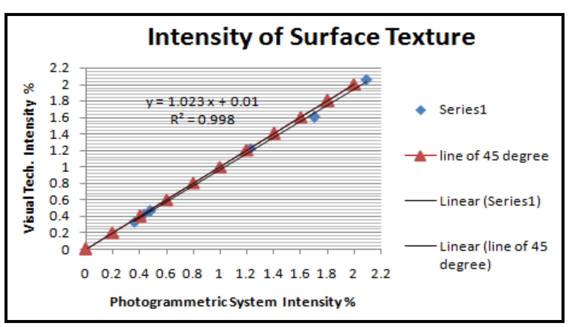

Correlation of photogrammetric macrotexture area with visual macrotexture area.

Figure 12. Correlation between two testing methods for evaluation of macrotexture of cement concrete pavement.

Table 1. The calibration report, camera: Canon EOS 600D.

Name	Value mm	Deviation (mm)
focal length	22.522933	0.008
xp	11.499973	0.005
yp	7.910362	0.005
f h - format height	15.113000	2.1x 10^{-004}
f w - format width	22.677364	2.2 x 10^{-004}
k1 - radial distortion 1	-2.519 x 10^{-005}	9.6 x 10^{-007}
k2 - radial distortion 2	4.488 x 10^{-008}	1.7 x 10^{-008}
k3 - radial distortion 3	0.000 x 10^{+000}	0.00 x 10^{-000}
p1 - decentering distortion 1	2.094 x 10^{-005}	9.4 x 10^{-007}
p2 - decentering distortion 2	1.125 x 10^{-004}	8.0 x 10^{-007}
pixel size	0.00470	———

Table 2. Part of coordinate ground control points coordinates.

stereo pair ID.	point ID.	Northing(m)	Easting (m)	Elevation (m)
1	3	3682416.52	442628.099	33.746
	5	3682416.09	442627.967	33.756
	6	3682416.176	442628.118	33.748

Table 3. Coordinates of the two points measuring by DGPS system.

point ID.	grid Northing (m)	grid Easting (m)	Elevation (m)
point1	3682104.053	442365.913	34.037
point2	3682314.976	442495.494	33.828

Table 4. Some of adjusted exterior orientation parameters.

tie point ID.	Northing (m)	Easting (m)	Elev. (m)	omega(ω)	phi (ϕ)	kappa (κ)
1	3682416.3421	442627.8161	34.7533	0.0442	-0.8727	-90.2681
2	3682416.4613	442628.2282	34.7491	-1.0044	0.0343	-87.8727

Table 5. Comparison result of rutting.

sections		no. of samples	sample ID.	area (m^2)		depth (mm)		intensity%	
section starting	section ending			visual inspection	photo. system	visual inspection	photo. system	visual inspection	photo. system
1+250	1+300	1	33	4.20	4.16	2.0	2.14	1.24	1.22
1+300	1+350	2	34	3.31	3.08	4.0	4.12	1.23	1.16
		3	38	0.88	0.85	4.0	4.17		
2+150	2+200	4	57	3.10	2.95	5.0	5.29	1.67	1.61
		5	59	1.60	1.57	5.0	5.09		
		6	60	0.97	0.96	4.0	4.26		
2+250	2+300	7	64	4.68	4.60	5.0	5.20	2.27	2.15
		8	65	2.10	1.94	7.5	7.20		
		9	67	8.40	7.86	4.0	4.67		
tested sample number		9	regression model	y = 1.060x - 0.049		y = 1.074x - 0.528		y = 1.067x - 0.038	
			R^2	0.997		0.985		0.996	

Table 6. Comparison result of macrotexture of asphalt concrete pavement.

sections		number of samples	sample ID.	area (m2)		depth (mm)		intensity%	
section starting	section ending			visual inspection	photo. system	visual inspection	photo. system	visual inspection	photo. system
0+450	0+500	1	17	8.47	8.39	0.73	0.64	5.81	5.65
		2	18	11.05	10.58	0.90	0.83		
0+700	0+750	3	25	15.00	14.69	0.84	0.76	13.35	13.10
		4	26	26.40	25.92	1.10	0.96		
1+300	1+350	5	78	2.04	1.97	0.95	0.83	1.88	1.15
		6	32	1.98	1.97	0.74	0.64		
		7	39	2.38	2.34	0.96	0.81		
2+150	2+200	8	56	42.00	41.39	1.37	1.22	19.17	18.90
		9	57	8.16	7.97	1.12	1.05		
		10	59	7.40	7.32	0.61	0.67		
		11	60	7.64	7.57	0.66	0.64		
tested sample number		11	regression model	y = 1.015x + 0.034		y = 1.099x + 0.015		y = 0.980x + 0.543	
			R^2	0.999		0.982		0.999	

Table 7. Comparison result of scaling of cement concrete pavement.

sections		number of samples	sample ID.	area (m^2)		depth (mm)		Intensity %	
section starting	section ending			visual inspection	photo. system	visual inspection	photo. system	visual inspection	photo. system
0+650	0+700	1	29	0.3280	0.3293	1.50	1.75	0.12	0.09
0+700	0+750	2	30	16.40	16.23	1.30	1.37	5.29	5.24
1+250	1+300	3	82	3.08	2.92	1.40	1.60	0.59	0.84
tested sample number		3	regression model	y = 1.007x + 0.063		y = 0.517x + 0.586		y = 1.027x - 0.112	
			R^2	0.999		0.990		0.998	

Table 8. Comparison result of surface texture of cement concrete pavement.

sections		number of samples	sample ID.	area (m^2)		depth (mm)		intensity%	
section starting	section ending			visual inspection	photo. system	visual inspection	photo. system	visual inspection	photo. system
0+300	0+350	1	6	0.59	0.53	0.99	0.85	1.6996	1.6001
		2	11	0.09	0.08	0.75	0.70		
		3	12	4.31	4.05	0.80	0.78		
		4	14	0.73	0.72	0.77	0.63		
0+350	0+400	5	31	1.100	1.096	0.54	0.47	0.36	0.33
0+450	0+500	6	16	4.11	4.09	1.33	1.16	1.224	1.218
1+350	1+400	7	40	4.66	4.55	0.68	0.52	2.09	2.06
		8	41	2.46	2.44	0.61	0.50		
1+400	1+450	9	46	1.49	1.47	0.85	0.79	0.433	0.425
2+200	2+250	10	61	1.11	1.05	0.73	0.66	0.48	0.46
		11	62	0.54	0.50	0.98	0.84		
		12	63	1.60	1.56	0.57	0.54		
tested sample number		12	regression model	y = 1.026x + 0.005		y = 1.086x + 0.036		y = 1.023x + 0.01	
			R^2	0.998		0.980		0.998	

Some Durability Test of No-Fine Concrete

Shakir Ahmed Salih
Professor
Department of Building and Construction
University of Technology
Email: professorshakir@uotechnology.edu.iq

Tuqa Alaa Fidel
Engineer
College of Engineering
University of Baghdad
Email: tuka_90_alaa@yahoo.com

ABSTRACT

In this study, two types of mixes were adopted by using two grading of coarse aggregate. The practical side of this study was to produce no-fine aggregate concrete by using crushed clay brick aggregates. The durability of the produced concrete and internal sulfate attack was studied. For durability assessment, it is found that the no-fine concrete made with crushed brick aggregate lost about (15-25) % of its compressive strength after being subjected to 60 cycles of wetting and drying with age 120 days. The curing condition showed that the water curing improved the compressive strength with a rate higher than that when sealed or air dry curing were used. The crushed brick no-fine concrete deteriorated in compressive strength after exposure to internal sulfate attack for 60 cycles; the percentage decrease was about (23.33-25) and (25-27.5) % for 0.57 and 0.83sulfate content respectively.

Keywords: compressive strength, durability, internal sulfate attack.

بعض فحوصات ديمومة الخرسانه الخاليه من الركام الناعم

شاكر أحمد صالح
أستاذ دكتور
قسم هندسه البناء والانشاءات الجامعه التكنلوجيه

تقى علاء فاضل
مهندسه
كليه الهندسه جامعه بغداد

الخلاصة

تم خلال هذه الدراسه استخدام نوعين من الخلطات الخرسانيه الخفيفه الوزن حاويه على تدرجين من الركام الخشن. تضمن الجانب العملي من البحث انتاج خرسانه خاليه من الركام الناعم باستخدام الركام الاعتيادي ومكسر الطابوق. وتم دراسة ديمومة الخرسانه الخفيفه في البحث. لتقيم الديمومه وجد ان مقاومه الانضغاط للخرسانه الخاليه من الركام الناعم تنخفض من (15-25) % بعد تعرضها الى 60 دورة ترطيب وتجفيف بعمر يعادل 120 يوم. كما وجد ان مقاومه لانضغاط عند انضاج النماذج في الماء افضل مقارنا مع انضاجها في الهواء الجاف او المغلفه باستخدام النايلون. كما دلت النتائج على تدهور الخرسانه الخاليه من الركام الناعم بعد تعرضها الى 60 دوره ترطيب وتجفيف كما وجد ان معدل النقصان في مقاومه الانضغاط يصل الى (25-27.5) % عندما يكون محتوى الاملاح 0.57 و 0.83 على التوالي.

الكلمات الرئيسيه: مقاومه الانضغاط, الديمومه, مقاومه الاملاح الداخليه.

1. INTRODUCTION

No-fine concrete, sometimes referred to as porous or open textured concrete, is a concrete consisting of cement, water, and coarse aggregate (size ranges 19.0- 9.5mm) only without fine aggregate. Thus it contains voids throughout the concrete matrix. [1] When fine aggregate is omitted a lightweight concrete is formed. It is an agglomeration of coarse aggregate particles surrounded by a coat of cement past up to about 1.3mm thick. Thus, large pores exist through the body of concrete and these pores are important factor for low strength, low thermal conductivity and its lightweight nature· The large sizes of these pores do not allow water to transit by capillary characteristics through concrete matrix. [2] No-fine concrete is commonly used in the manufacture of precast concrete and in the manufacture of interior and exterior walls of building units (bearing and non-bearing). It is also used in partition construction and insulations. Britain used no-fine concrete for commercial purposes in 1924. During World War II, studies and research on no-fine concrete started to rise and develop and resulted in about 130000 building that used this type of concrete in Britain between ,**1945and1961.**

Desai [3] studied the effect of the size of aggregates and proportions of cement, admixture, and water on the porosity of no fine concrete. His concluded that the samples in which aggregates above 20mm were used were not porous from the base because of the large voids in the cement slurry settled down. Also in all those cubes in which compaction was done, the cement slurry settled down and thus made a flat bottom surface. So the final conclusion was to use a maximum size of aggregates 10-19mm and not to compact it while filling. Also the density of this concrete was less than the normal concrete because fine aggregate were not used, and the strength was lower than that of normal concrete.

The high porosity of brick particles contributes to higher permeability; the porosity of the particles has also shown to provide enhanced durability performance in freeze-thaw testing. Most studies in this area have been performed on very small brick particles used as a partial replacement for fine aggregate. Litvan and Sereda added brick particles of approximately 0.5 mm in size to mortar and concrete mixtures in order to assess whether the porosity of the brick would enhance freeze-thaw durability. Testing was performed in accordance with ASTM C666, and ASTM C456 procedures to characterize the air void parameters including spacing factor. They concluded that incorporation of small particles (0.4 mm to 0.8 mm) with high porosity improved the freeze-thaw resistance of the mixtures.

Arulrajah et al. investigated the use of recycled crushed brick as pavement subbase material in Australia. The experiments included water absorption, Los Angeles abrasion loss. The Los Angeles abrasion loss value obtained was just above the maximum limits specified for pavement subbase material. At higher moisture ratio level, sheer strength of crushed brick was found to be reduced beyond the acceptable limits. The geotechnical testing results indicated that crushed brick may have to be blended with other durable recycled aggregate to improve its durability and to enhance its performance in pavement subbase applications.

2. MATERIALS USED IN THIS STUDY

2.1 Cement

Ordinary Portland cement (OPC) manufactured in Iraq with a commercial name of (Al-Mass) was used in no-fine concrete mixes throughout the present work. **Tables 1** and **2** show the chemical analysis and physical properties of the cement used respectively. Results indicate that the cement is conformed to the Iraqi Standard Specification (I.S.Q) **No.5/1984** .

Aggregate

A waste crush clay brick was used as coarse aggregate with single size (10mm and 20mm). It was brought from a project near the university and used as recycled materials. The aggregate grading conformed to Iraqi specification ,**No.45/1984.** as shown in **Tables 3** and **4. Table 5** illustrates the specific gravity; bulk density (S.S.D), absorption, and sulfate content of coarse aggregate used.

2.2 Water

Ordinary, tap water was used for washing, mixing and curing throughout this study.

2.3 Super Plasticizer

The super plasticizer used in this work is considering high range water reducing admixture. It is commercially know as SP603. **Table 6** shows its typical properties. This admixture complies with the requirement of the **ASTM C494-03**.

3. CONCRETE MIXES

Two concrete mixes with different grading of coarse aggregate were selected. The design of mixes was performed in accordance with ,**Shetty.** cannot be done due to very little cohesion between particles, experienced visual examination and trial and error method were used for deciding optimum water/cement ratio. In this study the water/cement ratio chosen was (0.3) for all mixes and after many trials and errors, the super plasticizer (0.8%) by weight of cement was used.

4. CASTINGAND CURING OF CONCRETE

According to **ASTM C192-88** .concrete casting was carried out in two layers each layer was compacted by simple Roding (25 blows). Mechanical compaction or vibratory method may cause the cement paste to run off the aggregate. All specimens were covered with plastic sheet to minimize water losses for 24±2 Hrs. After that, they were demoded and immersed in water tank up to age 28, 90, and 180 days except drying and wetting and sulfate attack were exposed to cycling at laboratory temperature of about (23±2 ºC).

5. TESTING PROGRAM

5.1 Exposure Durability Test

To assess the durability of no-fine concrete in this study, specimens were exposed to different environmental conditions. The no-fine concrete specimens were divided into four groups. In group one specimen were immersed in water up to 6 months. In group two specimens were exposed to air laboratory temperature up to 6 month. While in group three specimens were kept cover with nylon sheet (sealed) for the same period. And group four included two parts. In part one, the specimens were exposed to wetting and drying for 60 cycles (each cycle included one day of wetting and one day of drying). And in part two, specimens were exposed to wetting and drying for 20 cycles (each cycle included immersion in water for three days and then air drying for three days).

5.2 Effect of Internal Sulfate Attack

To determine the effect of internal sulfate attack on the physical properties of no-fine concrete The specimens were exposed to internal sulfate content by using crushed brick with sulfate content of 0.57 and 0.83 to study the effect of using crushed brick with high SO_3 % on the compressive strength of produced no-fine concrete.

Total SO3 obtained by following equations:

Y/Y * C + P/Y * S + X/Y * A

Where:

C: amount of SO3 in cement.

S: amount of SO3 in sand.

A: amount of SO3 in coarse aggregate.

Y/Y: ratio of cement to cement per kg/m^3.

P/Y: ratio of sand to cement per kg/m^3.

X/Y: ratio of coarse aggregate to cement per kg/m^3.

For example:

SO3= 1* 2.49 + 0+ 6*0.08= 2.97

SO3= 1*2.49+ 0+ 6*0.57 = 5.91

SO3= 1* 2.49 + 0+ 6*0.83= 7.47

6. RESULTS AND DISSUSTION

Figs. 1 and 2 show the variation of compressive strength with number of wetting and drying cycles (short and long interval) respectively. These results indicated that the compressive strength of no-fine concrete specimens decreased with the increase number of drying and wetting cycles. This is attributed to a reduction in the rate of hydration process after each drying period. Also it was found that the compressive strength of no-fine concrete made of large size aggregate particles was relatively less than that of no-fine concrete made of small size aggregate particles before and after subjecting the specimens to the cycles of wetting and drying. For example, the percentage decrease of compressive strength of Mb20 after 60 cycles of short interval and 20 cycles of long interval wetting and drying cycles was (20-25) % from Mb10.

Figs. 3 and 4 show the test results of air dry density for short and long intervals of wetting and drying cycles for all no-fine concrete specimens. These results indicated that the air dry density after subjecting the concrete to the long intervals of wetting and drying cycles was higher than the air dry density of no-fine concrete after being subjected to short intervals of wetting and drying cycles. This is attributed to erosion of materials for no-fine concrete due to the water evaporation from voids and pores which are more than those in short intervals of wetting and drying cycles.

Figs. 5, 6 and 7 show the data result of compressive strength of no-fine concrete specimens exposed to different types of curing (immersed in water, sealed, and exposed to laboratory environmental) for 28, 90, and 180 days. These results indicated that the no-fine concrete specimens cured in water improved the compressive strength as compared with the compressive strength of no-fine concrete specimens sealed in Nylon sheet and exposed to air. This is attributed to the development of hydration process more than no-fine concrete subjected to sealed and exposed to air. **Fig. 8** also indicates that the density of no-fine concrete specimens exposed to air or sealed with Nylon sheet was relatively less than the density of no-fine concrete specimens that were cured in water.

Fig. 9 shows the data results of compressive strength for crushed brick no-fine concrete specimens subjected to internal sulfate attack. These results indicated that the compressive strength of crushed brick no-fine concrete decreased when the cycles of wetting and drying increased. This is attributed to the chemical reaction of sulfate with the cement gel (hydration product) producing solid materials (calcium sulfoalominate) with larger volume that cause stresses and cracking of the matrix. **Fig. 10** shows the air dry density of no-fine concrete specimens after wetting and drying cycles.

7. CONCLUSION

1. The effect of long term interval of wetting and drying was higher than the effect of short term interval of wetting and drying on the density and compressive strength by about (0.8-1.36) % and (2.54-3.22) %, respectively.
2. The immersion of no-fine concrete in water improved the compressive strength with a rate (5.51-17.32) % at 28 days higher than that when sealed or air dry curing were used.
3. It is found that the increases of internal sulfate content increased the reduction of density and compressive strength of no-fine concrete. Maximum reduction (4.5) % and (27.5) % was found at sulfate content 0.83% for crushed brick no-fine concrete for density and compressive, strength respectively.

REFRENCE

- Short A., and Kinnibungh B., Lightweight Concrete, *3Ed*., Applied Science Publisher: London 1978, pp. 368.
- Neville A.M., Properties of Concrete, 5Ed., Longman Group, Ltd., 2010, pp. 713-716.
- Dhawal Desia, Pervious Concrete-Effect of Material Properties on Porosity, http://www.engineeringcivil.com/pervious-effect-of-material-properties-on-prosity.html. (2014).
- Litvan G.G., and Sereda P.J., Particulate admixture for enhanced freeze-thaw resistance of concrete, Cement and Concrete, Vol. 8, (1977), pp. 53-60.
- Arulrajah A., Pirapeethan J., Aatheesaan T. and M.W.Bo, Geotechnical Properties of Recycled Crush Brick in Pavement Applications, *Journal of Materials in Civil Engineering ASCE*, Vol. 23, No. 10 (2011), pp. 1444-1452.
- I. Q.S. Iraqi Standard Organization, 45-1984, For Aggregate.
- ASTM C494-03, Standard Specification for Chemical Admixture for Concrete, ASTM C494/C494-99 a, 1999.

- Shetty M.S., *Concrete Technology Theory and Practice*, (S. Chand and Company LTD, 2009), pp.518.
- ASTM C192-88, Standard Practice for Making and Curing Concrete Test Specimens in the Laboratory *Annual Book of ASTM Standard*, Vol. 4, No.2 (1989), pp. 112-118.
- I. Q.S. Iraqi Standard Organization," 5-1984, For Portland cement.

Acronyms

ASTM = American Society for Testing and Materials.

IQS = Iraqi Standard Organization

Mb10 = crushed brick no-fine concrete made with maximum size 10.

Mb20 = crushed brick no-fine concrete made with maximum size 20.

Table1. Chemical composition and main compounds of cement.

Oxide Composition	Abbreviation	Content (%)	Limits of Iraqi Specification No.5/1984
Lime	CaO	61	-
Silica	SiO_2	19.84	-
Alumina	Al_2O_3	5.28	-
Iron Oxide	Fe_2O_3	4.2	-
Magnesia	MgO	2.48	≤5.0%
Sulfate	SO_3	2.49	≤2.8%
Loss on Ignition	L. O. I.	3.8	≤4.0%
Insoluble residue	I. R.	1.13	≤1.5%
Lime saturated factor	L.S.F	0.92	0.66-1.02
Main Compounds (Bogue's equations)			
Tricalcium Silicate	C_3S	48.90	-
Dicalcium Silicate	C_2S	20.27	-

Tricalcium Aluminate	C_3A	6.89	-
Tetracalcium alumino-Ferrite	C_4AF	12.76	-

Table2. Physical properties of cement used throughout this work.

Physical Properties	Test Results	Limits of Iraqi Specification No.5/1984
Setting time (Vicat's apparatus) Initial hrs. : min. Final hrs. : min.	 1:40 4:00	 ≥ 45 min ≤ 10 hrs
Compressive strength of mortar 3days, MPa 7days, MPa	 21 27	 ≥ 15 ≥ 23

Table3. Grading of crushed brick aggregate single size 10mm.

Sieve Size (mm)	Percent passing	
	% Passing	Limits of Iraqi Specification No.45/1984
14	100	100
10	92.5	85-100
5	12.5	0-25
2.36	2.5	0-5

Table4. Grading of crushed brick aggregate single size 20mm.

Sieve size mm	Percent Passing	
	% Passing	**Limits of Iraqi specification No.45/1984**
37.5	100	100
20	92.5	85-100
10	12.5	0-25
5	2.5	0-5

Table5. Properties of crushed brick aggregate.

Property	Test Result Grading 10mm	Test Result Grading 20mm
Specific gravity	2.15	2.11
Bulk density (S.S.D)	1130	1131
Sulfate content	0.08	0.08
Absorption	27	26

Table 6. Typical Properties of super plasticizers type F.

From	Black Liquid
Color	Dark Brown
Specific gravity	1.21@ 25±2ºC
Chloride content	Nil
Flash point	N/A

Table7. Compressive strength of no-fine concrete mixes subjected to (short and long) intervals of wetting and drying.

Type of mix.	Compressive Strength MPa				
	No. Cycle (28days)	Short Interval		Long Interval	
		30 cycle	60 cycle	10 cycle	20 cycle
Mb10	8	7.6	6.8	7	6.4
Mb20	6	5.5	4.8	5	4.5

Table8. Air dry density of no-fine concrete mixes subjected to (short and long) intervals of wetting and drying.

Type of mix.	Air Dry Density kg/m^3				
	No. cycle (28days)	Short Interval		Long Interval	
		30 cycle	60 cycle	10 cycle	20 cycle
Mb10	1507	1485	1458	1457	1424
Mb20	1438	1410	1378	1398	1353

Table9. Compressive strength of no-fine concrete specimens under different types of curing with age.

Type of mix.	Compressive Strength Mpa								
	Cured in Water			Sealed in Nylon sheet			Exposed to Air		
	28 days	90 days	180 days	28 days	90 days	180 days	28 days	90 days	180 days
Mb10	8	9.6	10.2	7	6.4	6.1	5.9	5.3	4.9
Mb20	6	7	7.8	4.6	3.5	2.9	3.4	2.8	2.3

Table10. Fresh, 28-days (air dry and sealed), and surface saturated dry density.

Type of mixes.	Air Dry Density kg/m^3	Sealed Density kg/m^3	Surface Saturated Dry Density
Mb10	1507	1520	1530
Mb20	1438	1455	1465

Table11. Average test result of compressive strength of internal sulfate attack test.

Type of mixes.	` Reference Specimen 28 Days	Compressive Strength (Mpa) after Cyclic Wetting And Drying into Water					
		Sulfate content in crushed brick aggregate					
		0.08 sulfate content		0.57sulfate content		0.83 sulfate content	
		30 cycles	60 cycles	30 cycles	60 cycles	30 cycles	60 cycles
Mb10	8	7.6	6.8	7	6	6.6	5.8
Mb20	6	5.5	4.8	5.3	4.6	5.1	4.5

Table12. Air dry density of internal sulfate attack test for no-fine concrete.

Type of mixes.	Air Dry Density						
	At 28 days	0.08 sulfate content		0.57sulfate content		0.83 sulfate content	
		30 cycles	60 cycles	30 cycles	60 cycles	30 cycles	60 cycles
Mb10	1507	1485	1458	1473	1445	1468	1438
Mb20	1438	1410	1378	1402	1365	1395	1352

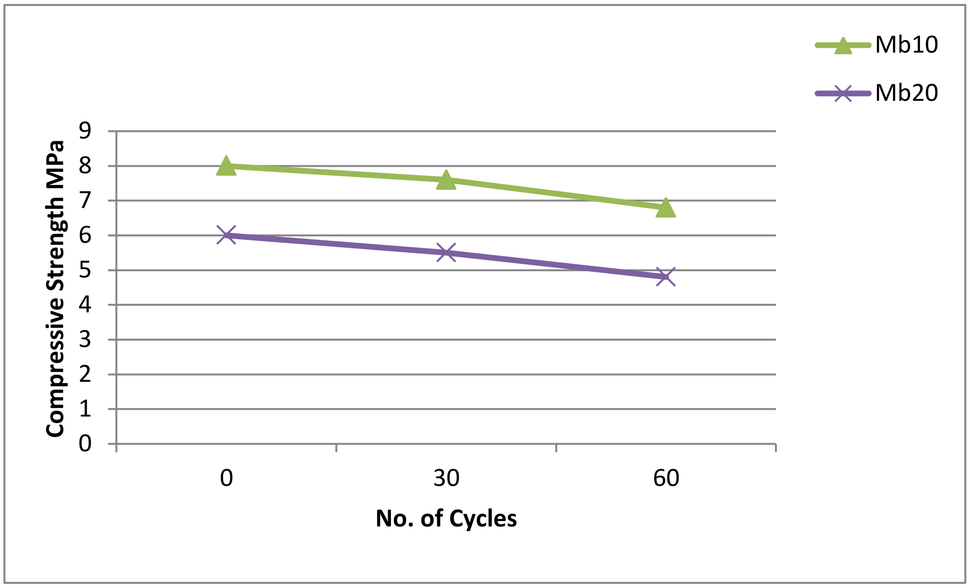

Figure1. Variations of compressive strength with no. of wetting and drying cycle (short intervals).

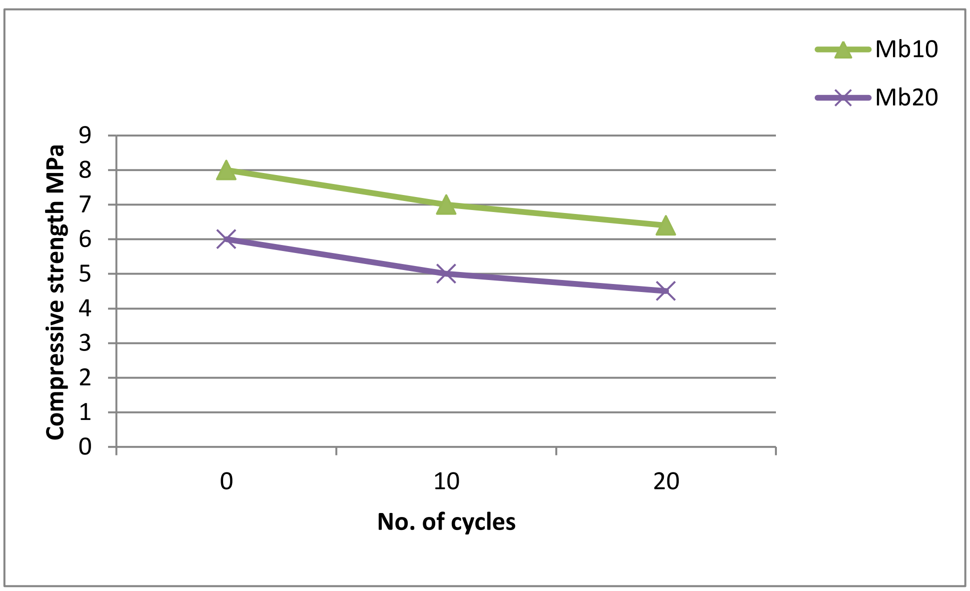

Figure2. Variations of compressive strength with no. of wetting and drying cycle (long intervals).

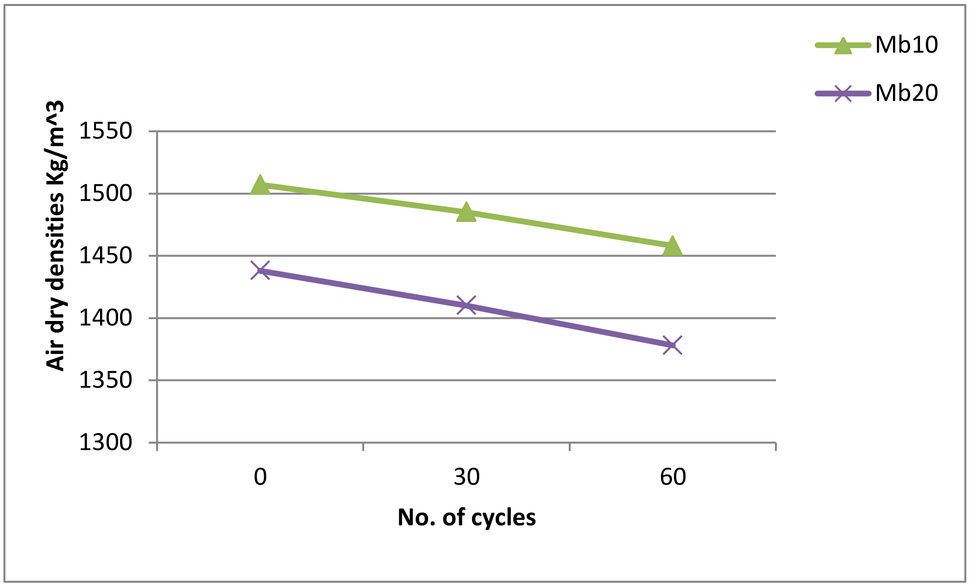

Figure3. Variation of air dry density of no-fine concrete with no. of wetting and drying cycle (short intervals).

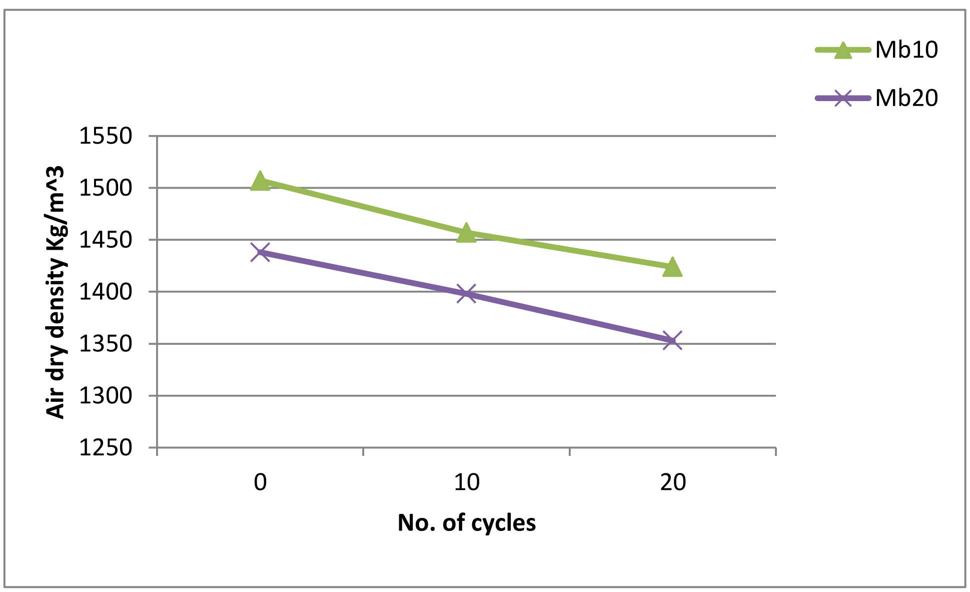

Figure4. Variation of air dry density of no-fine concrete with no. of wetting and drying cycle (long intervals).

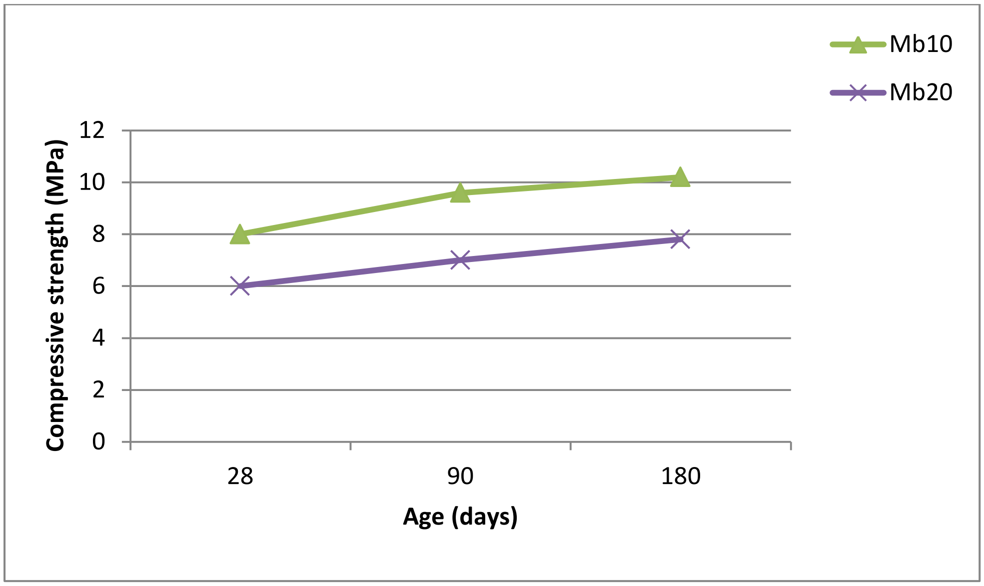

Figure5. Compressive strength of no-fine concrete with different age.

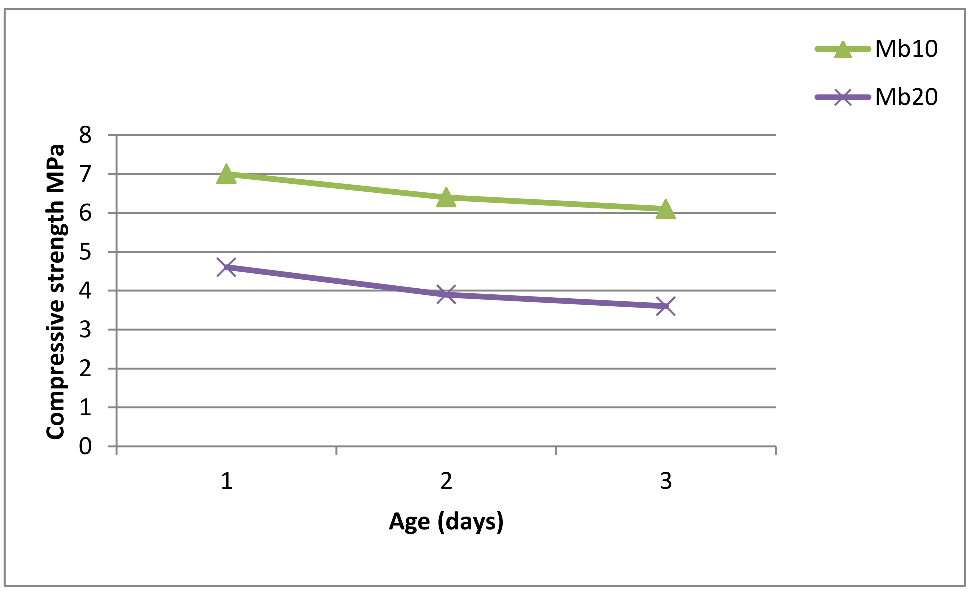

Figure6. Compressive strength with age for no-fine concrete specimens under sealed curing.

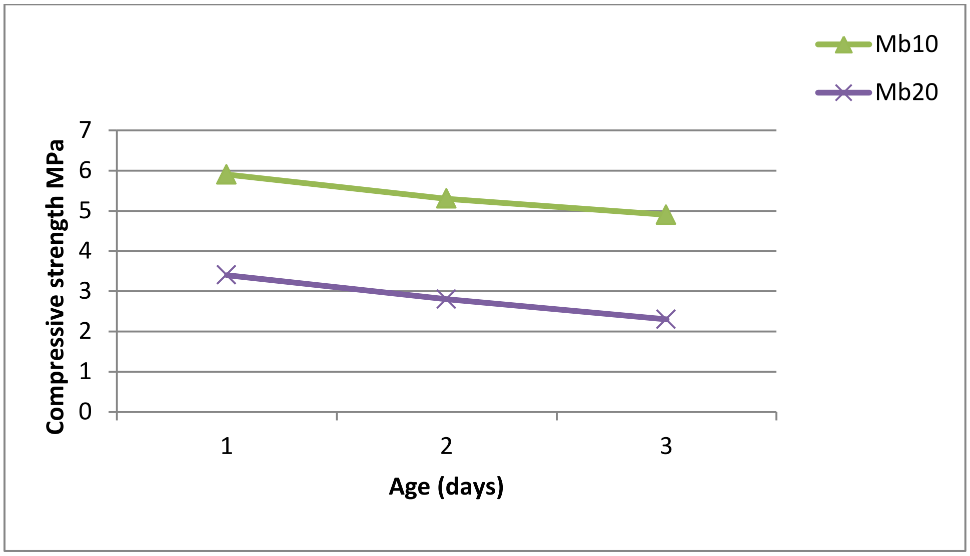

Figure7. Compressive strength with age for no-fine concrete specimens under air curing.

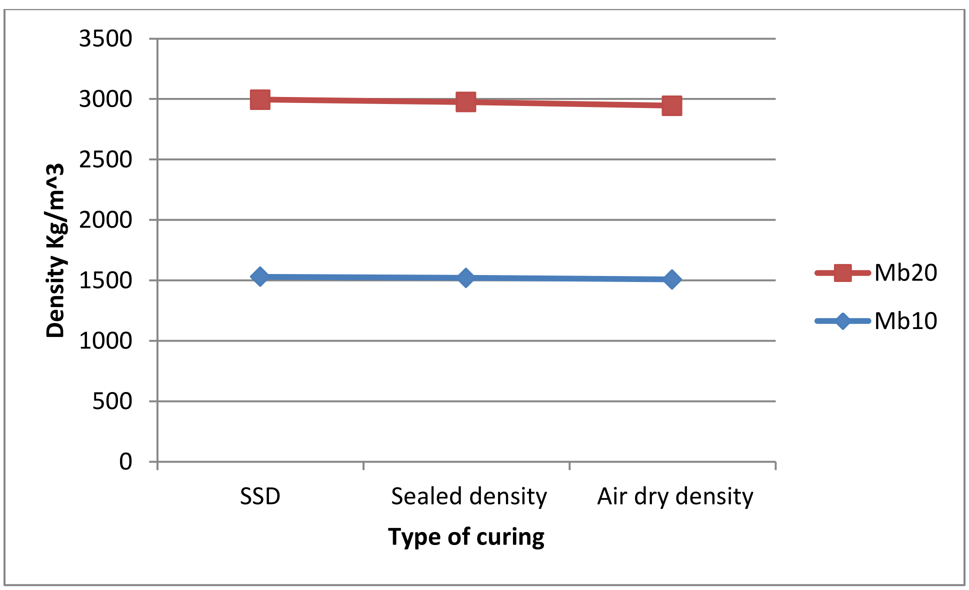

Figure8. Density at 28 days with type of curing.

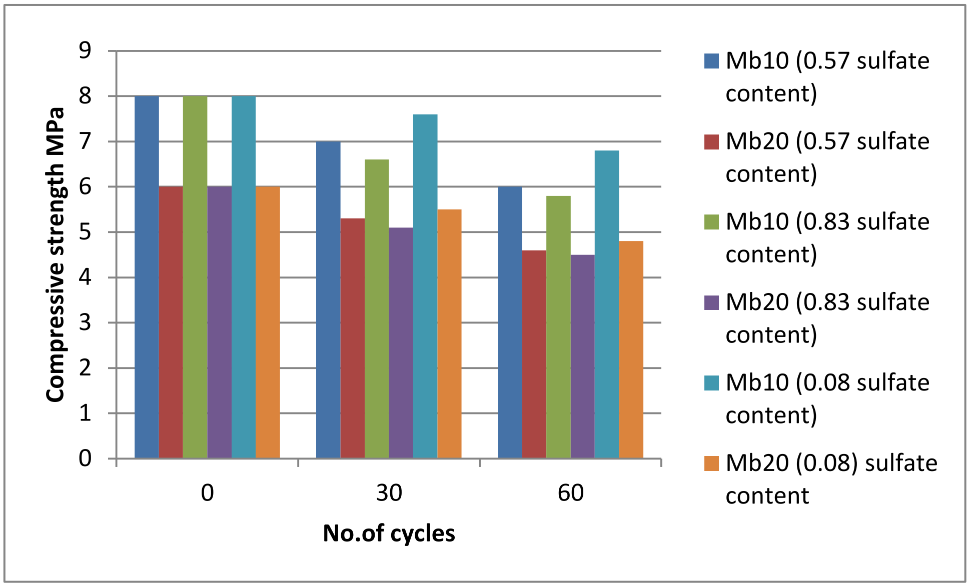

Figure9. Compressive strength with No. of cycles of wetting and drying for no-fine concrete specimens.

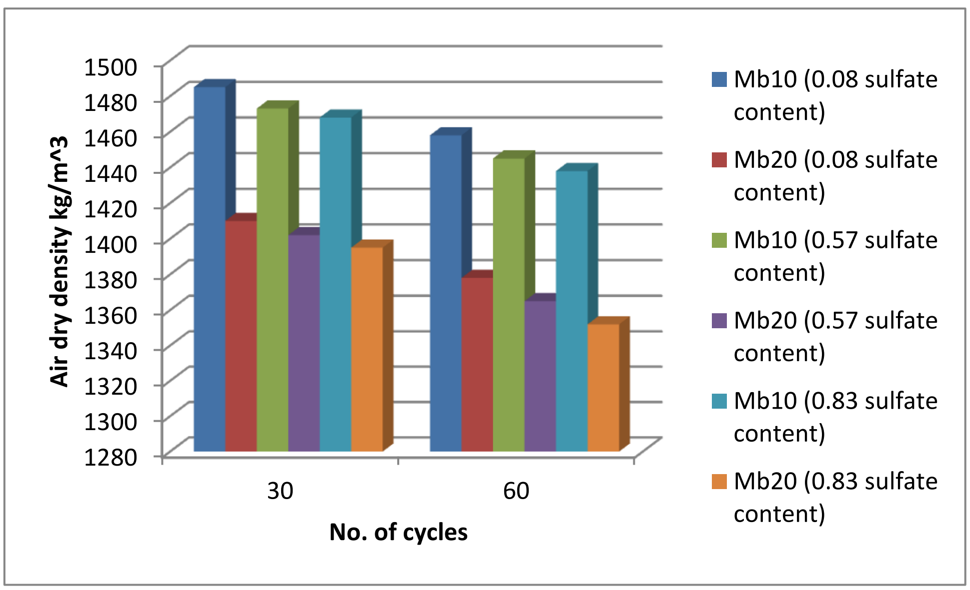

Figure10. Bulk density with No. of cycles of sulfate attack test for no-fine concrete specimens.

Some Properties of Polymer Modified Self-Compacting Concrete Exposed to Kerosene and Gas Oil

Ph. Dr. Nada Mahdi Fawzi
College of Engineering-University of Baghdad
E-mail:naljalawi@yahoo com

M.Sc. Aqeel Kareem Weli
Engineer in oil products distribution company
E-mail:abumalbaqer@yahoo.com

ABSTRACT

This thesis aims to study the effect of addition polymer materials on mechanical properties of self-compacting concrete, and also to assess the influence of petroleum products (kerosene and gas oil) on mechanical properties of polymer modified self-compacting concrete (PMSCC) after different exposure periods of (30 ,60 ,90 ,and 180 days).

Two type of curing are used; 28 days in water for SCC and 2 days in water followed 26 days in air for PMSCC.

The test results show that the PMSCC (15% P/C ratio) which is exposed to oil products recorded a lower deterioration in compressive strength's values than reference concrete. The percentages of reduction in compressive strength values of PMSCC (15% P/C ratio) was (6.03%) and (9.61%) up to 180 days of exposure to kerosene and gas oil respectively, relative to the same mix immersed in water, while the percentages of reduction in compressive strength values of SCC (reference concrete) was (21.18%) and (25.19%) up to 180 days of exposure to kerosene and gas oil respectively, relative to the same mix immersed in water.

Flexural strength results present improvement for all ages and for all concrete mixes with all percentages of polymer content.

The total water absorption values of PMSCC (15% P/C ratio) showed a better performance than reference concrete mix when exposed to oil products. It was (1.34, 2.21, 2.17) % up to 180 days with samples immersed in water, kerosene, and gas oil respectively, with percentages of reduction of (23.86%), (33.83%), and (31.33%) relative to the SCC (reference concrete).

Key words: polymer, self-compacting, kerosene, gas oil.

بعض خواص الخرسانة المعدلة بالبوليمر ذاتية الرص المعرضة إلى النفط وزيت الغاز

أ.د. ندى مهدي فوزي
كلية الهندسة/جامعة بغداد

م.عقيل كريم ولي
شركة توزيع المنتجات النفطية

الخلاصة

الهدف من هذا البحث هو دراسة تأثير أضافه مواد بوليمرية على الخواص الطرية والميكانيكية للخرسانة ذاتية الرص, وكذلك أيجاد تأثير المشتقات النفطية (النفط الأبيض وزيت الغاز) على الخواص الميكانيكية للخرسانة المعدلة بالبوليمر ذاتية الرص والخرسانة ذاتية الرص بعد التعرض لفترات مختلفة (30 ،60،90،180) يوم.

نوعين من الانضاج تم استعمالهما حيث كانت 28 يوم غمر بالماء للخرسانة ذاتية الرص بينما 2يوم غمر بالماء متبوعة 26 يوم بالهواء للخرسانة المعدلة بالبوليمر ذاتية الرص.

أظهرت نتائج فحص الخرسانة ذاتية الرص والخرسانة المعدلة بالبوليمر ذاتية الرص المغمورة بشكل مستمر في الماء تطوراً في خواصها الميكانيكية عند زيادة فترة الغمر بالماء . بينما تأثرت الخواص الميكانيكية للخرسانة ذاتية الرص والخرسانة المعدلة بالبوليمر ذاتية الرص المعرضة بشكل مستمر للمشتقات النفطية سلبياً.

سجلت نتائج فحص الخرسانة المعدلة بالبوليمر ذاتية الرص المعرضة للمنتجات النفطية ادني تدهور في قيم مقاومة الانضغاط من الخرسانة المرجعية. حيث كانت النسبة المئوية للنقصان في مقاومة الانضغاط (6,03)% ، (9,61)% بعد 180 يوما من التعرض للنفط الأبيض وزيت الغاز على التوالي نسبة الى نفس الخلطة للنماذج المغمورة في الماء, بينما النسبة المئوية

للنقصان في مقاومة الانضغاط للخرسانة المرجعية كانت (21,18)% و (25,19)% بعد 180 يوما من التعرض للنفط الأبيض وزيت الغاز على التوالي نسبة إلى نفس الخلطة للنماذج المغمورة في الماء.
أظهرت نتائج مقاومه الانحناء إلى حصول تحسن في كل الأعمار وفي جميع نسب البوليمر.
أظهرت نتائج امتصاص الماء الكلي للخرسانة المعدلة بالبوليمر ذاتية الرص وبنسبه استبدال 15% من مادة البوليمر إلى الاسمنت أداء أفضل من الخلطة المرجعية عند تعرضها للمنتجات النفطية, حيث كانت نسب الامتصاص الكلي هي (1.34 , 2.21 , 2.17) بعد 180 يوما من التعرض للماء والنفط الأبيض وزيت الغاز وبنقصان مقداره (23.86 ، 33.83 ، 31.33)% نسبة إلى الخرسانة ذاتية الرص (الخرسانة المرجعية).
الكلمات الرئيسية: بوليمر, ذاتية الرص, النفط الابيض, زيت الغاز.

1. INTRODUCTION

Oil has become one of the most vital energy resources from the beginning of the previous century for its unique economic and operative characteristics. This has enabled it to exceed the other available power resources, and its importance has increased rapidly with its wide spread use and the discovery of huge oil reserves in different parts of the world**, Ra'ed, 2002**.

The main problems that restrict the successful use of concrete to store fuel oil are: the leakage of oils especially the lighter products (that have specific gravity 0.875 at temperature $15C^0$) through the structure pores, shrinkage cracks and joints**, lea, 2004.**

There is a difference in behavior of the petroleum storage concrete tanks, and water storage concrete tanks**, Matti, 1976.** has shown that the leakage from concrete water tanks may reduce with time due to the closure of some of the voids, disconnection of the capillary channels and healing of some of the cracks due to the continuous hydration, and or accumulation of impurities. Because of the inert nature of the petroleum towards concrete, such continued hydration is less likely to occur in concrete petroleum tanks, but the wax deposits that are found in crude oil may decrease the permeability of concrete. So, it is very important to decrease the cracks to a lower bound to avoid any leakage of oil from the structure and to protect the concrete from deterioration**.**

Due to the dominant improvements in the properties of concrete containing different types of admixtures, it is very important to study the effect of these admixtures on the behavior of concrete exposed to oil products, **Al hamadani, 1997.**

1 .2: Polymer Modified Self-Compacting Concrete (PMSCC)

Polymer modified self-compacting concrete achieves the advantages of both Self-Compacting Concrete (SCC) and Polymer Modified Concrete (PMC). Polymer modified SCC may be used successfully in repair of concrete elements or construct new concrete elements especially when concrete is subjected to sever conditions, **Aliabdo , 2012.**

1.2.1 : Polymer modified concrete

One of the ways to make a material of high mechanical properties with satisfactory durability in various environment and high aesthetic values is through a polymer modification of concrete. These relatively new materials offer the advantages of higher strength ,improved durability, good resistance to corrosion, reduced water permeability and greater resistance to damage from freeze-thaw cycles.

The polymer materials are a group of carbon-containing (organic) materials, have macromolecular structure of this sort. Polymer Latexes (or dispersions) which consist of very small (0.05-5mm in diameter) polymer particles dispersed in water and usually produced by emulsion polymerization. The polymer latexes are copolymer systems of two or more different monomers, **Ohama, 1998**.

Styrene-Butadiene-Rubber (SBR) is the type of polymer (Elastomers) which is used in this study. It is a copolymer produced from butadiene and styrene. SBR has good low-temperature, good water and weather resistance**, Bolton, 1998.**

1.2.2 Self-compacting concrete

SCC represents one of the most outstanding advances in concrete technology during the last decade. At first developed in Japan in the last 1980s, SCC meanwhile is spread all over the world with a steadily increasing number of applications, **Holschemacher, and Klug, 2002.**

Due to the highly flowable nature of SCC, care is required to ensure excellent filling ability, passing ability and adequate stability. This ability is achieved by ensuring suitable rheological properties of fresh concrete: a low yield stress value associated with adequate plastic viscosity. The use of superplasticizer and optimization of fine-particles packing and flow behavior are those two of the central aspects of (SCC) mix proportioning . Fine particles including both cement and filler materials (Pozzolanic or non Pozzolanic) are used in mix proportioning. Among non Pozzolanic fillers, (limestone and dolomite) fines are most frequently used to increase the content of fine particles in mixes, **Bosiljkov, 2003.**

2. LITERATURE REVIEW

, Ali, 2006. has studied the effect of oil products on mechanical properties i.e. compressive, splitting tensile, and flexural tensile strength of original and polymer modified reactive powder concrete in different exposure periods. He has concluded that

- for the specimens made of mixes containing polymer in different percentages, it appears that, the increase in polymer to cement ratio (P/C) leads to continuous increase in compressive strength up to P/C ratio of 0.14. The percentage of increase in compressive strength for specimens cured in water up to 180 days was 10.8% compared with reference concrete (original reactive powder concrete).
- the specimens made of mixes containing polymer in different percentages, showed significant increase in flexural strength with the increase in P/C-ratio.
- for all types of concrete, the amount of increase in compressive, splitting tensile and flexural strengths for the specimens cured in water is larger than that obtained from specimens exposed to oil products up to the older ages of exposure to oil products.
- polymer modified reactive powder concrete shows higher reduction in total absorption for both specimens cured in water or exposed to oil products. The percentages of reduction in total absorption of polymer modified RPC compared to original RPC up to 180 days are (40%) , (31%) and (42.8)% , for water, kerosene and gas oil respectively.

, Ali, 2013. has studied the effect of oil products on properties of self-compacting concrete. He has concluded that:

- The compressive strength of SCC decreases as the exposure period to oil products increases. The reduction for exposure period at 60 -180 days is between 11.59 -27.93% and 14.62 -40.74% , 11.24 -37.69%and 2.66 % -23.81% for SCC continuously immersed in crude oil, motor oil, fuel oil and gas oil respectively.
- The modulus of rupture is reduced in the range of 3.74 -24.01%, 4-25.98% , 3.6-24.67% and 0.4 -21.92% after exposing to crude oil, motor oil , fuel oil and gas oil respectively for exposure period of 60 - 180 days.
- The total absorption for SCC specimens continuous immersion in different oil products increases as the time of continuously immersed increases. The percentage increase in exposure period of 180 days is 1.9%, 2.64%, 2.91%, 3.06% for SCC continuously immersed in crude oil ,gas oil ,motor oil and fuel oil respectively.

, Abed Al-Ameer, 2011. studied the influence of oil products (kerosene and diesel oil) on the mechanical properties of steel fiber reinforced concrete. The compressive strength of concrete decreases as the exposure period to oil products increases. At 120 days of exposure, the compressive strength of concrete cubes (with and without SF) decreases. The decrease occure in compressive strength for plain and for steel fiber reinforced concrete exposed to kerosene or diesel.

3. MATERIALS AND EXPERIMENTAL WORK

3.1 Materials

Ordinary Portland cement type (I) was used. **Tables 1** and **2** show the physical and chemical composition properties of the cement used in this investigation respectively. Natural sand from Al-Ukhaider region was used and crashed gravel with nominal maximum size of 14 mm from Al-Niba'ee region was used.

3.2: Admixture:

3.2.1: High range water reducing admixture(superplasticiser)

Superplasticizer used throughout this study is known commercially as Glenium 51.

Glenium 51 is differentiated from conventional superplasticisers in that it is based on a unique carboxylic ether polymer with long lateral chains. This greatly improves cement dispersion. At the start of the mixing process the same electrostatic dispersion occurs but the presence of the lateral chains, linked to the polymer backbone, generates a steric hindrance which stabilizes the cement particles capacity to separate and disperse. Glenium 51 is free from chlorides and complies with ASTM C494 Types A and F. Glenium 51 is compatible with all Portland cements that meet recognized international standards**, Degussa, 2002. Table 3** lists the properties of this product.

3.2.2 Polymer

Styrene-butadiene copolymer latex (SBR) which is commercially named "Rheomix 141" was used as a polymer modifier in this research. Rheomix 141 is a milky, white liquid, produced from styrene and butadiene by high pressure emulsion polymerization. The latex consists of microscopic particles of synthetic rubber dispersed in an aqueous solution. Rheomix 141 modified mixes may be slightly darker than corresponding unmodified mixes.

All cementitious mixes stated shall be modified with Rheomix 141, styrene butadiene copolymer Latex, manufactured by Basf or similarly approved supplier has the following specification shown in **Table 4**.

3.2.3 Fly Ash

Fly ash class F was used in this research according to **ASTM C618-03**, the chemical and physical properties of fly ash are given in **Table 5** and **Table 6**, respectively.

3.3 Oil Product

kerosene and Gas oil were used in this investigation. They were brought from AL – Daura Refinery and stored in airtight steel and plastic containers to avoid any losses.

3.4 Concrete Mixtures

Four types of concrete mixtures (R, P1, P2 and P3) were made with respect to the ratio of polymer (SBR) in concrete, mix design of SCC and PMSCC must satisfy the criteria of filling ability, passing ability and segregation resistance. The mix design method used in the present study is according to, **ERMCO, 2005**, then the proportions of materials were modified after obtaining a satisfactory self-compactability by evaluating fresh concrete tests. Several trial mixes were carried out to determine the suitable dosage of superplasticizer, with compressive strength of about 40 MPa at 28 days. Types of Mixture and its proportions shown in **Table 7**.

3.5 Casting and Curing of Specimens

The molds were cleaned and the internal surface was oiled to prevent adhesion of concrete after hardening. Then the specimens were covered with polyethylene sheet in the laboratory for about 24 hrs and then the specimens were remolded carefully and immersed in curing water for two days and for 26 days in air for PMSCC specimens, while the SCC was immersed in curing water for 28 days.

3.6 Type of Exposure to Oil Products

After curing, some of these specimens were taken out to dry in the air for one week under laboratory environment. After drying, some of these specimens were exposed to kerosene and the others were exposed to gas oil for different periods (30, 60, 90 and 180 days).

3.7 Tests of Fresh Concrete

The workability of self-compacting concrete is high, so the conventional methods for testing the workability cannot be used. Slump flow test, T50 cm test, V-Funnel test, L-Box test, and U-Box test were used as test methods for workability properties of SCC by many researchers and agencies. These methods are given in the European Federation dedicated to specialist construction chemicals and concrete systems SCC Guidelines**, ERMCO, 2005.**

3.8 Hardened Concrete Test

3.8.1 Compressive strength test

The compressive strength was determined by using cubes tests according to British Standard **B.S 1881: part 116, 1989**. Each concrete cube was taken out of the curing tank and placed in the compression device on one of its sides (after cleaning the faces of the cube) so that the compressive load is applied perpendicularly to the direction of concrete placement in the moulds at a constant rate.

3.8.2 Modulus of rupture

Prismatic specimens of (100*100*400) were used in the Modulus of Rupture (flexural strength) test and cured as those of compressive strength, according to **ASTM C78-02**, with clear span supported by 300 mm. The average of the two specimens was recorded.

3.8.3 Total water absorption

Total absorption in hardened concrete was determined according to **ASTM C642–06** [(74)]. This test method is useful in developing the data required for conversion between mass and volume for concrete. It can be used to determine conformance with specifications for concrete and to show differences from place to place within a mass of concrete.

4. RESULTS AND DISCUSSIONS

4.1 Fresh Properties of SCC and PMSCC

The four mixes (R, P1, P2 and P3) were prepared, then the fresh properties of each of them were evaluated by four tests, which were, Slump Flow and T50 test, V-Funnel test, L-Box test, and U-Box test. **Table 8** shows the results of these tests for all mixes.

4.1.1: High range water reducing admixture dosages

Dosages of superplasticizer were adjusted to give the required flow. The effect of polymer/cement ratio (p/c) content on the dosage of chemical admixture (superplasticizer) is shown in **Table 9**. From this Table, it is clearly that the increase in polymer/cement ratio content is lead to decrease in the dosage of required superplasticizer. This effect may be due to the plasticizing effect of polymers. The reduction in a dosage of superplasticizer is 15%, 25% and 35% for polymer modified self-compacting concrete with 5.0%, 10.0% and 15.0% styrene butadiene rubber, respectively compared with that of self-compacting concrete. From this table, it is seen water content is constant.

4.2 Hardened Properties of SCC and PMSCC

4.2.1 Compressive strength

The results of compressive strength tests on reference concrete (SCC) and the polymer modified self-compacting concrete (PMSCC) exposed to oil products up to 180 days of exposure are given in **Tables 10**. The graphical representations of these relations are shown in **Figs. 1 to 4.**

The compressive strength of Polymer modified self-compacting concrete immersed in water is higher than that of reference concrete (SCC) at all test periods and the percentages of increasing rise with the increase in P/C ratio. This behavior may be due to the addition of polymers (SBR) which leads to form a continuous three dimensional polymer network which interpenetrates the cement paste, and the partial filling of the pores with the polymer particles reduces the porosity of the polymer modified self compacting concrete.

The test results showed that there's no difference in compressive strength for specimens which exposed to kerosene and gas oil for 30 days, in comparison with the same mixes immersed in water and at the same age. This is due to the pores inside the SCC and PMSCC which were still partially filled with water leading to further hydration that delays, the deterioration of concrete**, Al-Hadithi, 2005**. Also, it may be due to the low permeability of SCC and PMSCC mix produced in this investigation since the presence of flyash leads to a modification in the microstructure of concrete. This will delay the deterioration of all mixes subjected to oil products.

The compressive strength for all mixes exposed to oil products decreases moderately with time in comparison with the same mixes immersed in water at the same age. The deterioration in compressive strength may be due to the extension of gel pores and spreading solid hydration components due to penetration of oil products into the microstructure of SCC and PMSCC leading to weak adhesion and cohesion forces in cement in addition to the effects of oil products on the SCC surface interactions. After exposure to the oil products, reference SCC indicates that the maximum percentages reduction values in compressive strength were up to 21.2% for the specimens exposed to kerosene and 25.2% for the specimens exposed to gas oil for 180 days respectively in comparison with the same mixes immersed in water at the same age. While the percentages of reduction in compressive strength for concrete mixes P1, P2, and P3 were 13.7%, 9.2%,and 6% for the specimens exposed to kerosene, and 14.8%, 11%,and 9.6% for the specimens exposed to gas oil for exposure periods of 180 days respectively, and when compared with the reference concrete it can be seen that the rate of deterioration decreased with the increase in P/C ratio at all test ages. The reasons for this behavior is the good compatibility for styrene butadiene rubber (SBR) Latex and bond strength, low porosity, in addition to the excellent strength and durability properties of the SBR itself, and the other reason for this behavior is the reference mixes enables them to gain a reasonable strength by the hydration operation only, whereas, for concrete mixes containing polymer (SBR) both the cement hydration and production of polymer film by polymerization are responsible for strength gain. In addition, the secondary hydration products around the pozzolan particles tend to fill the capacity void and reduce their size**, Mehta, 2002.**

4.2.2 Modulus of Rupture

The results of modulus of rupture tests on reference concrete (SCC) and the polymer modified self compacting concrete (PMSCC) exposed to oil products are given in **Table 11.** The graphical representations of these relations are shown plotted in **Figs. 5 to 8.**

The results of modulus of rupture of Polymer modified self-compacting concrete exposed to water is higher than that of reference concrete (SCC) at all test periods . Also this increase arises with the increase in P/C ratio at all ages. The reasons for this behavior in addition the reasons aforementioned in the compression are a considerable increase in the strength characteristics of the flexural section especially at tension side, because the transition zone elasticity will be utilized to large degree as compared with that of reference concrete.

The modulus of rupture for all mixes exposed to oil products decreases moderately with time. The reduction in modulus of rupture may be due to the extension of gel pores and spreading solid hydration components due to penetration of oil products into the microstructure of SCC and PMSCC leading to weak adhesion and cohesion forces in cement in addition to the effects of oil products on the SCC surface interactions.

For the reference concrete (SCC) exposed to the oil products, the maximum reduction values were up to 23.3% for the specimens exposed to kerosene and 27.6% for the specimens exposed to gas oil for 180 days respectively in comparison with the same mixes immersed in water. While the reduction in modulus of rupture for concrete mixes,P1, P2, P3 was 20.1%, 17.3%, 13.7% for the specimens exposed to kerosene, and 23.9%, 18.7%, 15.6% for the specimens exposed to gas oil for exposure periods of 180 days respectively in comparison with the same mixes immersed in water, and when compared with the reference concrete it can be seen that the rate of reduction in modulus of rupture is improved with the increase in P/C ratio at all test ages. The reasons for this behavior is the good compatibility between Styrene butadiene rubber (SBR) Latex and bond strength, low porosity, in addition to the excellent strength and durability properties of the SBR itself. The other reason for this behavior is the reference mixes make them gain a reasonable strength at early ages, as the hydration operation responsible for this strength, whereas, for concrete mixes containing polymer (SBR) both the cement hydration and production of polymer film by polymerization are responsible for strength gain. In addition, the secondary hydration products around the pozzolan particles tend to fill the capacity void and reduce their size.

4.2.3 Total Water Absorption

The results of total absorption tests for reference concrete (SCC) and the polymer modified self-compacting concrete (PMSCC) exposed to oil products are given in **Tables 12**. The graphical representations of these relations are shown plotted in **Figs. 9 to 12**.

Test results indicate that the total absorption of all specimens immersed in water decreases continuously with the progress of age. This is because of the partial filling of pores by the hydration and polymerization reaction which reduces capillary porosity, which is confirmed by other investigations.

The total water absorption decreases with the increase in P/C ratio of all specimens immersed in water at all test periods. This behavior is because of the low porosity of polymer modified self-compacting concrete compared with reference concrete and the dispersion of polymer particles (which fill or envelope the large pores) which create a tight membrane around these pores causing discontinuity of capillary pores**, Bolton, 1998. And, Mangat, 1978.** This polymeric system controls the water movement through the concrete structure. It is clear that the addition of polymer leads to decrease the absorption ratio in all conditions, where the percentage of decrease in absorption at the age of 28 day is (22.86, 28.31, 32.73)% for P1 , P2, P3 respectively, in comparison with the reference mixes

The total absorption of all mixes exposed to oil products increases with time. The total absorption for reference concrete increases gradually (2.43%, 2.71%, 2.86% and 3.34%) after exposure to kerosene, and (1.93%, 2.29%, 2.47% and 3.16%) after exposure to gas oil ,for soaking periods of 30,60, 90 and 180 days respectively, whereas, for concrete mixes P1, the total absorption increases gradually (2.18%, 2.47%, 2.51% and 2.94%) after exposure to kerosene, and (1.81%, 2.12%, 2.25% and 2.89%) after exposure to gas oil ,for soaking periods of 30,60, 90 and 180 days respectively , whereas, for concrete mixes P2, the total absorption increases gradually (2.02%, 2.31%, 2.43% and 2.77%) after exposure to kerosene, and (1.74%, 1.96%, 2.03% and 2.43%) after exposure to gas oil, for soaking periods of 30,60, 90 and 180 days respectively, whereas, for concrete mixes P3, the total absorption increases gradually (1.84 %, 1.94 %, 2.08 % and 2.21 %) after exposure to kerosene, and (1.68%, 1.84%, 1.89% and 2.17 %) after exposure to gas oil ,for soaking periods of 30,60, 90 and 180 days respectively. This is due to the harmful effects of oil products on the microstructure of the concrete(microstructure of cement paste) and the bond between aggregate and cement paste formation of micro crack in the interfacial transition zone which leads to increase the porosity and then increase the absorption of concrete**, Matti, 1976.**

Polymer modified self-compacting concrete mixtures (P1, P2 and P3) exposed to the oil products showed significant reduction in total absorption when compared with the reference concrete exposed to the oil products, and the rate of reduction in total absorption was raised with the increase in P/C ratio at all test ages. The percentages of reduction in mixes P1 compared to Reference concrete were (13.61%) and (9.34%) up to 180 days for specimens exposed to kerosene and gas oil respectively, whereas, for concrete mixes P2, the percentages of reduction in mixes P2 compared to Reference concrete were (17.07%) and (23.1%) up to 180 days for specimens exposed to kerosene and gas oil respectively, whereas, for concrete mixes P3, the percentages of reduction in mixes P3 compared to Reference concrete were (33.83%) and (31.33%) up to 180 days for specimens exposed to kerosene and gas oil respectively. This is due to the fact that polymer modified concrete has a structure in which the larger pores can be filled with polymers or sealed with continuous polymer films. In general, the effect of polymer filling or sealing increases with a rise in the polymer content or polymer-cement ratio. These features are reflected in reduced water absorption, **Ohama, 1998.**

5. CONCLUSIONS

Based on the experimental results of this research, the following conclusions can be drawn:

1. For constant water content, the polymer content (SBR) reduces the dosage of superplasticizer when added to the concrete mixes and the percentage of reduction increases with the increase in the P/C ratio.
2. The compressive strength and modulus of rupture, for SCC and PMSCC specimens continuously immersed in water after curing increase with age, while the total absorption and voids for SCC and PMSCC specimens continuously immersed in water after curing decrease with age.
3. The effect of polymer on modulus of rupture is higher than that on compressive strength in specimens immersed in water after curing. For modulus of rupture, the percentage of

increase in mix P3 up to 180 days is (43.61%), whereas, for compressive strength is (17.18%) in comparison with the reference concrete.

4. The test results for the compressive strength and modulus of rupture of all mixes exposed to kerosene and gas oil for 30 days showed that there's no difference in values when comparison with the same mixes immersed in water at the same age, then they drop continuously up to 180 days exposure.
5. The compressive strength of all mixes deteriorated as the exposure period to oil products increases. The percentage of reduction in reference concrete for exposure period at 180 days is (21.2%, and 25.2%), whereas, for concrete mixes P1 it is (13.7%, 14.8%). For concrete mixes P2 it is (9.2%, and 11%). For concrete mixes P3 it is (6%, and 9.6%). After exposure to kerosene, and gas oil ,respectively in comparison with the same mixes immersed in water at the same age.
6. The modulus of rupture of all mixes deteriorated as the exposure period to oil products increases. The percentage of reduction in reference concrete for exposure period at 180 days is (23.3 %, and 27.6%), whereas, for concrete mixes P1 it is (20.1%, 23.9%), whereas, for concrete mixes P2 it is (17.3%, and 18.7%). For concrete mixes P3 it is (13.7%, and 15.6%). After exposure to kerosene, and gas oil, respectively in comparison with the same mixes immersed in water at the same age.
7. The total absorption of all mixes increases as the exposure period to oil products increases. The percentage of increase in reference concrete for exposure period of 180 days is (89.77%, and 79.55%), whereas, for concrete mixes P1 it is (78.18%, 75.15%), and for concrete mixes P2 it is (85.91%, and 63.09%). For concrete mixes P3 it is (64.93%, and 61.94%). After exposure to kerosene, and gas oil, respectively in comparison with the same mixes immersed in water at the same age.
8. The development of strength with age for mix P3, when exposed to oil products is larger than that obtained for reference concrete specimens immersed in water at the same age. The compressive strength up to 180 days for mix P3 was (57.7 and 55.5) MPa after exposed to kerosene and gas oil, while it was (52.4) MPa for reference concrete.

REFERENCE

- Al hamadani, Z.K., 1997, *Improvement of the Performance of Concrete Against Oil Products*, M.Sc. Thesis, University of technology Baghdad.

- Alaa Abed Al-Ameer, S. A., 2011, *Effect of Petroleum Products on Steel Fiber Reinforced Concrete*. University of Baghdad in, M.s.c. Thesis.

- Al-Hadithi, A. I., 2005, *Flexural, Impact and Thermal properties of Polymer Modified Concrete".* PhD Thesis, University of Technology.

- Ali A. A., 2013, *Properties of Self-Compacting Concrete Exposed to Oil Products*, M.Sc. Thesis, University of Technology.

- Ali, A. S., 2006, *Mechanical Properties and Durability of Original and Polymer Modified Reactive Powder Concrete Exposed to Oil Products*, Ph.D. Thesis, University of Technology.

- Aliabdo , A. A., 2012, *Experimental Investigation on the Properties of Polymer*

Modified SCC, Construction and Building Materials,V34, No.1, PP.(584-592).

- ASTM C 618-03, 2003, "*Standard Specification for Coal Fly Ash and Raw or Calcined Natural Pozzolan for Use in Concrete*", Annual Book of ASTM Standards, Vol.04-02, February 2003, p. 3.

- ASTM C 642-06, 2006, *"Standard Test method for Density, Absorption, and Voids in Hardened Concrete.* ,Annual Book of ASTM Standards, V.04.02 ,PP.1-3.

- ASTM C 78-2, 2005, *''Standard Test Method for Flexural Strength of Concrete'.* , American Society for Testing and Materials.

- B.S 1881: Part 116, 1989, *''Method for Determination of Compressive Strength of Concrete Cubes''.* , British Standards Institution.

- Bolton, W., 1998, *Engineering Materials Technology*, 3rd.ed., Butterworth Heinemann. Oxford, Boston.

- Bosiljkov, V. B., 2003, *SCC Mixes with Poorly Graded Aggregate and High Volume of Limestone Filler*, Cement and Concrete Research, V.33, PP.1279-1286.

- Degussa, 2002, *Construction Chemicals" Glenium 51 Technical Date Sheet*, 06 /97 MBT-ME.

- ERMCO, 2005, *The self-compacting concrete European project group* ,The European Guidelines for Self-Compacting Concrete, PP43-56.

- Holschemacher, K, and Klug, Y., 2002, *A Database for the Evaluation of Hardened of SCC*, LACER No. 7, PP.123-134.

- Lea. F.M, 2004., *The Chemistry of Concrete". London*, Arnold, pp.338.

- Mangat, P.S., and Evans, D.A., 1978, *Influence of Polymer Admixtures on the Strength, Deformation, and Fracture of High Strength Concrete*, Second International Congress of Polymers in Concrete, College of Engineering, University of Texas, Austin, pp.67-86.

- Matti. M.A, 1976.,*Some Properties and Permeability of Concrete in Direct Contact with Crude Oil*, Ph. D. Thesis, University of Sheffield.

- Mehta, P. K., and Monterio, J. M., 2002, *"Concrete Microstructure, Properties and Materials,*" , pp. 23-31.

- Ohama, Y., 1998., *Polymer-based Admixtures*, Nihon University, Koriyama, Fukushima-ken, Japan.

- Ra'ed, K.H, 2002., *Behavior of High Performance Concrete in Direct Contact with Oil Products*, M.Sc. thesis, University of Technology, Baghdad.

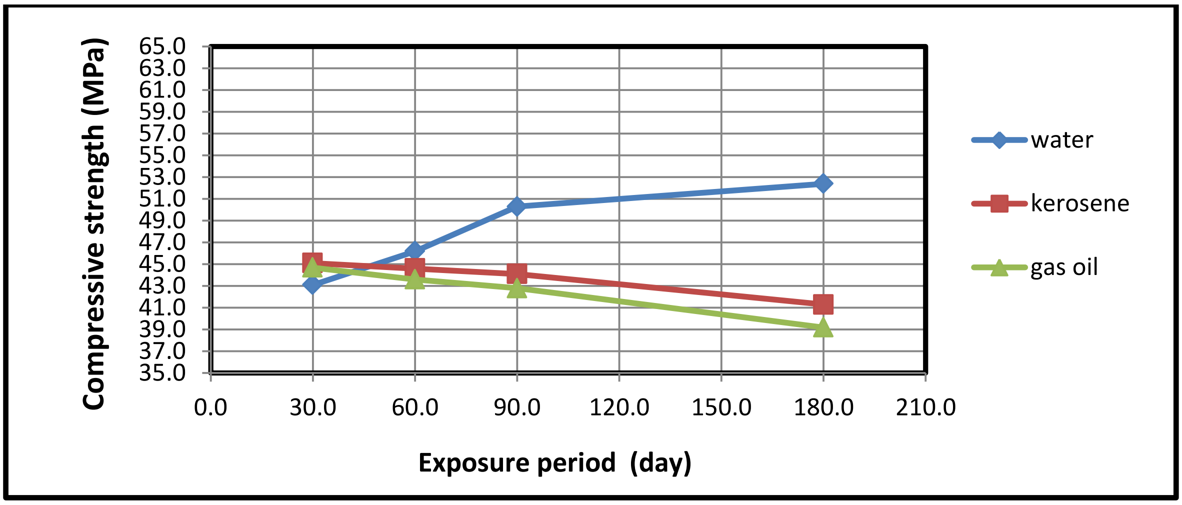

Figure 1. Relationship between compressive strength for mix R and durations of immersion in water, kerosene and gas oil.

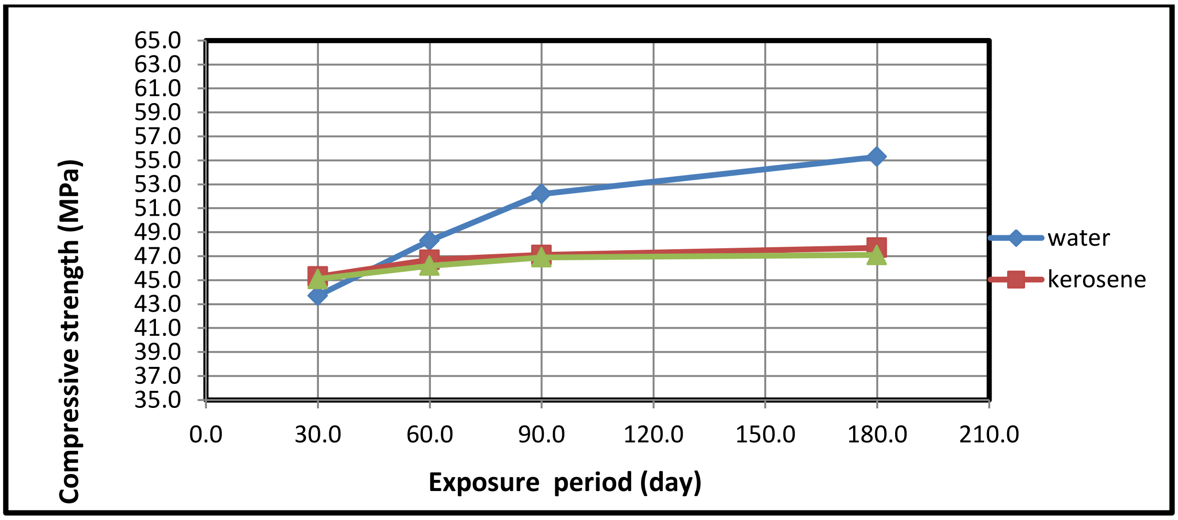

Figure 2. Relationship between compressive strength for mix P1 and durations of immersion in water, kerosene and gas oil.

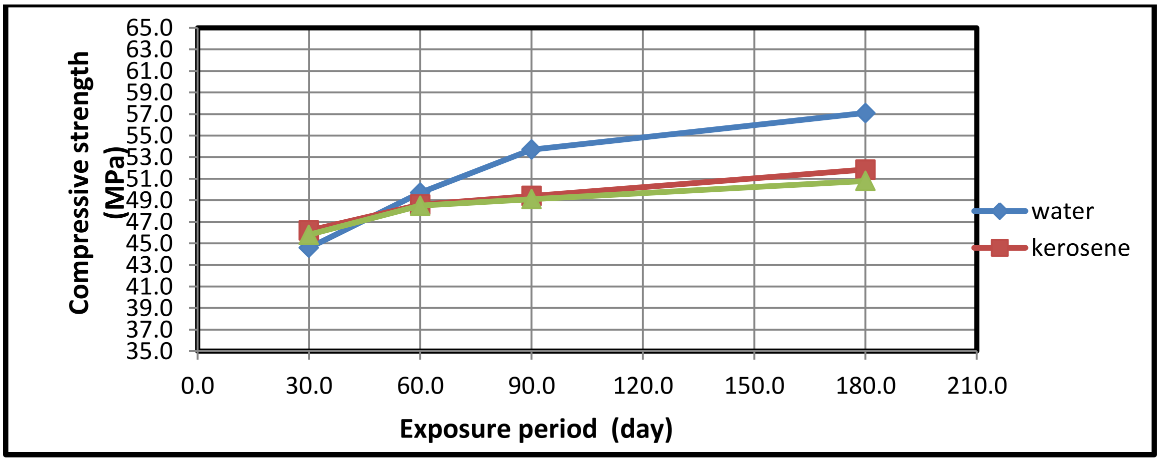

Figure 3. Relationship between compressive strength for mix P2 and durations of immersion in water, kerosene and gas oil.

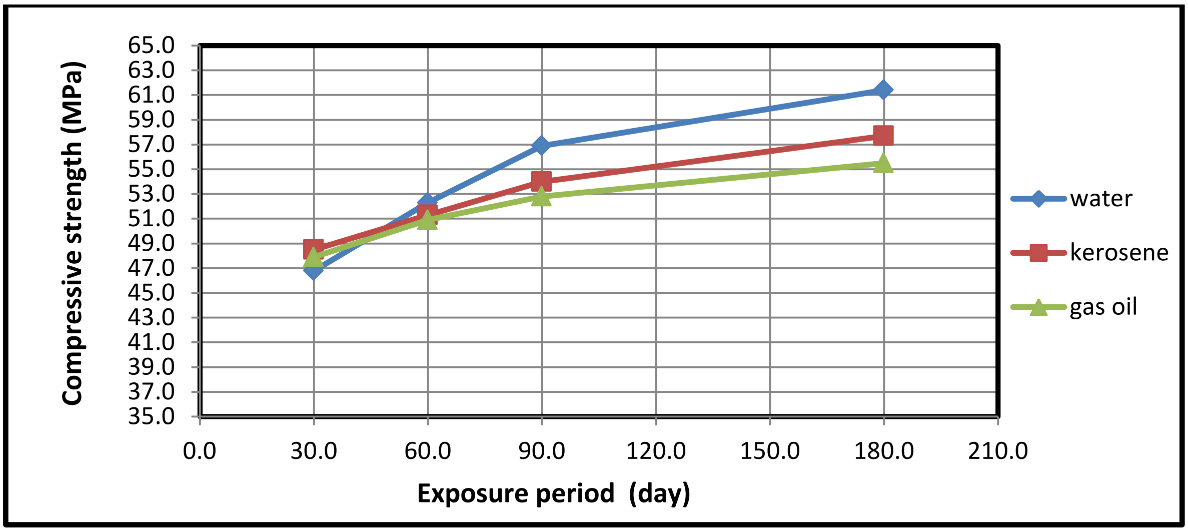

Figure 4. Relationship between compressive strength for mix P3 and durations of immersion in water, kerosene and gas oil.

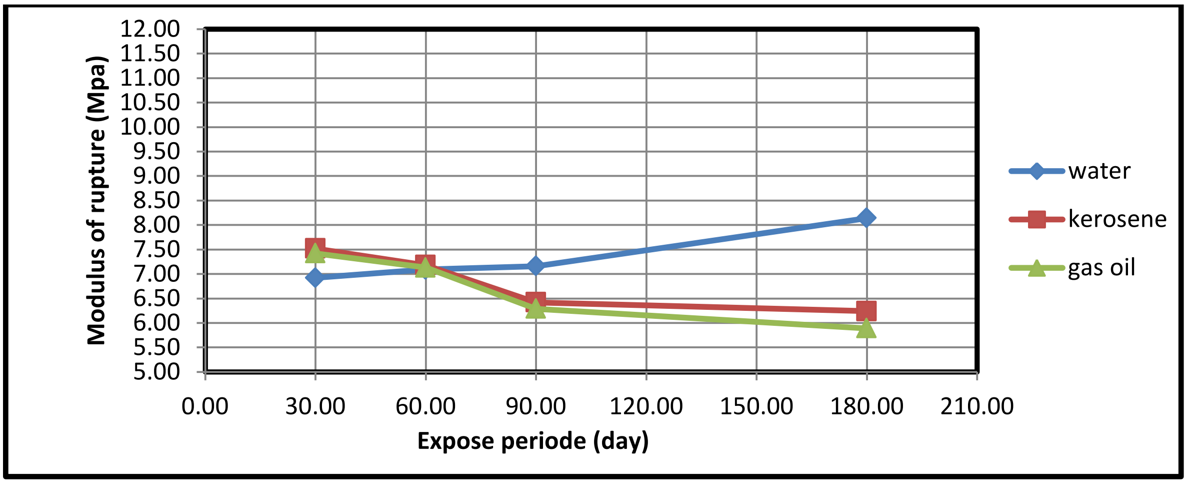

Figure 5. Relationship between modulus of rupture for mix R and durations of immersion in water, kerosene and gas oil.

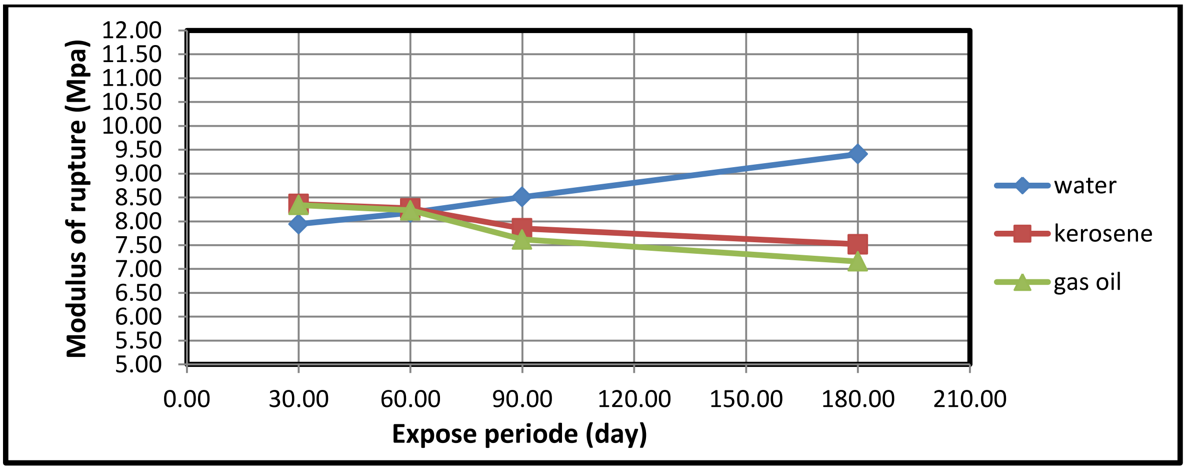

Figure 6. Relationship between modulus of rupture for mix P1 and durations of immersion in water, kerosene and gas oil.

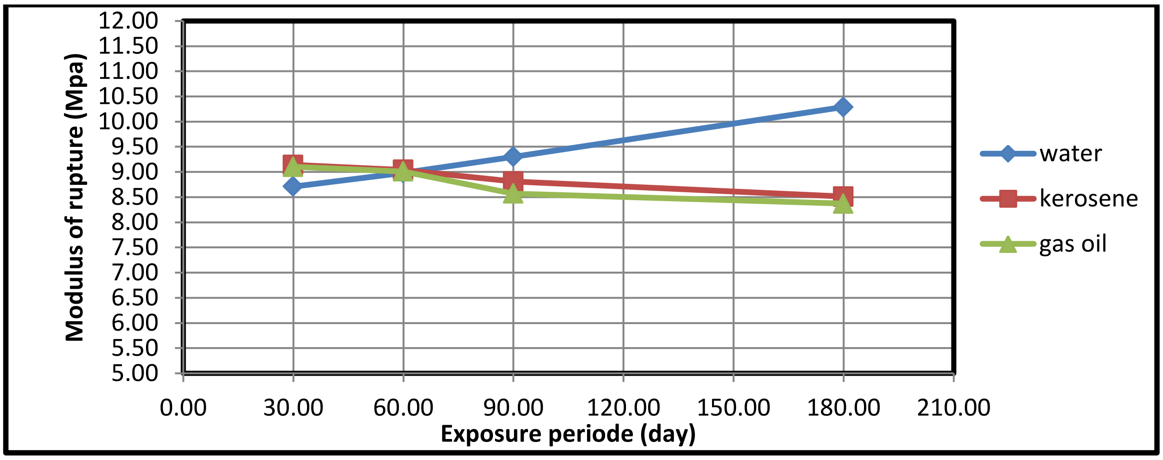

Figure 7. Relationship between modulus of rupture for mix P2 and durations of immersion in water, kerosene and gas oil.

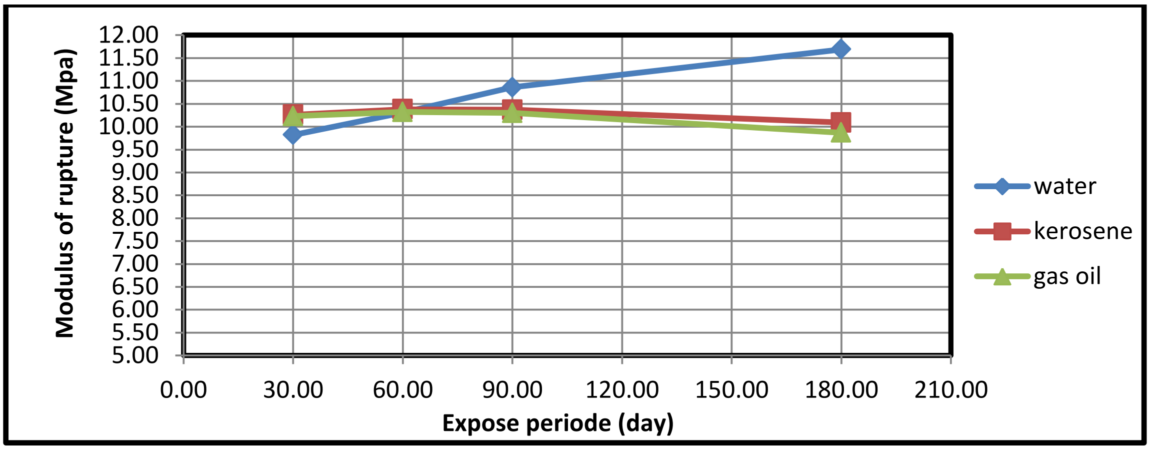

Figure 8. Relationship between modulus of rupture for mix P3 and durations of immersion in water, kerosene and gas oil.

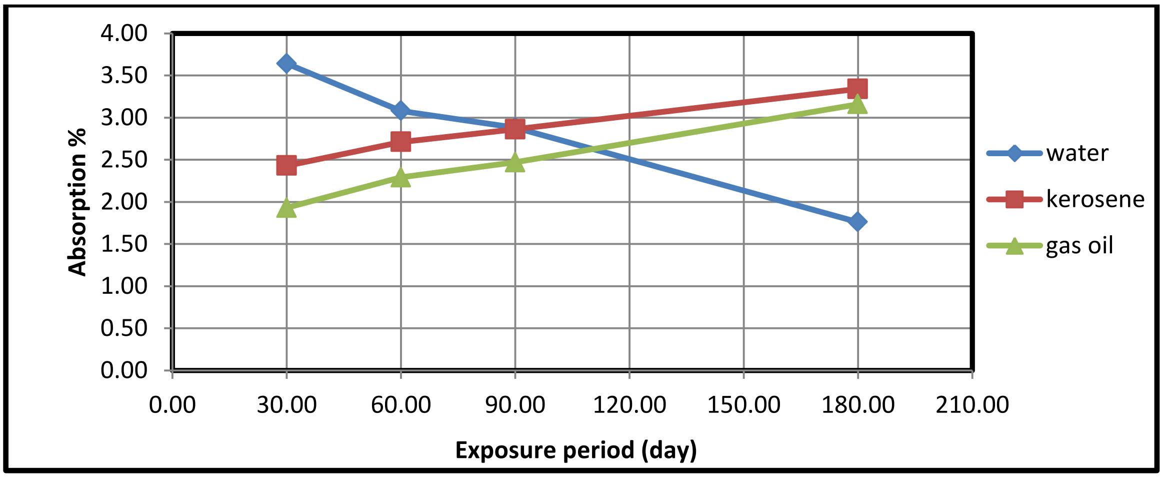

Figure 9. Relationship between total absorption for Reference concrete (R1) and durations of immersion in water, kerosene and gas

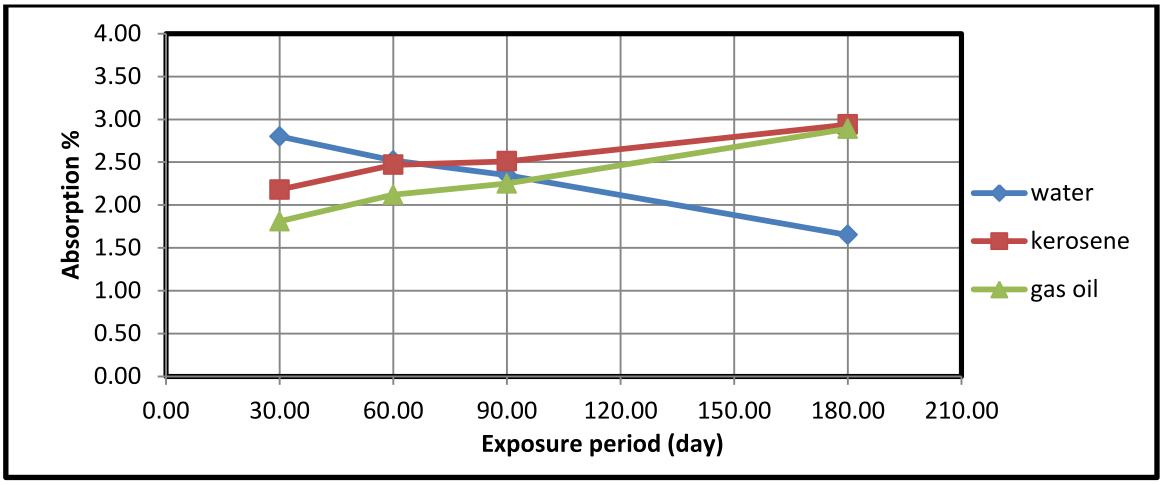

Figure 10. Relationship between total absorption for mix P1 and durations of immersion in water, kerosene and gas oil.

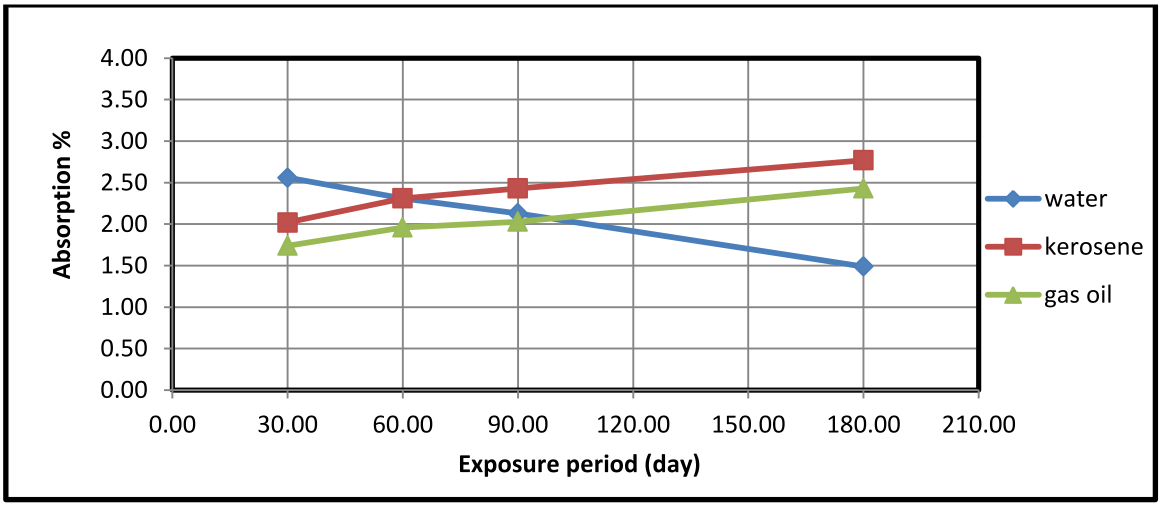

Figure 11. Relationship between total absorption for mix P2 and durations of immersion in water, kerosene and gas oil.

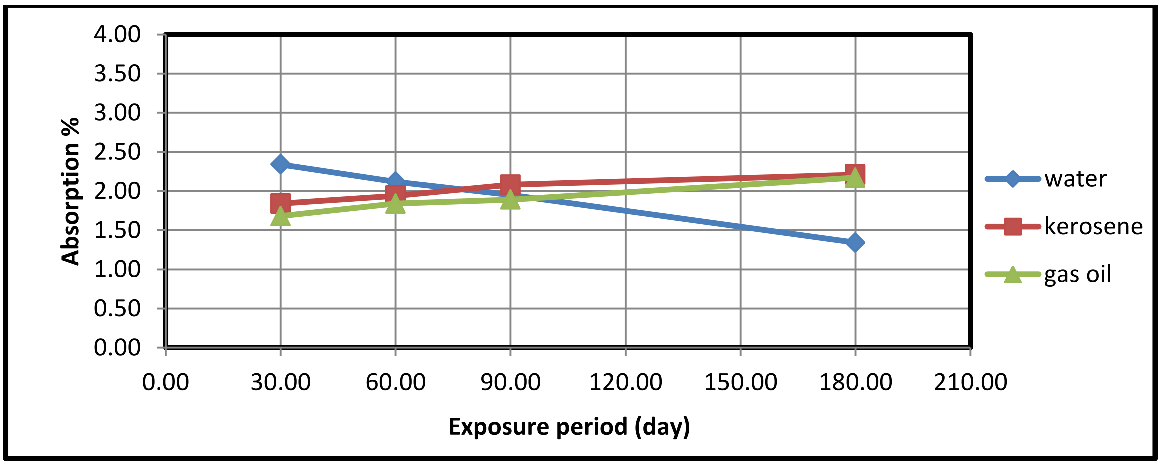

Figure 12. Relationship between total absorption for mix P3 and durations of immersion in water, kerosene and gas oil.

Table 1. Physical properties of cement.

Physical properties	Test result	Limit of Iraqi Specification No. 5/1984
Specific surface area (Blaine method), cm^2/gm	2900	≥2300
Setting time (Vicat's apparatus) Initial setting time, hrs: min. Final setting, hrs: min.	 1:50 4:29	 ≥ 0:45 ≤10:0
Compressive strength 3days, N/mm^2 7days, N/mm^2	 20.4 31.6	 ≥15 ≥23

Table 2. Chemical composition and main compounds of cement.

Oxide Composition	Abbreviation	Content (%)	Limit of Iraqi Specification NO. 5/1984
Lime	CaO	58.98	-
Silica	SiO_2	19.74	-
Alumina	Al_2O_3	3.72	-
Iron Oxide	Fe_2O_3	3.54	-
Magnesia	MgO	3.78	≤5.0%
Sulfate	SO_3	2.73	≤2.8%
Loss on Ignition	L.O.I.	3.46	≤4.0%
Insoluble residue	I.R.	0.74	≤1.5%
Lime saturation Factor	L.S.F.	0.92	0.66-1.02
Main Compounds (Bogue's equations)			
Tricalcium Silicate	C_3S	52.26	-
Dicalcium Silicate	C_2S	17.17	-
Tricalcium Aluminate	C_3A	3.87	-
Tetracalcium alumino-ferrite	C_4AF	10.77	-

Table 3. Typical properties of (Glenium 51).

NO.	Main action	Concrete super plasticizer
1	Form	Viscous liquid
2	Color	Light brown
3	Relative density	1.1 at 20°C
4	pH value	6.6
5	Viscosity	128 +/ - 30 cps at 20°C

Table 4. Typical properties of styrene butadiene copolymer Latex.

Properties	Description
Composition	A milky, white styrene butadiene copolymer latex, specifically made for use with Portland cement.
Ph	10.5.
Specific gravity	1.00 – 1.03
Mean particle size	0.17 micron.
Butadiene content	40% by weight of Rheomix 141 polymer.
Styrene	60 (% by weight)

Table 5. Chemical properties of Fly Ash.

Chemical Properties	Oxide content %	ASTM C 618-03
Silica (SiO_2)	54.7	
Alumina (Al_2O_3)	31.91	
Iron Oxide (Fe_2O_3)	8.79	
Calcium Oxide (CaO)	1.5	
Magnesia Oxide (MgO)	0.21	
Sulfate (SO_3)	0.06	$\leq$ 5 %
Loss on Ignition	2.05	$\leq$ 6 %
SiO_2+Al_2O_3+Fe_2O_3	95.4	$\geq$ 70

Table 6. Physical properties of Fly Ash.

Physical Properties	Test Results
Colour	Grey
Specific gravity	2.15
Strength Activity Index	93%

Table 7. Types of concrete mixtures and Mix proportions.

Type of Mixing	Mix proportions (Kg/m3)							w/b	plasticize/C	Polymer/C	Reduction S.P.
	cement	water	F.A.	C.A.	Fly Ash	Polymer	Plasticize (S.P)				
R	410	175	840	850	41	0	5.33	0.38	1.3	0%	0%
P1	396.8	175	840	850	41	13.2	4.53	0.4	1.14	5%	15%
P2	383.6	175	840	850	41	26.4	4	0.41	1.04	10%	25%
P3	370.5	175	840	850	41	39.5	3.46	0.43	0.93	15%	35%

Table 8. Results of fresh properties tests for all mixes.

Set No.	Dosage of S.P l/m^3	Slump flow (mm)	T50 (Sec.)	L-Box blocking ratio (H2/H1)	U-Box filling height (H2-H1) Mm	V-Funnel Time (Sec.)	Segregation Index (visual)
R	5.33	720	4	0.90	12	10	homogeneous
P1	4.53	710	5	0.85	15	11	homogeneous
P2	4	725	3.5	0.91	10	9	homogeneous
P3	3.46	715	5	0.88	13	10	homogeneous

Table 9. Average compressive strength results of all mixes at various periods of immersion in water and oil products.

Set no.	Compressive strength (MPa) after 28 days curing	Compressive strength of all mixes after different exposure periods (MPa)											
		Duration of exposure (Age) day											
		30(65)			60(95)			90(125)			180(215)		
		Water	Kerosene	gas oil	water	Kerosene	gas oil	Water	kerosene	gas oil	water	Kerosene	gas oil
R	40.6	43.1	45.1	44.7	46.2	44.6	43.6	50.3	44.1	42.8	52.4	41.3	39.2
P1	40.8	43.7	45.3	45.1	48.3	46.7	46.2	52.2	47.1	46.9	55.3	47.7	47.1
P2	41.5	44.6	46.2	45.8	49.7	48.6	48.5	53.7	49.4	49.1	57.1	51.9	50.8
P3	42.8	46.8	48.5	47.9	52.3	51.3	50.9	56.9	54.0	52.8	61.4	57.7	55.5

Table 10. Modulus of rupture results of all mixes at various periods of immersion in water or oil products.

Set no.	Modulus of rupture (MPa) after 28 days curing	Modulus of rupture of all mixes at different exposure periods (MPa)											
		Duration of exposure (Age) day											
		30(65)			60(95)			90(125)			180(215)		
		Water	Kerosene	gas oil	water	Kerosene	gas oil	Water	Kerosene	gas oil	water	Kerosene	gas oil
R	6.85	6.92	7.52	7.42	7.09	7.18	7.13	7.16	6.42	6.29	8.14	6.24	5.89
P1	7.35	7.94	8.36	8.34	8.18	8.27	8.23	8.51	7.85	7.62	9.41	7.52	7.16
P2	7.77	8.71	9.14	9.10	8.98	9.04	9.01	9.30	8.81	8.57	10.29	8.51	8.37
P3	8.65	9.82	10.26	10.23	10.31	10.38	10.32	10.86	10.37	10.30	11.69	10.09	9.87

Table 11. Total water absorption results of all mixes at various periods of immersion in water or oil products.

Set no.	Total absorption (%) after 28 days curing	Total absorption of all mixes at different exposure periods (%)											
		Duration of exposure (Age) day											
		30(65)			60(95)			90(125)			180(215)		
		Water	Kerosene	gas oil	water	Kerosene	gas oil	Water	Kerosene	gas oil	water	Kerosene	gas oil
R	3.85	3.64	2.43	1.93	3.08	2.71	2.29	2.88	2.86	2.47	1.76	3.34	3.16
P1	2.97	2.80	2.18	1.81	2.52	2.47	2.12	2.35	2.51	2.25	1.65	2.94	2.89
P2	2.76	2.56	2.02	1.74	2.31	2.31	1.96	2.13	2.43	2.03	1.49	2.77	2.43
P3	2.59	2.34	1.84	1.68	2.12	1.94	1.84	1.95	2.08	1.89	1.34	2.21	2.17

Studying the Combination Effect of Additives and Micro Steel Fibers on Cracks of Self-Healing Concrete

Muhannad Hussien Muhsin
Asst. Dr.
Department of Civil Engnieering
University of Baghdad
Email: Mhnd7@yahoo.com

Israa Hameed AbdElzahra
Engineer
Department of Civil Engnieering
University of Baghdad
Email: is90raa@yahoo.com

ABSTRACT

In this study, the effect of the combination of micro steel fibers and additives (calcium hydroxide and sodium carbonate) on the size of cracks formation and healing them were investigated. This study aims to apply the use of self-healing phenomenon to repair cracks and to enhance the service life of the concrete structures. Micro steel fibers straight type were used in this research with 0.2% and 0.4% by volume of concrete. A weight of 20 and 30 kg/m^3 of $Ca(OH)_2$ and 2 and 3 kg/m^3 of Na_2CO_3 were used as a partial cement replacement. The results confirm that the concrete cracks were significantly self-healed up to 30 days re-curing. Cracks width up to 0.2 mm were completely self-healed after re-curing for 90 days by using the combination of micro steel fiber of 0.4% by volume of concrete and 25 kg/m^3 of $Ca(OH)_2$ and 2.5 kg/m^3 of Na_2CO_3 as a partial replacement of cement. Products of Self-healing are observed by Scanning Electron Microscopy (SEM) with Energy Dispersive X-Ray Analysis (EDX). It was found that self-healing occurred mainly due to precipitation of calcium carbonate.

Key words: healing agents, cracking of concrete, self-healing concrete.

دراسة ألتأثير المشترك لكل من المواد المساعدة على شفاء الشقوق والالياف الحديدية الدقيقة على تكون الشقوق وشفاؤها في الخرسانة ذاتية الشفاء

مهند حسين محسن
م. دكتور
جامعة بغداد - كلية الهندسة

اسراء حميد عبد الزهرة
مهندسة
جامعة بغداد قسم الهندسة المدنية

الخلاصة

في هذا البحث تم دراسة اصلاح شقوق الخرسانة ذاتيا باستعمال مواد مضافة تساعد على التئام الشقوق وتأثير ذلك على خواص الخرسانة ، حيث يهدف البحث من خلال تطبيق طريقة الشفاء الذاتي لشقوق الخرسانة الى تقليل اصلاحات الخرسانة وكلفتها و تحسين ديمومتها من خلال معالجة الشقوق و تقليل الاضرار الناتجة عنها.تم استخدام الالياف الحديدية الدقيقة و المواد المضافة المساعدة على شفاء الشقوق والمتمثلة ب(هيدروكسيد الكالسيوم وكاربونات الصوديوم) والتي تم استبدالها بنسب من وزن السمنت ،تم اضافة الالياف الحديدية بنسب 0.2% و 0.4% و المواد المساعدة على الشفاء بنسب استبدال 20كغم /م3 الى 30 كغم/م3 لهيدروكسيد الصوديوم ،وبنسب استبدال 2كغم/م3 و 3كغم/م3 لكاربونات الصوديوم و من ثم دراسة التأثير المشترك لكل من الالياف الحديدية الدقيقة والمواد المساعدة على الشفاء. النتائج اعطت تغير واضح جدا بسمك الشقوق بعمر 30يوم واعطت التئام تام للشقوق بعمر 90يوم ، حيث ان الشقوق لغاية سمك 0.2ملم تم شفاؤها تماما وافضل نتائج كانت للخلطات الحاوية على الياف حديدية بنسبة 0.4 والمواد المساعدة على الشفاء بنسبة 25 كغم/م3 من هيدروكسيد الكالسيوم و 2.5كغم/م3 من كاربونات الصوديوم. اظهرت نتائج فحص المجهر الالكتروني الماسح لتحليل المادة المالئة للشقوق ان كاربونات الكالسيوم هي المادة التي ترسبت في الشقوق وأدت الى غلقها وشفاؤها.

الكلمات الرئيسية: المواد المساعدة على الشفاء، تشقق الخرسانة، الخرسانة ذاتية الشفاء.

1. INTRODUCTION

1.1 General

Concrete is widely used as a building material due to its high strength, durability, availability, versatility. These properties added to the low production cost and recyclability make concrete the most commonly used building material in the world. However, concrete is quasi-brittle material, effective in compression and quite week in tension, and susceptible to many sources of damage, caused by external loading (dynamic or static loading), differential thermal exposure cycles, drying shrinkage, chemical attacks, corrosion, and other environmental conditions. Cracks are one of various types of damages, **Ramos et al., 2013.**Concrete elements, under bending or in tension loading condition, easily crack. Cracks formation is considered a natural feature of the concrete material. Because of this, reinforcements are installed. Inert reinforcements are activated once the concrete cracks.

1.2 Micro Cracks

Cracking plays an important role in concrete's response to load in both tension and compression. As matter of fact, reinforced concrete structures are linked with cracks from the beginning of their service life. The stresses transfer capability of these cracks may powerfully influence the service life of some concrete structures such as foundations, underground structures, and offshore structures, especially when water gets through cracks, this promotes corrosion process and accelerates the damage of concrete structures, **Homma et al., 2009.**

The crack width should not exceed a recommended limit. Too wide cracks may reduce the ability of the concrete material to protect the reinforcements against corrosion. The serviceability limit of concrete structures is mainly governed by the extent of their damages, **Tittelboom et al., 2013.**

Cracks in concrete structures may indicate main structural problems and also may ruin the monolithic construction appearance. In addition, they can expose reinforcements to oxygen and moisture, and so make them more susceptible to corrosion.

However, if it was possible to know and understand the reasons of the different behaviors of concrete structures, subjected to mostly similar loading conditions, it might have the basis to design high durability concrete structures with low or negligible repair and maintenance costs needed. Moreover, the limit of serviceability of the concrete material by cracking could be overcome by cracks width control methodologies. The improvement of service life of structures would decrease the demand for concrete cracks rehabilitation and repair. The employment of concrete self-healing technologies has high capability as an excellent repair technique for cracked concrete exposed to a water leakage of underground structures such as foundations, pipes, culverts, and tunnels, **Ahn et al., 2010.**

Fine cracks in fractured concrete, if admitted to close without tangential displacement may heal completely under moist conditions. This is known as autogenous healing. It is primarily due to the occurrence of hydration of the unhydrated cement clinker, which becomes exposed to water upon the opening of the cracks. Healing is also aided by the creation of insoluble calcium carbonate from the reaction of calcium hydroxide in hydrated cement if carbonation takes place. Some mechanical blocking of the cracks may also occur if very fine material is suspended in the water, **Neville, 2011.**

1.3 Self-Healing Phenomena

Self-healing concrete is one of the modern and smart concretes, in which the cracks can be healed by themselves. These are due to un-hydrated cement particles interaction with moisture in the crack, **Truong et al., 2013.**

Edvardsen, 1999, explained that calcium carbonate crystallization within the crack fracture surface was the major mechanism for self-healing of matured concrete. In particular, a calcite formation in the region of water-effecting cracks takes place in the material arrangement $CaCO_3$-CO_2-H_2O corresponding to the following reactions

$$Ca^{2+} + CO_3{}^{2-} \leftrightarrow CaCO_3 (pH_{water} > 8) \tag{1}$$

$$Ca^{2+} + HCO_3{}^{-} \leftrightarrow CaCO_3 + H^{+} \qquad (7.5 < pH_{water} > 8) \tag{2}$$

A reaction between the calcium ions Ca2+, obtained from the concrete materials, and the in-water available carbonates CO_3^{2-}, or bicarbonates HCO_3^{-} produces the water-insoluble $CaCO_3$. Furthermore, CO_2 partial pressure in the water, pH value of the water, and water temperature favor the $CaCO_3$ precipitation in the crack. Calcium carbonate is a compound almost like stalactite, and has high cut off performance with great stability **Edvardsen, 1999.**

Also, there is the man-created self-healing concrete ability (autonomic healing). It includes a replacement of a small amount of cement or sand materials by self-healing additives. The self-healing concrete material is known as one of the recent smart concretes that can heal its cracks and other minor imperfections by itself. The healing is the results of the interaction of the moisture with the unhydrated cement clinker and, or other materials in the region of crack surfaces under some special circumstances, **Truong et al., 2013.**

2. MATERIALS

The materials used in this research are:

2.1Cement

Ordinary Portland cement produced in Iraq supplied from Taslooja cement factory was used in this work. It was stored in a dry and shaded place to avoid exposure to the atmospheric conditions like humidity. The chemical properties of the cement are shown in **Tables 1**; results conform to the, **Iraqi specification No.5/1984.**

2.2Fine Aggregate

Natural sand supplied from Al-Ekhadir quarry was used in concrete mixes of this work. The grading and physical and chemical properties of fine aggregate are shown in **Tables 2 and 3**. The test results indicated that the sand grading is within the limits specified by the **Iraqi Standard IQS No. 45/1984** and lies in Zone 3.

2.3 Coarse Aggregate

Natural gravel was used as coarse aggregate with a nominal aggregate size of (5-19 mm) for all mixes. It was obtained from Al-Nibaee region. The grading and physical and chemical properties of the used aggregate conform to **Iraqi Standard IQS No. 45/1984** as shown in **Tables 4** and **5**.

2.4Mixing Water

Ordinary drinking tap water was used throughout this work in the mixing of concrete.

2.5Calcium Hydroxide ($Ca(OH)_2$)

Conventional type of $Ca(OH)_2$ supplied from supplier was used.. **Fig. 1** shows Calcium hydroxide used in tests.

2.6 Crystallization Material Na_2CO_3

Conventional type of Na_2CO_3 supplied from supplier was used. **Fig. 2** shows Na_2CO_3 used in tests.

2.7 Micro Steel Fiber

Micro steel fiber straight type was used in this research with 0.2% and 0.4% by volume of concrete. The properties of the micro steel fiber used in research are shown in **Table 6** according to supplier. **Fig. 3** shows micro steel fiber used in tests.

3. MIX DESIGN

Design of Concrete mixes is made according to the **American Method ACI 211-91** to achieve cubs with compressive strength of 35 MPa , with slump of 75 to 100 mm, water to cement ratio (w/c) equal to 0.45, fineness modulus of fine aggregate equal to 2.4, maximum size of coarse aggregate equal to 19 and non-air-entrained concrete with unit mass equal to 2280 kg/m3. According to the mix design procedure, the mix proportion is (1:1.217:2.281). The mix proportions by weight of the concrete materials are given in **Table 7.**

4. THE EXPERIMENTAL PROGRAM

The experimental program consists of 7 concrete mixes **Table 8** gives the details for each mix.

4.1 Mixing Procedure

The mixing process was performed by a hand mixer. The saturated surface dry fine aggregate was placed in smooth, clean, non-absorbent metal pan, after that the cement was mixed with the required quantity of $Ca(OH)_2$ and Na_2CO_3 added to the fine aggregate. The saturated surface dry coarse aggregate was added to the mix, and the whole dry materials were well mixed for about two minutes. The required amount of water was added gradually and the whole constituents were mixed for further two minutes to get a homogenous mix, for the case of fiber reinforced concrete, the micro steel fibers were added manually to the mix. Then, the constituents' materials were mixed for about three minutes, until a homogenous concrete was obtained.

4.2 Curing

All specimens were cured in water with laboratory environments.

4.3 Cracking of Specimens

A compressive force was applied on the specimens of (100×100×100) mm concrete cubes using a digital compression machine till 40% of the ultimate load of each cube to form compressive micro-cracks in the concrete cubes. The cracking load was chosen according to **ACI Committee 224R-09 ,2009.**

4.4 LABROTATRY TESTS

4.4.1 Ultrasonic pulse velocity test

Concrete cubes (100×100×100) mm were used to determine the ultrasonic pulse velocity (UPV) test according to **ASTM C 597-02**, using a device commercially known as PUNDIT. Transducers (55 KHZ) were used to transmit and receive ultrasonic waves the direct method was applied, in which the transducers were placed on opposite faces of the concrete cube to be tested after lubricating with grease to get a smooth surface and to ensure the transition of the greatest amount of energy to the specimen. The method of measuring (U.P.V.) depends on the time (T) needed for the waves to pass a distance (L) in concrete. The following equation is used to calculate UPV:

$V = L/T$

Where:

V: Ultrasonic pulse velocity (km/sec);

L: Average length of specimen (mm);

T: Transit time (microsecond).

4.4.2 Microscopic observation

Cracks are introduced at age of 30 days from casting, and all the cracked cubes were observed by microscope and cracks widths were measured for all the cubes and the cracks up to 0.2 mm were fixed and measured again after 30 and 90 days from the day of cracking. A microscope with a lens that magnifies and clarifies the micro cracks up to 10X was used. The crack meter microscopic devise is shown in **Fig. 4.**

4.1.6 Scanning electron microscope

Scanning Electron Microscopy (SEM) with Energy Dispersive X-Ray Analysis (EDX) was used to observe the products of Self-healing. Two specimens of (2×2×1) cm were used; the first was from the cracked surface specimen of concrete mix M2, and the second sample was taken from the cracked surface specimen of concrete mix M6. The test was carried out in Physics Department in College of Science / University of Nahrain.

5. RESULTS AND DISSCUSIONS

5.1 Ultrasonic Pulse Velocity (UPV)

Ultrasonic pulse velocity test gives information about microstructure properties of concrete like density, porosity, and micro cracks. Also, there is a relationship between the increases of UPV and the increases of compressive strength, **Zhong and Yao, 2008.** So, the UPV was used to show the difference between concrete mixes and demonstrate the deterioration after cracking and the recovering of compressive strength and micro cracks of deteriorated samples after curing. Cubes specimens having dimensions (100× 100×100) mm were used for all concrete mixes (M1, M2, M3, M5, M6, M7, and M8) to measure the time between the transmitter and receiver transducers; from measured time, the wave velocity was calculated. The speed was calculated for each cube before cracking (at age of 28 days from casting), immediately after cracking (at age of 28 days from casting), and after 90 days of curing from cracking day (after healing). The changes in velocity before and after cracking reflect the inner micro cracks as the UPV related to the microstructure properties. For all concrete mixes the results show that the UPV decreases after cracking due to micro cracks producing. After 90 days of curing, the results of concrete mix M1 show very slight increasing in UPV as shown in **Fig. 5**. This could be most likely attributed to the very simple development in hydration process by hydration of unhydrated cement particles. For concrete mixes M2 and M3 the results show very clear increasing in UPV, and that indicates recovering of compressive strength, and healing of micro cracks due to the products results from self-healing reactions. Also, it indicates that the percentage of increasing in UPV increases with increasing of healing agents percentage so that the results of UPV of M3 are higher than that of M2 as shown in **Fig. 6**, and **Fig. 7**. For concrete mixes M5 and M6 the results show simple increasing in UPV and that refers to simple development in compressive strength. Also, the micro steel fiber bridges across some micro cracks and bonds the two sides of micro crack leading to simple healing in crack due to hydration of the unhydrated cement particles, **Homma et al., 2009**, but it still has a simple effects and appears through very small micro cracks. Also the results show that the concrete mix of higher micro steel fiber content M6 gives better regaining in UPV results after curing than concrete mix M5 as shown in **Figs. 8** and **9.** For concrete mixes M7 and M8 the results show a complete recovering of UPV and give the best results in comparison with other mixes. This could be most likely attributed to the recovering in compressive strength and healing of micro cracks resulting from the combination effect of micro steel fiber and healing agents. Concrete mix M8 gives higher recovering than mix M7 due to the higher Vf of micro steel fiber and higher content of healing agents as shown in **Figs. 10** and **11.**

5.2 Microscopic Observation

Cracks width was measured for the specimens of all concrete mixes after cracks production and after curing of 90 days from cracking. The measured cracks width for reference concrete (M1) after cracking and after curing of 90 days from cracking shown in **Fig. 12**. According to microscopic observation, no healing of cracks appears after curing, so, crack width after curing did not change in most of specimens. For concrete mixes M2 and M3 the crack width decreased due to the precipitation of products of self-healing, and the results indicate that the amount of healing agents affects the self-healing of cracks so concrete mix M3 give better results than concrete mix M2 and that attributed due to the higher concentration of Ca^{2+} and CO_3^{2-} ions. That leads to increasing the precipitation of self-healing products $CaCO_3$ as shown in **Figs.13** and**14.** In concrete mixes containing micro steel fiber without healing agents (M5) and (M6)the results show small changes in crack width before and after curing and that refers to the effect of micro steel fibers in bridging across the crack which decreases the crack width.

That leads to decreasing the distance between crack faces, connecting the particles to facilitate and accelerating the healing of cracks due to hydration products of unhydrated cement particles, **Homma et al, 2009**, but the healing appears only in small micro cracks. The concrete mix with higher percent of Vf of micro steel fiber (M6) shows the better results as shown in **Figs. 15 and 16**. For concrete mixes containing a combination of micro steel fiber and healing agents, the microscopic reading of cracks width give the better result due to the precipitation of self-healing products and the effect of micro steel fiber in bridging across the crack and facilitating the healing of micro cracks. The results gave a very remarkable changing in the width of cracks even in cracks of (0.25-0.3) mm and the microscopic image shows a very clear healing of cracks especially in concrete mix M8, with higher content of healing agents and higher Vf of micro steel fiber as shown in **Figs. 17** and **18. Figs. 19** and **20** show the microscopic images for self-healed cracks from concrete mixes M7 and M8**.**

5.3 Scanning Electron Microscope Results

The products of Self-healing are observed by Scanning Electron Microscopy (SEM) with Energy Dispersive X-Ray Analysis (EDX). For this observation, two samples were taken from the cracked surface of specimens of two concrete mixes. The first one was from the cracked surface of concrete mix M2, and the second sample was taken from the cracked surface of concrete mix M6 to observe the self-healing products for each sample. **Fig. 21** and **Table 9** show the EDX analysis for the chemical composition of self-healed zone in cracks of sample from concrete mix M6. The SEM image shows distribution of self-healing products along the crack surfaces resulting from partial self-healing of crack. The results show that self-healing products are composed of (C-S-H), and $CaCO_3$. This indicates that the hydration of unhydrated cement particles lead to producing (C-S-H) in the micro cracks, **Huang et al, 2013** and also the combination of calcium ions (Ca^{2+}) which are derived from the concrete and the carbonate ions (CO_3) which are derived from the in water dissolved CO_2 lead to precipitate $CaCO_3$ (Edvardsen, 1999).

6. CONCLUSIONS

Based on the results obtained from experimental investigations, the following conclusions can be stated:

1. The self-healing of cracks was confirmed.
2. The UPV is increased as the age of curing in water increases and the maximum increasing in UPV for all concrete mixes was at 90 days. The percentage of increasing in UPV increases with increasing of healing agents' percentage.
3. The compressive strength increased for micro steel fiber reinforced concrete specimens, and higher Vf gives higher percent of increasing since the first week.
4. Specimens of concrete with higher percentage of calcium hydroxide, and sodium carbonate give better sealing of cracks than other specimens. The increase in compressive strength appears slightly in the first week and the sealing percentage increases with increasing the time of curing.
5. The specimens of concrete with only micro steel fibers give a slight decreasing in cracks due to further hydration of unhydrated cement particles.

6. The best result of cracks sealing was for specimens having a combination of micro steel fibers and with healing agents ($Ca(OH)_2$, and Na_2CO_3), due to the further effect of micro steel fibers in addition to the effect of healing agents.
7. The healing products are mainly composed of calcium carbonate for concrete mix with calcium hydroxide, and sodium carbonate additives, so the healing of cracks is mainly attributed to the precipitation of calcium carbonate due to the reaction of calcium ion with carbonate ions.
8. The results of UPV of self-healed specimens show high recovering in compressive strength and the maximum recovering occurs in concrete mixes containing a combination of micro steel fibers and healing agents ($Ca(OH)_2$, and Na_2CO_3).

REFERNCES

- ACI Committee 211, 1991, *Standard Practice for Selecting Proportions for Normal, Heavyweight, and Mass Concrete*, ACI Manual of Concrete Practice.
- ACI Committee 224, 2009, *Control of Cracking in Concrete Structures (ACI 224R-09*), ACI Manual of Concrete Practice.
- Ahn T. H., and Kishi T., 2010, *Crack Self-healing Behavior of Cementitious Composites Incorporating Various Mineral Admixtures,* Journal of Advanced Concrete Technology, pp. (171-188).
- ASTM C293, 2006, *Standard Test Method for Flexural Strength of Concrete, Using Simple Beam With Center-Point Loading*.
- ASTM C496-04, 2006, *Standard Test Method for* splitting tensile strength of cylindrical concrete specimens.
- ASTM C597, 2006, *Standard Test Method for Pulse Velocity through Concrete.*
- B.S.1881, Part 116, 1989, *Method for Determination of Compressive Strength of Concrete Cubes*, British Standards Institution.
- Edvardsen C., 1999, *Water Permeability and Autogenous Healing of Cracks in Concrete*, ACI Materials Journal.
- Homma D., Mihashi H., and Nishiwaki T., 2009, *Self-healing capability of fiber reinforced cementitious composites*, Journal of Advanced Concrete Technology, pp. (217-228).
- Huang H., Ye G., and , Damidot D., 2013, *Characterization and Quantification of Self-Healing Behaviors of Micro Cracks Due to Further Hydration in Cement Paste*, Cement And Concrete Research.
- Neville, A. M., 2011, *Properties of Concrete*, Fifth and final Edition, pp. (330).
- Ramos J.A., Dekeyser B., and Rahier H., 2013, *Method to Study The Cure Kinetics of Poly (Urethane) as Healing Agent for Self-Healing Concrete*, International Conference on Self-Healing Materials.
- Tittelboom K., V., Snoeck D., Wang J., and Belie N. D., 2013, *Most Recent Advances in the Field of Self-Healing Cementitious Materials*, International Conference on Self-Healing Materials.
- Truong P. V., Kishi T., and Kayondo M., 2013, *Crack Self-Healing Effect on Performance of Reinforced Concrete Members Subjected to Water Supply and Cyclic Loading*, International Conference on Self-Healing Materials.
- Zhong W., and Yao W., 2008, *Influence of Damage Degree on Self-Healing of Concrete*, Construction And Building Materials.

- م ق ع1984/5,السمنت البورتلاندي,الجهاز المركزي للتقييس والسيطرة النوعية,العراق.
- م م ق ع 1984/45, ركام المصادر الطبيعية المستعمل في الخرسانة والبناء,الجهاز المركزي للتقييس والسيطرة النوعية,العراق.

Table 1. Chemical composition and main compounds of ordinary Portland cement used in this research.

Oxide composition	Result	Limits of IQS No. 5/1984
Lime (CaO)	62	-
Silica (SiO_2)	20.1	-
Alumina (Al_2O_3)	4.24	-
Iron oxide (Fe_2O_3)	4.16	-
Sulfate (SO_3)	2.15	$\leq$ 2.8%
Magnesia (MgO)	3.65	$\leq$ 5%
Loss on ignition (L.O.I.)	3.42	$\leq$ 4%
Lime saturation factor (L.S.F.)	0.89	0.66-1.02
Insoluble residue (I.R.)	0.71	$\leq$ 1.5%
Main compounds (Bogues eq.) of cement ASTM C 150-00		
Tricalcium silicate (C3S)		59.02
Dicalcium silicate (C2S)		29.65
Tricalcium aluminate (C3A)		4.21
Tetracalcium aluminoferrite (C4AF)		12.65

Table 2. Grading o fine aggregate.

Sieve size (mm)	Passing % of sand	Limits of IQS No. 45/1984/Zone 3
4.75	97.4	90-100
2.36	90.2	85-100
1.18	79.1	75-100
0.6	61.88	60-79
0.3	21.7	12-40
0.15	3.22	0-10

Table 3. Physical and chemical properties of natural sand.

Properties of sand	**Test result of sand**	**Limits of IQS No. 45/1984**
Fineness modulus	0.2	-
Specific gravity	2.414	-
Absorption	1.01%	-
SO_3	0.28 %	≤ 0.5%
Dry rodded density	1680 kg/m³	-

Table 5. Grading of coarse aggregate.

Sieve size (mm)	**Passing % of gravel**	**Limits of IQS No. 45/1984 (5-20) mm**
37.5	100	100
20	100	95-100
10	41.8	30-60
4.75	2.5	0-10

Table 6. Physical and chemical properties of coarse aggregate.

Properties of gravel	**Test result of gravel**	**Limits of IQS No. 45/1984**
Specific gravity	2.606	-
Absorption	0.8%	-
SO_3	0.06%	≤ 0.1%
Dry rodded density	1600 kg/m³	-

Table 6. Properties of micro steel fiber.

Length	13 mm
Diameter	0.2 mm
Density	6800 kg/m^3
Tensile strength	2600 MPa
Aspect ratio	65

Table 7. The mix proportion by weight of concrete materials.

The materials	The mix proportion by weight (kg/m^3)
Water	205
Cement	456
Coarse aggregate	1040
Fine aggregate	555

Table 8. Details of mix design for concrete mixes .

Mix No.	W/C	Micro steel fiber % by volume	$Ca(OH)_2$ kg/m^3 as partial Replacement of cement	Na_2CO_3 kg/m^3 as partial replacement of cement
M1	0.45	0	0	0
M2		0	20	2
M3		0	30	3
M5		0.2	0	0
M6		0.4	0	0
M7		0.2	25	2.5
M8		0.4	25	2.5

Table 9. Chemical composition of self-healing products of M6.

Oxides	Percentage (%)
CaO	73.9
SiO_2	20.8
Al_2O	3.9
MgO	1.4

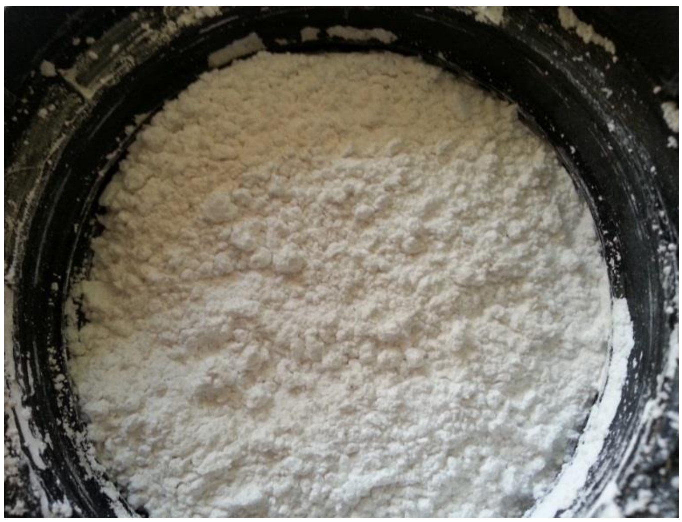

Figure 1. Calcium hydroxide.

Figure2. Sodium carbonate.

Figure3. Micro steel fibers.

Figure4. Microscopic observation device.

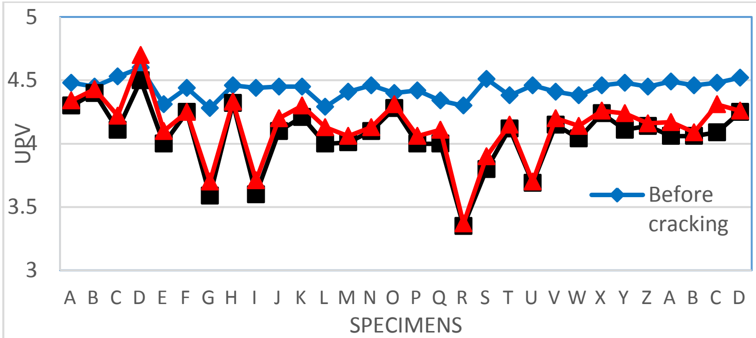

Figure5. The changes of UPV before and after cracking for M1.

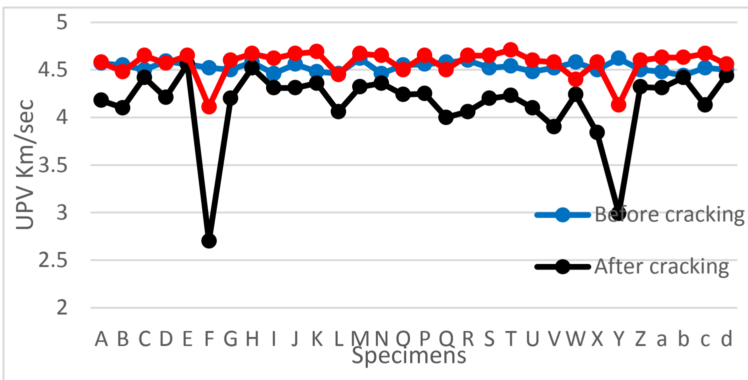

Figure 6. The changes of UPV before and after cracking for M2.

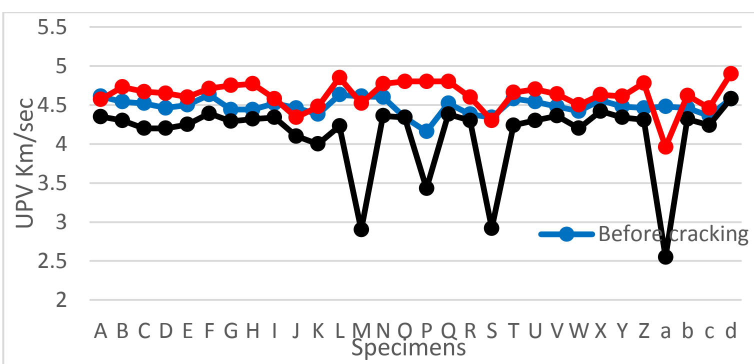

Figure 7. The changes of UPV before and after cracking for M3.

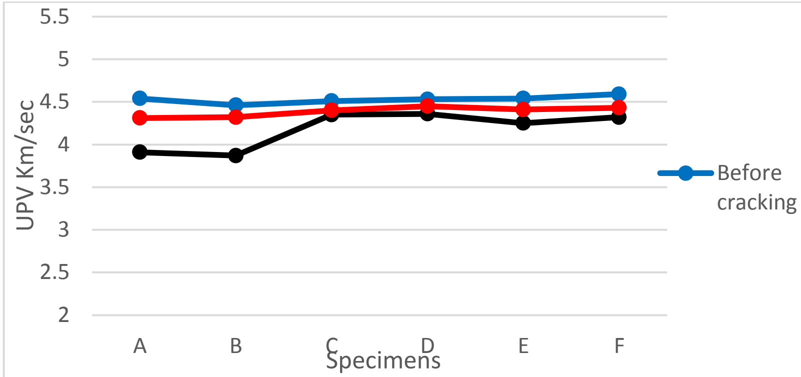

Figure 8. The changes of UPV before and after cracking for M5

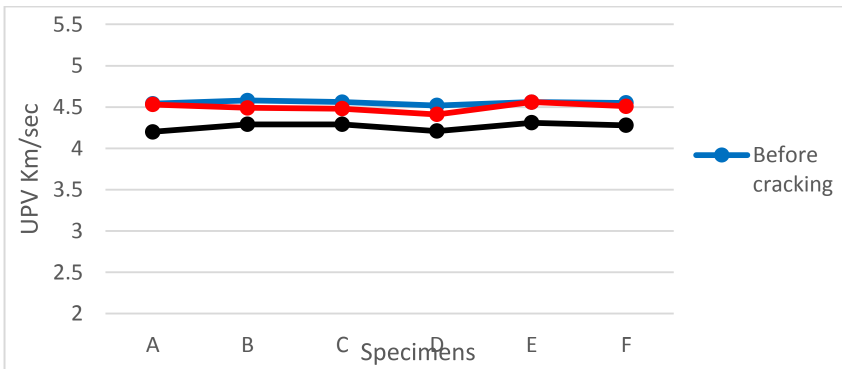

Figure 9. The changes of UPV before and after cracking for M6

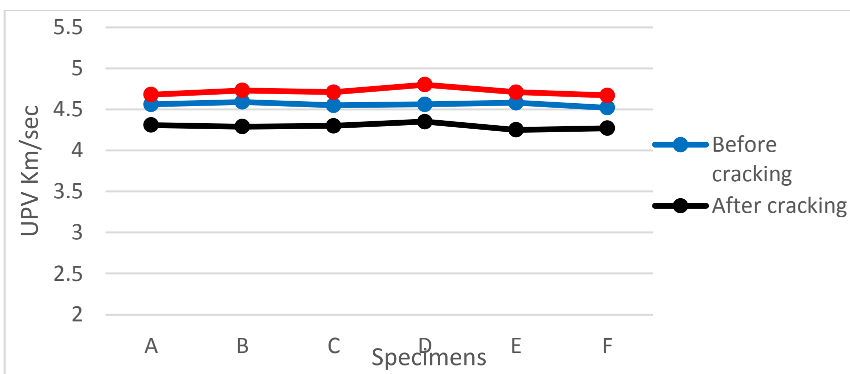

Figure 10. The changes of UPV before and after cracking for M7.

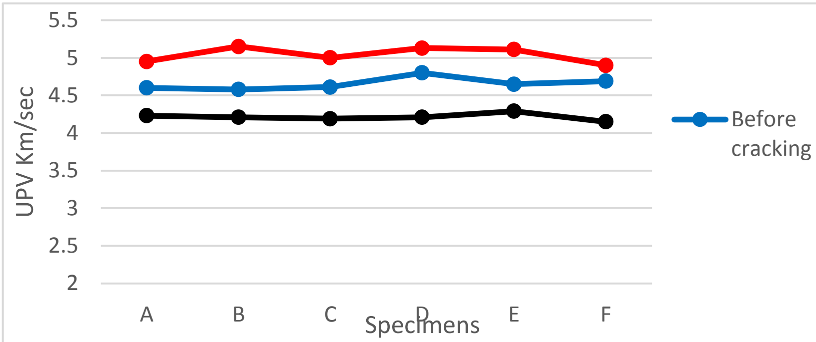

Figure 11. The changes of UPV before and after cracking for M8.

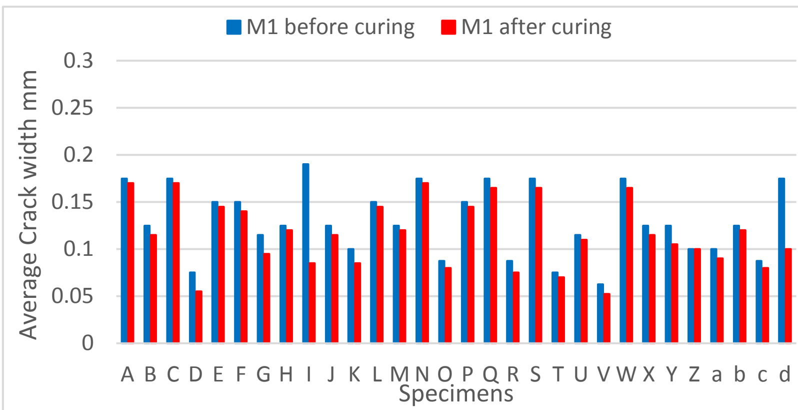

Figure 12. Changes of crack widths for concrete mix M1.

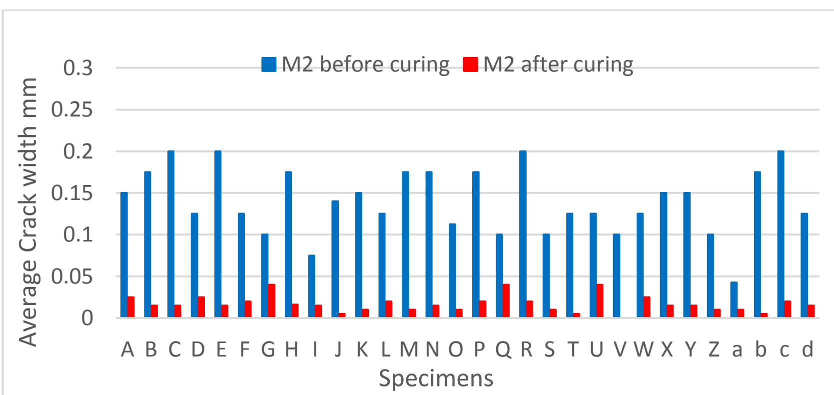

Figure 13. Changes of crack widths for concrete mix M2

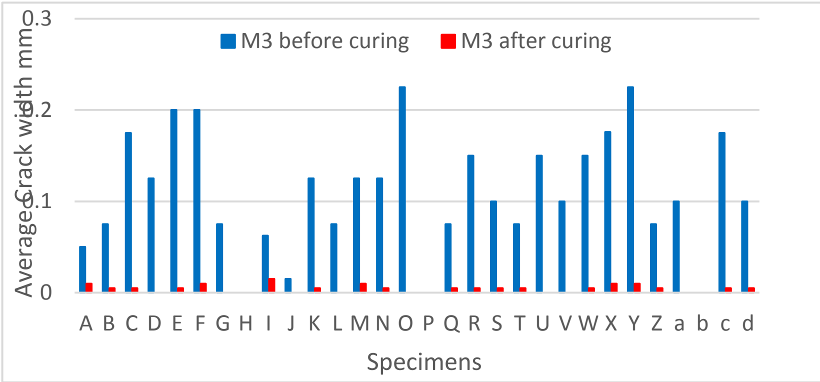

Figure 14. Changes of crack widths for concrete mix M3

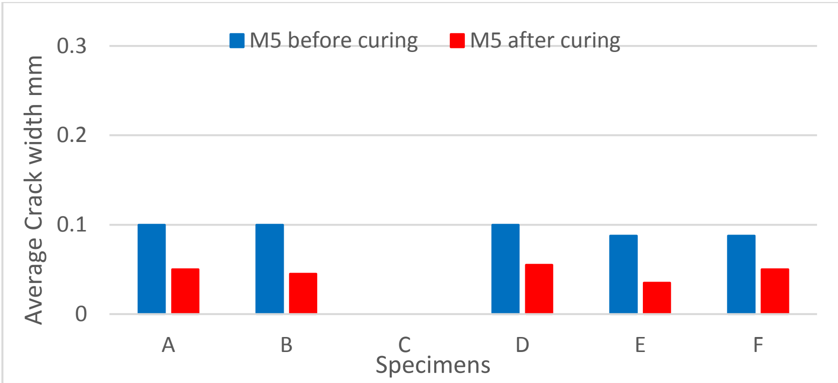

Figure 15 . Changes of crack widths for concrete mix M5.

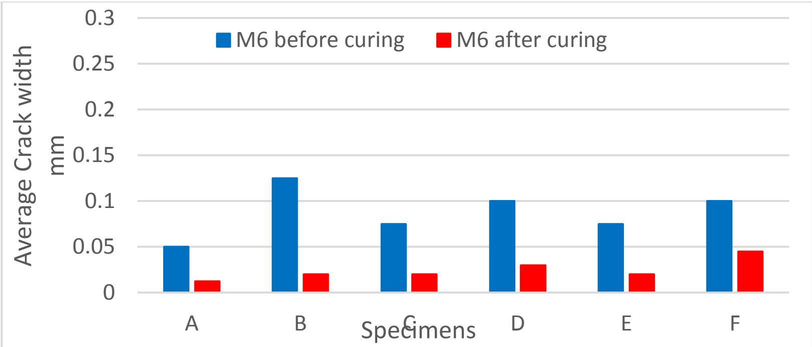

Figure 16 . Changes of crack widths for concrete mix M6.

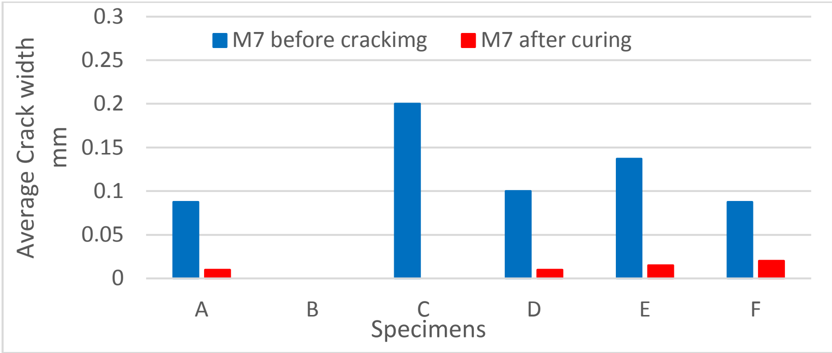

Figure 17 . Changes of crack widths for concrete mix M7.

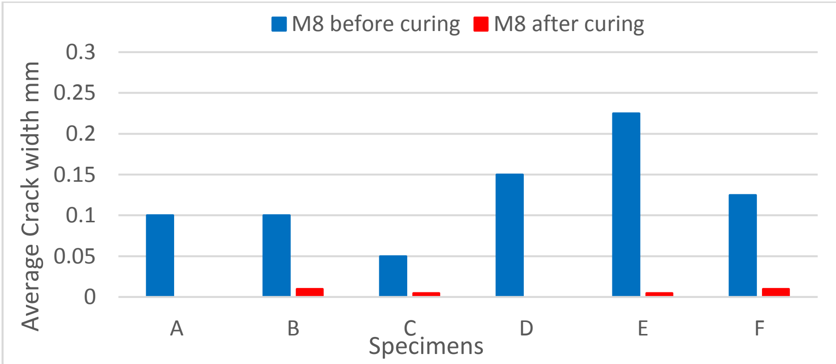

Figure 18. Changes of crack widths for concrete mix M8.

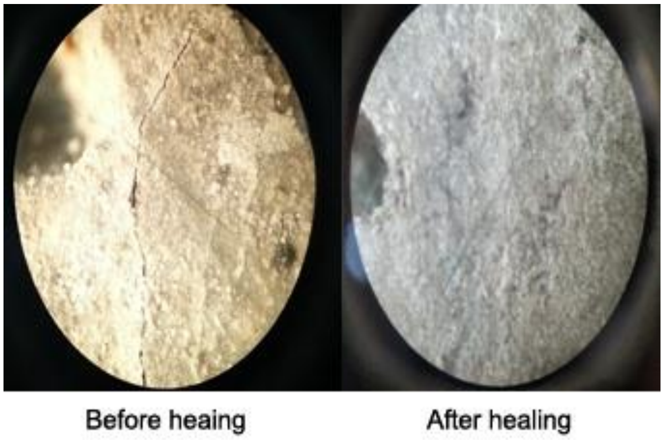

Figure 19. Microscopic image for self-healed sample from concrete mix M7.

Figure 20. Microscopic image for self-healed sample from concrete mix M8.

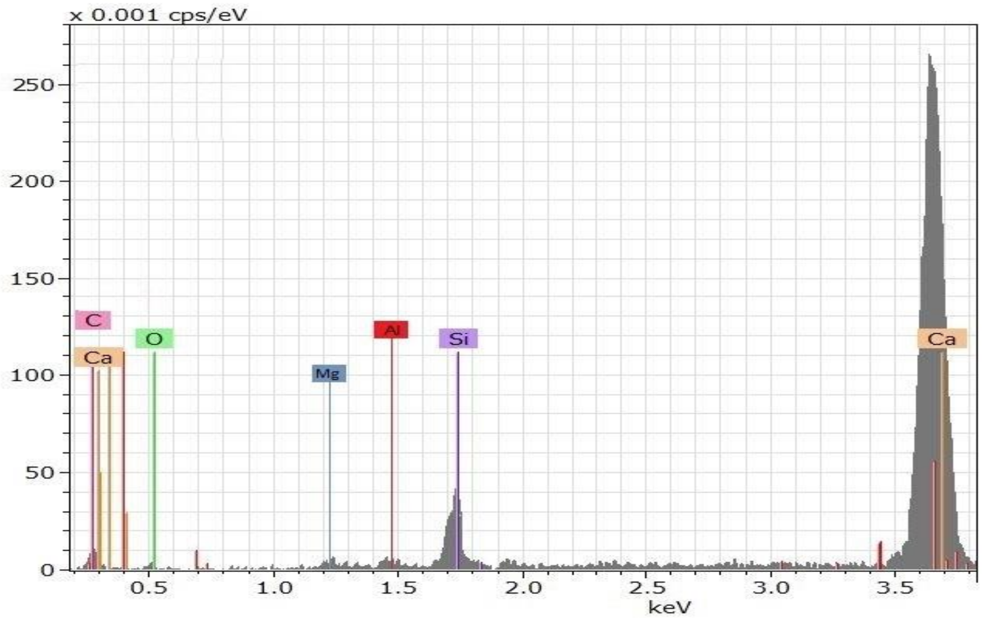

Figure 21. EDX analysis for self-healing products of M6.

Zirconium Sulfate as Catalyst for Biodiesel Production by Using Reactive Distillation

Prof. Dr. Wadood Taher Mohammed
Department of Chemical Engineering
College of Engineering
University of Baghdad
email:dr.wadood@yahoo.com

Asst. Lect. Marwa Faeq Abdul Jabbar
Department of Chemical Engineering
College of Engineering
University of Al-Nahrain
email:marwa84_2007@yahoo.com

ABSTRACT

Production of fatty acid esters (biodiesel) from oleic acid and 2-ethylhexanol using sulfated zirconia as solid catalyst for the production of biodiesel was investigated in this work.

The parameters studied were temperature of reaction (100 to 130°C), molar ratio of alcohol to free fatty acid (1:1 to 3:1), concentration of catalyst (0.5 to 3%wt), mixing speed (500 to 900 rpm) and types of sulfated zirconia (i.e modified, commercial, prepared catalyst according to literature and reused catalyst). The results show the best conversion to biodiesel was 97.74% at conditions of 130°C, 3:1, 2wt% and 650 rpm using modified catalyst respectively. Also, modified catalyst gave identical results to that of commercial one. Simulation study was adopted from basic principles of reactive distillation and the results were close to an acceptable degree.

Keywords: biodiesel, reactive distillation, sulfated zirconia, heterogeneous catalyst

كبريتات الزركونيوم كعامل مساعد لأنتاج البايوديزل بأستخدام التقطير التفاعلي

أ.د. ودود طاهر محمد
قسم الهندسة الكيمياوية
كلية الهندسة/جامعة بغداد

م.م مروة فائق عبد الجبار
قسم الهندسة الكيمياوية
كلية الهندسة/جامعة النهرين

الخلاصة

في هذا البحث تم دراسة أنتاج البايوديزل باستخدام التقطير التفاعلي خلال تفاعل حامض الاوليك مع كحول ٢– أثيل هكسانول واستخدام كبريتات الزركونيوم كعامل مساعد صلب. مثل هذه العوامل المساعدة يمكن فصلها بسهولة من محلول التفاعل واعادة استخدامها مرة أخرى وليس كما في العوامل المساعدة السائلة وكذلك ممكن أستخدامها في العمليات المستمرة. على الرغم من أن كفاءتها أعلى من السائل الا انها مستخدمة في السنوات الاخيرة.

المتغيرات التي تم دراستها هي درجة حرارة التفاعل, النسبة المولية للكحول الى الحامض الشحمي, تركيز العامل المساعد, سرعة الخلط, طرق مختلفة لتحضير كبريتات الزركونيوم. أظهرت النتائج ان أعلى تحول يصل ال ٩٧.٧٤% عند ظروف ١٣٠ م°, ٣:١ , ٢% وزنا, ٦٥٠ دورة/دقيقة عند أستخدام العامل المساعد المحسن. كذلك أظهرت النتائج أن التجاري أقرب الى العامل المساعد المحسن. تم أيضا دراسة محاكاة لنتائج التقطير التفاعلي ولوحظ أن هناك تقارب بينهم.

الكلمات الرئيسية: بايوديزل، التقطير التفاعلي، كبريتات الزركونيوم، العوامل المساعدة الصلبة

1. INTRODUCTION

The synthesis of biodiesel has been receiving more attention all over the world since the raw materials (vegetable oils and animal fats) are often locally available, renewable, and environmental friendly. In addition, biodiesel can be used without modification of diesel engines **Ma,** and **Hanna, 1999 and Gerpen, 2005**. The transesterification of triglycerides (TGs) and esterification of free fatty acids (FFAs) contained in vegetable oils and animal fats are the two main reactions for converting vegetable oils and animal fats into biodiesel. Biodiesel is currently produced in batch processes which are penalized by important shortcomings such as: high alcohol demand required to shift equilibrium towards fatty esters, necessity of catalyst neutralization causing a salt waste stream, high separation costs of fatty ester products from the reaction mixture, high costs caused by complex processes including multiple reactors and separation units **Meng, et al., 2009, Kiss, et al., 2008 and Omota, et al., 2003**. As a result, process intensification technologies like reactive distillation have become more attractive in recent years, **Noshadi, et al., 2012**. Reactive distillation (RD) is a well-known example of process intensification, in which chemical reaction and thermodynamic separation occur at the same time and in the same place of the column, **Keller, et al., 2011**. In comparison to conventional reactor–separator sequences, RD allows for higher reactant conversion, product selectivity and energy savings with favorable investment and operating costs. However, there are several constraints that limit the successful application of RD, such as complex design, difficult scale-up and advanced process control, **Schoenmakers** and **Bessling, 2003**. Reactive distillation can be effectively used to improve the selectivity of a reaction especially when an intermediate product is desired in the series or combination of series and parallel reactions. Removing one of the products from the reaction mixture or maintaining low concentration of one of the reactants can lead to reduction in the rates of side reactions, **Vinay, et al., 2013**.

Use of solid acid catalysts can also greatly improve the economics of biodiesel synthesis because of their ability to be reused and the decreased need for many separation steps. In particular, solid acid catalysts can carry out transesterification and esterification simultaneously using low cost feed stocks without multiple reaction and post-treatment steps, greatly improving the economics of biodiesel production, **Lotero, et al., 2005, Furuta, et al., 2004, Suwannakarn, et al., 2009 and Garcia, et al., 2008**. Heterogeneous catalysis for biodiesel production has been extensively investigated in the last few years. The catalyst efficiency depends on several factors such as specific surface area, pore size, pore volume and active site concentration, **Smith, et al., 2006**. The structure of metal oxides is made up of positive metal ions (cations) which possess Lewis acidity, i.e. they behave as electron acceptors, and negative oxygen ions (anions) which behave as proton acceptors and are thus Brønsted bases. This has consequences for adsorption. Recently, sulfated zirconia (SO_4/ZrO_2) catalysts have found many applications in several acid catalyzed reactions, **Arata, et al., 2003**. These compounds are active for hydrocarbon conversion at temperatures lower than the most of the generally used solid catalysts, normally at temperatures from 100 to 200°C or lower, **Ardizzone, et al., 1999**. S-ZrO_2 is promised as an active catalyst for esterification due to its high acid strength.

The aim of this work is the study of the production of biodiesel in a reactive distillation column using zirconium sulfated as heterogeneous catalyst at different process conditions: temperature, oleic acid: 2-ethylhexanol ratio, catalyst concentrations and different preparation methods of sulfated zirconia.

2. EXPERIMENTAL Work

2.1 Materials

Oleic acid (purity 98%) was supplied from Thomas baker, india. 2-Ethylhexanol alcohol (purity 99% from GC analysis) was maintained from Ministry of Science and Technology as industrial alcohol. Since this alcohol is typically a waste alcohol from the manufacturing of butanol, this process makes sense from an economic viewpoint. Zirconium oxychloride and sulfuric acid was used for preparing zirconium sulfate as catalyst, ethanol and phenolphthalein for titration.

2.2 Reaction Procedure

The reaction was carried out in a lab scale reactor with a volume of 250 ml. The fatty acid was fed into the reactor in order to be preheated it before the catalyst and the alcohol were added. When the desirable reaction temperature was reached, the catalyst and the alcohol were adjoined into the reactor and the reaction started. The stoichometry amount of molar ratio alcohol:oleic acid is 1:1; however, since we are on the presence of an equilibrium reaction, a higher amount of alcohol should be used in order to display the reaction towards the desirable product. The withdrawn samples, taken at specific established times, allowed to cool and then centrifuged to separate out any catalyst particles to limit further reaction. After that was analyzed by a titration procedure to measure the residual acidity. A weighted amount of the sample was dissolved in ethanol; a few drops of phenolphthalein were added as indicator. A 0.1 N alkaline solution of KOH was used to perform the titration. The amount of KOH consumed was registered and the acidity was calculated using the following equation:

$$a = \frac{V\times 1000\times Mwt.\times C}{W} \tag{1}$$

where a: acidity index; V: volume of KOH solution employed for titration, ml; Mwt..: molecular weight of KOH, g/mol; C: concentration of the solution used for titration, mol/l; W: weight of the sample taken to analyzed, g.
Using Eq.(2), the conversion of free fatty acid (X) was calculated:

$$X = \frac{a_i - a_t}{a_i} \tag{2}$$

Where a_i is the initial acidity of the mixture and a_t is the acidity at ‘‘t” time.

2.3 Preparation of Zirconium Sulfate (SZ)

(a) Preparation of SZ by the Solvent-Free Method

SZ by the solvent free method (SF) was prepared by grinding $(NH_4)_2SO_4$ and $ZrOCl_2.8H_2O$ at a molar ratio of 6:1 in an agate mortar for 20 min at room temperature. After that calcined at 600°C for 5 h, **Sun, et al., 2005**.

(b) Preparation of SZ by the Conventional Method

Zirconium oxy-chloride ($ZrOCl_2.8H_2O$) of 20 g was dissolved in 200 ml water, then the solution reached to pH of 9 using 25% w/w NH_3 solution and constant mixing to permit zirconium hydroxide to precipitate. The precipitation of zirconium hydroxide was washed to remove chloride salts, then filtered with a Buchner funnel. In the next step, the zirconium hydroxide was dried for 24 h at 100°C and impregnated with 1 M H_2SO_4 under constant mixing for 30 min. Then, the SO_4^{2-}/ZrO_2 was dried at 100°C for 24 h and calcined in air for 3 h at 650°C, **Yadav** and **Nair, 1999**.

(c) Preparation of Modified SZ Catalyst

50 g of zirconium oxychloride ($ZrOCl_2.8H_2O$) supplied from local market was dissolved in 500 ml water, then zirconium hydroxide allowed to precipitate at pH of 9 using 25% w/w NH_3 solution under constant mixing for 30 min. The white precipitation was washed with water to remove the chloride salts until the pH of the solution reached 7, then filtered with conical funnel.

In the next step, the zirconium hydroxide dried at 110°C for 18 h, then impregnated with 1 M H_2SO_4 under constant mixing for 8 h. After precipitation for 24 h, the SO_4/ZrO_2 was dried for 24 h at 110°C and then calcined in air for 3 h at 650°C.

3. PROCESS SIMULATION

The UNIQUAC model was applied to consider the nonideal liquid- phase behavior. The degree of deviation from ideality in liquid phase is represented by γ_i (activity coefficient). It was employed for the vapor–liquid equilibrium (VLE) calculations in MATLAB.
Activity coefficient consists of two terms, residual and combinatorial

$$\ln\gamma_i = \ln\gamma_i^C + \ln\gamma_i^R \tag{3}$$

$$\ln\gamma_i^C = 1 - J_i + \ln J_i - 5q_i\left(1 - \frac{J_i}{L_i} + \ln\frac{J_i}{L_i}\right) \tag{4}$$

$$\ln\gamma_i^R = q_i\left[1 - \sum_k\left(\theta_k\frac{\beta_{ik}}{s_k} - e_{ki}\ln\frac{\beta_{ik}}{s_k}\right)\right] \tag{5}$$

The process simulation software, Matlab R2011, was used in this work. The main processing unit include a reactive distillation column with 4 stages. The first column stage is the condenser and the fourth stage is the reboiler. The same experimental conditions were used in the simulation process. Composition was obtained on all stages assuming very small reflux ratio using the following equations, **Zapata, et al., 2012**:

- **For Condenser** (k =1, i=1-4))

$$\frac{dx_{1(i)}}{dt} = \frac{V_{(1)}y_{2(i)} - L_{(1)}x_{1(i)}}{H_{(1)}} \tag{6}$$

- **For Column** (k =2,3 and i=1-4)

$$\frac{dx_{k(i)}}{dt} = \frac{V}{M_{in}}\left(y_{k+1(i)} - y_{k(i)}\right) + \frac{L}{M_{in}}\left(x_{k-1(i)} - x_{k(i)}\right) \tag{7}$$

- **For Reboiler** (k=N and i=1-4)

$$\frac{dx_{N(i)}}{dt} = \frac{\left(L_{(k)}x_{N-1(i)} - V_{(k)}y_{N(i)}\right)}{H_{(k)}} + \text{Rate of reaction} \tag{8}$$

Where
H = holdup
K = stage

i = component

Equilibrium ratio (k=2 to N)

$$y_{k(i)} = \frac{\alpha_i x_{k(i)}}{\sum_{j=1}^{i} \alpha_j x_{k(j)}} \quad (9)$$

Where
α_i is the relative volatility
x is composition of liquid phase
y is composition of vapor phase

4. CHARACTERIZATION OF MODIFIED CATALYST

4.1 X-Ray Diffraction (XRD)

The powder X-ray diffraction patterns of sample was recorded using a Shimadzu XRD-6000 diffractometer with Ni filtered CuKα radiation (λ = 0.154 nm) in the range of 2θ = 10-60°. It has been generally realized that the crystalline phase of the SZ catalysts plays a very important role in catalytic activity and zirconia with tetragonal structure showing a higher catalytic activity than that of monoclinic ZrO_2. **Fig. 1** displays the XRD for S/ZrO_2. The S/ZrO_2 sample reveal well crystalline structure. The phase shown for sulfated zirconia was orthorhombic at 2θ =25.35, 27.59, 29.55, 32.88 and 36.32°.

4.2 Fourier Transform Infrared Spectroscopy (FTIR)

Fig. 2 shows FTIR of sulfated zirconia. The band at 1332.72cm^{-1} is due to the splitting of the S=O asymmetric stretching, which implies the existence of sulfate species. While the band at 790 and 710 due to S-O stretching vibration. The bands at 1138 and 1267.14cm^{-1} are normally stands for chelating bidentate sulfate ions coordinated to the zirconium cation. The peaks of t-ZrO_2 has also been observed at 649.97, 613.32, 588.25cm^{-1}.

4.3 Thermal Gravimetric Analysis (TGA)

The TGA/DTA analysis was performed with an EXSTAR 6000 series instrument and shown in **Fig. 3**. A 34.541 mg of sample was heated in the air (20 °C/min) from 50 to 900 °C. The weight loss and heat flow were measured as a function of temperature. Thermal analysis results for SZ catalyst after calcination was depicted in **Fig. 3**. TGA showed that SO_4/ZrO_2 was thermally stable. There was no weight loss observed from 50 to 670°C but for higher temperature 670-800°C weight loss approximately 20% due to decomposition of sulfate. The beak in DTA curve due to phase transition hence, the sample was calcinated at 650°C.

4.4 Scanning Electron Microscopy (SEM)

The SEM of SO_4/ZrO_2 is shown in **Fig. 4**. The SEM of SO_4/ZrO_2 showed that the surface of ZrO_2 was distinctly altered, exhibiting considerable surface shining after sulfation. SEM images taken at higher magnification clearly showed the alternation and shining of the surface. This may be due to the presence of highly charged species, i.e. sulfate ions.

The textural properties were determined from the nitrogen adsorption isotherm determined after degassing at 200°C under vacuum at 5 – 10 mbar. The surface area was calculated using the

Brunauer–Emmett–Teller (BET) equation and the pore volume was determined at a relative pressure of 0.98. The most important results are given in **Table 1**. In principle, the specific surface area depends on the calcination temperature.

5. RESULTS AND DISCUSSION

5.1 Effect of Mixing Speed

Fig. 5 illustrates the variation of conversion with time at different mixing speeds varied from 500 to 900 rpm keeping other variables constants, temperature of 130°C, the molar ratio of acid:alcohol of 1:1 and concentration of SZ catalyst of 2wt%.

The results indicate the conversion of oleic acid increased from 64.64% at 500 rpm to 75.63% at 900 rpm to reach high value 90.16% at speed 650 rpm after 60 min reaction time. Increasing the mixing speed could tremendously shorten the reaction time, but for high speed inverse effect can be seen because droplet became very small rigid sphere and its surface cannot renewal. Conversions at end of reaction time (after 120 min) were 82.74%, 91.4% and 86.39% for 500, 650 and 900 rpm speed respectively. There are probably two reasons that mixing speed can intensify the esterification catalyzed by SZ:

stirring promotes the mixing of oleic acid and 2-ethylhexanol; 2-ethylhexanol lies on the top of oleic acid without stirring. The 2-ethylhexanol and acid layers break up and the reactants forms droplets once stirring starts, **Stamenkovic, et al., 2007**.

Also, SZ is insoluble in the reaction mixture and stirring is needed to help the mixing of catalyst with the reactants and decreases the resistance to mass transfer.

5.2 Effect of Reaction Temperature

Fig. 6 illustrates the relationship between conversion and time at temperatures of 100, 110, 120 and 130°C for molar ratio of oleic acid:2-ethylhexanol of 1:1 and concentration of SZ was 2wt%.

There are sharp increasing in conversion between higher temperature (130°C) and lower temperature (100°C). The oleic acid conversion was 91.4% at 130°C after about 60 min while at 100°C the conversion reached 66.78% after 120 min at the same conditions. The higher temperature helps to destroy the bonds between fatty acid molecules and permit alcohol molecules to insert between in the presence of sulfated zirconia that have acidic active sites.

5.3 Effect of Alcohol to Free Fatty Acid Molar Ratio

Fig. 7 demonstrates the effect of molar ratio of alcohol to acid ranging from 1:1 to 3:1 on conversion with time at constant temperature of 130°C and concentration of sulfated zirconia was 2wt%. It can be clearly seen when ratio increased from 1 to 3, the conversion was found to increase from 91.4% to 97.74%. This increment can be explained by the fact that higher molar ratio increases the solubility of acid in 2-ethylhexanol and therefore allow a better contact between the species over the heterogeneous catalyst. Also, the viscosity of 2-ethylhexanol /oleic acid mixture decreases when the 2-ethylhexanol to oleic acid ratio increases. This is because of lower viscosity of 2-ethylhexanol in comparison to the free fatty acid. When the viscosity decreased, the impact of diffusion of the reactants towards the catalyst particles decreased, and hence improved the interparticle diffusion that led to higher conversion.

On further increasing of alcohol concentration, there is little difference of conversion between 1:2 and 1:3. This can be explained by competitive adsorption of reactants on catalyst. Further increasing alcohol in the reaction mixture, majority of the sites on the catalyst surface were occupied by alcohol molecules.

5.4 Effect of Catalyst Concentration

By increasing the amount of catalyst, the reaction rate, hence conversion after a certain time can be further increased. Thus sulfated zirconia is suitable for reactive distillation applications where high activity is required in a short time, **Kiss, et al., 2008**. The effect of SZ amount (0.5-3%wt) on the reaction at constant temperature of 130°C and molar ratio of oleic acid :2-ethylhexanol of 1:1 was studied, and the results are shown in **Fig. 8**.

Conversion increased as time increase for all concentration and also increase as concentration of catalyst increase but it take different time to reach best conversion, for example at High concentrations the conversion achieved were 81.7%, 86.35% and 87.5% at 1%, 2% and 3%wt concentration respectively after 45 min reaction time. While for low concentration 0.5%wt more time needed to reach conversion of 79.74% after 90 min.

At low catalyst amounts, there were not enough active sites for the reaction. After 45 min the conversion for catalyst amount 2%wt was nearly the same that for 3%wt this may be due to blocking of active site, **Patel, et al., 2013**, poisoning, pore fillings or combination of these deactivation mechanism, **Lopez, et al., 2008**. In the same figure, can be seen there is a sharp difference in final conversion for catalyzed and non catalyst reaction, conversions were 91.4%, 84.9% and 49.88% for 2%, 0.5wt% and no catalyst respectively after 120 min reaction. The reaction without catalyst is very slow is start with 39.4% and end with 49.88% after 120 min.

5.5 Effect of Catalyst Preparation Method

According to preparation method, SZ activity effect the esterification reaction. The performance of various SZ was tested at constant reaction temperature of 130°C, alcohol:acid of 3:1, concentration of SZ of 2wt% and mixing speed of 650 rpm. The results depict in **Fig. 9**.

For oleic acid and 2-ethylhexanol, modified SZ was prepared and compared with one prepared by conventional method and other prepared by free solvent method. The results display that modified SZ awarded better conversion than other types, and its activity is identical to commercial one which achieved conversion of 96% in short time, nearly 30 min while for other methods, the conversion of oleic acid was 75% and 65% for conventional catalyst and free solvent catalyst respectively at the same time. The activity of modified method may be due to the strength, number of sites and Bronsted acidity.

For reused catalyst, the activity was below that of the fresh catalyst, it gave 76.35% conversion after 60 min compared to 90.16% conversion for modified catalyst at the same duration time. The decrease in reaction rate may be attributed to sulfur leaching, pore filling and small population of active site may have been lost during deactivation.

5.6 Testing of Biodiesel Obtained from Oleic Acid

Biodiesel obtained from oleic acid for best experiment was analyzed by ASTM (American Standard for Testing Material). **Table 2** shows biodiesel from this experiment.

5.7 Simulation Results

The presentation for comparing experimental and theoretical results shown in **Figs. 10** and **11** at various conditions of molar ratio of alcohol: acid, reaction temperature and catalyst concentration of 2wt% for oleic acid esterification.

There are good agreement between predicted and experimental composition at condition of 2:1 molar ratio, reaction temperature of 130°C and concentration of sulfated zirconia of 2wt% as indicated in **Fig. 10** for oleic acid. While for stochimetric ratio of 1:1 lower agreement observed as shown in **Fig. 11**.

From **Figs. 12** and **13** for oleic acid-biodiesel compositions at stochimetric ratio of 1:1 and different temperatures of 100°C and 130°C with SZ catalyst concentration of 2wt% and 0.5wt%, there are significant difference occurring between experimental and theoretical composition for FFA and biodiesel. This may be due to non ideality have very negative effect on composition at this ratio.

6. CONCLUSIONS

1- The conversion increased with increasing time and temperature but at different duration of time to reach best conversion, it take 60 min to reach 84.57% and 90.16% for temperature 120°C and 130°C respectively. While for lower temperatures take more time to reach the best conversion.

2- The best molar ratio of alcohol to fatty acid was 2:1 and when increased this ratio less effect was shown.

3- There is sharp difference in conversion for esterification reaction with and without catalyst. Also as concentration increased higher than 2wt% the conversion decreased as a result of active site of catalyst was broken.

4- The best mixing speed of stirring was 650 rpm.

REFERENCES

- Arata, K., Matsuhashi, H., Hino, M., and Nakamura, H., 2003**,** *Synthesis of Solid Superacids and Their Activities for Reactions of Alkanes* , Catal. Tod., Vol. 81, P.17.

- Ardizzone, S., Bianchi, C.L., Ragaini, V., and Vercelli, B., 1999, *SO_4-ZrO_2 Catalysts for the Esterification of Benzoic Acid to Methyl Benzoate* , Catal. Lett., Vol. 62, PP. 59.

- Bhatia, S., Ahmad, A.L., Mohamed, A.R., and Chin S.Y., 2006, *Production of Isopropyl Palmitate in a Catalytic Distillation Column: Experimental Studies*, Chem. Eng. Sci., Vol. 61, PP.436–7447.

- Furuta, S., Matsuhashi, H., and Arata, K., 2004, *Biodiesel Fuel Production with Solid Amorphous Zirconia Catalysis in Fixed Bed Reactor under Atmospheric Pressure*, Catal. Commun, Vol 5, PP. 721-723.

- Garcia, C.M., Teixeira, S., Marciniuk, L.L., and Schuchardt, U., 2008, *Transesterification of Soybean Oil Catalyzed by Sulfated Zirconia*, Bioresour Technol., Vol. 99, issue 14, PP. 6608-6613.

- Gerpen, V., 2005, *Biodiesel Processing and Production*, J. Fuel Processing Technology, Vol. 86, PP. 1097-1107.
- Keller, T., Roth, T., Mackowiak, J. F., Kreis, P., Gorak, A., and Tankiewicz, A., 2011, Prozessintensivierung in der Fluidverfahrens technik. Chemie Ingenieur Technik, Vol. 83, PP. 935–951.

- Kiss, A.A., Dimian, A.C. and Rothenberg, G., 2008, *Biodiesel by Catalytic Reactive Distillation Powered by Metal Oxides*, Energy Fuels, Vol. 22, P. 598.
- Liu, Y.J., Lotero, E., and Goodwin, J.G., 2006, *Effect of Water on Sulfuric Acid Catalyzed Esterification*, J. Mol. Catal. A:Chemical, Vol. 245, P. 132.

- Lopez, D. E., Goodwin, J. G., Bruce, D. A. and Furuta, S., 2008, *Esterification and Transesterification Using Modified Zirconia Catalysts*, Applied Catalysis A: General, Vol. 339, PP. 76–83.

- Lotero, E, Liu, Y.J., Lopez D.E., Suwannakarn, K., Bruce D.A., and Goodwin J.G., 2005, *Synthesis of Biodiesel via Acid Catalysis*, Ind. Eng. Chem. Res., Vol. 44, P. 5353.
- Ma F.R., and Hanna M.A., 1999, *Biodiesel Production :a Review*, Bioresour Technol., Vol. 70, PP. 1-15.

- Meng, X., Chen, G., and Wang, Y., 2009, *Biodiesel Production from Waste Cooking Oil via Alkali Catalyst and its Engine Test*, Fuel process Technol., Vol. 89, P. 851–857.

- Noshadi I., Amin N.A.S. and Parnas R. S., 2012, *Continuous Production of Biodiesel From Waste Cooking Oil in A Reactive Distillation Column Catalyzed by Solid Heteropolyacid: Optimization Using Response Surface Methodology (RSM)*, Fuel, Vol. 94, PP. 156–164.

- Omota, F., Dimian, A.C., and Bliek, A., 2003, *Fatty Acid Esterification by Reactive Distillation Part 1: Equilibrium-Based Design*, Chem. Eng. Sci., Vol. 58, PP. 3159–3174.

- Patel, A., Varsha, B., and Singh, N. 2013, *Biodiesel Production by Esterification of Free Fatty Acid over Sulfated Zirconia*, Renewable Energy Vol. 51, PP. 227-233.

- Schoenmakers, H., and Bessling, B. 2003, *Reactive and Catalytic Distillation from an Industrial Perspective*, Chemical Engineering and Processing, Vol. 42, PP. 145–155.

- Smith, G.V. and Notheisz, F., 2006, *Heterogeneous Catalysis in Organic Chemistry*, Academic Press Inc., New York.

- Stamenkovic, O. S., Lazic, M. L., Todorovic, Z. B., Veljkovic, V. B. and Skala, D. U., 2007, *The Effect of Agitation Intensity on Alkali-Catalyzed Ethanolysis of Sunflower Oil*, Bioresour. Technol., Vol. 98, PP. 2688-2699.

- Sun, Y., Ma, S. Du, Y., Yuan, L., Wang, S., Yang, J., Dang, F., and Xiao, F.S., 2005, *Solvent-Free Preparation of Nanosized Sulfated Zirconia with Brønsted Acidic Sites from a Simple Calcination*, J. Phys Chem. B, V. 109, PP. 2567–2572.

- Suwannakarn, K., Lotero, E., Ngaosuwan, K., and Goodwin, J.G., 2009, *Simultaneous Free Fatty Acid Esterification and Triglyceride Transesterification Using a Solid Acid Catalyst with in sSitu Removal of Water and Unreacted Methanol*, Ind Eng Chem Res, Vol. 48, PP. 2810-2818.

- Vinay A., Nistala, S. H., Mahajani, S. M.M and Malik, R. K., 2013, *Optimization Based Conceptual Design of Reactive Distillation for Selectivity Engineering*, Computers and Chemical Engineering, Vol. 8, PP. 209–217.

- Yadav, G.D., and Nair J.J., 1999, *Sulfated Zirconia and its Modified Version as Promising Catalysts for Industrial Processes*, Microporous Mesoporous Mater., Vol. 33, PP. 1–48.

- Zapata R. B., Villa A. L. and Correa C. M., 2012, *Modeling and Simulation of a Batch Distillation Column for Recovering Limonene Epoxide*, Rev. EIA. Esc. Ing., No. 8.

NOMENCLATURE

a= acidity, mg KOH/g_{FFA}
N= concentration of KOH solution, mole/l.
mwt.= molecular weight of KOH solution, g/mole.
V= volume of KOH solution, ml.
m= weight of sample, g.
X= conversion, dimensionless.
γ_i^C = combinational term for activity coefficient
γ_i^R = residual term for activity coefficient

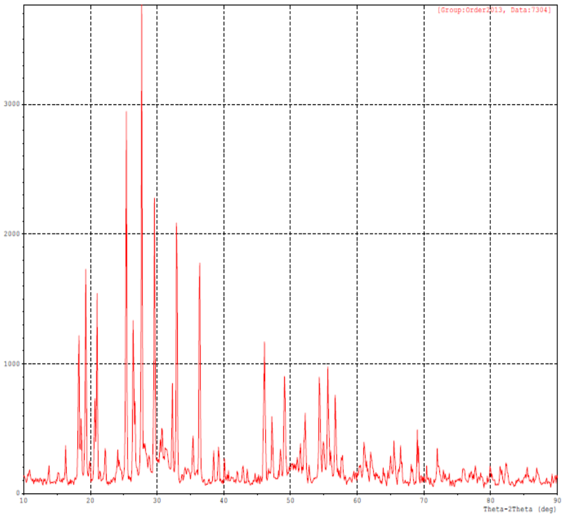

Figure 1. XRD of modified sulfated zirconia.

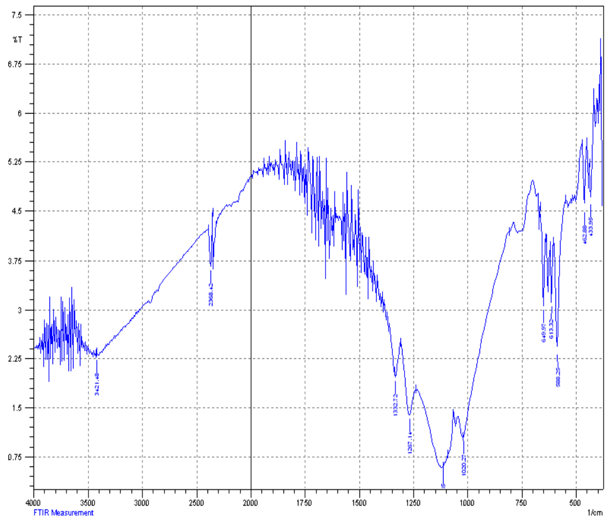

Figure 2. FTIR of modified sulfated zirconia.

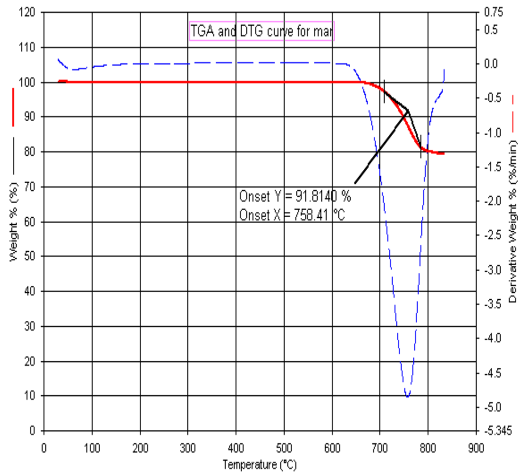

Figure 3. TGA of modified sulfated zirconia.

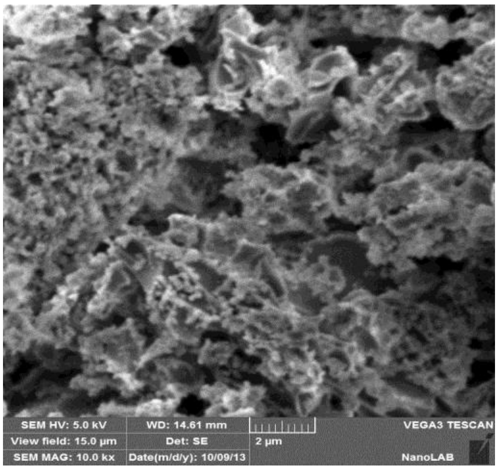

Figure 4. SEM of modified sulfated zirconia.

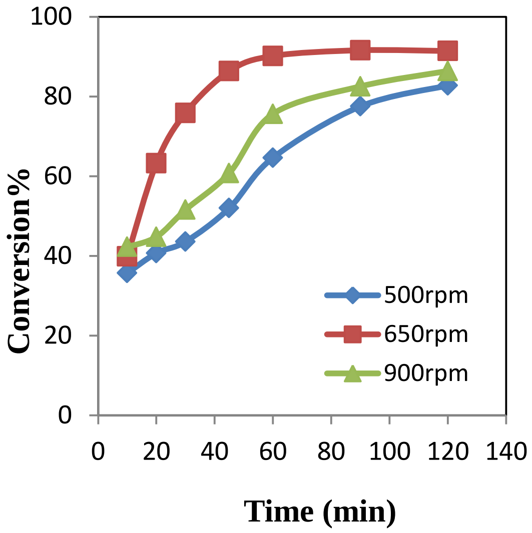

Figure 5. Effect of mixing speed on conversion of oleic acid.

[**Operating conditions**:molar ratio of free fatty acid: alcohol was 1:1, reaction temperature 130°C and concentration of sulfated zirconia 2wt%]

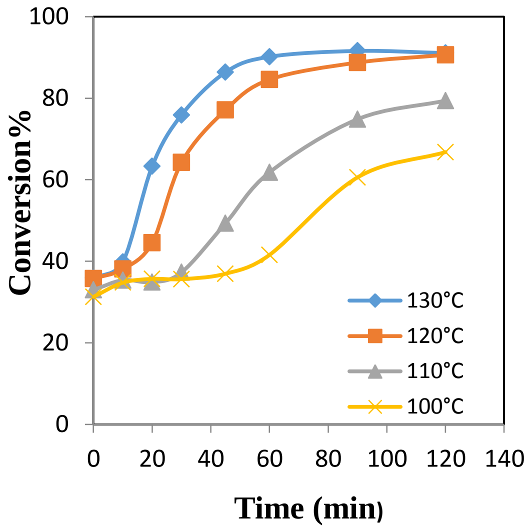

Figure 6. Effect of temperature on oleic acid conversion.

[**Operating conditions**: molar ratio of alcohol:FFA 1:1, heterogeneous catalyst of concentration 2wt% (SZ) and mixing speed 650 rpm]

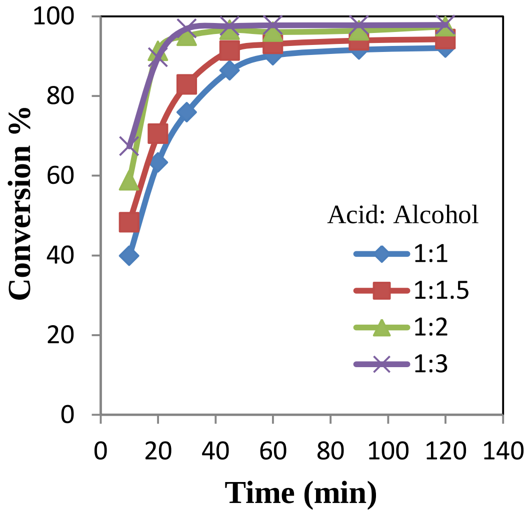

Figure 7. Effect of Acid: Alcohol molar ratio on oleic acid conversion.

[**Operating conditions**: reaction temperature 130°C, concentration of heterogeneous catalyst 2wt% (SZ) and mixing speed 650 rpm]

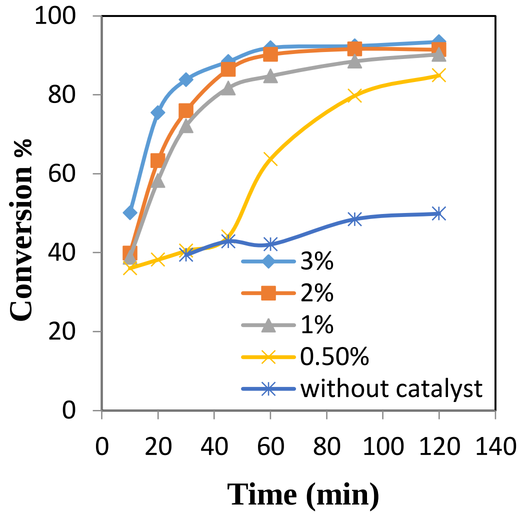

Figure 8. Effect of heterogeneous catalyst concentration on oleic acid conversion.

[**Operating conditions**: reaction temperature 130°C, molar ratio of 2-ethylhexanol:oleic acid 1:1 and mixing speed 650 rpm]

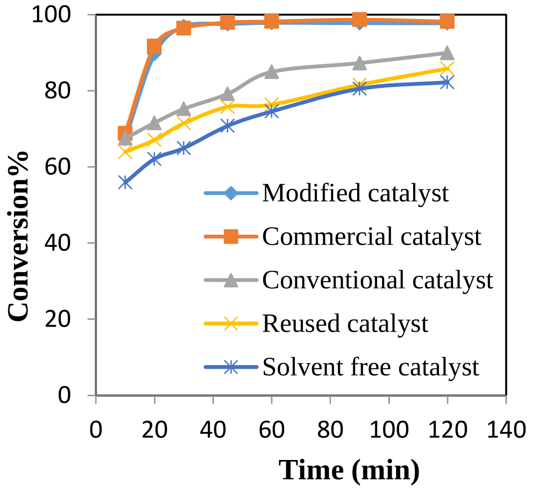

Figure 9. Different types of SZ catalysts for oleic acid conversion.

[**Operating conditions**: molar ratio of oleic acid :2-ethylhexanol 1:3, reaction temperature 130°C, catalyst concentration 2wt% (SZ) and mixing speed 650 rpm]

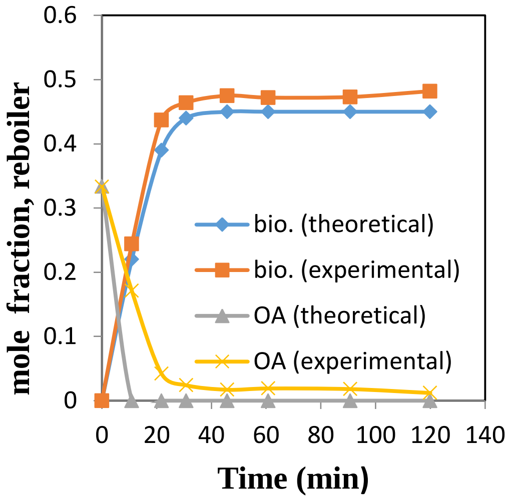

Figure 10. mole fraction of oleic acid and its biodiesel.

[**Operating conditions**: molar ratio 2:1 (alcohol:acid), reaction temperature 130°C and heterogeneous catalyst of concentration 2wt%(SZ)]

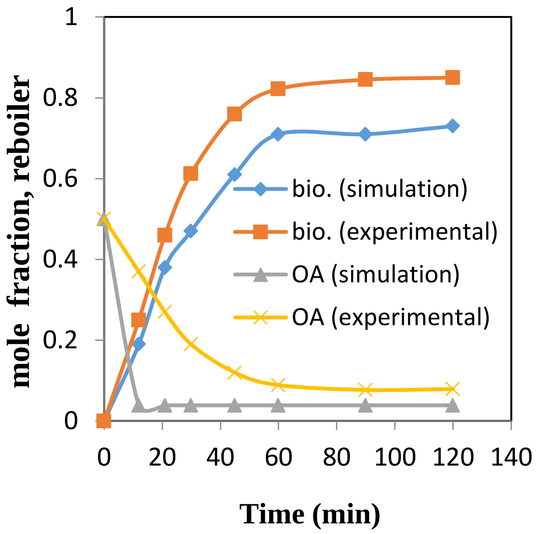

Figure 11. mole fraction oleic acid and its biodiesel.

[**Operating conditions**: molar ratio of alcohol: acid of 1:1, reaction temperature 130°C and concentration of sulfated zirconia 2wt%]

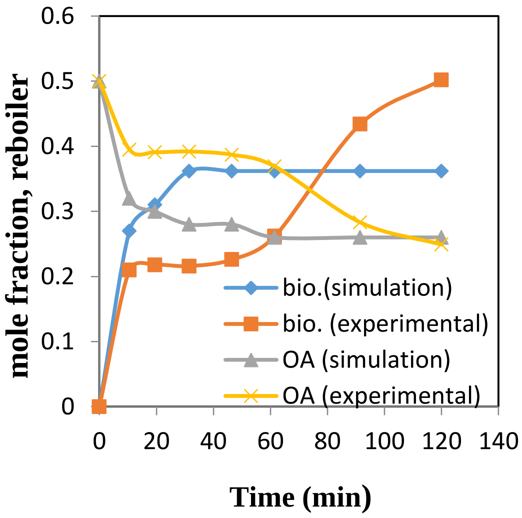

Figure 12. mole fraction of oleic acid and its biodiesel.

[**Operating conditions**: molar ratio of alcohol: acid was 1:1, reaction temperature of 100°C and concentration of sulfated zirconia 2wt%]

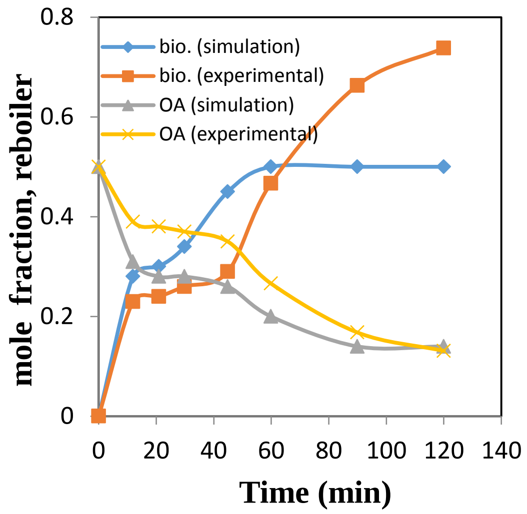

Figure 13. mole fraction of oleic acid and its biodiesel.

[**Operating conditions**: molar ratio of alcohol: acid of 1:1, reaction Temperature of 130°C and concentration of sulfated zirconia 0.5wt%]

Table 1. Textural properties of modified sulfated zirconia.

Parameter	Value
Surface area (m^2/g)	125.23
Pore volume (cm^3/g)	0.063
Bulk density (g/ml)	1.994
SO_4	8.3%
S/SZ	2.77%

Table 2. Biodiesel vs. Petroleum diesel.

Fuel properties	**Biodiesel** **Lotero, et al., 2005**	**Diesel** **Lotero, et al., 2005**	**Present work**
Flash point °C	100–170	60–80	106
Kinematic viscosity (mm/s) @40°C	1.9–6.0	1.3–4.1	6.2289
Specific Density @60/60	0.88	0.85	0.87
Pour point °C	-15 to 10	-35 to –15	-14
Cloud point °C	-3 to 12	-15 to 5	-11
Boiling point °C	182-338	188-343	274
Carbon residue			0.013

Mobile Position Estimation using Artificial Neural Network in CDMA Cellular Systems

Omar Waleed Abdulwahhab
Assistant Professor
Collage of Engineering - University of Baghdad
E-mail: omer_waleed110@gmail.com

Sally Antoin Jergees
Collage of Engineering - University of Baghdad
E-mail: sally_anton@yahoo.com

ABSTRACT

Using the Neural network as a type of associative memory will be introduced in this paper through the problem of mobile position estimation where mobile estimate its location depending on the signal strength reach to it from several around base stations where the neural network can be implemented inside the mobile. Traditional methods of time of arrival (TOA) and received signal strength (RSS) are used and compared with two analytical methods, optimal positioning method and average positioning method. The data that are used for training are ideal since they can be obtained based on geometry of CDMA cell topology. The test of the two methods TOA and RSS take many cases through a nonlinear path that MS can move through that region. The results show that the neural network has good performance compared with two other analytical methods which are average positioning method and optimal positioning method.

Keywords: feed forward neural network, time of arrival, received signal strength, back propagation, optimal positioning method, and average positioning method.

تقدير موقع الهاتف المحمول بأستعمال الشبكة العصبية الصناعيــة في أنظمة CDMA الخلويــة

عمر وليد عبد الوهاب
أستاذ مساعد
كلية الهندسة - جامعة بغداد

سالي انطوان جرجيس
كلية الهندسة- جامعة بغداد

الخلاصة

ان استعمال الشبكات العصبية كنوع من الذاكرة المترابطة سيطرح ضمن هذا البحث من خلال تقديم مشكلة تقدير موقع الهاتف المحمول حيث ان الهاتف سيقوم بتقدير موقعة بالاعتماد على شدة الاشارة المستلمة من قبل عدة محطات مجاورة له حيث ان الشبكة العصبية ممكن ان تبنى داخل الهاتف. استخدمت طرق تقليدية مثل طريقة زمن الوصول وطريقة قوة الاشارة المستلمة وتمت مقارنتها مع طرق تحليلية و هي طريقة المعدل والطريقة الفضلى. وكانت البيانات التي استخدمت في تدريب الشبكة مثالية اعتمدت من التصميم المعتمد ضمن النظام الخليوي للCDMA ثم تم اختبار هذه الشبكة على مسار تم تحديده ضمن منطقة معينة ومقارنة نتائج الشبكة مع الطريقتين التحليليتين.

كلمات رئيسة: التغذية الامامية للخلايا العصبية، زمن الوصول، شدة الاشارة المستلمة، الانتشار العكسي، الطريقة المثلى لتحديد الموقع، طريقة المعدل لتحديد الموقع.

1. INTRODUCTION

Mobile positioning consider as an essential application nowadays mobile station (MS) position may be found with assistant of cellular network that mean network-based techniques or by using GPS and this mean hand set- based techniques the purposes and methods that found for MS location estimation are many some of purposes are for security and for emergency calls and other for services. About methods researchers and authors use these methods theoretically or by simulation or empirically the aim of the paper are to explain how to develop the feed forward neural network as an associative memory for purpose of MS positioning through simulation using matlab. Considering the importance of mobile positioning in daily life applications many techniques and methods were proposed that depend on signal transmitted between MS and BS. Some of these methods are hand set based methods and the other are network based methods, **Karray** and **Silva, 2004.** The common methods used in mobile positioning are time of arrival (TOA), received signal strength (RSS) and angle of arrival (AOA). All of them depend on the radio signal travelling between MS and BS. The idea began when three points which represent base stations BS centered each cell of CDMA have known. Fixed position three circles will be formed when taking appoint of MS with three BSs. The position of MS will be the intersection of these circles, but due to NLOS error that affects the signal, the intersection point will be an uncertainty region and the aim is to find MS position inside this region. **Cong,** and **Zhuang, 2002**, Proposed a scheme that combined the time difference of arrival (TDOA) measurements from the forward link pilot signals with the angle of arrival (AOA) measurement from the reverse link pilot signal. A two-step least square location estimator was developed based on a linear form of the AOA equation in the small error region. **Chen, et al., 2010**, illustrated hybrid proposed schemes that combine time of arrival (TOA) at three BSs and angle of arrival (AOA) information at the serving BS to give location estimate of the MS. The proposed schemes mitigate the NLOS effect simply by the weighted sum of the intersections between three TOA circles and the AOA line without requiring a *priori* information about the NLOS error. **Ping, et al., 2006**. The model of the data fusion with multi-parameters of TOA/TDOA/AOA is set up to optimize network hybrid location, and the inaccuracy or fuzzy problem produced by conventional location algorithm can be overcome effectively, **Sheen, et al.,2002.** An adaptive fuzzy logic estimator for locating mobiles in a direct sequence code division multiple access (DS/CDMA) cellular system is proposed. The location estimation is based on the measured pilot signal strengths by the mobile station (MS) from a number of nearby base stations (BSs). A smoother, which uses past and current output data from the fuzzy estimator to produce a more accurate estimate, is used to improve the accuracy of the location estimation. In **Caffery,** and **Stuber, 1998,** two methods are considered measured times of arrival (TOA) and angles of arrival (AOA). The TOA measurements are obtained from the code tracking loop in the CDMA receiver, and the AOA measurements at a base station (BS) are assumed to be made with an antenna array. **Venkatraman, et al., 2004,** proposed a location technique that estimates the line-of-sight (LOS) ranges based on NLOS range measurements. The approach utilizes a constrained nonlinear optimization approach for range measurements available from three base stations. The constraints were extracted from bounds on the NLOS error and the relationship between the true ranges. A hybrid location scheme, presented by, **Chen,** and **Feng, 2005**, which combined the satellite-based and the network-based signals, the proposed scheme utilizes the two-step Least Square method for estimating the three-dimensional position (i.e. the longitude, latitude, and altitude) of the mobile devices. The Kalman filtering technique was exploited to both eliminate the measurement noises and to track the trajectories of the mobile devices. A fusion algorithm was employed to obtain the final location estimation from both the satellite-based and the network-based systems. **Zhou, et al., 2009**, designed a directional propagation model, the Modified Directional Propagation Model (MDPM), which makes use of a common signal propagation model to perform location estimation. It is a signal strength based algorithm which estimates the location of the Mobile Station by signal strength received from the nearly base stations. **Wei,** and **Lenan, 2009,** presented a mobile station location method using constrained least-squares (CLS) estimation in the non-line of sight (NLOS) conditions. When some of the measurements are from NLOS paths, the location errors can be very large. The proposed method mitigates possible large TOA error measurements caused by NLOS. The memorization capability of a multilayer interpolative neural network in, **Abdlwahhab, 2014** is exploited to estimate a mobile position based on three angles of arrival. The neural network is trained with ideal angles-position patterns distributed uniformly throughout the region. In **Chen,** and **Lin, 2011** a novel algorithm was proposed that combines both time of arrival (TOA) and angle of arrival (AOA) measurements to estimate the MS in NLOS environments. The proposed algorithm utilizes the intersections of two circles and two lines, based on the most resilient back-propagation (Rprop) neural network learning technique, to give location estimation of the MS. The traditional Taylor series algorithm (TSA) and the hybrid lines of position algorithm (HLOP) have convergence problems, and even if the measurements are fairly accurate, the performance of these algorithms depends highly on the relative position of the MS and BSs. Different NLOS models were used to evaluate the proposed methods.

2. PAPER ORGANIZATION

This paper is organized as follows. After a brief review on the nature of the work of the paper and some of related works in the same field the structure of the neural network used would be presented in section two that network used to find the position of the mobile inside the CDMA cellular system which described in section three and compared the network design with two other methods which are average positioning method that described in section four while section five talked a bout the other method which is optimal positioning method section six shows how to train the network using the generated pattern where section seven shows how to calculate this pattern uniformly (any generated pattern can be used) the results of testing the network would be shown in the section eight finally conclusions were obtained through the period of the work would be presented in section nine.

3. ARCHITECTURE OF NUERAL NETWORK

The architecture of NN consist of three layers, input layer with three neurons that represent measurements received from three base stations and a single hidden layer with forty neurons and unipolar sigmoid as activation function and output layer of two neurons that represent position of mobile station with linear activation function. As shown in **Fig.1.**

Where S= $[s_0\ s_1\ s_2]^T$ input of the neural network.

O=$[x\ y]^T$ output of the neural network.

V_{ji}= 40 * 4 the hidden layer weight matrix with bias.

W_{kj}= 41 *2 the output layer weight matrix with bias.

4. THE PROPOSED CELLULAR SYSTEM LAYOUT

A two dimensional model of a CDMA cellular system was assumed. Where the area is divided into contiguous cells each cell is served by a single base station as shown in the **Figs. 2 and 3**.

5. AVERAGE POSITIONING METHOD

It is an analytical method in which intersection of three circles centered by base station can be shown in **Fig. 5** and found mathematically as

a. Intersection of circle of BS_0 and circle of BS_1

$$X_A = \frac{\left(0.5*(y_1-y_0)*(d_0^2-d_2^2+\ x_2^2-x_0^2+y_2^2-\ y_0^2)-0.5*(y_2-y_0)*(d_0^2-d_1^2\ +\ x_1^2-x_0^2+y_1^2-\ y_0^2)\right)}{\left((x_2-x_0)*(y_1-\ y_0)-(x_1-x_0)*(y_2-y_0)\right)} \qquad (1)$$

$$Y_A = \ (0.5*(d_0^2-d_1^2+\ x_1^2-x_0^2+y_1^2-\ y_0^2)-(x_1-x_0)*\ X_A)/(y_1-y_0) \qquad (2)$$

b. Intersection of circle of BS_0 and circle of BS_2

$$X_B = \frac{\left(0.5*(y_1-y_0)*(d_1^2-d_2^2+x_2^2-x_1^2+y_2^2-y_1^2)-0.5*(y_2-y_1)*(d_0^2-d_1^2+x_1^2-x_0^2+y_1^2-y_0^2)\right)}{\left((x_2-x_1)*(y_1-y_0)-(x_1-x_0)*(y_2-y_1)\right)} \qquad (3)$$

$$Y_B = \ (0.5*(d_0^2-d_1^2+\ x_1^2-x_0^2+y_1^2-\ y_0^2)-(x_1-x_0)*\ X_B)/(y_1-y_0) \qquad (4)$$

c. Intersection of circle of BS_1 and circle of BS_2

$$X_C = \frac{\left(0.5*(y_2-y_0)*(d_1^2-d_2^2+x_2^2-x_1^2+y_2^2-y_1^2)-0.5*(y_2-y_1)*(d_0^2-d_2^2+x_2^2-x_0^2+y_2^2-y_0^2)\right)}{\left((x_2-x_1)*(y_2-y_0)-(x_2-x_0)*(y_2-y_1)\right)} \qquad (5)$$

$$Y_C = \ (0.5*(d_0^2-d_2^2+\ x_2^2-x_0^2+y_2^2-\ y_0^2)-(x_2-x_0)*\ X_C)/(y_2-y_0) \qquad (6)$$

The average point will be

$$X_{MS} = \frac{X_A+\ X_B+X_C}{3}$$

$Y_{MS} = \frac{Y_A+Y_B+Y_C}{3}$ and the position of this method will be (X_{MS}, Y_{MS})

6. OPTIMAL POSITIONING METHOD

This method finds mobile station (MS) location by minimizing the sum of squares of a nonlinear cost function. If the mobile has the position (x_0,y_0) and transmit a signal at time t_0, *n* number of base stations will be found to receive this signal. The base stations (BS's) positions are (x_1,y_1),

(x_2,y_2), ……,(x_N,y_N) and receive the signal at time t_1, t_2, …., t_N. as in, **Liu, et al., 2007.**The cost function is represented by Eq. (7):

$$F(x) = \sum_{i=1}^{N} \alpha_i^2 \; f_i^2(x) \tag{7}$$

Where α_i the reliability of signal received at measuring unit.

And $f_i(x)$ is

$$f_i(x) = c(t_i - t) - \sqrt{(x_i - x)^2 + (y_i - y)^2}$$

Where c is speed of light. Finding the values of x, y and t that make $f_i(x)$ equal to zero**.**

7. TRAINED NEURAL NETWORK

NN is trained with online backpropagation algorithm where the weight of the hidden layer designated by V and weight of output layer designated by W were initialized in a random manner with values between -0.5and 0.5. These weights are updated when each input pattern is presented to the NN. The stopping criteria depend on the value of root mean square error (RMS) error defined by Eq. (8).

$$E_{RMS} = \sqrt{\frac{1}{P}\sum_{i=1}^{P}(d^{(i)} - o^{(i)})^T(d^{(i)} - o^{(i)})} \tag{8}$$

Where:

P is the number of training patterns,

$\boldsymbol{d}^{(i)}$ is the i 'th desired value for the output of the neural network.

$\boldsymbol{o}^{(i)}$ is the i 'th actual output of the neural network.

Figs. 5, 6, 7 and 8, show the final steps of learning process that the network is trained because each time oscillation occurs, learning process must be stopped and less the learning rate value and retrain the network in a convergence manner. For time of arrival method different number of neurons in the hidden layer are experimented to reach a value of RMS equal to 12.

Figs.9, 10, 11, 12, 13 and 14, show the final steps of learning process that the network was trained because each time oscillation occurs, learning process must be stopped and less the learning rate value and retrain the network in a convergence manner. For received signal strength method different values of σ and k are used to train the neural network for different propagation environments.

7. GENERATION OF TRAINING PATTERNS

Based on geometry of CDMA cell topology there will be a triangle form from the location of three base stations. Many points inside this region can be found randomly or according to a mathematical algorithm where the position of three BSs are known and value of R (radius of cell) and h (height of cell) are known in this paper a uniform distribution of training patterns used to train the network, these points can be calculated as:

$$x = \frac{3R}{2n_x} \times i \qquad \text{where i} = 0, 1, \dots, n_x$$

$$y = y_{min} + \frac{y_{max} - y_{min}}{n_y} \times j \quad \text{where} \quad j = 0, 1, \dots, n_y$$

Where n_x and n_y are the number of subintervals on the $x-$ axis and y−axis, respectively.

8. SIMULATION RESULTS AND DISCUSION

The performance of the previously trained neural networks was compared with two conventional methods to find the mobile location, namely the average position method and the optimal position method using Matlab R2010a. The testing points can be individual points or paths choose randomly or described by mathematical representation. In this paper the parabolic path represented by the Eq. (9) and shown in **Fig.13** used to test the performance of the trained neural network.

$$y = 300 + x - 0.0027x(x - 200) \tag{9}$$

The comparisons of the neural network with other analytical methods were illustrated in the **Figs.16-22** for different environment situations, the **Fig. 16** illustrates how the NN even with smaller number of neurons overcome the two other methods especially when error in the signal increase also the figure illustrate that NN with higher number of neurons has better performance. The **Fig. 17** shows that the NN is better than the two other methods this is clearly shown from the linear behavior of the NN with increasing the error when kind of environment situation represented by the values of $k = 2$ and $\sigma = 2$. **Fig. 18** shows that the NN still on the same behavior while other two methods show bad results. **Fig. 19** shows again the good performance of the NN over the two other methods.In **Figs. 20, 21 and 22** illustrate that the NN shows less performance in worse environment but still better than other methods. The model which is used in the work is log normal shadowing and its equation in dB is:

$$PL(d)[dB] = PL(d_0) + 10\,k\log\left(\frac{d}{d_0}\right) + X_\sigma$$

Where σ is the standard deviation and k is path loss exponent which are the important factors of the equation that statistically describe the path loss so that the value of k depend of a specific propagation environments for example free space equal to 2 and have larger values when obstruction are presented that mean better results obtained with lower values of k as cleared in **Theodore S. Rappaport, 2001**.

9. CONCLUSION

a. When there is no error in the measured signal characteristics, the direct analytical methods (such as average position and optimal position methods) give exactly the actual position of the mobile station while the trained neural network approximates the mobile position with some error.

b. In the presence of measurement error (due to NLOS and noise) the performance of the analytical methods begins to degrade because of the presence of the region of uncertainty while the neural network begins to exploit its memorization and generalization capabilities to handle this region. Therefore, as the percentage error of the distance measurements increases, the neural network begins to outperform the analytical methods.

c. A single hidden layer NN is capable of estimating the mobile location

d. The performance of the neural network to find location based on the time of arrival method is better than that of signal strength method because the distance obtained from time of arrival method can be calculated due to linear equations while in signal strength method it obtained from nonlinear equations.

REFERENCES

- Abdulwahhab, O. W., 2014, *Mobile Position Estimation based on Three Angles of Arrival using an Interpolative Neural Network,* International Journal of Computer Applications (0975 – 8887), Vol 100, No.7.

- Caffery, J. and St¨uber, G. L., 1998, *Subscriber Location in CDMA Cellular Networks*, IEEE Transactions on Vehicular Technology, Vol. 47(2/May), PP. 406-416.

- Chen, C. and Feng, K., 2005, *Hybrid Location Estimation and Tracking System for Mobile Devices*, IEEE 61st Vehicular Technology Conference, Vol. 4, PP. 2648-2652.
- Chen, C. and Lin, J., 2011, *Applying Rprop Neural Network for the Prediction of the Mobile Station Location,* Sensors, Vol. 11(4), PP. 4207-4230.
- Chen, C., Su, S., and Lu, C., 2010, *Geometrical Positioning Approached for Mobile Location Estimation*, 2nd IEEE International Conference on Information Management and Engineering, PP. 268-272.
- Cong, L. and Zhuang, W., 2002, *Hybrid TDOA/AOA Mobile User Location for Wideband CDMA Cellular Systems,* IEEE Transactions on Wireless Communications, Vol. 1(3/July), PP. 439-447.
- Karray, F. O. and Silva, C. D., 2004, *Soft Computing and Intelligent Systems Design*, England, Pearson education.

- Liu, H. Darabi, H. Banerjee, P. and Liu, J., 2007, *Survey of Wireless Indoor Positioning Techniques and Systems,* IEEE Transactions on Systems, Man, and Cybernetics—Part C: Applications and Reviews, Vol. 37(6/November).

- Ping, Z., Ling-Yan, L. and Hao-Shan, S., 2006, *A hybrid Location Algorithm Based on BP Neural Networks for Mobile Position Estimation*, International Journal of Computer Science and Network Security (IJCSNS), Vol.6, No.7A, PP.162-167.

- SHEN, X. MARK, J. W. and YE, J., 2002, *Mobile Location Estimation in CDMA Cellular Networks by Using Fuzzy Logic*, Wireless Personal Communications, Vol. 22(1),PP. 57-70.

- Theodore S. Rappaport, 2001, *Wireless communication principle and practice*, 2nd edition, prentice H
- all.

- Venkatraman, S., Caffery, J. and You, H., 2004, *A Novel ToA Location Algorithm Using LoS Range Estimation for NLoS Environments*, IEEE Transactions on Vehicular Technology, [online] Vol. 53(5/September), PP. 1515-1524.

- Wei, K. and Lenan, W., 2009, *Constrained Least Squares Algorithm for TOA-Based Mobile Location under NLOS Environments*, 5th International Conference on Wireless Communications, Networking and Mobile Computing, PP. 1-4.

- Zhou, J., Chu, K. M., and Ng, J. K., 2009, *A Probabilistic Approach to Mobile Location Estimation within Cellular Networks*, 15th IEEE International Conference on Embedded and Real-Time Computing Systems and Applications, PP. 341-348.

Nomenclature List

S=input of the neural network.

O=output of the neural network.

d_i=distance between MS and BS_i, m.

c=speed of light, m/μsec.

t_i=time that signal takes from BS_i to MS, μsec.

V_{ji}=connected weights between input layer and hidden layer.

W_{kj}= connected weights between hidden layer and output layer.

α_i= the reliability of signal received at measuring unit.

E_{RMS}= root mean square error value, m.

x_i=position of BS_i in x-axis.

y_i= position of BS_i in y-axis.

σ=standard deviation ranging from 2 to 6 db.

k= The exponent k is dependent on the propagation environment and varies between 2 and 6.

$\delta_{(k)}$=error signal of output layer of neural network.

$\delta_{(j)}$=error signal of hidden layer of neural network.

R=the radius of the cell, m.

h=is the height of the cell, m.

y_{min}=is the lower line of the triangular region of three BSs used in the scheme.

y_{max}=is the upper line of the triangular region of three BSs used in the scheme.

P=is the number of training patterns.

$d^{(i)}$=is the *i* 'th desired stored response.

$o^{(i)}$=is the *i* 'th actual output

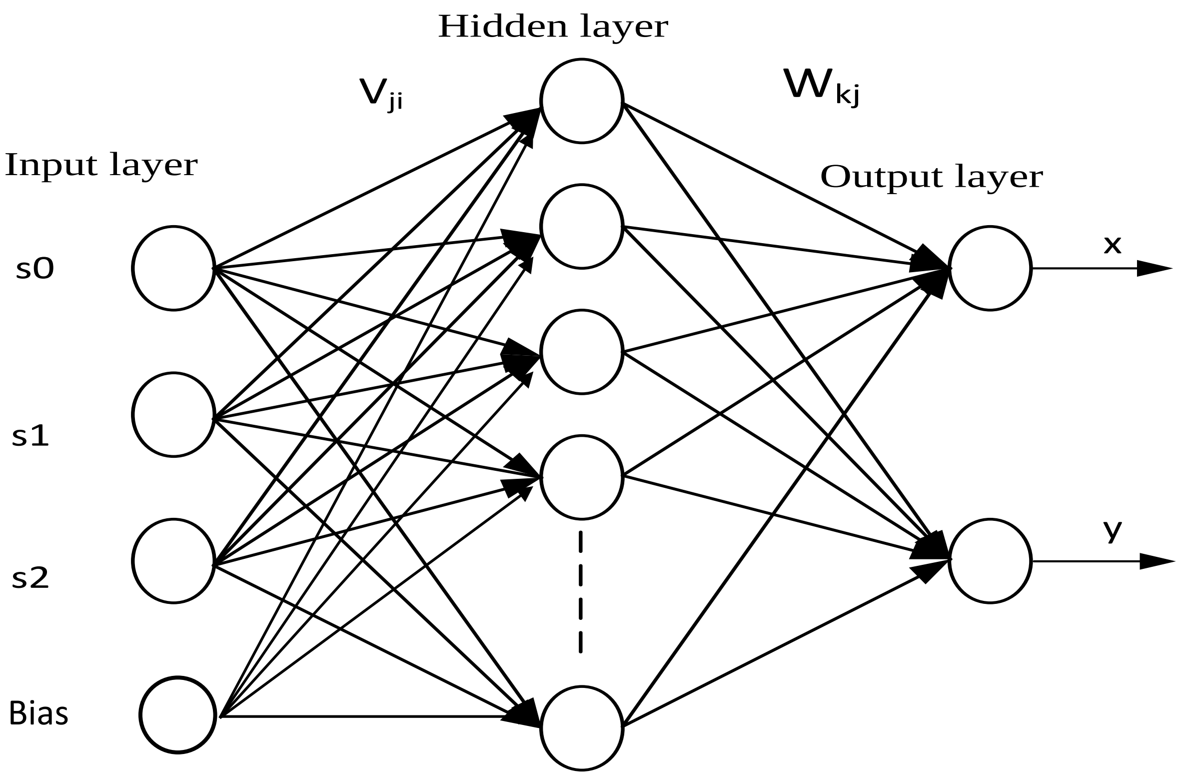

Figure 1. The architecture of the neural network.

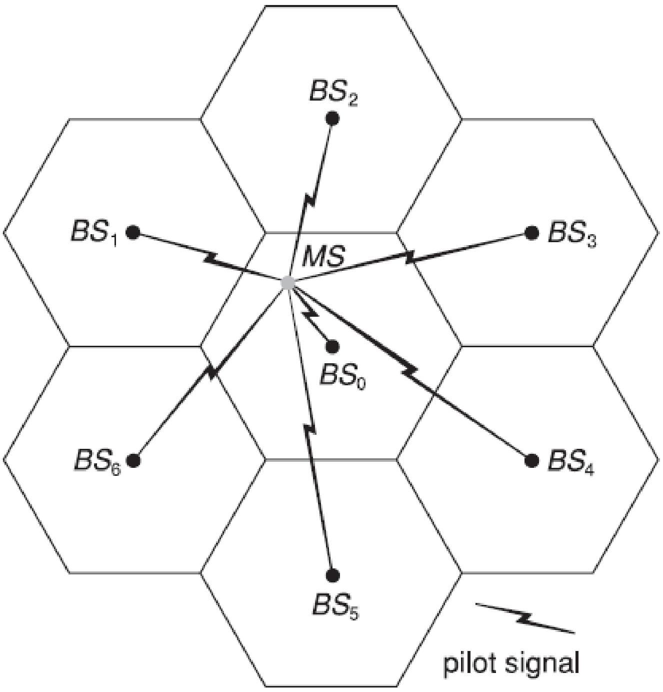

Figure 2. CDMA cellular topology.

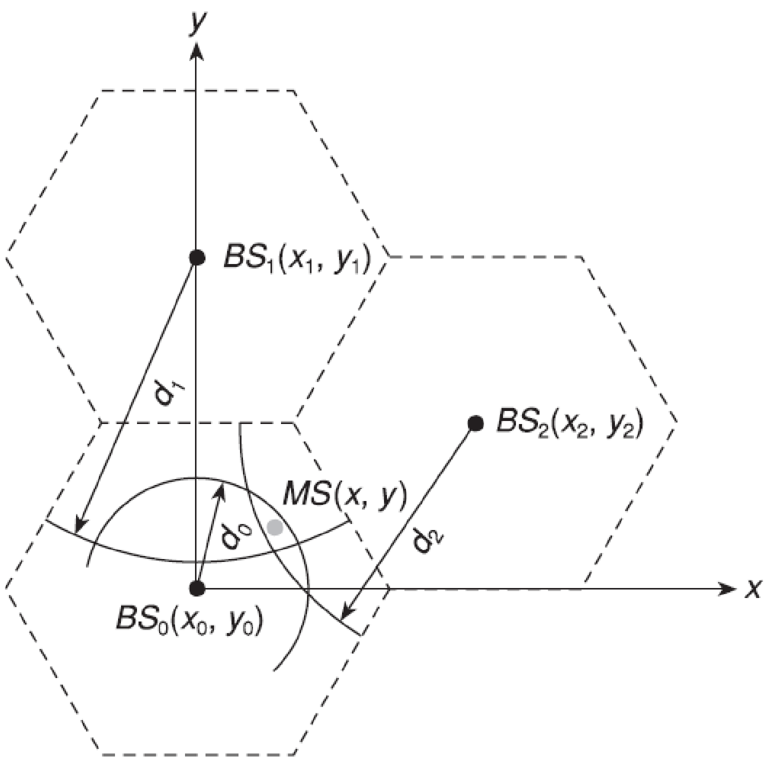

Figure 3. The lateration methods (time of arrival and signal strength**).**

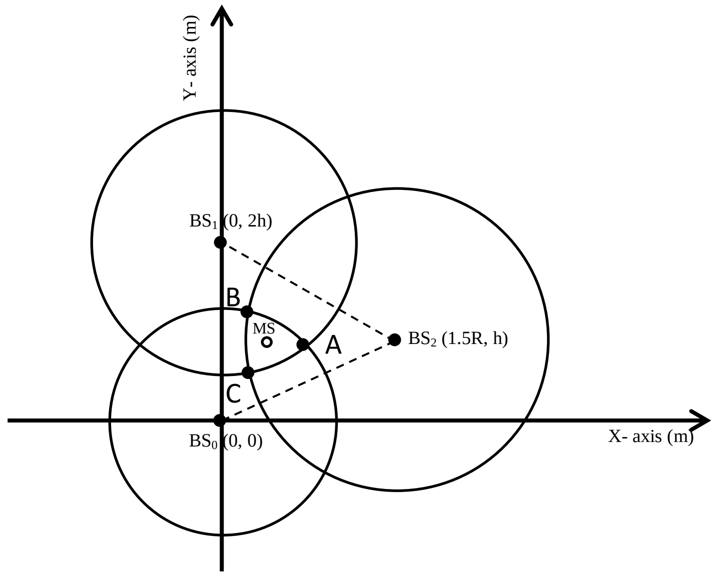

Figure 4. Average positioning method.

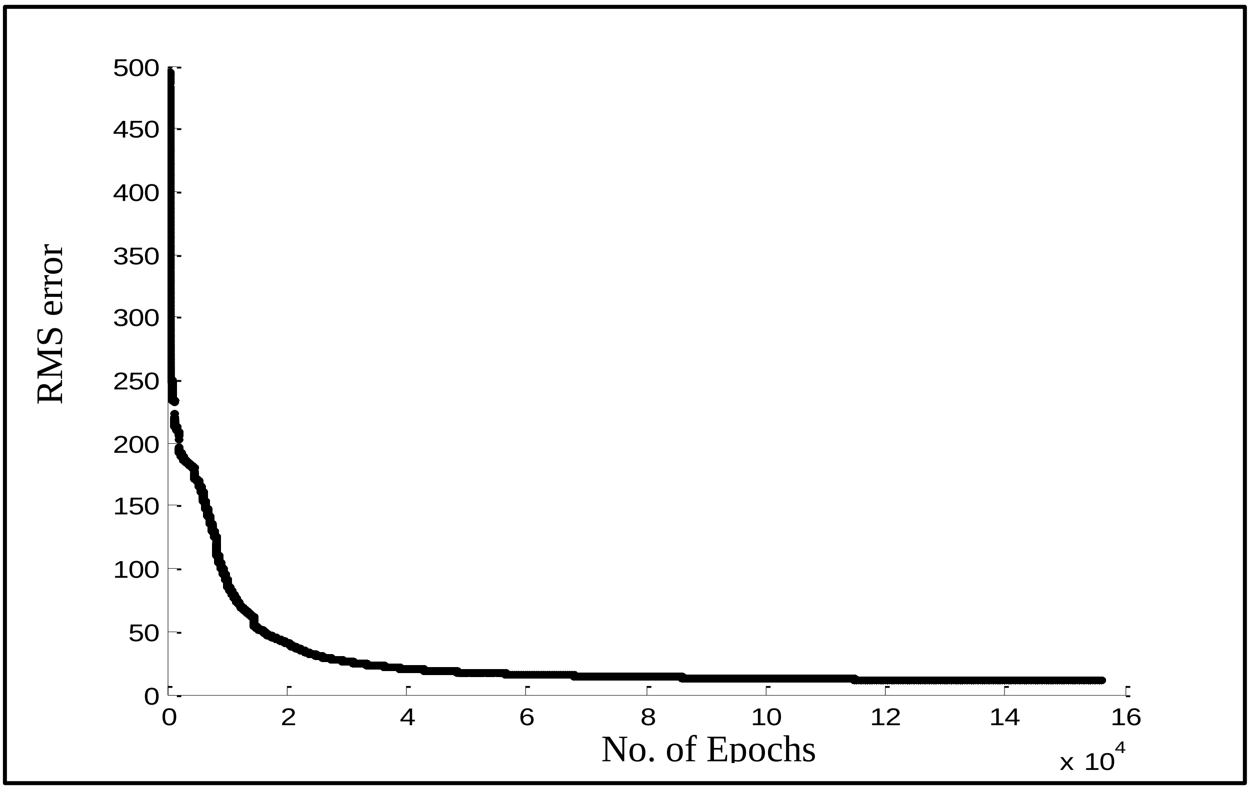

Figure 5. Online training of NN with five neurons in the hidden layer.

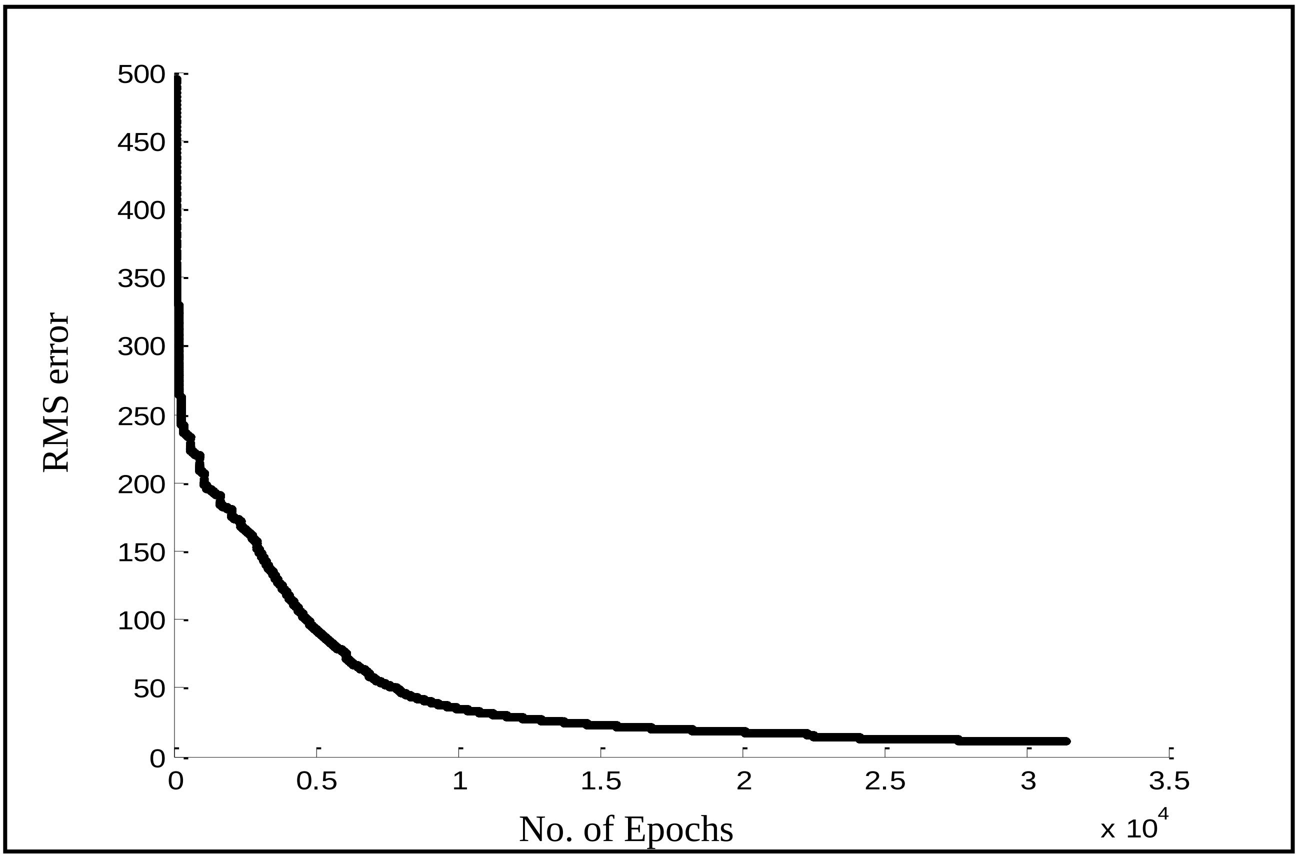

Figure 6. Online training of NN with ten neurons in the hidden layer.

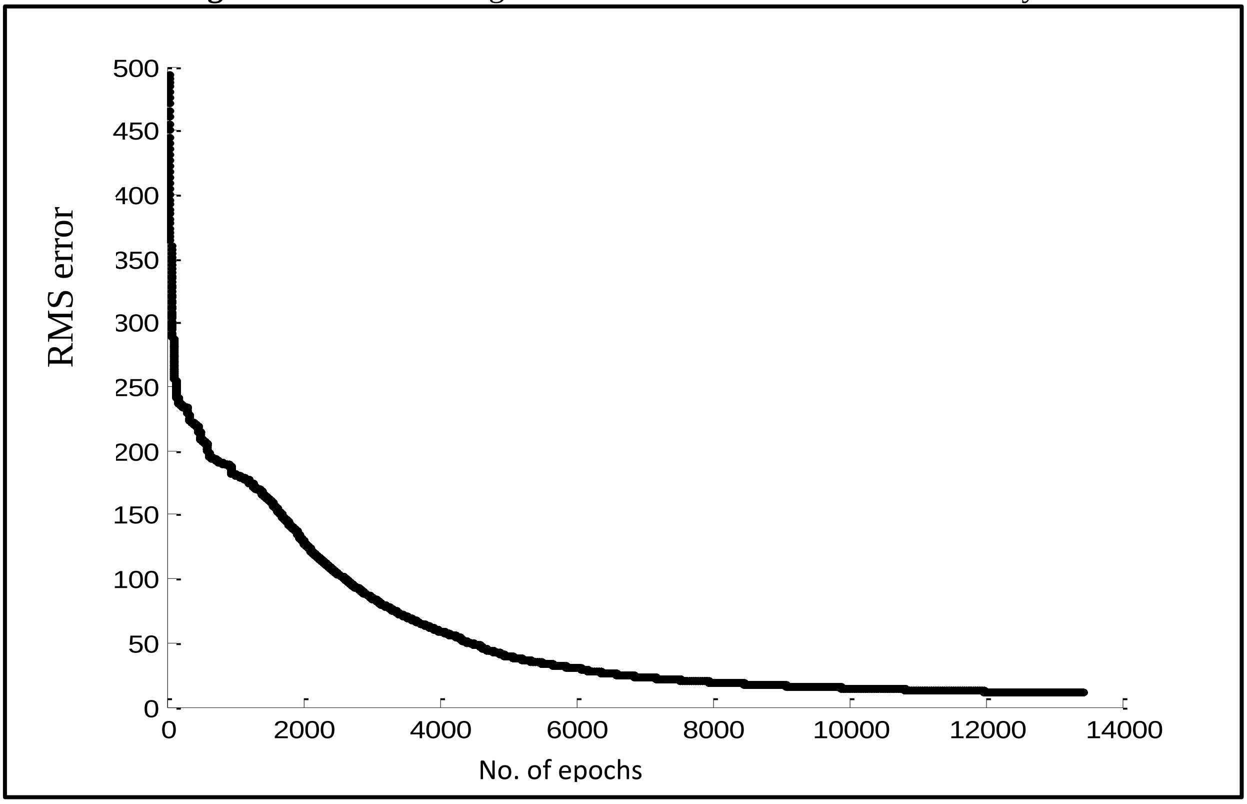

Figure 7. Online training of NN with twenty neurons in the hidden layer.

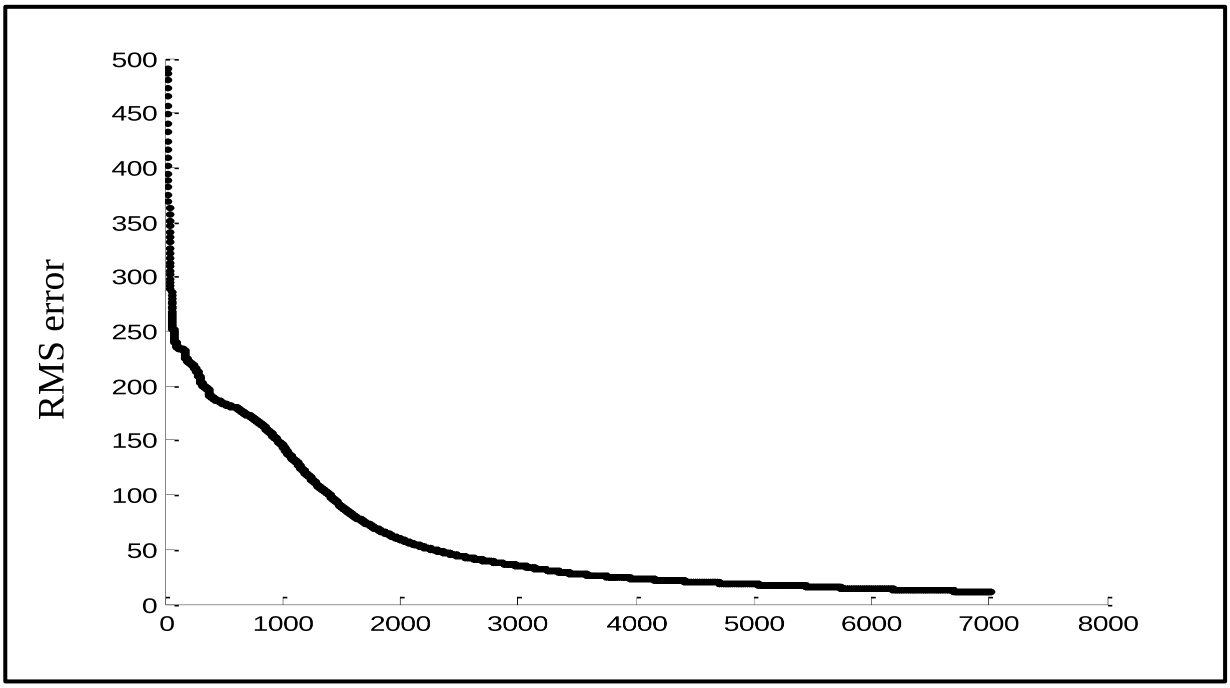

Figure 8. Online training of NN with forty neurons in the hidden layer.

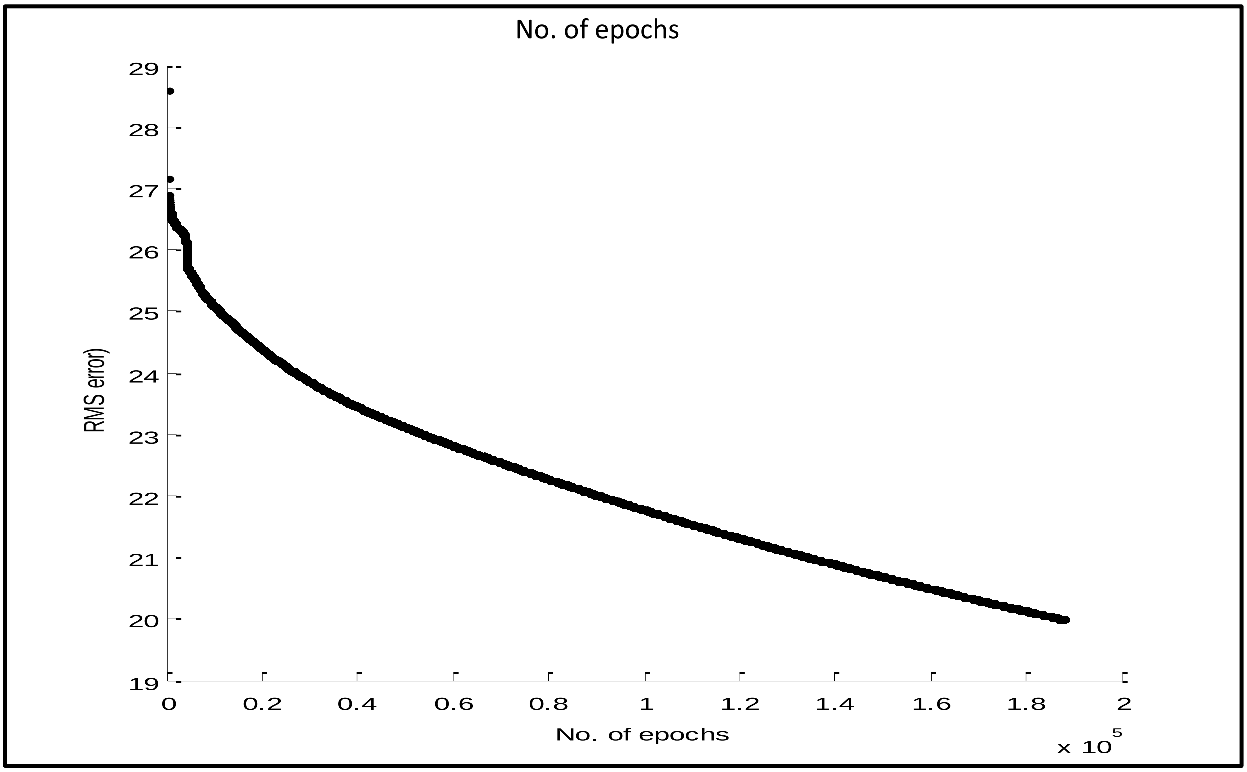

Figure 9. Final step of learning process of forty neurons in the hidden layer for an RMS error value of 20 with $k = 2$ and $\sigma = 2$.

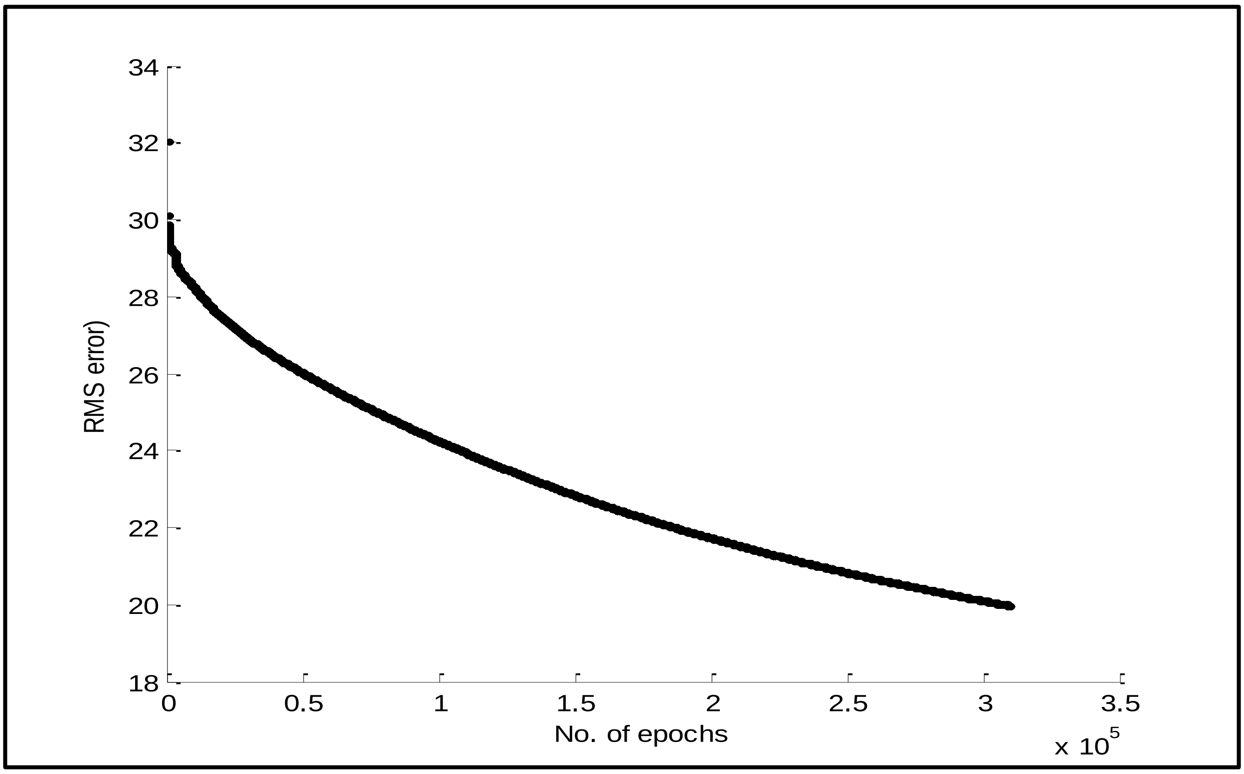

Figure 10. The final step of learning process of forty neurons in the hidden layer for an RMS error value of 20 with $k = 2$ and $\sigma = 4$.

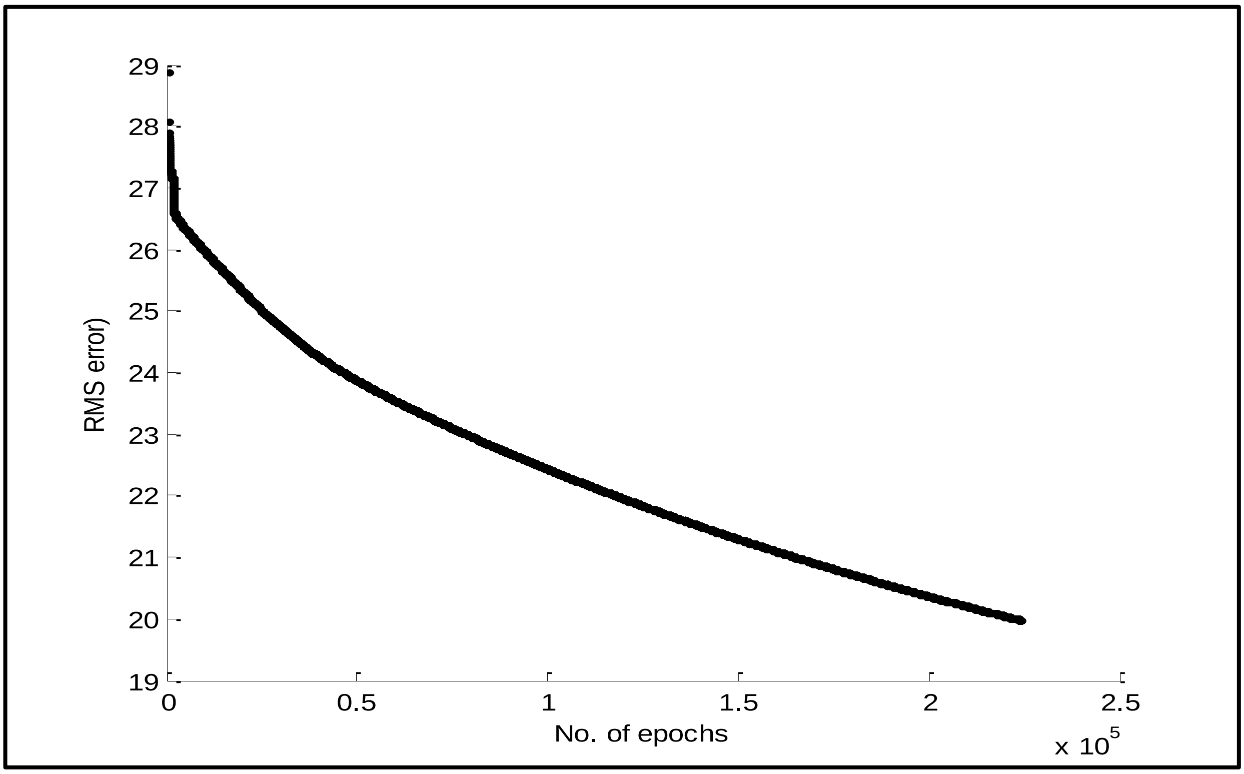

Figure 11. The final step of learning process of forty neurons in the hidden layer for an RMS error value of 20 with $k = 2$ and $\sigma = 6$.

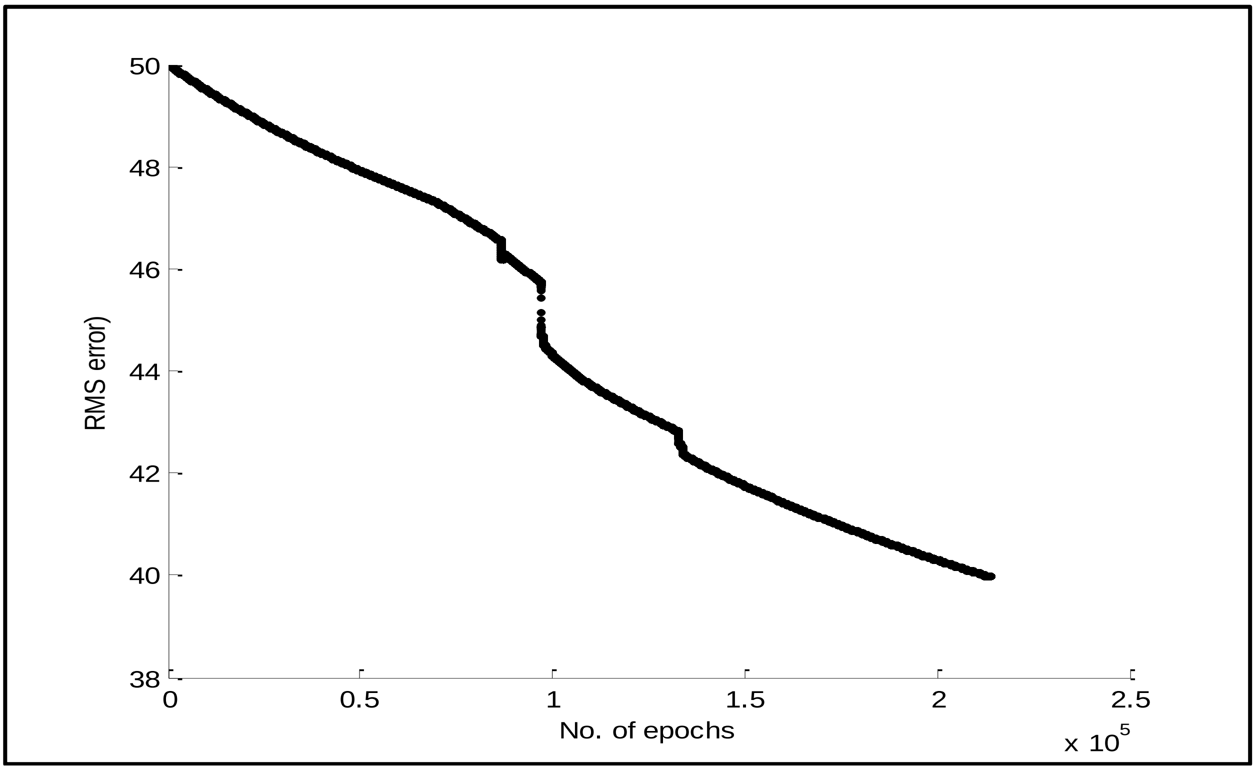

Figure 12. The final step of learning process of forty neurons in the hidden layer for an RMS error value of 40 with $k = 4$ and $\sigma = 2$.

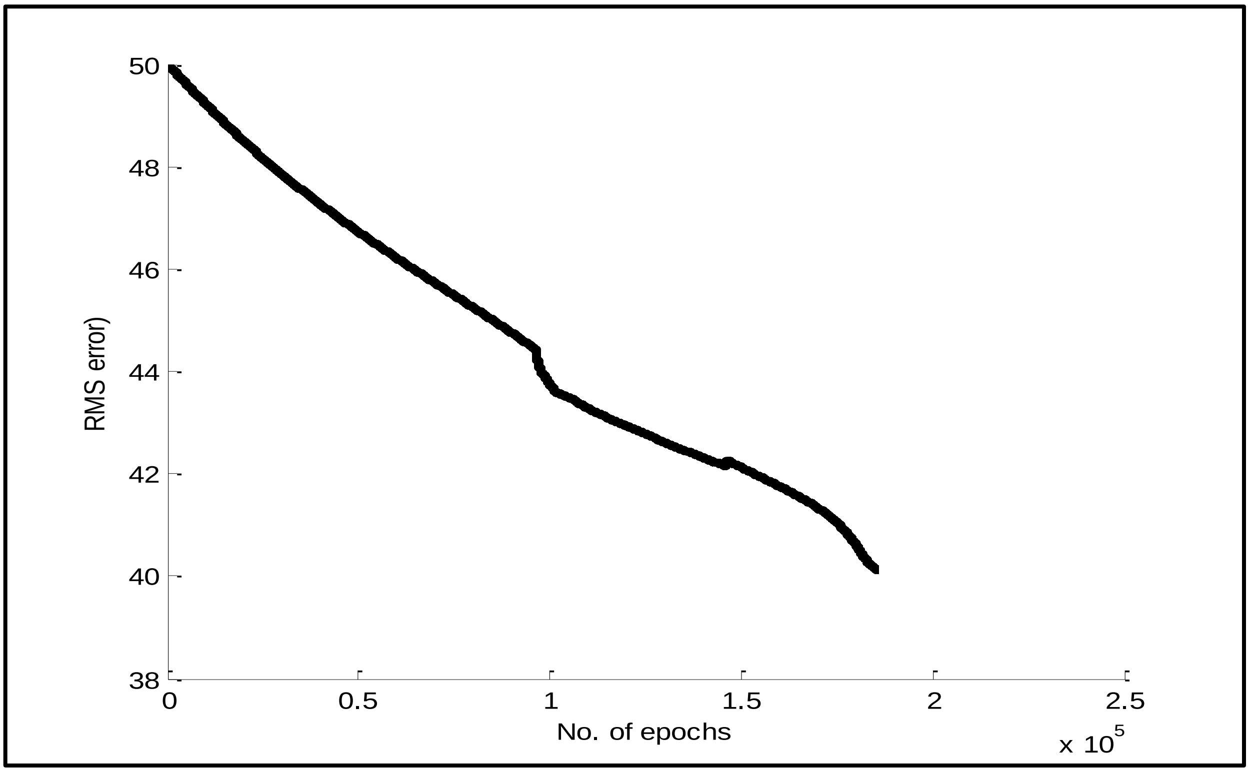

Figure 13. The final step of learning process of forty neurons in the hidden layer for an RMS error value of 40 with $k = 4$ and $\sigma = 4$.

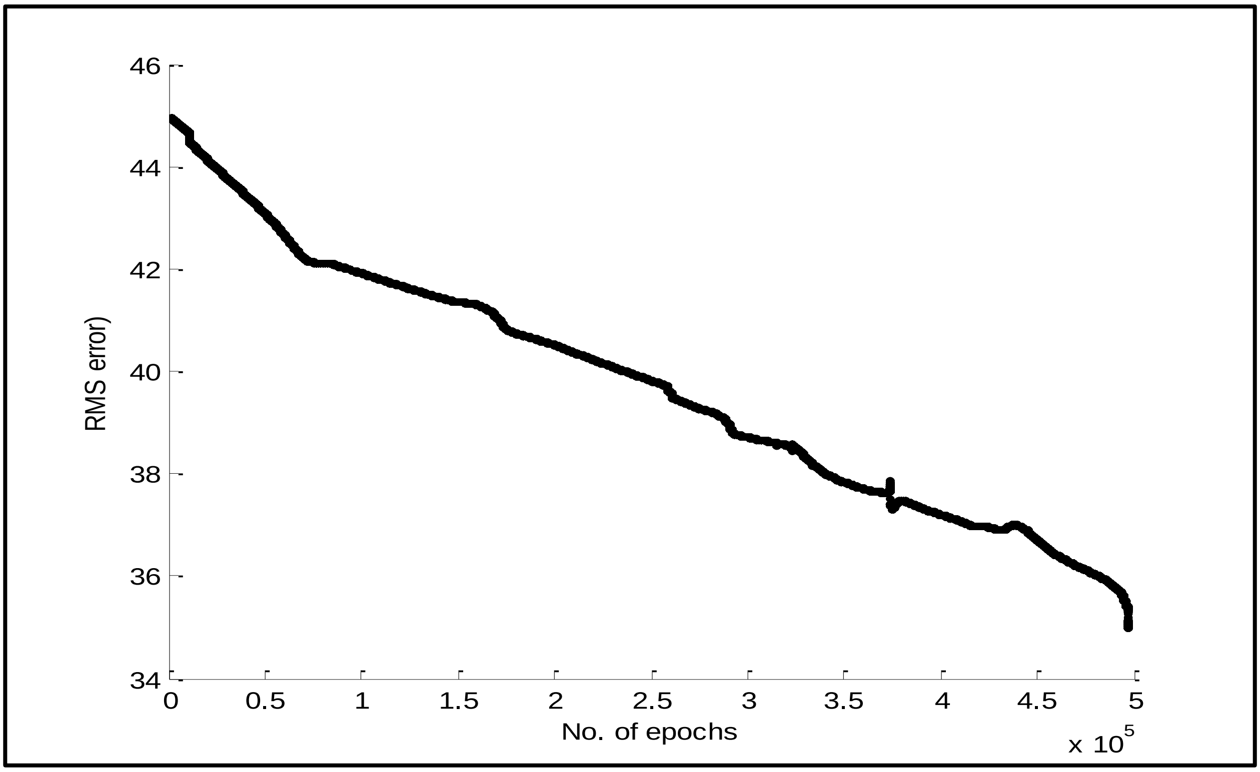

Figure 14. The final step of learning process of forty neurons in the hidden layer for an RMS error value of 35 with $k = 4$ and $\sigma = 6$.

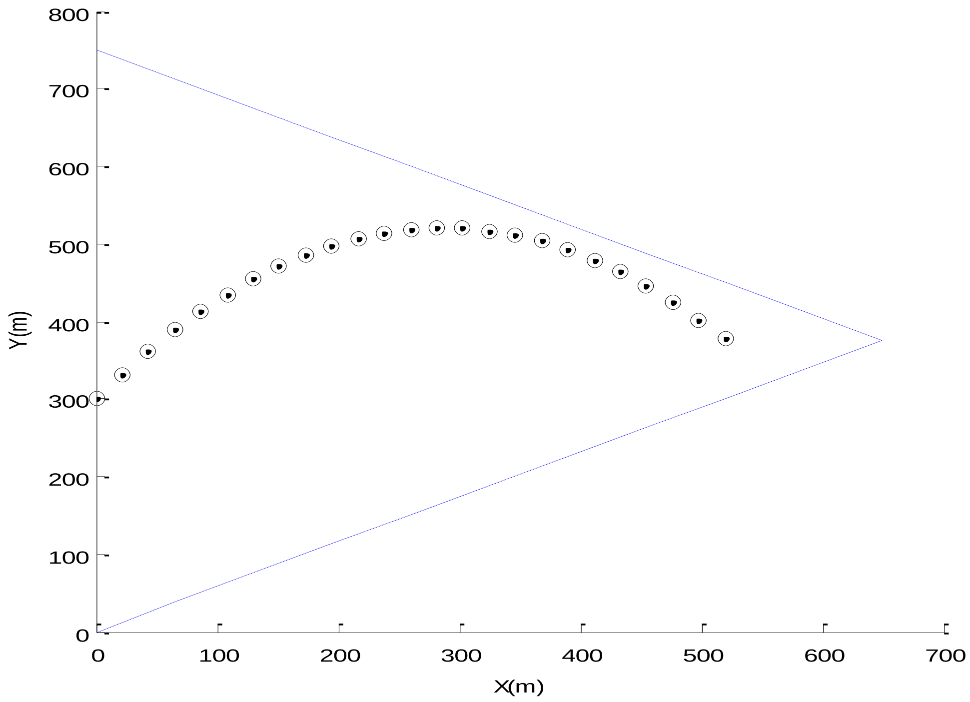

Figure 15. The testing path.

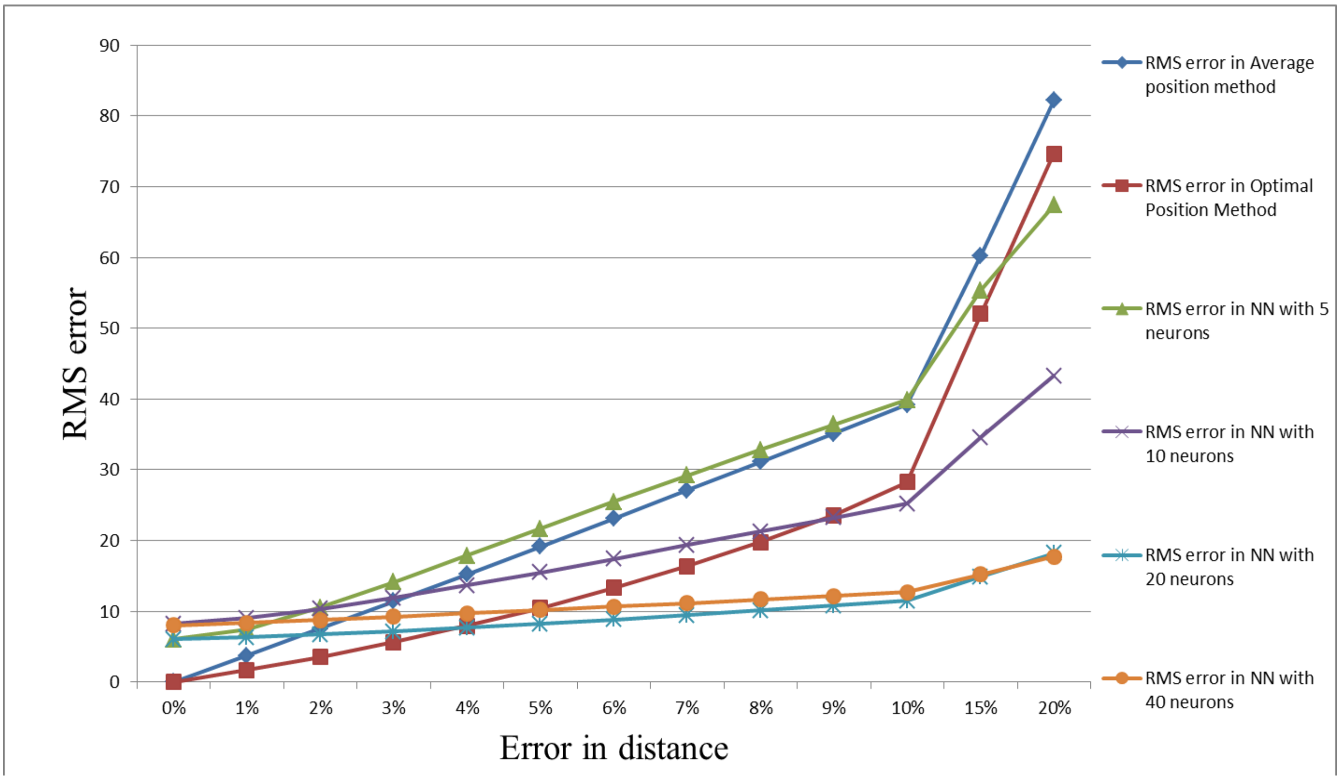

Figure 16. A comparison of NN with four different values of neurons with the average position method and the optimal position method.

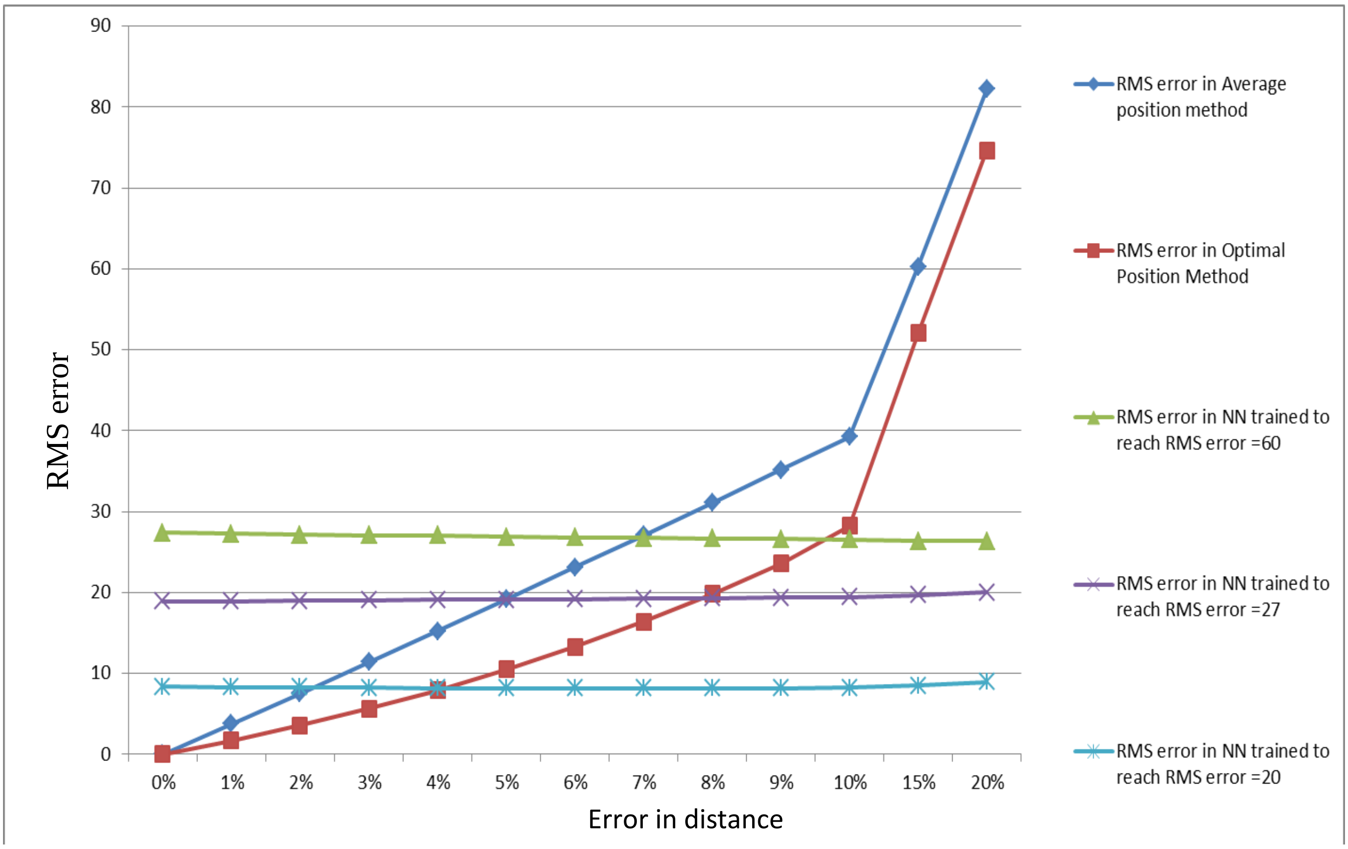

Figure 17. A comparison of NN of forty neurons (k =2 and σ =2) with the average position method and the optimal position method.

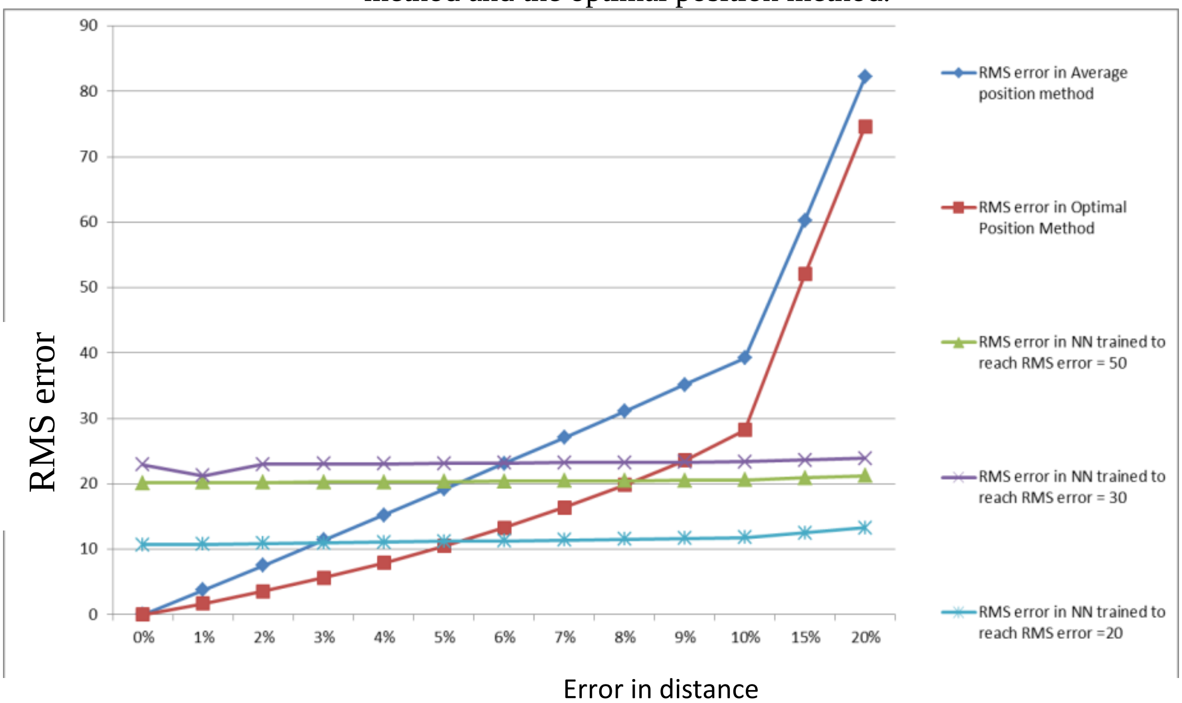

Figure 18. A comparison of NN of forty neurons (k =2 and σ =4) with the average position method and the optimal position method.

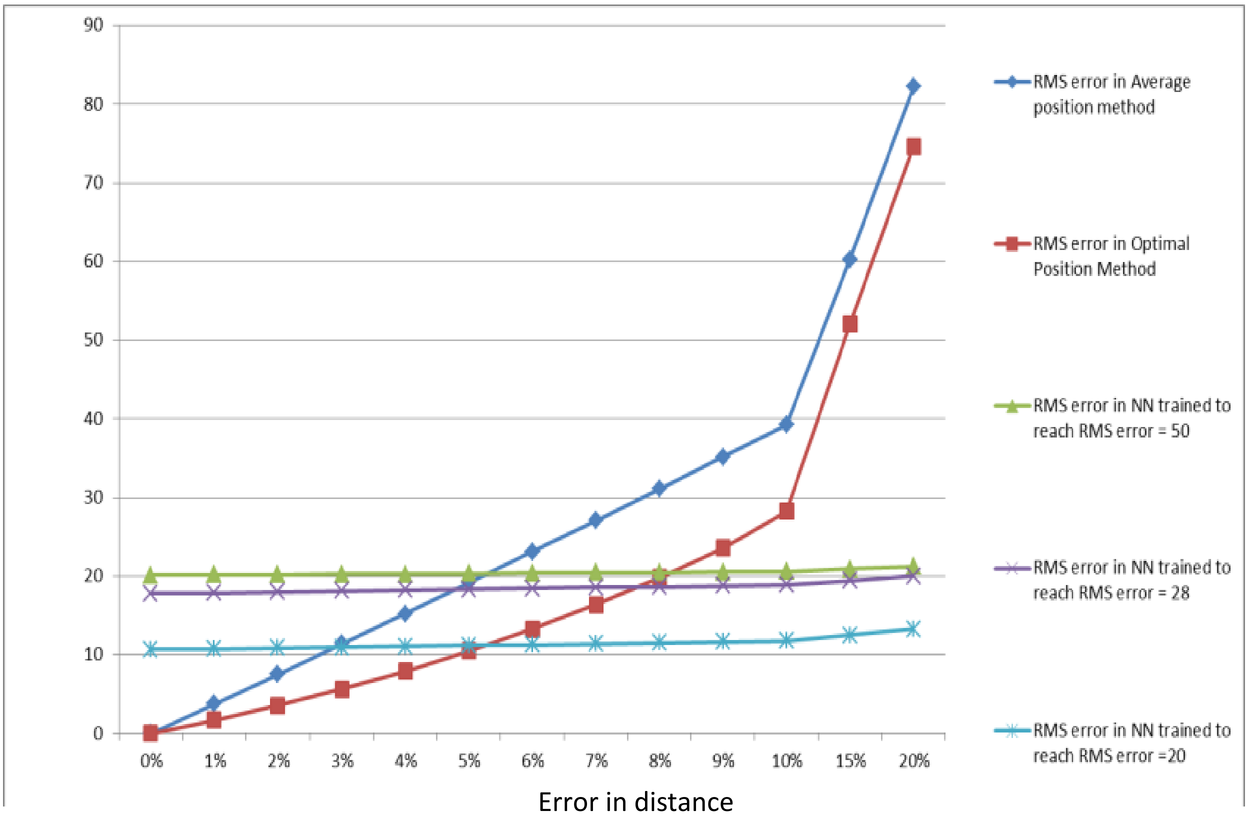

Figure 19. A comparison of NN of forty neurons (k =2 and σ =6) with the average position method and the optimal position method.

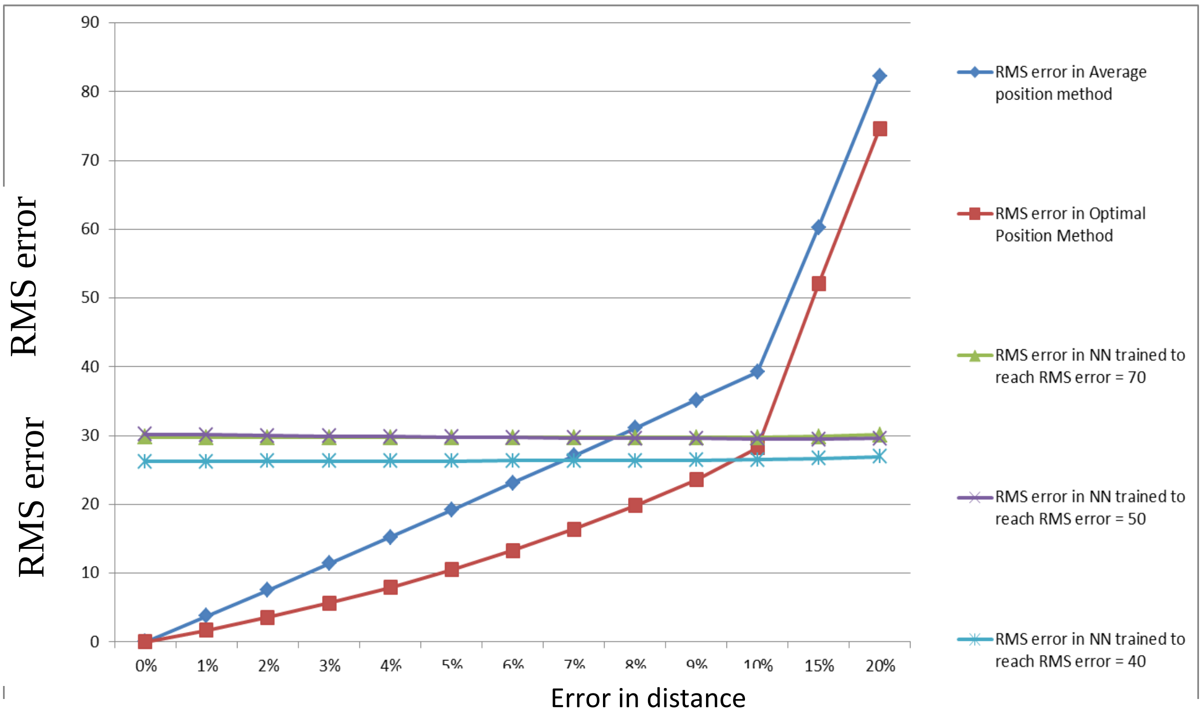

Figure 20. A comparison of NN of forty neurons (k =4 and σ =2) with the average position method and the optimal position method.

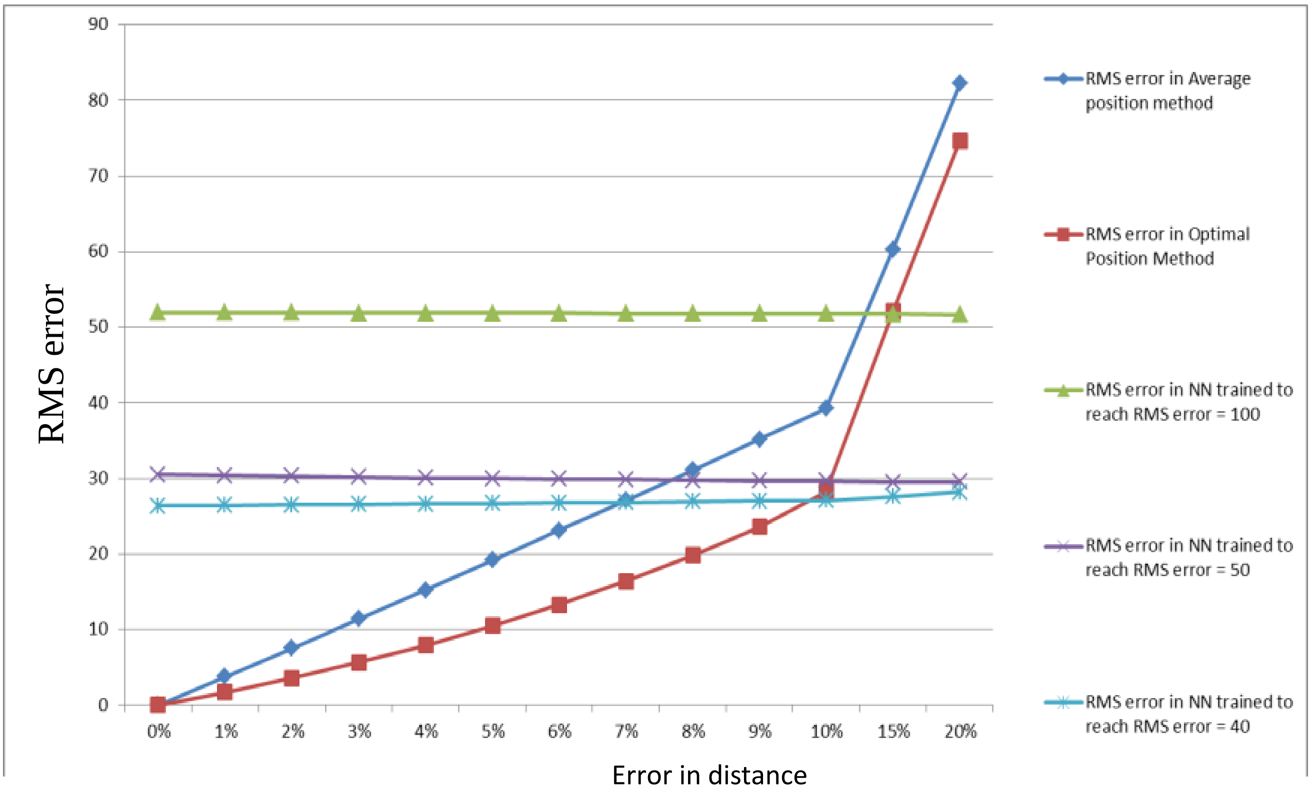

Figure 21. A comparison of NN of forty neurons (k =4 and σ =4) with the average position method and the optimal position method.

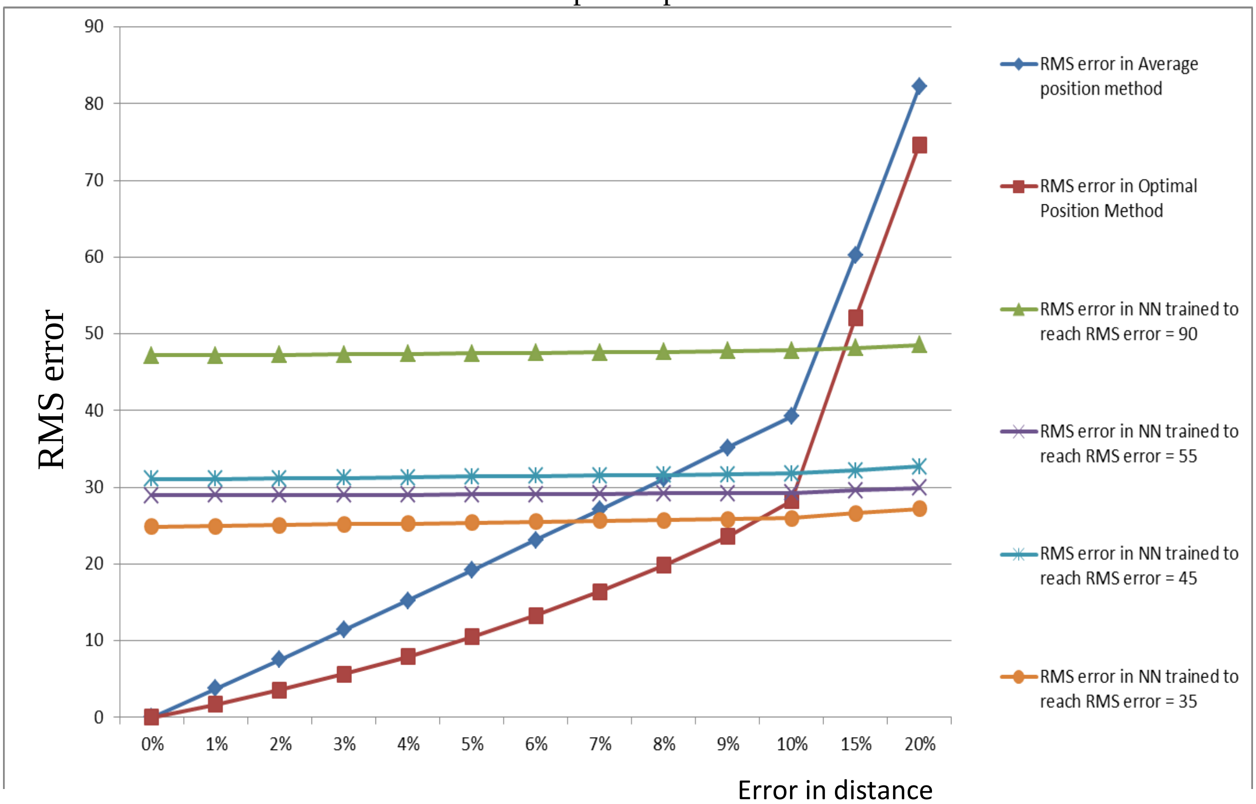

Figure 22. A comparison of NN of forty neurons (k =4 and σ =6) with the average position method and the optimal position method.

Enhanced Chain-Cluster Based Mixed Routing Algorithm for Wireless Sensor Networks

Husam Kareem Farhan
Assistant Lecturer
Ministry of Education / Directorate of Baghdad Education (Karkh 3)
E-mail: husam_kf@yahoo.com

ABSTRACT

Energy efficiency is a significant aspect in designing robust routing protocols for wireless sensor networks (WSNs). A reliable routing protocol has to be energy efficient and adaptive to the network size. To achieve high energy conservation and data aggregation, there are two major techniques, clusters and chains. In clustering technique, sensor networks are often divided into non-overlapping subsets called clusters. In chain technique, sensor nodes will be connected with the closest two neighbors, starting with the farthest node from the base station till the closest node to the base station. Each technique has its own advantages and disadvantages which motivate some researchers to come up with a hybrid routing algorithm that combines the full advantages of both cluster and chain techniques such as CCM (Chain-Cluster based Mixed routing). In this paper, introduce a routing algorithm relying on CCM algorithm called (Enhanced Chain-Cluster based Mixed routing) algorithm E-CCM. Simulation results show that E-CCM algorithm improves the performance of CCM algorithm in terms of three performance metrics which are: energy consumption, network lifetime, and (FND and LND). MATLAB program is used to develop and test the simulation process in a computer with the following specifications: windows 7 (32-operating system), core i5, RAM 4 GB, hard 512 GB.

Keywords: wireless sensor networks, energy efficiency, cluster routing algorithm, chain routing algorithm.

الخوارزمية المحسنة سلسلة المجموعة على اساس التوجيه المختلط لشبكات الاستشعار اللاسلكية

حسام كريم فرحان
مدرس مساعد
وزارة التربية / المديرية العامة للتربية / بغداد / الكرخ 3

الخلاصة

كفاءة الطاقة هي جانب هام في تصميم بروتوكولات توجيه قوية لشبكات الاستشعار اللاسلكية **(WSNs)**. بروتوكول التوجيه الموثوق يجب أن يكون كفوء في استخدام الطاقة ومتكيف مع حجم الشبكة. لتحقيق الحفاظ العالي على الطاقة وتجميع البيانات، يوجد اثنين من التقنيات الرئيسية**:** مجموعات وسلاسل. في تقنية التجميع، غالبا ما تنقسم شبكات الاستشعار إلى مجموعات فرعية غير متداخلة تسمى مجموعات. في أسلوب السلسلة، سيتم ربط عقد الاستشعار مع أقرب جارين، بدءا من ابعد عقدة عن المحطة الأساسية حتى أقرب عقدة إلى المحطة الأساسية. كل تقنية لها مزايا وعيوب خاصة بها الأمر الذي حث بعض الباحثين الى طرح خوارزمية التوجيه الهجينة التي تجمع بين المزايا الكاملة لكلا الطريقتين المجموعات والسلاسل مثل **CCM** (سلسلة-المجموعة على اساس التوجيه المختلط). في هذا البحث، نقدم خوارزمية توجيه بالاعتماد على خوارزمية **CCM** يسمى (الخوارزمية المحسنة سلسلة-المجموعة على اساس التوجيه المختلط) **E-CCM.** نتائج عملية المحاكاة تبين ان خوارزمية **E-CCM** تحسن من أداء خوارزمية **CCM** من حيث ثلاثة معايير للأداء وهي : استهلاك الطاقة , عمر الشبكة, و **(FND and LND).** تم استخدام برنامج **MATLAB** لتطوير واختبار عملية المحاكاة في حاسوب يحمل المواصفات التالية : ويندوز **7** (نظام التشغيل **32** بت), كور **i5**, ذاكرة الوصول العشوائي **4 GB**, القرص الصلب **512 GB**.

1. INTRODUCTION

A wireless sensor network (WSNs) consists of number of sensor nodes that communicate wirelessly and have the ability to sense the surrounding environment including pressure, temperature, humidity and illumination **Oda, et al., 2014**. As WSNs are generally powered by small batteries, energy consumption is the critical aspect that faces the operation of WSNs which has prime effect on the network lifetime. Many researches have been focusing on developing routing algorithms that can decrease the energy consumption and consequently extend the network lifetime. The biggest share of the energy is consumed by data routing, particularly by data transmission which is proportional to the square of the distance between sender and receiver **Tang, et al., 2012**. Thus many algorithms have been proposed to decrease the distance of transmission which leads to decrease the energy consumption and eventually increase the network lifetime.

The earliest routing algorithm aimed to use the above strategy is Low Energy Adaptive Clustering hierarchy (LEACH) **Heinzelman, et al., 2000**. LEACH divides the network into small group and each group forms a cluster and elects one of the sensor nodes within the group to function as a cluster head. The head of each cluster aggregate their data received from other nodes and send it to the base station. This algorithm is the first hierarchical algorithm that proposed to maximize the network lifetime. Another routing algorithm has proposed as an improvement to LEACH which is Power Efficient Gathering in Sensor Information System (PEGASIS) **Lindsey**, and **Raghavendra**, **2002**. PEGASIS utilize chain technique instead of clustering technique in order to achieve more energy conservation. Each node will connect to the two closest neighbors starting with the farthest node from the base station up to the closest node to the base station. In this paper, try to use a hybrid scheme that combines the cluster and chain technique. The proposed algorithm divides the network into multiple chains and works within two stages.

2. RELATED WORK

The emergence of LEACH and PEGASIS in the area of designing a hierarchical routing algorithms leads to many valuable researches that came up with different hierarchical routing algorithms. Moreover, the increasing interest in WSNs and ongoing development in its applications and techniques become the inspiration for the researchers' efforts in order to explore the details of applications, characteristics and communication mechanisms of WSNs. However, there are wide variety of WSNs hierarchical routing algorithm, it can be classified into three categorize which are cluster, chain and hybrid routing algorithms **Kareem, et al., 2014**. **Yu and Song, 2010** utilized chain technique to propose an algorithm which called EECB (Energy Efficient Chain Based Routing Protocol). EECB algorithm can solve the problem that happen when the sensor node are relatively distant from its closest neighbors.

Taking advantage of chain strategy, **Gao, et al., 2012** come up with a routing algorithm which designed with a predetermined job (transmission line monitoring system). The proposed algorithm, in addition to chain technique, it utilizes the Ant colony optimization method to create a reliable real-time monitoring algorithm. This algorithm is mainly divided into two stages. The first stage is routing establishment which includes three steps: preparation, building process, and local search mechanism. After finalizing the establishment process and specifying the optimum path, the second stage of the routing algorithm will start which involves data transmission. This algorithm has a great advantage that can effectively jump out of the local optimization and rapid access to superior solutions. Thus, this algorithm when compared with basic ant colony algorithms it will show is more appropriate for long-chain wireless sensor networks. On the other hand, it cannot fit with various applications except the transmission lines or the applications that requires long chains of sensor nodes so it cannot be considered a general algorithm for different WSNs applications. **Mahajan, et al., 2013** introduced an algorithm called IECBSN (Improved Energy Efficient Chain Based Sensor Network) that adopts new factor for the process of selecting the chain head, this factor called selection value *SV*. It combines two parameters in an equation to calculate the *SV* value, which are the remaining energy for each individual node and the distance between each sensor node and the base station. Eq. (1) is used to calculate *SV* value for each node. The node that has the maximum *SV* will be chosen to operate as a chain leader. Moreover, IECBSN algorithm consists of four stages: network construction, chains formation, leader selection, and data transmission.

$$SV_i = E_{r(i)} \frac{1}{adist\ (ni\ ,\ nBs)} \tag{1}$$

Where SVi represents the factor that define the relationship between the residual energy and the distance to the base station for each node in the chain and $E_{r(i)}$ represents the residual energy of the node number i , while *adist (ni, nBs)* stands for the distance between the node i and the base station.

Hong, and **Han, 2014** put forward a routing algorithm that can accomplish a maximum lifetime for the network at the same time with a maximum number of alive nodes. The proposed algorithm of **Hong,** and **Han, 2014** is called Cost-Efficient Routing Protocol (CERP) on Wireless Sensor Networks. CERP basic idea is to make the lifetime of each single node within the network same with other nodes. Therefore, the entire network will be dead almost at the same time then it will assure a reliable operation when the network alive because almost all the nodes are alive. **Kareem, et al., 2014** proposed a new routing algorithm called Two Stage Chain Routing Protocol for Wireless Sensor Networks (TSCP) which is based on chain technique. TSCP algorithm is mainly compatible with WSNs which have grid topology. It divides the network into multiple chains and forwards the data using multi-hop communication.

Ahmed, et al., 2008 introduced a clustering routing algorithm that employed a new technique (decision tree) to select the cluster head node. The decision tree is based on four factors (the distance between the node and the center of the cluster, residual energy of the node, mobility of the node, and Vulnerability index. Authors of Assisted LEACH (A-LEACH) introduced a modified routing algorithm that depends on LEACH as a bench mark **Kumar,** and **Pal, 2013**. Since LEACH represents the first hierarchical routing algorithm that used clustering technique, A-LEACH and other related algorithms are fall in cluster category of hierarchical routing algorithms for wireless sensor networks. A-LEACH uses a modified strategy to minimize the energy dissipated by separating the tasks of data routing and aggregating. It presented an idea of assisted nodes that can help the cluster head nodes for multi-hop routing. Another improvement has been done based on LEACH algorithm when **Balavalad, et al., 2014** introduced their algorithm which is called Multipath-LEACH. It is dividing the network into cells and each cell has a cluster head. The cluster head nodes communicate with each other to forward their data to the base station using multipath strategy.

Unlike other routing algorithms, which aim mainly to extend the network lifetime regardless other factors, such as mobility, traffic, and end to end connection. A routing algorithm based on clustering technique has been introduced in **Velmani,** and **Kaarthick, 2015** which is called Velocity Energy-efficient and Link-aware Cluster-Tree (VELCT) scheme for data collection in WSNs. VELCT aims to be an efficient solution for coverage distance, traffic, delay, tree intensity, mobility, and end-to-end connection problems. VELCT creates a Data collection tree (DCT) depending on the cluster head (CH) location. The node that is responsible for data collection will not involve in sensing operation in the particular round. The main job for the data collection node is to collect the data packets from the cluster head nodes and delivers them to the base station **Velmani,** and **Kaarthick, 2015**. The strategies that implemented in VELCT lead to reduce the traffic and end-to-end delay in cluster head in WSNs.

The last category of hierarchical routing algorithms is hybrid algorithm. Hybrid routing algorithm combine both cluster and chain techniques. A hybrid routing algorithm has been proposed such as CCM algorithm **Tang, et al., 2012**. It combines the advantage of chain technique which is low energy consumption at the same time utilize the fast data delivery advantage from the clustering mechanism. On the other hand, CCM algorithm has small drawback, which is the way of selecting the cluster head in the second stage. CCM uses the residual energy factor in order to decide upon which node is going to be the cluster head without considering the distance between the node and the base station. It is very normal that the node has maximum residual energy at the same time it is located very far from the base station which leads to high energy consumption during data transmission. Therefore, using only the residual energy to select the cluster head is neither efficient nor reliable. (REC+) **Taghikhaki, et al., 2013**. They proposed a Reliable and Energy-efficient Chain-cluster based routing protocol (REC+). REC+ aims to achieve the maximum reliability in a multi-hop communication by using the proper place for the Cluster Head (CH) and the best shape/size of the clusters without using any error controlling technique that can add extra overhead in terms of computation and communication. **Table 1** summarizes routing technique, performance metrics, and simulation tool used to evaluate each algorithm mentioned above.

3. E-CCM ALGORITHM

In this section, will present the proposed algorithm E-CCM (Enhanced Chain-Cluster Based Mixed Routing) which is a modified version of CCM algorithm that can improve the lifetime for the entire WSN by decreasing the energy consumption in each sensor node. E-CCM enhancement is in the second stage, specifically during the process of selecting the cluster head. As we mentioned before, CCM algorithm uses only the residual energy to decide upon which node is going to be the cluster head in the second stage without considering the distance between that node (cluster head) and the base station. Therefore, it is very normal to select a node with maximum residual energy but it is located very far from the base station which consequently consumes too much energy due to transmitting the aggregated data to the base station. In order to overcome this defect, E-CCM algorithm is presented. E-CCM algorithm utilizes another factor, which is the distance between the sensor node and the base station in addition to maximum residual energy to select the cluster head for the entire network. An equation is implemented, that combine both residual energy and distance from sensor nodes to the base station and then produce a factor called Si, node with maximum Si will be the cluster head in the second stage.

E-CCM algorithm works within two stages, initialization stage and transmission stage. Moreover, it is mainly applicable for WSNs that use grid topology and the location of each sensor node is known to the base station.

3.1 Initialization Stage

Since the topology of the network is based on grid topology. Therefore each sensor node has an x and y coordinates. The E-CCM algorithm will divide the network into sub-sets based on the (y) coordinate of each sensor node. The nodes that have the same (y) coordinate will be on the same group. Then, one of the nodes in each group will be selected periodically to act as a head for other nodes in its own group. The periodic way of selection means that in the first sensing round, the first node in each group will be selected as group head, in the second sensing round, the second sensor node in each group will be the group head and so on. Assume that there is N

number of nodes distributed in (n × n) fashion, *n* represents the number of groups in the network and the number of nodes in each group. So that, the selection of the head is based on the output of the Eq. (1) where *i* represents the number of current sensing round and n is the number of sensor nodes in each group.

$$H_{node\_id} = i \; mod \; n \tag{2}$$

A description for the operation of first stage of E-CCM algorithm is summarized in the flowchart in **Fig. 1**.

3.2 Transmission Stage

This stage includes two steps, horizontal chains formation and vertical chain formation.

3.2.1 Multiple Chains Formation:

Each group of sensor nodes in the network will construct a horizontal chain. Each sensor node transmits its data to the closest neighbor that leads to the chain head which is selected in the first stage. When a node receives data from its neighbor, it aggregates the received data packet with its own data packet and then sends the aggregated packet to the closest neighbor that leads to the chain head and so on until all data are collected in the chain head.

3.2.2 Single cluster formation:

When all the sensed data packets are collected in the chain head nodes, the chain head nodes will form a cluster contains all head nodes. After forming the cluster, one of the sensor nodes that belong to the cluster will be selected to function as a cluster head and a main head for the entire network. The cluster head will be responsible for aggregating the data received from the chain head nodes and send the aggregated packet to the base station. The selection of cluster head node is based on two factors which are the residual energy of the sensor node and the distance between the node and the base station. Utilize Eq. (1) from **Mahajan, et al., 2013** in order to decide upon which node is going to be the cluster head in each sensing round.

The flowchart of the second stage is shown in **Fig. 2**.

3.3. Radio Model for Communication

The radio model utilized in the proposed algorithm is first order radio model which is used in wide variety research related to sensor networks such as **Lindsey**, and **Raghavendra**, **2002**, **Mahajan, et al., 2013** and **Kareem, et al., 2014**. First order radio model assumptions are used in to determine the energy consumption due to data transmission and receiving. The transmission cost E_{TX} and receiving cost E_{RX} are calculated by the Eq. (3) and (4), respectively.

Energy consumption due to data transmission:

$$E_{TX}(kd) = E_{elec} \times k + E_{amp} \times k \times d^2 \tag{3}$$

Energy consumption due to data receiving:

$$E_{RX}(k) = E_{elec} \times k \tag{4}$$

Where *k* represents the size of data packet, *d* represents the distance between the sender and receiver. While E_{elec} stands for the energy the energy required to run the transmitter or the receiver and E_{amp} is the energy consumed in order to run the amplifier. **Fig. 3** shows the first order radio model used in the proposed system **Kareem, et al., 2014**.

4. SIMULATION

MATLAB software is used to evaluate the performance of the E-CCM algorithm and compare its performance with the original CCM algorithm depends on three performance metrics: network lifetime, energy consumption, and first node and last node died (FND and LND).

4.1 Network Model

In simulation, assumed that the sensing area is a square matrix and sensor nodes are distributed evenly in a 2-dimensional array. 100 sensor nodes are distributed in (10×10) fashion 10 meters between each node and its closest neighbor.

- All sensor nodes are homogenous and have the same initial energy.
- The base station is located outside the sensing field at (50, 150) position, it is fixed and it is not energy constrained.
- All nodes have the ability to communicate directly with the base station.
- The energy consumed during the transmission of data packet depends on the size of the data packet and the distance between the node and the base station.
- The energy consumed due to data aggregation is 5nJ/bit/message **Lindsey**, and **Raghavendra**, **2002**.

ZigBee network is designed for reliable wirelessly networked monitoring and control networks **Lee, et al., 2007**. Further, ZigBee offers a unique advantages for wireless application such as low cost, and low power consumption. Therefore, It is recommended to use ZigBee network with E-CCM algorithm. Since it is assumed that all sensor nodes have the ability to communicate with the base station, all sensor nodes must be a router type so that each node can communicate with all other nodes and can communicate to the base station directly. The coordinator node is interfaced to the base station. **Fig. 4** shows the sensor nodes deployment in the sensor field and the location of the base station with respect to the sensor network.

4.2 Simulation Parameters:

Some parameters used to simulate the E-CCM algorithm and compare its behavior with CCM algorithm. It is worth mentioning that the sensing field is assumed to be a square field with 100m×100m area. The sensor nodes are assumed to be stationary and their locations are known to the base station. The number of sensor nodes and the distance between each node and its closest neighbor should be specified before starting the simulation, for example 100-stationar sensor nodes are placed in the sensing area with a fixed distance 10 meter between each node and its closest neighbor**. Table 2** shows more details about the simulation parameters used in the simulation.

5. RESULTS AND ANALYSIS:

In this section, will show and analyze the simulation results in order to highlight the advantages of E-CCM algorithm in comparison with CCM algorithm using three performance metrics: Network life time, Energy consumption, and First node and Last node died (FND and LND).

5.1 Network Lifetime:

The period of time from the deployment of sensor nodes till the network considered as non-functional is defined as network lifetime **Kannan**, and **Paramasivan**, **2014.** The moment that the

network considered as non-functional is user defined. In other words, it is based on the application of WSN. Therefore, it can be the moment when first node dies, the moment when specific percentage of sensor nodes die or the moment when all sensor nodes in the network dies. In simulation, will consider the lifetime of the network ends when all sensor nodes in the network die. **Fig. 5** shows the performance comparison of E-CCM algorithm and CCM algorithm based on the network lifetime.
Eq. (5) is used to determine the improvement of E-CCM algorithm over CCM algorithm. This equation is generally used to calculate the percentage of increase for different applications.

$$POI = \frac{Second\ Value - First\ value}{First\ value} \times 100\ \% \qquad (5)$$

Where POI represents the percentage of increase and in this performance metric it represents the percentage of improvement in network life time. First value represents the last sensing round when the sensor network was alive using CCM algorithm. Second value represents the last sensing round when the sensor network was alive using E-CCM algorithm. It is clear from **Fig. 4** and **Table 2** that E-CCM algorithm outperforms CCM algorithm in term of network lifetime. Implementing Eq. (5) show that E-CCM algorithm has an improvement about 14% over CCM algorithm. The reason is that when include the distance factor along with the remaining energy in each node to select the cluster head, it gives an advantage which consequently extends the lifetime for the entire network.

5.2 Energy Consumption:

Three factors are considered to be responsible for consuming the energy during data routing which are: data send, data receive and data aggregate. Using equation 1 and 2 to calculate the energy cost of data send and receive, considering the same assumption used in **Lindsey**, and **Raghavendra**, **2002** to calculate energy cost for data aggregation. **Fig. 6** shows the amount of energy consumption in each algorithm versus sensing rounds.
From **Fig. 5**, it can be clearly seen that the amount of energy consumption during the network lifetime of E-CCM algorithm is less in comparison with CCM algorithm. In other words, E-CCM algorithm outperforms CCM algorithm in term of energy conservation. Once again, adding the distance factor to select the cluster head resulted in conserving more energy during the network lifetime.

5.3 FND and LND (First Node and Last Node Died):

In order to ensure the robustness and reliability of the routing algorithm, have to examine the performance of the network using different performance metrics. In this section, will compare the performance of E-CCM algorithm and CCM algorithms when first node in the network dies FND and when the last node in the network dies LND **Chen**, and **Zhao, 2005**.
From **Table 3** and **Fig. 7**, can see that E-CCM algorithm outperforms CCM algorithm in terms of FND and LND. Moreover, the results of utilizing Eq. (5) show that E-CCM algorithm achieve an improvement over CCM algorithm in about 16% and 14% when first node died and last node died respectively. Therefore, E-CCM algorithm shows a remarkable performance in compare with CCM algorithm in terms of FND and LND.

6. CONCLUSION

In this paper, proposed an energy efficient routing algorithm that minimize the energy consumption of WSN and consequently extend the network lifetime. The proposed algorithm E-CCM divides the sensor nodes into multiple groups and the form a chain from each group. After chain formation, one node from each chain will function as chain head periodically. All sensor nodes in each chain will send their data to the head of their chain using multi-hop communication. After that, all chain head nodes will form a cluster and select a cluster head based on the remaining energy of each node and the distance between the node and base station. The cluster head node is responsible for receiving the data from cluster members, aggregate the received data with its own data and send the aggregated data packet to the base station. MATLAB program is used as simulation tool in order to evaluate the performance of E-CCM algorithm and compare it with the previous work. Moreover, the evaluation process is conducted based on three performance metrics which are network lifetime, energy consumption and (FND and LND). Utilizing simulation results in Eq. (5) show that E-CCM algorithm could achieve an improvement in the network lifetime in about 14% in comparison with CCM algorithm. Furthermore, E-CCM algorithm shows a significant improvement in term of FND (first node died) in about 16% in comparison with CCM algorithm. Therefore, combining the distance factor with the remaining energy during the selection of cluster head leaded to a remarkable impact on the entire networks' lifetime and the energy conservation in wireless sensor network.

REFRENCES

- Oda, H. Hisamatsu, H and Noborio, H., 2012, *Proposal and Evaluation of an Information Dissemination Method Based on Flooding for Energy Efficiency in Wireless Sensor Networks*, Journal of Advances in Computer Networks, Vol. 2.

- Tang, F., You, I., Guo, S., Guo, M., and Ma, Y. 2012, *A chain-cluster based routing algorithm for wireless sensor networks*, journal of intelligent manufacturing, Vol. 23, No. 4, PP.1305-1313.

- Heinzelman, W. R., Chandrakasan, A., and Balakrishnan, H., 2000, *Energy-efficient communication protocol for wireless microsensor networks*, In System sciences, Proceedings of the 33rd annual Hawaii international conference on, IEEE , Vol. 2, pp. 10.

- Lindsey, S., and Raghavendra, C. S., 2002, *PEGASIS: Power-efficient gathering in sensor information systems*, In Aerospace conference proceedings, IEEE, Vol. 3, PP. 1125-1130.

- Kareem, H., Hashim, S., Sali, A., and Subramaniam, S., 2014, *A Survey of State of the Art: HIierarchical Routing Algorithms for Wireless Sensor Networks*, Journal of Theoretical & Applied Information Technology, Vol. 62, No. 3, PP. 769-781.

- Yu, Y., and Song, Y., 2010, *An Energy-efficient Chain-based Routing Protocol in Wireless Sensor Network*, In Computer Application and System Modeling (ICCASM), International Conference on, IEEE, Vol. 11, PP. 486-489.

- Ahmed, G., Khan, N. M., Khalid, Z., and Ramer, R., 2008, *Cluster head selection using decision trees for wireless sensor networks*, In Intelligent Sensors, Sensor Networks and Information Processing, ISSNIP International Conference on, IEEE, Vol., PP. 173-178.

- Mahajan, S., Malhotra, J., and Sharma, S., 2013, Improved enhanced chain based energy efficient wireless sensor network, Wireless Sensor Network, Vol. 5 No. 4, PP. 84-89.

- Hong, S., and Han, K. H., 2014, *Cost-efficient routing protocol (CERP) on wireless sensor networks,* Wireless Personal Communications, Vol. 79, No. 4, PP. 2517-2530.

- Kareem, H., Hashim, S., Subramaniam, and Sali, A., 2014, *Energy Efficient Two Stage Chain Routing Protocol (TSCP) for WirelessSensor Networks,* Journal of Theoretical and Applied Information Technology, Vol. 59, No. 2, PP. 442-450.

- Gao, J., Wei, L., Zhu, Y., and Li, L., 2012, *Routing Optimization Based on Ant Colony Algorithm for Wireless Sensor Networks with Long-Chain Structure*, In Internet of Things, Springer Berlin Heidelberg, PP.91-97.

- Kumar, S. V., and Pal, A., 2013, *Assisted-leach (a-leach) Energy Efficient Routing Protocol for Wireless Sensor Networks,* International Journal of Computer and Communication Engineering, Vol. 2, No. 4, PP. 420-424.

- Balavalad, K. B., Katageri, A. C., B. M. Biradar, B. M., Chavan, D., and Angadi, B. M., 2014, *Multipath-LEACH an Energy Efficient Routing Algorithm for Wireless Sensor Network*, Journal of Advances in Computer Networks, Vol. 2, No. 3, PP. 229-232.

- Velmani, R., and Kaarthick, B., 2015, *An Efficient Cluster-Tree Based Data Collection Scheme for Large Mobile Wireless Sensor Networks*. Sensors Journal, IEEE, Vol. 15, No. 4, PP. 2377-2390.

- Taghikhaki, Z., Meratnia, N., and Havinga, P. J., 2013, *A Reliable and Energy-efficient Chain-cluster Based Routing Protocol for Wireless Sensor Networks*, In Intelligent Sensors, Sensor Networks and Information Processing, IEEE Eighth International Conference on, PP. 248-253.

- Lee, J. S., Su, Y. W., and Shen, C. C., 2007, *A comparative study of wireless protocols: Bluetooth, UWB, ZigBee, and Wi-Fi.* In Industrial Electronics Society, IECON, IEEE 33rd Annual Conference on, PP. 46-51.

- Kannan, K. N., and Paramasivan, B., 2014, *Enhancing Energy Efficiency in Wireless Sensor Networks Using Optimal Gradient Routing Protocol*, International Journal of Computer and Communication Engineering, Vol. 3, No. 6, PP. 408-412.

- Chen, Y., and Zhao, Q., 2005, *On the lifetime of wireless sensor networks,* Communications Letters, IEEE, Vol. 9, No. 11, PP. 976-978.

NOMENCLATURE

Symbol	Description	Unit
N	number of sensor nodes of the entire network.	Unit less
N	number of the sensor nodes groups and number of sensor nodes in each group. (assumed equal).	Unit less
I	number of the current sensing round.	Unit less
S_i	the factor that define the relationship between the residual energy and the distance to the base station for each sensor node.	Joule/meter
$E_{r(i)}$	the residual energy of the node number i.	Joule
adist (ni, nBs)	the distance between the node i and the base station.	Meter
E_{TX} ***(kd)***	energy consumption due to transmission of data packets.	Joule
E_{RX} ***(k)***	energy consumption due to receiving data packets.	Joule
K	size of data packet.	Bit
D	the distance between the sender and the receiver.	Meter
E_{elec}	the energy required to run the transmitter or the receiver.	nJ/bit
E_{amp}	the energy consumed in order to run the amplifier.	PJ/bit/m^2
POI	percentage of increase	Unit less
FND	first node died in the network	Unit less
LND	last node died in the network	Unit less

Table 1. Simulation tool, performance metric(s) and routing technique used in each algorithm.

Algorithm name	**Simulation tool**	**Performance metric(s)**	**Routing technique**
Leach	MATLAB	Network lifetime	Cluster
Pegasis	C language	Network lifetime	Chain
EECB	Not mentioned	Network lifetime	Chain
Gao, et al.	MATLAB	Find an optimal path	Chain
CERP	Not mentioned	Energy deviation for each mode in the sensor network	Chain
TSCP	MATLAB	Load Balancing, Network Lifetime and stability interval, energy consumption	Chain
Ahmed, et al.	MATLAB	Network lifetime	Cluster
A-LEACH	C language	Network lifetime and energy consumption	Cluster
Multipath-LEACH	MATLAB	Network lifetime and energy consumption	Cluster
VELCT	NS-2	Energy consumption, throughput, end-to-end delay, and network lifetime	Cluster
CCM	SWANS	Energy consumption, transmission delay, and Energy × Delay	Hybrid
REC+	Not mentioned	Network lifetime, Energy × Delay, Energy consumption, Delay, End-to-End reliability	Hybrid

Table 2. Simulation Parameters.

Parameter	*Value*
Area of the sensing field	(100×100) m^2
Base station position	(50,150)
Number of sensor nodes	100
Behavior of the nodes	Stationary
Network type	Assumed to be ZigBee
Initial energy of each sensor node	0.5 Joule
E_{elec}	50 nJ/bit
E_{amp}	100 PJ/bit/m^2
Size of data packet	2000 bit

Table 3. FND and LND.

Metric	**E-CCM** (Sensing Rounds)	**CCM** (Sensing Rounds)
FND	1652	1420
LND	2142	1877

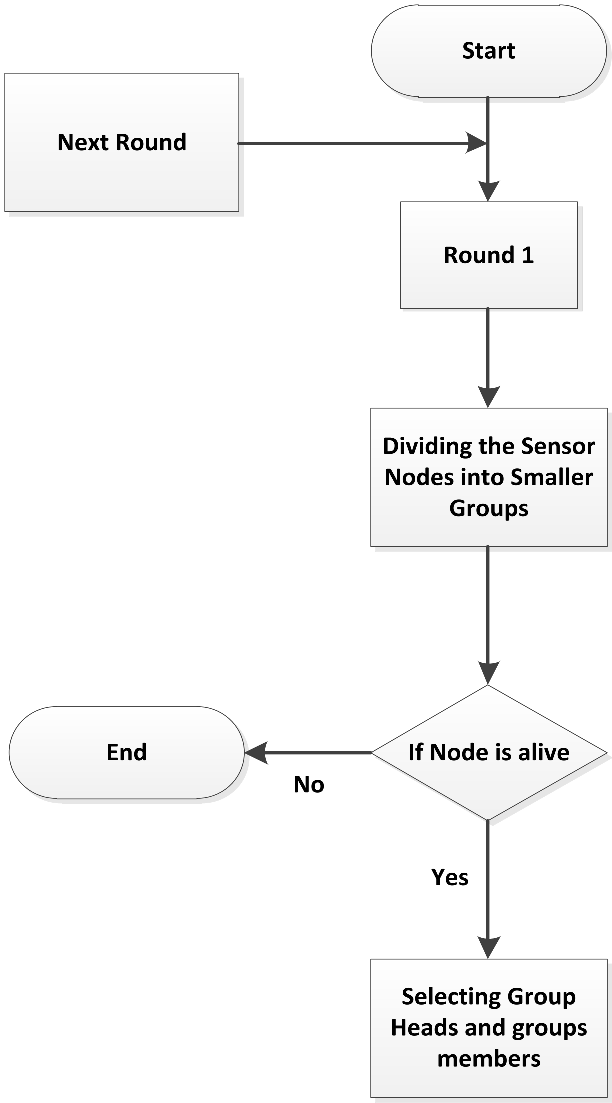

Figure 1. Flowchart of the initializing stage of E-CCM algorithm.

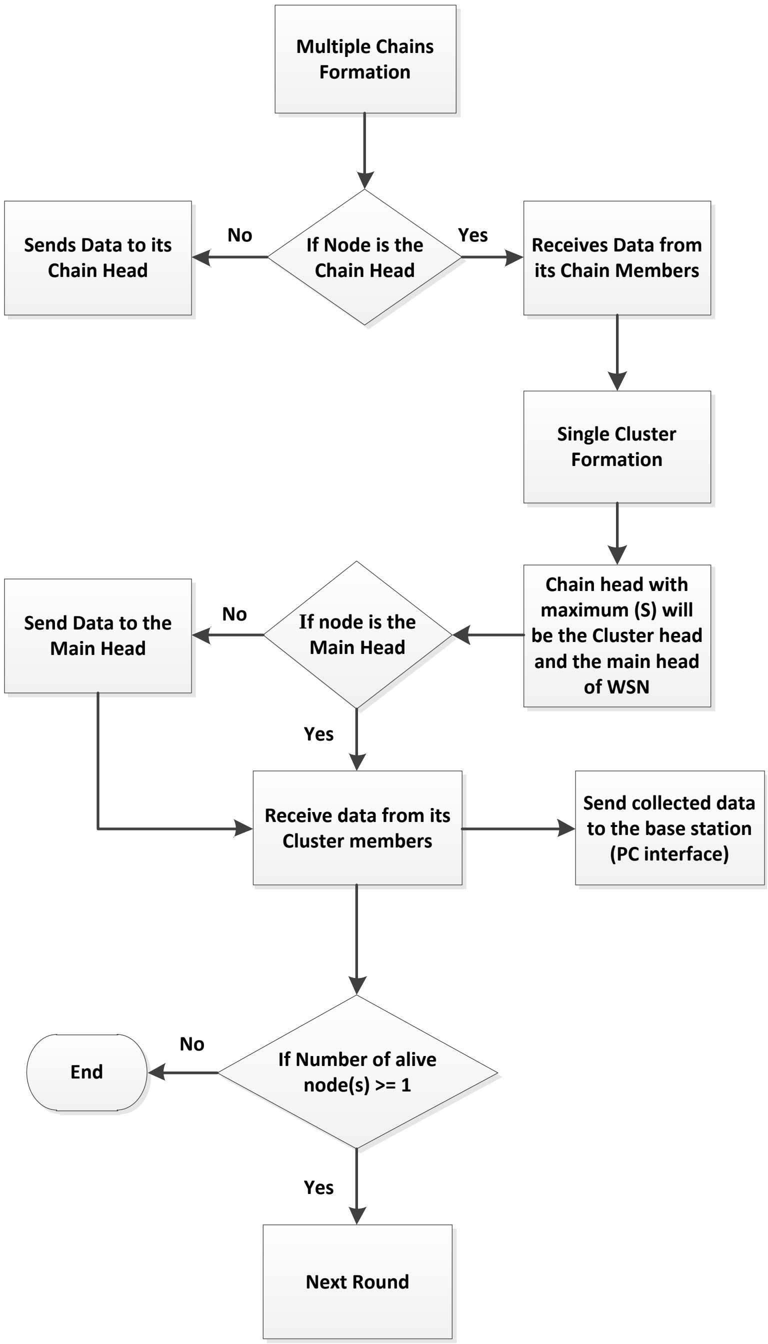

Figure 2. Flowchart of the Transmission stage of E-CCM algorithm.

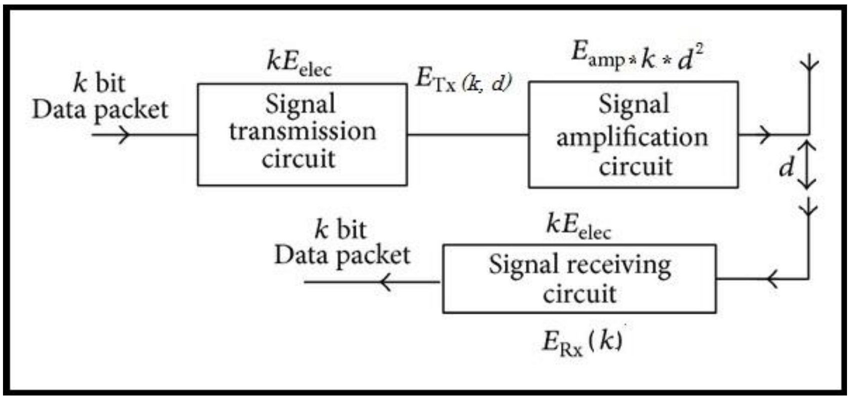

Figure 3. Radio model used in the system.

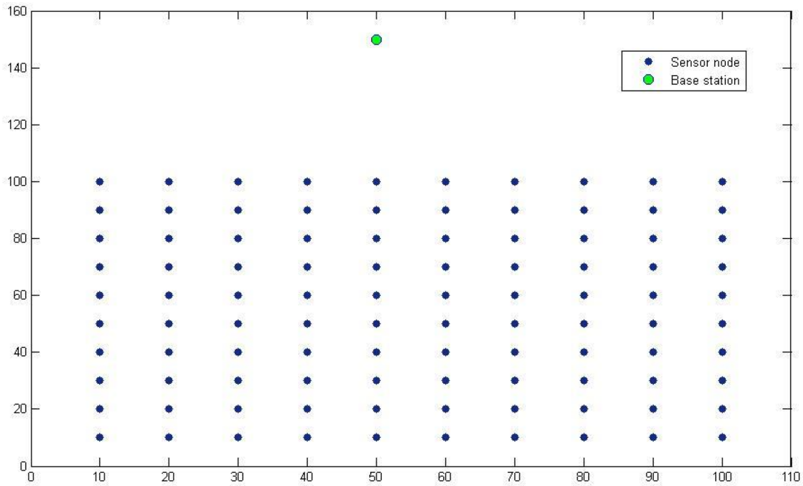

Figure 4. Network architecture.

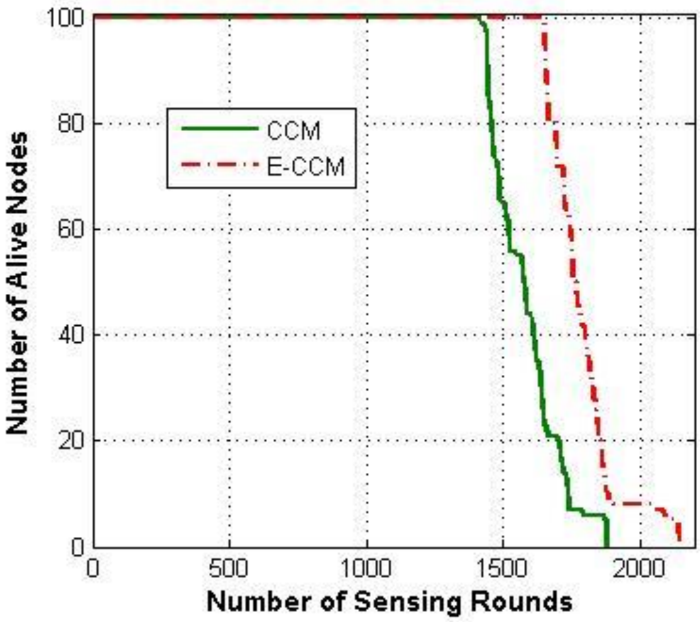

Figure 5. Network Lifetime.

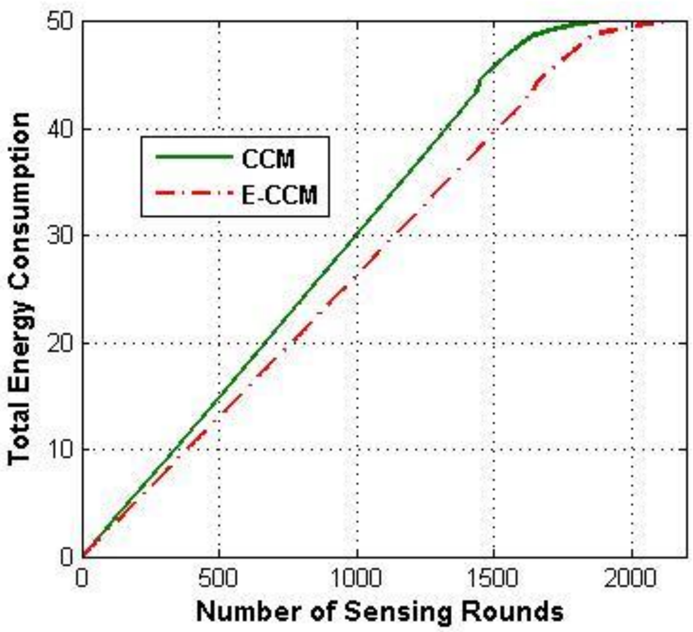

Figure 6. Energy Consumption.

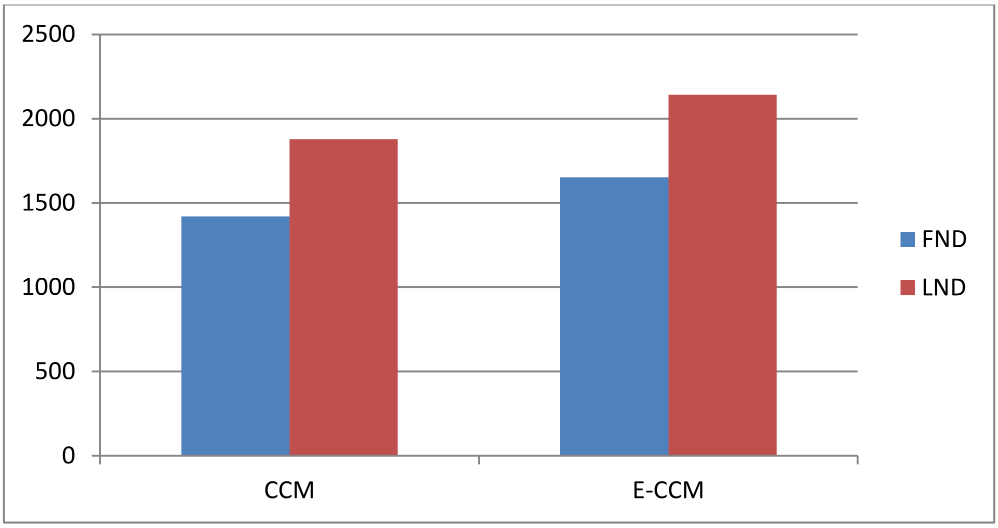

Figure 7. FND and LND.

A Mathematical Model of a Thermally Activated Roof (TAR) Cooling System Using a Simplified RC-Thermal Model with Time Dependent Supply Water Temperature.

Dr. Khalid Ahmed Joudi
Professor
College of Engineering-University of Baghdad, Baghdad
email: khalid47joudi@yahoo.com

Kamal Mohammed Ali
PhD student
College of Engineering-University of Baghdad, Baghdad
email: al_ssafar2005@yahoo.com

ABSTRACT

This paper presents a computer simulation model of a thermally activated roof (TAR) to cool a room using cool water from a wet cooling tower. Modeling was achieved using a simplified 1-D resistance-capacitance thermal network (RC model) for an infinite slab. Heat transfer from the cooling pipe network was treated as 2-D heat flow. Only a limited number of nodes were required to obtain reliable results. The use of 6^{th} order RC-thermal model produced a set of ordinary differential equations that were solved using MATLAB - R2012a. The computer program was written to cover all possible initial conditions, material properties, TAR system geometry and hourly solar radiation. The cool water supply was considered time dependent with the variation of the ambient wet bulb temperature. Results from RC-thermal modeling were compared with experimental measurements for a second story room measuring 5.5 m x 4 m x 3 m at Amarah city/ Iraq (31.865 ˚N, 47.128 ˚E) for 21 July, 2013. The roof was constructed of 200 mm concrete slab, 150 mm turf and 50 mm insulation. Galvanized 13 mm steel pipe coils were buried in the roof slab with a pipe occupation ratio of 0.12. The walls were constructed of 240 mm common brick with 10mm cement plaster on the inside and outside surfaces and 20 mm Styrofoam insulation on the inside surface and covered with PVC panel. Thermistors were used to measure the indoor and outdoor temperatures, TAR system water inlet and outlet temperatures and temperature distribution inside the concrete slab. The effect of pipe spacing and water mass flow rate were evaluated. Agreement was good between the experimental and RC-thermal model. Concrete core temperature reaches the supply water temperature faster for lower pipe spacing. Heat extracted from the space increased with water mass flow rate to an optimum of 0.0088 kg/s.m².

Keywords: concrete core conditioning, thermally activated roof, RC- thermal model, thermo-active building simulation.

نموذج رياضي لمنظومة تبريد باستخدام سقف محفز حراريا باستخدام موديل RC الحراري المبسط باستخدام ماء متغير درجة الحرارة مع الوقت.

د. خالد احمد جودي
استاذ
كلية الهندسة - جامعة بغداد
قسم الهندسة الميكانيكية

كمال محمد علي
طالب دكتوراه
كلية الهندسة - جامعة بغداد
قسم الهندسة الميكانيكية

الخلاصـــــة

يستعرض هذا البحث نموذج محاكاة باستخدام الحاسوب للسقوف المنشطة حراريا (TAR) باستخدام ماء بارد من برج تبريد من النوع الرطب. تمت النمذجة باستخدام ما يسمى دائرة المقاومة- المتسعة الحرارية (نموذج RC) لسطح متناهي الابعاد. أعتبر انتقال الحرارة من شبكة الانابيب, ثنائي البعد (2-D) حيث نحتاج الى عدد قليل من العقد(nodes) للحصول على نتائج واقعية. أن استخدام النمذجة الحرارية (RC) من الرتبة السادسة سينتج عنه مجموعة من المعادلات التفاضلية الاعتيادية التي تم حلها باستخدام برنامج ماتلاب (Matlab R2012a). تمت صياغة البرنامج بحيث يغطي كل الاحتمالات الممكنة من ظروف ابتدائية و نوع مواد البناء و ابعاد منظومة TAR و التغير الزمني في شدة الاشعاع الشمسي. أعتبر الماء البارد المجهز متغير درجة الحرارة بسبب التغير الزمني لدرجة الحرارة الرطبة للهواء الخارجي. قورنت النتائج المتحصلة من النمذجة الحرارية(RC)مع النتائج العملية المستخلصة من غرفة تقع في الطابق الثاني ذات ابعاد 5.5 x 4 x 3 م في مدينة العمارة جنوب العراق (31.865 ˚N, 47.128 ˚E). يتركب السقف من 200 ملم خرسانة و 50 ملم عازل حراري و 150 ملم تراب. دفنت اربع شبكات انابيب من الحديد المغلون بقطر 13 ملم داخل الصبة الخرسانية للسقف مع نسبة اشغال انابيب بلغت 0.12. تتركب الجدران من 240 ملم طابوق عادي مع 10 ملم سمنت على جانبي الجدارين الداخلي و الخارجي و 20 ملم عازل الستايروفوم من الداخل الذي تم تغليفه بصفائح البلاستك الملونة. استخدمت متحسسات لقياس درجة حرارة الهواء الداخلية و الخارجية و درجة حرارة الماء الداخل و الخارج من منظومة TAR و التوزيع الحراري داخل الخرسانة. تمت دراسة تأثير التباعد بين الانابيب و الموقع العمودي لشبكة الانابيب داخل الخرسانة و تأثير معدل جريان الماء على اداء المنظومة. وجد ان هناك تطابق جيد بين النتائج العملية و تلك المتحصلة من نموذج RC الحراري وقد اعطى استخدام هذا النموذج نتائج قريبة من القياسات العملية. ان اقتراب درجة حرارة الخرسانة من درجة حرارة الماء المجهز يكون اسرع عند تباعد انابيب بمسافات اصغر. ازدادت الحرارة المسحوبة من الغرفة مع زيادة معدل جريان الماء الى 0.0088 كغم/ثا.م^2 و بعدها كان هناك تغير طفيف.

الكلمات الرئيسية: تكييف كتلة الكونكريت, سقف مثار حراريا, نموذج حراري, محاكاة البنايات المحفزة حراريا.

1. INTRODUCTION

Concrete core conditioning (CCC) is a system of thermal conditioning of buildings which uses water pipes embedded in the center of the floor/ceiling construction for heating and cooling, **Rietrkerk, 2010**. Water provided to CCC systems is provided by refrigeration, boiler, ground coupled source or any other low or high grade energy source at a temperature within a preset control limit. Recently, it has been used as an alternative for conventional installations and emerged as an energy efficient and cost effective system that realizes a good thermal indoor environment, **Koschnez and Lehmann, 2000**. These systems are mainly used in multistory office buildings with a low heating load in winter (10 to 30 W/m^2) and a moderate cooling load in summer (30 to 60 W/m^2), **Olesen, 2002**. Conductive, convective and radiative heat transfer all play an important role in describing the thermal behavior of CCC in buildings.

A TAR system is one of the CCC systems activated with water through pipes embedded in the concrete structure. Numerical simulation models can provide solutions to complex dynamic systems of buildings and technical installations, **Karlson, 2006**. Very often, a numerical solution is adopted to calculate 3D or 2D models for the temperature distribution in the concrete slab of a CCC building. Heat transfer processes are time dependent and change with the use of the building, the outdoor climate and the supply of cold/hot water to the building integrated cooling/heating system. **Sourbroun, 2012** used a finite difference method to model a full CCC system. **Antonopoulos and Tzivanidis, 1997** compared a 3-D and 2-D FD-method with experimental results. **Russell, and Surendran, 2001** used an FD-model to analyze the cooling capacity and perform some parametric analysis. **Olesen et al., 2006** presented an FD-model which is incorporated in the European standard EN15377 on water based embedded heating and cooling systems. A commonly used method to describe transient heat transfer in a multi-layer material is the thermal Resistance-Capacitance or RC-model. It is a simplified model where thermal resistances and capacities are lumped in a small number of nodal points **Weber, and Johannesson, 2005**. **Pedersen et al., 2005** used a 'space mapping' technique to optimize the performance of a computationally inexpensive RC network model. A detailed Finite Control Volume (FCV) model was used to enhance the accuracy of the simplified RC model. Furthermore, nothing was found regarding circulation of cooled water produced by a wet cooling tower, or hot water produced by an evacuated glass tubes solar collectors through embedded pipes in concrete slabs, neither experimentally (prototype or full scale) nor by using simulation packages, for residential comfort.

2. SYSTEM DESCRIPTION

2.1 Room Description

The room that was constructed to evaluate the mathematical model was located in the second story of a residence located in Amarah city/ south of Iraq (31.865 ˚N, 47.128 ˚E). It measures 5.5 m x 4 m x 3 m as shown in **Fig. 1**. The roof was constructed of 200 mm heavyweight concrete, 50 mm insulation and 150 mm turf which is a conventional roof construction in the south of Iraq. Walls were constructed of 240 mm common brick and finished with 10 mm cement plaster on both sides with 20 mm Styrofoam insulation on the inside and covered with a PVC panel as an architectural wall siding material. The external steel door included a double glazed aperture measuring 1 m x 1m with a 10 mm air space. Infiltration through door cracks is minimized by air tight gaskets. Opaque venetian blinds were used as an external shading device. A 400 mm overhang shaded the eastern wall and external door. The ground floor below the room was conditioned.

2.2 TAR system description

The TAR system was constructed of 13 mm galvanized steel pipes embedded in the 200 mm concrete slab with 170 mm pipe spacing. **Fig. 2** is a section through the room showing the cooling tower and temperature sensor locations. Pipe coils were located 80 mm above the bottom side of the concrete slab. Therefore, the pipe deepness ratio is 0.4. The pipe deepness ratio can be defined as the ratio between the pipe level height to the concrete thickness. The TAR system included four pipe coils with the option of either parallel or series connection. **Fig. 3** shows the piping system and the external connections. Each coil pipe pass was 5.5 m long. Anti-corrosion paints were used on the outside of these pipes. Water pipe loops were attached to the steel reinforcement bars firmly to prevent them from floating during concrete pouring. Lime stone was added to the concrete mix to prevent steel corrosion, **Verlmon, 2008**. The percentage of total surface area of the pipes to the effective area of the roof is defined as the pipe occupation ratio index which was 12 % for this roof. A wet cooling tower of 2 kW capacity, 0.206 l/sec and L/G = 0.623 was designed and constructed at 22 °C design wet bulb temperature and 4 °C approach to provide cold water to the TAR system. Cold water to the TAR system made the concrete slab a heat sink panel. The system water was treated with Potassium Dichromate tablets to prevent pipe corrosion and phenol to prevent algae and other green living forms.

2.3. Instrumentation and Measurements

Temperature measurements were made using 14 temperature calibrated thermistors type LM35. This type does not require any calibration or trimming to provide typical accuracies of ±0.25˚C at room temperature. Eight of them were distributed across the roof span between pipes to measure the temperature distribution across the concrete. Another four, were used to measure the indoor and outdoor dry and wet bulb temperatures. Two sensors were used to measure the inlet and outlet water temperatures across TAR (cooling tower) system. These sensors were connected to a data acquisition system manufactured by Lab-Jack company of Lakewood, Colorado, USA, model U3 LV. Data were saved in spread sheet format. A rotameter 2-26 l/min with accuracy of $\pm 3.14\ \%$ manufactured by SKC, was installed to measure the water flow rate in the system. System power consumption was measured by an (A-V-O) digital clamp meter supplied by Fluke 323 company with current and voltage range of 0-400 A with an accuracy of 1.5 ± 5 % and a voltage range of 0-750 V with accuracy an of 2 ± 5 %.

3. COOLING LOAD ESTIMATION

Olesen, 2002 suggested that thermally activated systems are suitable for buildings with moderate cooling loads of approximately 30 W/m² to 60 W/m². Several modifications were applied to decrease the cooling load of this test room. The heat gain was minimized using thermal insulation, air tight sealing, double glazing, external shading and an overhang.

Internal heat sources were limited to a 45 W lighting and a ceiling fan of 60 W powers. The Space cooling load was maximum on 21 July at a value of 51.6 W/m² which is a moderate value and suitable for TAR system installation. **Fig. 4** shows the cooling load of the space using the radiant time series (RTS) method for 21 July **ASHRAE, 2009**. The exterior glazed door has a peak cooling load in the morning because it faces east while walls and roof have a peak load at night due to the thermal mass storage of these structures. The total load is of a maximum near mid-night.

4. RC-THERMAL MODELLING

Hourly temperature distribution through the roof layers was determined using a simplified RC thermal network. Input temperatures to the model were from experimental measurements of the test room for 21 July as shown in **Fig. 5**. Other input data include the solar radiation intensity and supply water temperature. Input data included the material thermal properties and water flow rate which are independent of time. Six nodes were used across the roof thickness which rendered a 6th order model. The internal nodal points have thermal capacities. Whereas, the surface nodal point thermal capacities are set to zero. Modeling was carried out with the experimental data of 21 July, 2013 as input.

A general sinusoidal equation for nodal temperatures introduced by Joseph, 2012 is used in the present model as;

$$T_{ml} = T_m + A \sin (2\pi/24 \, (t \pm \emptyset)) \quad (°C) \qquad (1)$$

$$T_m = (T_{max} + T_{min}) / 2, \quad (°C) \qquad (2)$$

$$A = (T_{max} - T_m), \quad (°C) \qquad (3)$$

Where $\emptyset$ is the phase shift (hr), and $\pm$ signs are for descending and ascending directions.

4.1 Temperature Modeling

The sol-air temperature, outdoor, indoor and supply water temperature were modeled for computer program implementation.

The sol-air temperature is a fictitious temperature that defines a value for the outdoor air temperature which would, in the absence of all radiation exchanges, give the same rate of heat flow into the outer surface as the actual combination of temperature difference and radiation exchanges, **Kreider et al., 2002**. It takes into account, the daily temperature range which affects the heat storage, the color of the outside surface which affects solar heat absorption rate, the latitude and month, **Duffie, 2006**. In equation form;

$$T_e = T_{do} + \alpha \frac{I_t}{h_o} - \frac{\varepsilon \Delta R}{h_o} \qquad (4)$$

The solar irradiance is given as;

$$I_t = 0, \qquad (1 \le t \le 6) \tag{5}$$

$$I_t = 980 \sin(2\,\pi/24\,(t-6)), \quad (6 \le t \le 18) \tag{6}$$

$$I_t = 0, \qquad (18 \le t \le 24) \tag{7}$$

Where 980 W/m² was the maximum total solar radiation calculated on a horizontal surface for 21 July at Amarah city **ASHRAE, 2009** assumes the following equation to evaluate the sol-air temperature for horizontal surfaces,

$$T_e = T_{do} + 0.026\, I_t - 4 \qquad (°C) \tag{8}$$

From experimental data of 21 July, 2013 and Eq.(1), the ambient dry bulb temperature T_{do}, ambient wet bulb temperature T_{wo}, indoor dry bulb temperature T_{di} and cooling water supply temperature T_s with an approach of 4 ˚C, can be written as;

$$T_{do} = 38 + 8 \sin(2\pi/24(t-8)), \quad (1 \le t \le 24) \qquad (°C) \tag{9}$$

$$T_{wo} = 21 + 4 \sin(2\pi/24(t-8)), \qquad (°C) \tag{10}$$

$$T_s = 25 + 4 \sin(2\pi/24(t-8)) \qquad (°C) \tag{11}$$

$$T_{di} = 30.3 + \sin(2\pi/24(t+6)) \qquad (°C) \tag{12}$$

Fig. 6 compares the experimental measurements of the outdoor temperature and Eq. (9).

So, sol-air temperature is modeled using Eqs. (5), (6), (7), (8) and (9) as;

$$T_e = 38 + 8\, sin(2\pi/24(t-8)) + 0.026\, I_t - 4, \qquad (°C) \tag{13}$$

4.2 TAR system modeling

The roof slab was regarded as an infinite slab with four internal nodal points and two for the upper and lower surfaces. The governing equations for typical exterior and interior nodes shown in **Fig. 7** are:

Exterior node 1; $$0 = \frac{1}{R_o}(T_e - T_1) + \frac{1}{R_1}(T_2 - T_1) \tag{14}$$

Internal node 3; $$C_2 \frac{dT_3}{dt} = \frac{1}{R_2}(T_2 - T_3) + \frac{1}{R_3}(T_4 - T_3) \tag{15}$$

For node 4; $$C_3 \frac{dT_4}{dt} = \frac{1}{R_3}(T_3 - T_4) + \frac{1}{R_5}(T_6 - T_4) + \frac{1}{R_4}(T_5 - T_4) \tag{16}$$

For the pipe node 5; $C_5 \frac{dT_5}{dt} = \frac{1}{R_4}(T_4 - T_5)$ (17)

Where, C_5 is the thermal capacitance of the pipe material.

Replacing $\frac{dT}{dt}$ by $\frac{\Delta T}{\Delta t} = \frac{(T^{new} - T^{old})}{\Delta t}$ and solving the resulting equation system, the following matrix equation evolves;

[A][T]= [B] (18)

Where [A] is the thermal coefficient matrix, [T] is the new temperatures matrix and [B] is the old temperatures matrix.
The resistance R_5 is 3-dimensional but may be given as a 1-dimensional relation as, **sourbroun, 2012**;

$$R_5 = \frac{S \ln\left(S/_{\pi d}\right)}{2\pi k_p} \quad (19)$$

The main concept in TAR geometry is shown in **Fig. 8**.

Where : $l_4/(l_3 * s) > 0.3$, $d/s < 0.2$.
The temperature at node 5 is assumed the same as the pipe temperature and can be related to the supply water temperature by;

$$\dot{q}_{wr} = \dot{m}\ c_p (T_r - T_s), \qquad (W) \quad (20)$$

And, $$\dot{q}_{4-5} = \frac{(T_4 - T_5)}{R_5} \qquad (W) \quad (21)$$

By assuming a linear temperature rise along the pipe length, the pipe temperature can be approximated as;

$$T_5 \cong \frac{T_s + T_r}{2}, \qquad (^\circ C) \quad (22)$$

Solving Eqs. (20), (21) and (22) gives;

$$T_5^{old} = T_s - \frac{1}{2}\left(\frac{\frac{1}{R_5}(T_5^{old} - T_4^{old})}{\dot{m}\ c_p}\right) \qquad (^\circ C) \quad (23)$$

Substituting Eq. (11) in Eq. (23) gives;

$$T_5^{old} = 25 + 4\sin\left(\frac{2\pi}{24}(t-8)\right) - \frac{1}{2}\left(\frac{\frac{1}{R_5}\left(T_5^{old} - T_4^{old}\right)}{\dot{m}\ c_p}\right) \quad (^\circ C) \qquad (24)$$

So, T_5^{old} was calculated each time interval iteratively to determine the pipe temperature at node 5. The thermal resistances (R) and capacitances (C) are parameters with constant values that are based on the properties of each of the construction layers as;

$$C = \rho c_p V \qquad (J\,/^\circ K) \qquad (25)$$

Performance of TAR system can be evaluated once the node temperatures at each time step are determined. The rate of heat transferred between the roof and the water supplied to the TAR system is calculated as;

$$\dot{q}_{tr} = \dot{m}\, c_p (T_r - T_s) \qquad (W) \qquad (26)$$

Or, the heat extracted from the concrete slab by the TAR piping system can be calculated as;

$$\dot{q}_c = \pi d\, L\, (T_4 - T_5)/R_5 \qquad (W) \qquad (27)$$

The heat extracted from the room by the TAR system across the lower roof surface, can be calculated as;

$$\dot{q}_i = h_i A\ (Ti - T6) \qquad (W) \qquad (28)$$

The rate of heat transferred from the upper roof surface transmitted to the surrounding and is calculated as;

$$\dot{q}_{sur} = h_o A\ (T_e - T_1) \qquad (W) \qquad (29)$$

TAR system instantaneous efficiency $\eta_{\,TAR}$, in this work is defined as the ratio of the heat extracted from the room by the TAR system to the heat extracted from the concrete slab by the cooled water as;

$$\eta_{\,TAR} = \dot{q}_i/\dot{q}_c \qquad (30)$$

Effectiveness of the TAR system is defined as the ratio of the heat extracted from the concrete slab by the cool water to the mechanical power spent to drive the TAR system as **Sourbroun, 2012**;

$$\in_{\,TAR} = \dot{m}\, c_p (T_r - T_s)/P_{con.} \qquad (31)$$

$$P_{con.} = A_{\,l} * V_{\,l} * (P.F) * \eta_b \qquad (W) \qquad (32)$$

Where: $P_{con.}$ is the power consumed in driving the cooling tower fan and pump, P.F is the power factor = 0.75 and η_b is the brake efficiency which is assumed equal to 0.85 for tower fan and pump.

5. COMPUTER IMPLEMENTATION

Fig. 9 is a flow chart of the main procedures in the computer model using for the Matlab program. Matlab R2012a computer program was used to solve the set of six linear algebraic equations. The program input command identifies the initial conditions, material thermal properties and geometry. Using the 'solve' Matlab command statement, the nodal temperatures are determined for a certain time step which then become old temperatures for the next time step except T_5^{old} which is calculated each time interval depending on the instantaneous supply water temperature. A time step of 1800 seconds (30 minutes) was used in this model. The 'Input' Matlab statement provides several initial conditions, several material properties and geometrical dimensions for system flexibility and to determine their effects on the temperature distribution through the concrete slab and the heat exchange rate with the piping network and surroundings.

6. RESULTS AND DISCUSION

6.1 Concrete temperature history

Fig. 10 shows the temperature history of the concrete core and the mean measured concrete temperature. The deviation is partly thought to be due to neglecting conduction in the pipe material and forced convection of water flow which were lumped as one parameter in T_5. Also, the assumption of linear rise of the supply water temperature could generate part of this discrepancy. The deviation of results between model and measured concrete temperature is depicted as a time lag of approximately one hour. Possibly, the thermal capacitance of components in the model do not account for this time lag. One of the more important results of the RC-thermal analysis is the hourly temperature distribution across the roof deck as shown in **Fig. 10**. Node positions in **Fig. 11** are at, 0 cm, 8 cm, 23 cm, 33 cm and 40 cm from the roof lower surface. They are nodes 1, 2, 3, 4 and 6 in the RC-network respectively. The amplitude of temperature variation is lower near the roof lower surface. This is due to the high thermal mass storage and insulation of the upper part of the roof. Temperature history of node 4, at the pipe level, shows the lowest amplitude due to the supply cold water temperature.

6.2 TAR system efficiency

TAR system efficiency varies with time due to the hourly variation of the ambient temperature, indoor temperature and slight variation of the cool supply water temperature. It is noted that efficiency attains values greater than unity as shown in **Fig. 12**. This is invalid because $\dot{q}_i < \dot{q}_c$. This occurs due to the time lag between the heat extracted by the concrete from the cool TAR water ($\dot{q}_c$) and the heat extracted from the room ($\dot{q}_i$). If this time lag is set to zero by slight modulation in **Fig. 12**, the efficiency takes the form shown in **Fig. 13**. Efficiency is of maximum at night. The rate of heat extracted from the space is of maximum at night when the cooling load is maximum. **Fig. 14** compares hourly cooling load $\dot{q}_{cl}$ and heat extracted from the room $\dot{q}_i$ which highlights the TAR system contribution to space cooling load. It shows that the extracted heat from the space is larger than the instantaneous cooling load for the period 13:00 – 19:00 hrs.

6.3 TAR System Geometry Effect

The effect of pipe spacing on the hourly temperature distribution through the concrete slab was evaluated for spacing of 10, 12, 14, 16 and 18 cm. Supply water temperature T_s shown in **Fig. 15** is the model temperature of node 4. It is noticed that the change in spacing causes a change in temperature amplitude and time delay due to the change in thermal mass storage. Low spacing reduces the time needed to approach the supply water temperature. Also, the experimental temperature of the node 4 falls between the model temperature for 15 cm and 18 cm spacing which is an excellent verification of the model.

The effect of pipe deepness ratio in the heat extracted from the space by RC model and experimental measurements is shown in **Fig. 16.** The higher the ratio the lower the heat extracted from the space and vice versa. The experimental representation in this figure is illustrated as a single point due to the fixed deepness ratio of the present work. A small deviation was noted. This may be due to the using the mean water temperature to compute the heat extracted by RC model.

6.4 Effect of Water Mass Flow Rate

The water temperature and flow rate influence the thermal performance of the TAR system strongly. Lower water temperatures mean better performance as shown in **Fig.17**. Moreover, TAR system effectiveness increases with flow rate up to $\dot{m}$ = 0.0088 l/s.m² beyond which there is only a slight improvement as shown in the figure. It is more efficient to change the water supply temperature T_s than to increase the water flow rate.

7. CONCLUSIONS

Based on the results the following conclusion can be drawn:

1- There is a small deviation between concrete nodal temperatures obtained by the RC-model and the measured temperatures at spacing of 17 cm.
2- TAR effectiveness improves significantly with lower supply water temperature and only slightly with increased water flow rate beyond 0.0088 l/s.m².
3- Increasing pipe spacing causes an increase in concrete temperature amplitude and time shift.
4- The heat extracted from the space decreased with pipe deepness ratio.

REFERENCES

- Antonopoulos, K. A., Tzivanidis, C. G., 1977, *Numerical Solution of Unsteady Three-Dimensional Heat Transfer during Space Cooling using Ceiling Embedded Piping.* In Energy, Elsevier, Vol. 22, No. 1, pp. 59-67.

- ASHRAE Handbook, Fundamentals, ASHRAE, Inc., Atlanta, GA, USA, 2009.

- Duffie A. and Beckman W. A., 2006, *Solar Engineering and Thermal Process*, Third ed. John Wiley and Sons, New York .

- Joseph M., 2012, *Calculus for the Life Sciences II Lecture, Notes – Trigonometric Functions*. Department of Mathematics and Statistics Dynamical Systems Group Computational Sciences Research Center, San Diego, State University San Diego.

- Karlson J. H., 2006, Thermal system analysis of embedded building integrated heating. thesis for the degree of licentiate of engineering, Department of Civil and Environmental Engineering, Chalmers University of Engineering, Göteborg, Sweden.

- Koschenz, M., and Lehmann, B., 2000, Thermo-active building systems TABS, EMPA Energiesysteme / Haustechnik, Duebendorf (Switzerland).

- Kreider S., Curtiss U., Rab L., 2002, *Heating and Cooling of Buildings*, 2nd ed., McGraw-Hill, New York, USA.

- Olesen W.B., 2002, *Control of Slab Heating and Cooling Systems Studied by Dynamic Computer Simulations*. Symposium, ASHRAE Transaction, V. 108, Pt. 2.

- Olesen, W., Carli, M. D., Scarpa, M., and Koschenz, M., 2006, *Dynamic Evaluation of the Cooling Capacity of Thermo-Active Building Systems*. ASHRAE Transactions 112, 2.

- Pedersen, F., Weitzmann, P. and Svendsen, S., 2005, *Modeling thermally active building components using space mapping*. Proceedings of the 7th Symposium on Buildings Physics in the Nordic Countries. Reykjavík, Iceland.

- Rietkerk J., 2010, *Evaluation of the Concrete Core Conditioning Performance for Flexible Building Zone Configurations*. 8th International conference on system simulation in buildings, Liege, (Paper P102), (pp. 20).

- Russell, M. B., and Surendran, P. N., 2001, *Influence of Active Heat Sinks on Fabric Thermal Storage in Building Mass*. Applied Energy 70, 17–33.

- Sourbroun M., 2012, *Dynamic Thermal Behavior of Buildings with Concrete Core Activation*. PhD thesis, Arenberg Doctoral School of Science.

- Vermolen F. J., 2008, *Predicting Critical Conditions for Bacterial Self-Healing of Concrete and Sand*. PhD thesis, Delft University of Technology, Delft Institute of Applied Mathematics, Mekelweg42628 CD Delft, The Netherlands.

- Weber, T., and Johannesson, G., 2005, *An Optimized RC-Network for Thermally Activated Building Components*. Building and Environment 40, 1–14. pages 23, 50, 89, 137, 140, 163.

NOMENCLATURE

A	temperature amplitude	(A)
A_l	line current	(A)
A_r	roof area.	(m^2)
C	capacitance.	(kJ/℃)
c_p	specific heat.	(kJ/kg. ℃)
d	diameter.	(m)
h	convective heat coeff.	($W/m^2.^\circ C$)
I_t	total solar radiation Intensity.	(W/m^2)
k	thermal conductivity.	(W/m.˚C)
l	thickness.	(m)
L	pipe Length.	(m)
$\dot{m}$	mass flow rate	(kg/s)
P	power.	(W)
$\dot{q}$	heat transfer rate.	(W)
R	thermal resistance.	(m^2. ˚C/W)
ΔR	the difference between incident and emitted radiation from black body.	(W/m^2)
s	spacing.	(m)
T	temperature.	(˚C)
T_e	sol-air temperature.	(˚C)
t	time.	(s)
V	volume	(m^3)
V_l	line voltage	(Volt)
w	slab width.	(m)

Greek symbols

α	surface absorptance.
ε	surface emittance.
ϵ_{TAR}	TAR effectiveness.

Ø	phase shift.	(hr)
η_b	brake efficiency.	
η_{TAR}	TAR efficiency.	
ρ	density.	(kg/m^3)

Subscripts

c	concrete.
con.	consumed.
d	dry bulb
i	indoor.
cl	cooling load.
max	maximum.
min	minimum.
m	mean.
ml	model.
o	outdoor.
p	pipe.
r	return.
s	supply.
sur	surround.
w	wet bulb
wr	water

Abbreviations

CCC	concrete Core Conditions.
FD	finite difference.
FCV	finite control volume.
PVC	poly vinyl chloride.
RC	resistance capacitance.
RTS	radiant time series.
TAR	thermally Activated Roof.

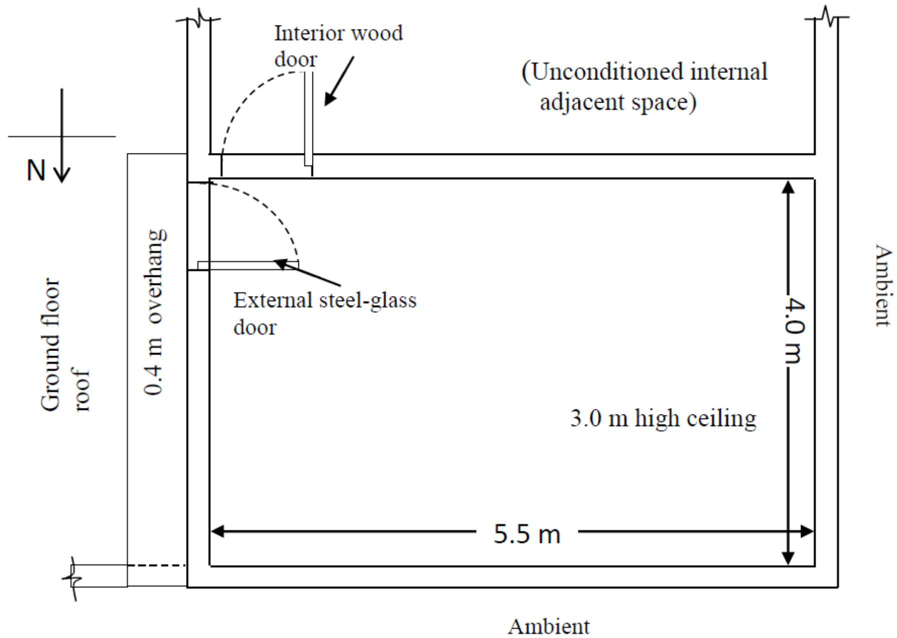

Figure 1. Plan view of the experimental room.

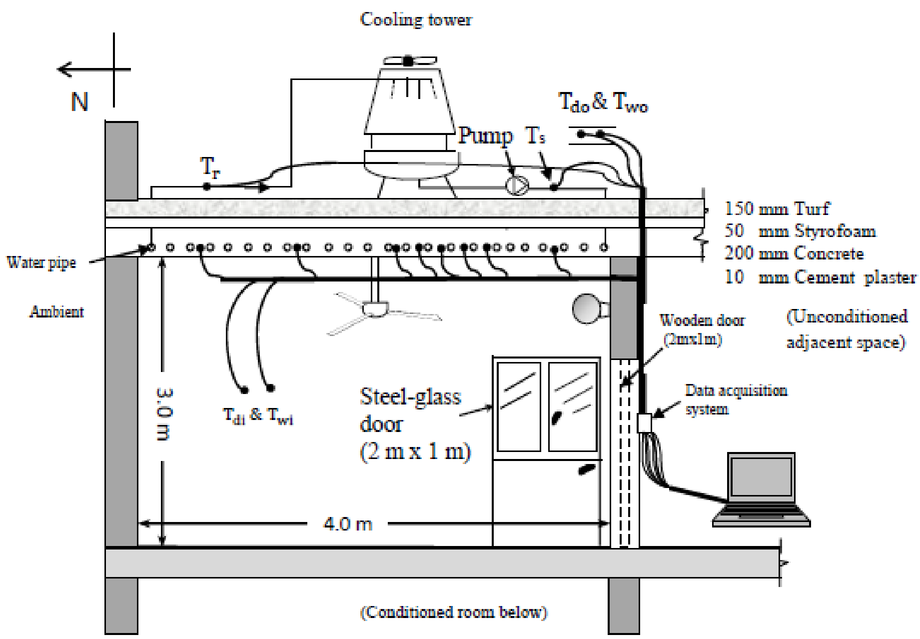

Figure 2. A front section of the test room. (•) temperature sensor.

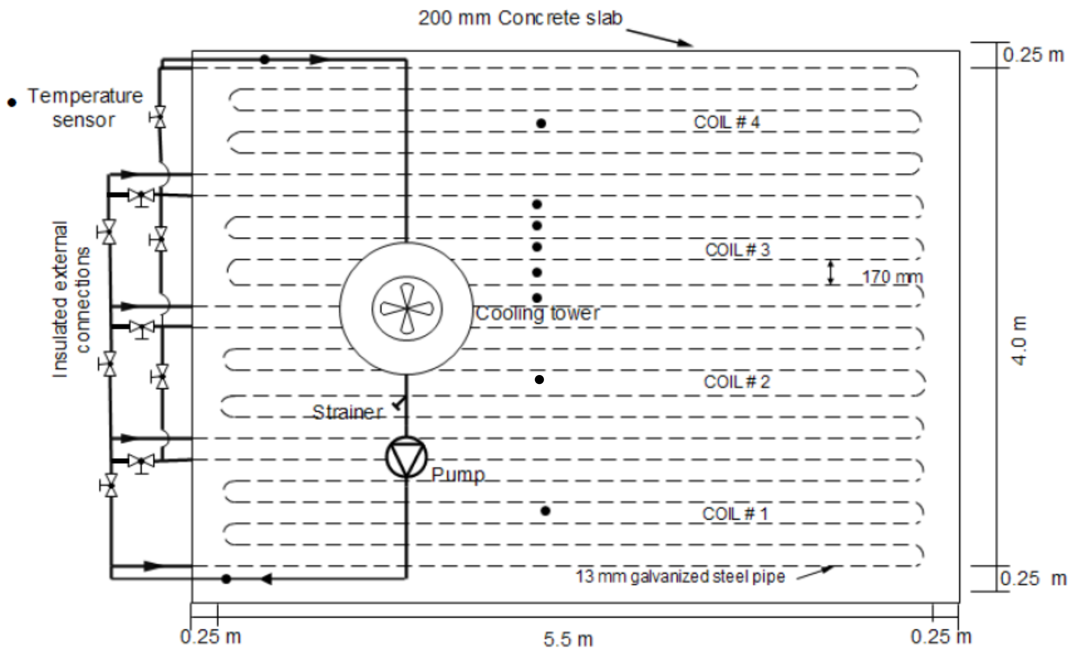

Figure 3. Pipe coils of the TAR system with coils external connections.

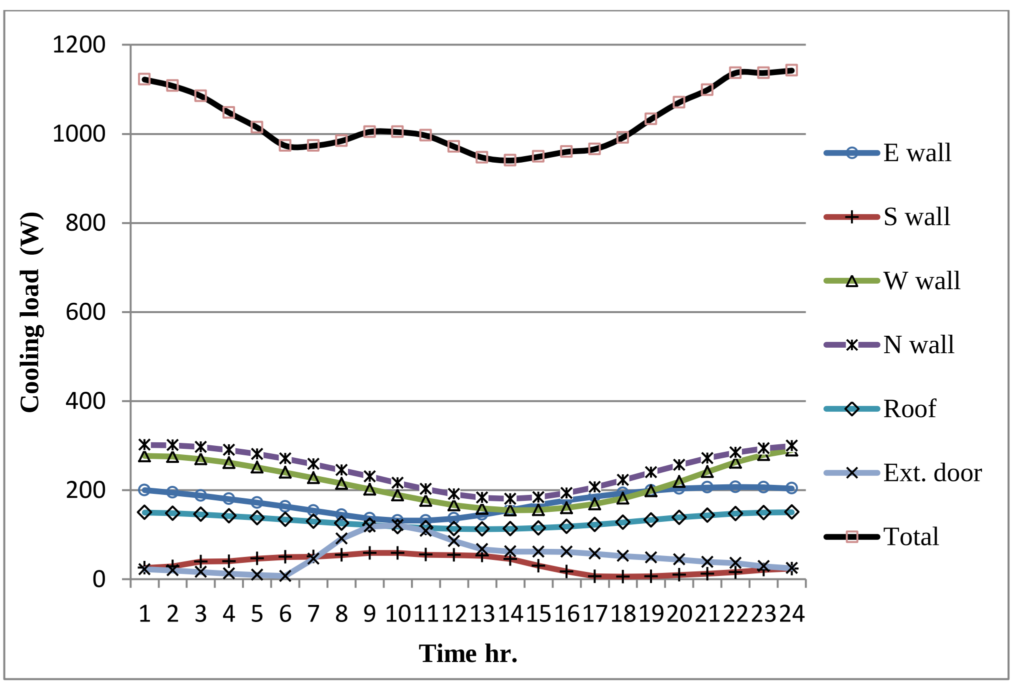

Figure 4. Cooling load components of the test room on 21 July.

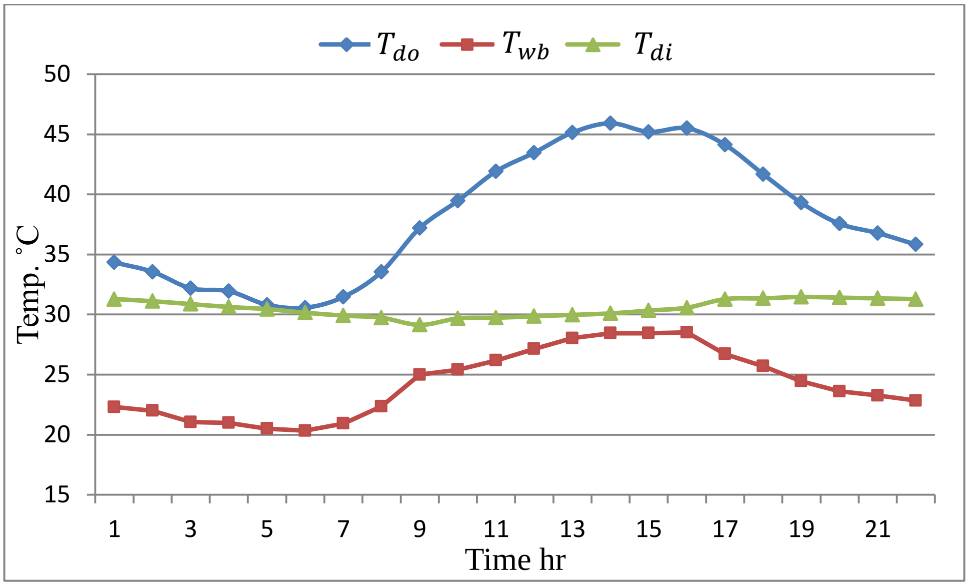

Figure 5. Experimental temperature measurements for 21 July, 2013.

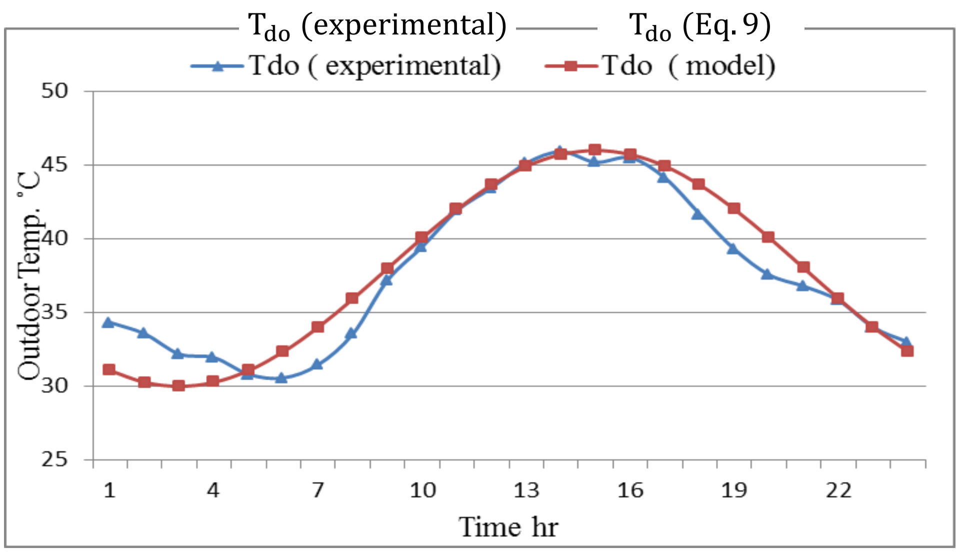

Figure 6. Experimental and model outdoor temperature profile.

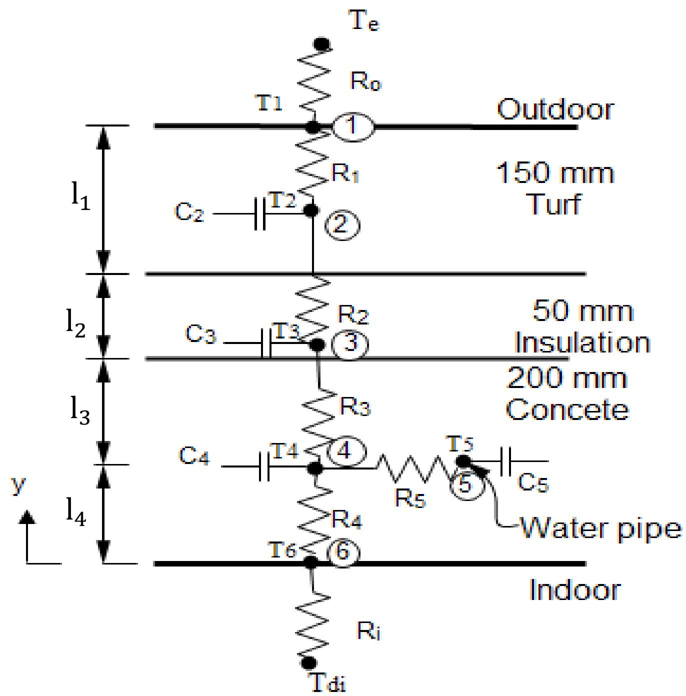

Figure 7. RC-thermal network model.

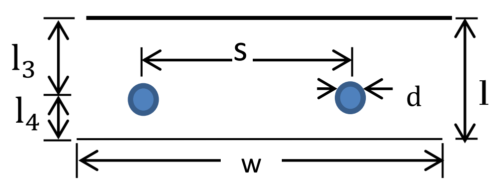

Figure 8. TAR geometry concept.

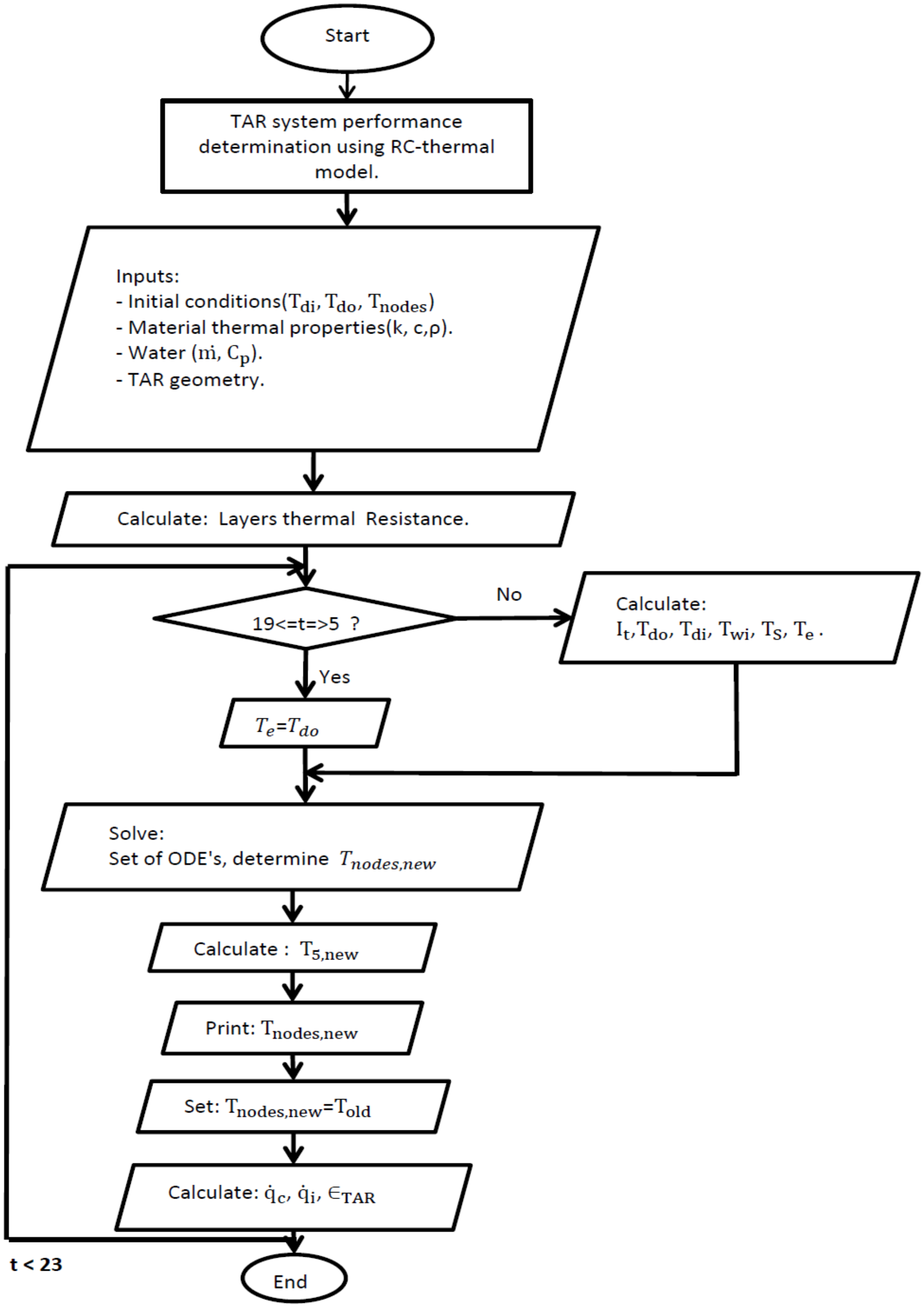

Figure 9. Flow chart of the computer model.

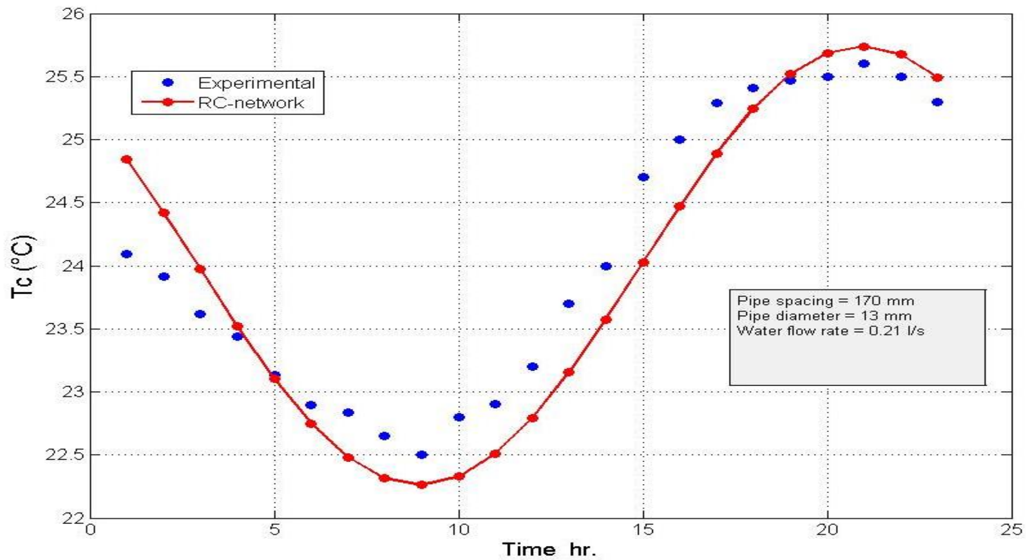

Figure 10. Concrete core temperature history.

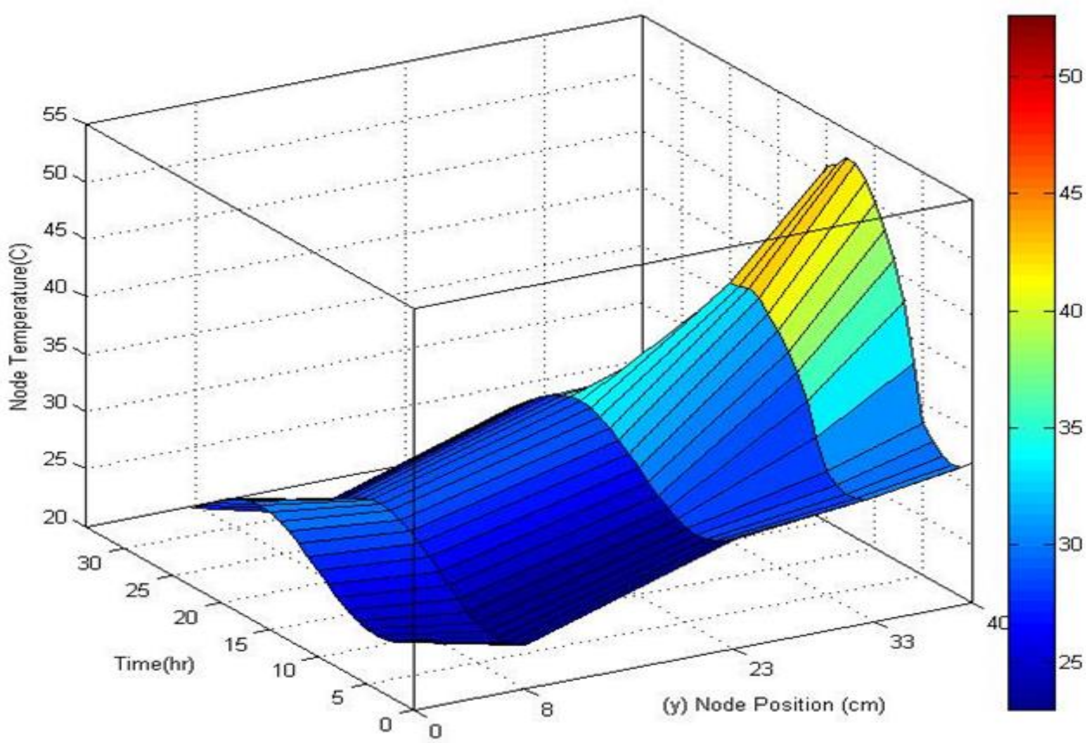

Figure 11. Nodal temperatures variation with time.

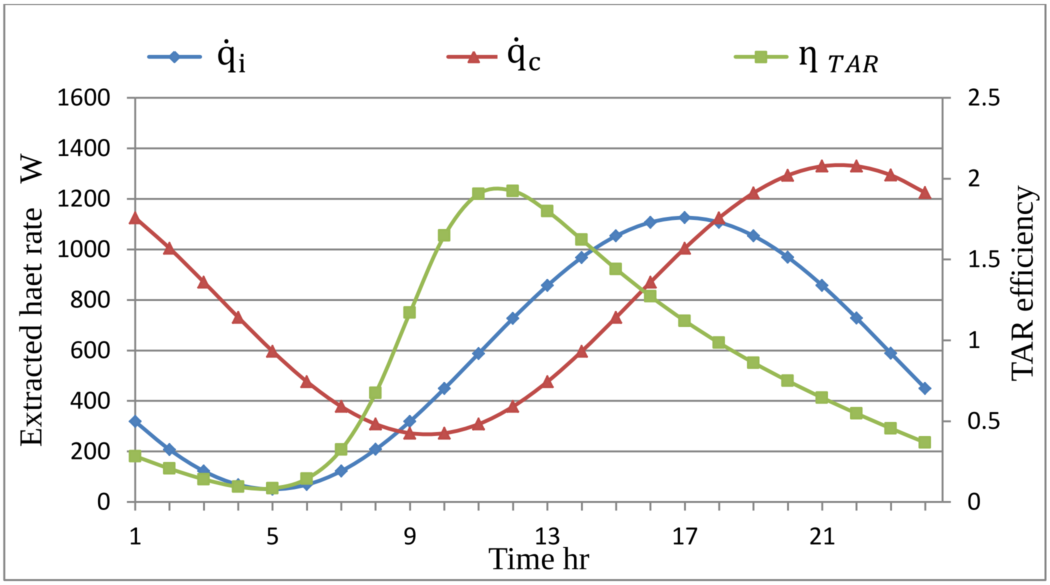

Figure 12. The effect of time lag on TAR efficiency.

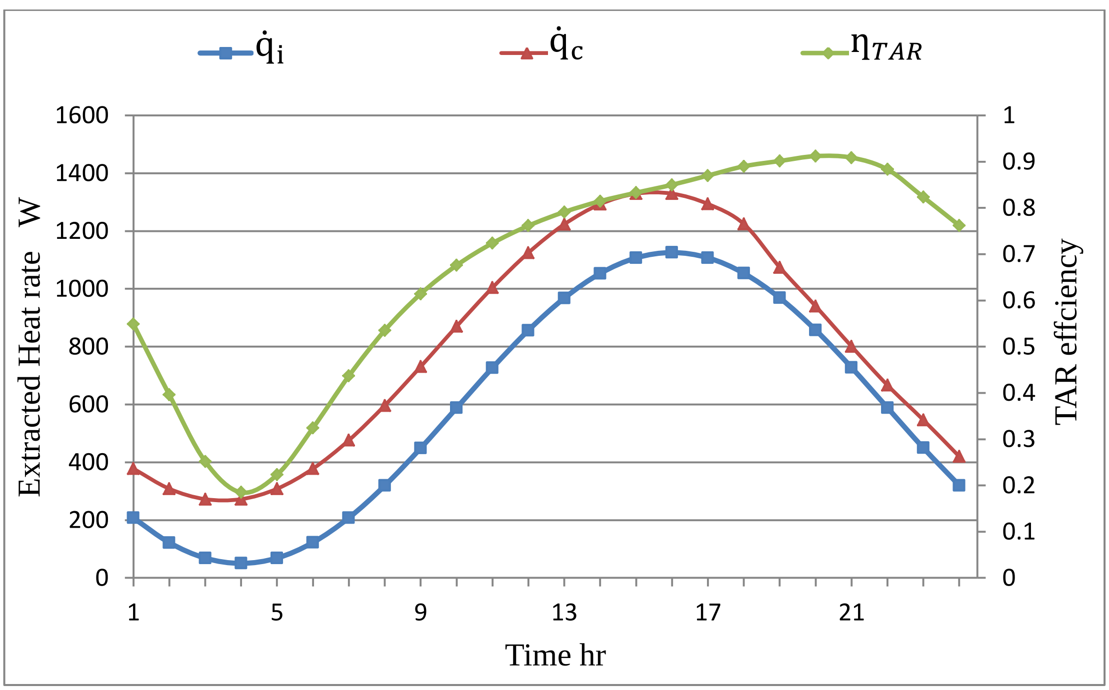

Figure 13. TAR system efficiency when time lag is set to zero.

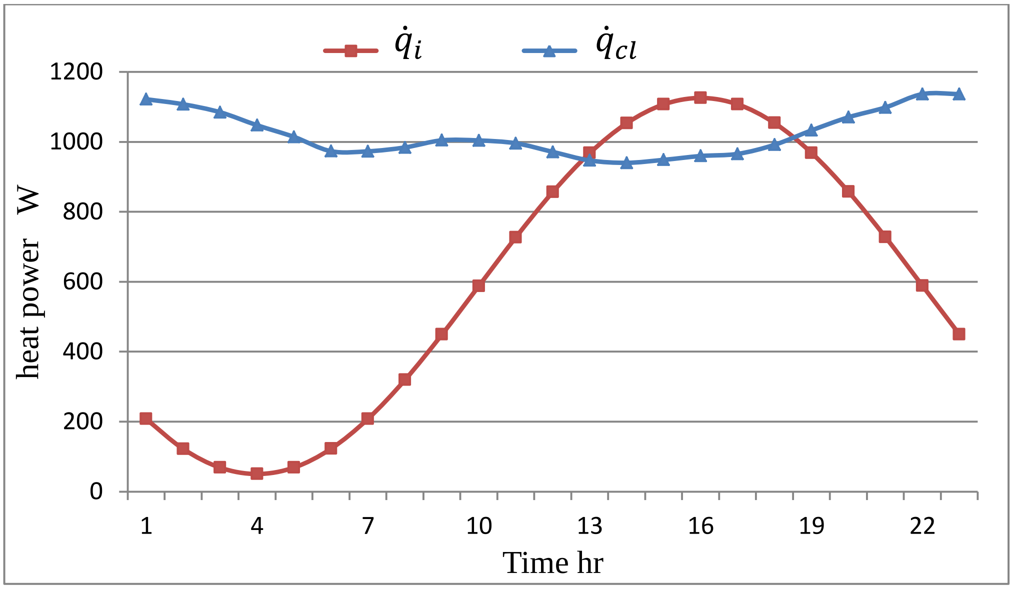

Figure 14. TAR system contribution in the heat extracted by TAR system compared with space cooling load on 21 July.

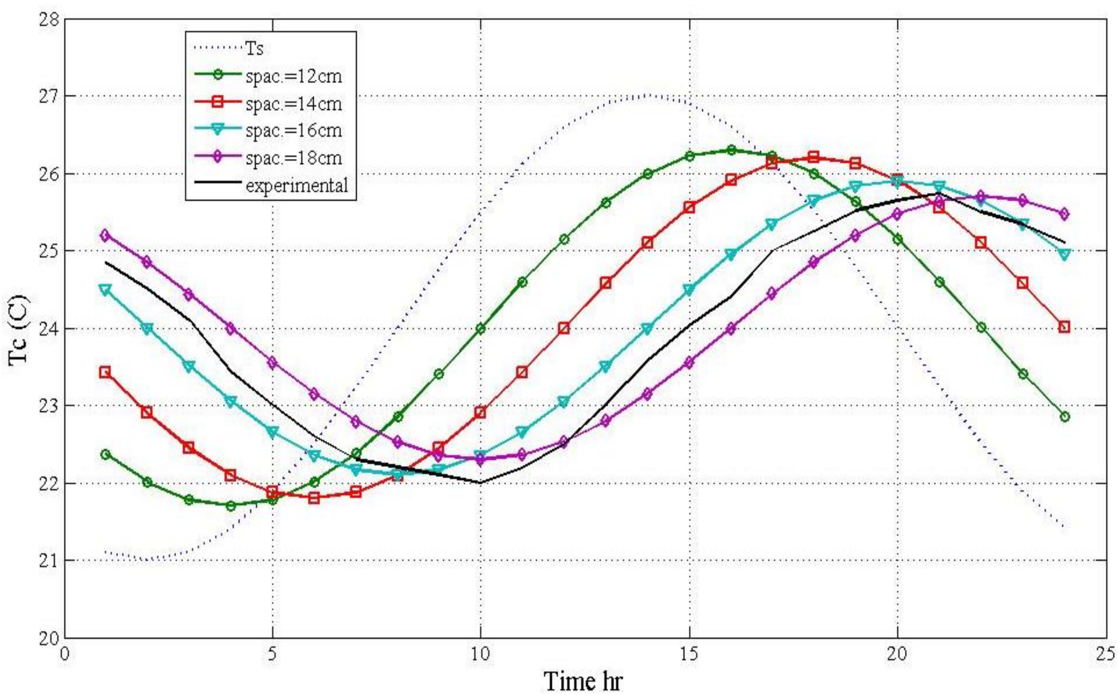

Figure 15. Pipe spacing effect on concrete temperature at node 4.

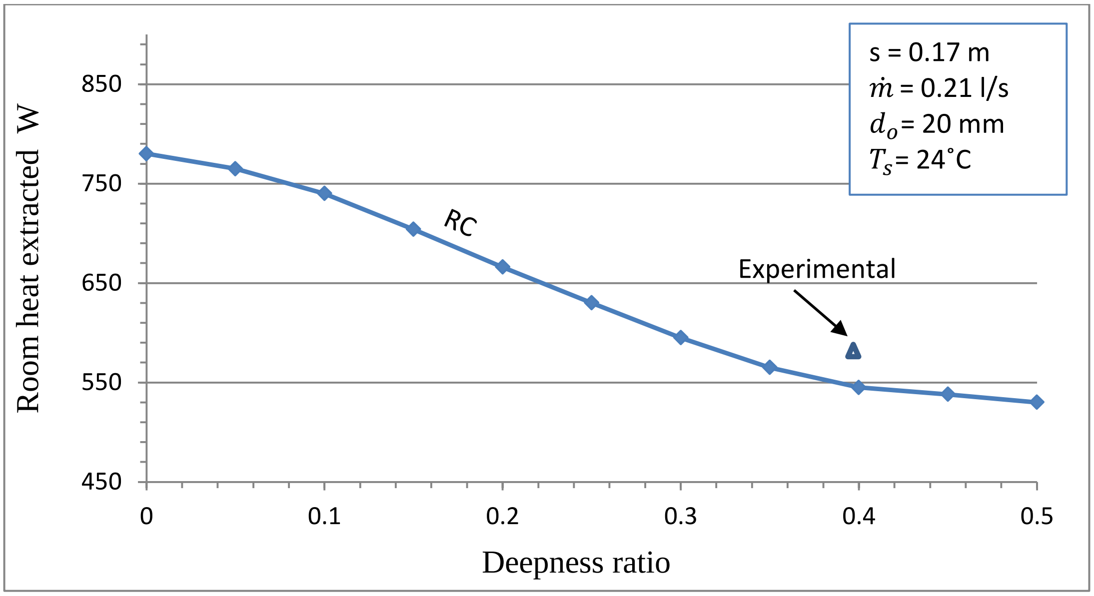

Figure 16. The pipe deepness ratio effect on the heat extracted from the space.

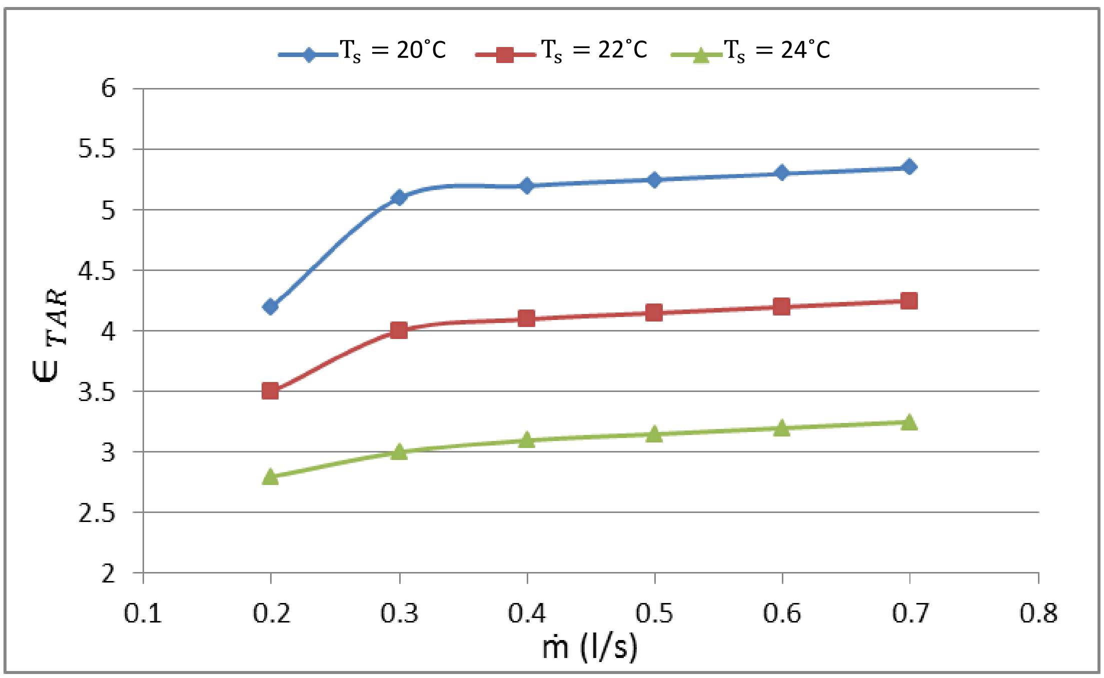

Figure 17. The effect of water mass flow rate and water supply temperature on TAR system effectiveness.

Thermal Characteristics of Closed Wet Cooling Tower Using Different Heat Exchanger Tubes Arrangement

Qasim Saleh Mahdi
Professor
College of Engineering -Al-Mustansiriyah University
E-mail:qasim602006@yahoo.com

Hayder Mohammed Jaffal
Lecturer
College of Engineering -Al-Mustansiriyah University
E-mail:hayder.jaffal@yahoo.com

ABSTRACT

This paper presents thermal characteristics analysis of a modified Closed Wet Cooling Tower (CWCT) based on heat and mass transfer principles to improve the performance of this tower in Iraq. A prototype of CWCT optimized by added packing was designed, manufactured and tested for cooling capacity of 9 kW. Experiments are conducted to explore the effects of various operational and conformational parameters on the thermal performance. In the test section, spray water temperature and both dry bulb temperature and relative humidity of the air measured at intermediate points of the heat exchanger and packing. Heat exchangers consist of four rows and eight columns for an inline tubes arrangement and six rows and five columns for staggered tubes arrangement. According to experimental data, the inline tubes arrangement has a better thermal performance than the staggered tubes arrangement. The inline tubes arrangement enhanced thermal efficiency more than (7%) compared to the staggered tubes arrangement. Furthermore the effect of added packing to CWCT on thermal performance was significant compared to CWCT without packing. Comparing CWCT with packing, it has been observed that the best performance for the CWCT with packing under heat exchanger. It can be watched that the thermal efficiency for CWCT with packing under heat exchanger and CWCT with packing above heat exchanger approximately (28%) and (16%) higher than that CWCT without packing respectively. This study provides correlations to predict heat and mass transfer considering the influences of operational parameters for both inline and staggered heat exchanger tubes arrangement.

Key words: Closed Wet Cooling Tower (CWCT), heat exchanger, packing, thermal performance

الخصائص الحرارية لبرج تبريد رطب مغلق باستخدام ترتيب مختلف لانابيب المبادل الحراري

قاسم صالح مهدي
استاذ
كلية الهندسة-الجامعة المستنصرية

حيدر محمد جفال
مدرس
كلية الهندسة-الجامعة المستنصرية

الخلاصة

يتناول هذا البحث تحليل الخصائص الحرارية لبرج تبريد مغلق مطوّر وفقاً لمبادئ انتقال الحرارة والكتلة لتحسين أداء هذا البرج في العراق. تم تصميم وتصنيع واختبار نموذج لبرج تبريد رطب مغلق مطوّر بإضافة الحشوات لسعة تبريد (9kW) . أجريت التجارب لبيان تأثيرات المعاملات التشغيلية والتصميمة على الأداء الحراري للبرج. في مقطع الاختبار تم قياس درجة

حرارة ماء الرش وكلاً من درجة الحرارة الجافة والرطوبة النسبية للهواء في نقاط متوسطة للمبادل الحراري والحشوة . المبادل الحراري يتكون من أربعة صفوف وثمانية أعمدة للترتيب المتتالي للأنابيب و ستة صفوف وخمسة أعمدة للترتيب المتعاقب للأنابيب.أوضحت النتائج المستحصلة إن الأداء الأفضل للمبادل الحراري هو عند ترتيب الأنابيب المتتالي مقارنة بالترتيب المتعاقب .الترتيب المتتالي للأنابيب يحسن الكفاءة الحرارية بمقدار يزيد على (7%) مقارنة مع الترتيب المتعاقب. علاوة على ذلك فان إضافة الحشوة إلى البرج المغلق له تأثير فعّال على الأداء الحراري للبرج .مقارنة مع برج التبريد المغلق بوجود الحشوة لوحظ أن افضل أداء في حالة إضافة الحشوة اسفل المبادل الحراري .لوحظ إن الكفاءة الحرارية عند إضافة الحشوة اسفل واعلى المبادل الحراري بأفضية تصل إلى نسبة (40%) و(25%) مقارنة مع برج التبريد المغلق بدون إضافة الحشوة على التوالي . زودت هذه الدراسة عدد من العلاقات التجريبية للتنبؤ بمعاملي انتقال الحرارة والكتلة بدلالة للمتغيرات التشغيلية للترتيب المتتالي والمتعاقب لأنابيب المبادل الحراري .

الكلمات الرئيسية: برج تبريد مغلق رطب ,مبادل حراري, حشوة ,أداء حراري

1. INTRODUCTION

Cooling towers are heat reject equipment used in much industrial process such as power generation units, refrigeration and air conditioning industries, **Stabat, 2004**. With respect to design of heat exchanger surface, there are two types of cooling towers: open and closed cooling towers. A direct, open circuit cooling tower is an enclosed structure that distributes warm water over a labyrinth-like packing, or fill, which provides an expansion of the interface between the air and water for heating of the air and evaporation to take place. An indirect, or closed circuit cooling tower, does not involve any contact between the air and the fluid being cooled. This tower has two separate fluid circuits, one in which circulated liquid on the outer surface of the second circuit, which is a bundle of tubes (closed coils) through which the hot water is flowing.

Much attention has been paid to issues on CWCTs relating to experimental studies and developed correlations of heat and mass transfer coefficients as a function of operating conditions. **Oliveira, and Facao, 2000**, designed a new CWCT in order to examine the effects of operating parameters on the saturation efficiency for a CWCT modified for use with chilled ceilings in buildings. Thermal performance of two evaporative cooled heat exchangers, Investigated by **Hasan, and Sirén, 2003**. They studies two heat exchangers; plane and plat-finned circular tube types occupy the exact volume and the ratio of total area (finned tubes /plate tubes) is four. **Shim, et al., 2008 and 2010** investigated experimentally the thermal performance of two heat exchangers in closed-wet cooling tower having a rated capacity of 2RT. Both heat exchangers have multi path that is consumed as the entrance of cooling water and are consisting of bare-type copper tubes of 15.88 mm and 19.05 mm. **Heyns, and Kroger, 2010** investigated the thermal performance characteristics of an evaporative cooler, which consist of 15 tube rows with 38.1 mm outer diameter galvanized steel tubes arranged in a triangular pattern of 76.2 mm. **Al-Tayyar, 2011,** modified an available open circuit cooling tower (WL 320 Demo cooling tower, constructed by GUNT company in Germany) to make utilized likewise closed circuit cooling tower by designing furthermore manufacturing a heat exchanger located under packing. **Zheng, et al., 2012,** investigated thermal performance of an oval tube CWCT based on heat and mass transfer under different operating conditions.

Most of above studies involved thermal performance of CWCT with heat exchanger either inline or staggered tubes arrangement. In this study, thermal performance of modified counter flow forced draft CWCT in hot and arid environmental Iraqi weather conditions will be evaluated in order to use for the chilled ceiling of the building in Iraq. The modification based on addition packing to the conventional CWCT. To clarify the effect of heat exchanger tubes arrangements on tower performance, two heat exchangers with different tubes arrangement (inline and staggered) are used in this study.

2. EXPERIMENTAL APPARATUAS AND PRCEDURE

2.1. Description of Test Rig

A new CWCT was designed and constructed in which different operating parameters could be varied and tested in the laboratories of Environmental Engineering Department of Al-Mustansiriya University College of Engineering. The general arrangement of the equipment is shown photographically in **Fig.1**. In general, the apparatus consists essentially of cooling column and three major systems, Spray water, Cooling water and Air blowing.

The tower fabricated from galvanized steel sheet to provide protection from rusting and corrosion, each sheet of 1.5mm thickness, connected together by screws and nuts as a rectangular box of external dimensions (700 mm×400 mm×2300 mm), mounted rigidly on a frame which is welded construction with a channel section at the base welded together from the rectangle. As exists in every forced cooling, the test section consists of three zones: spray, fill (cooling zone) and rain zones. Spray zone is at height of 180 mm suitable to ensure water distribution uniformly to all points in the fill section. Fill zone at 1000 mm height and characterized as consisting of three places for sliding removable drawer rectangular boxes at same dimensions manufacturing for packing and heat exchangers to ensure change the locations and types of heat exchangers and height of packing to study the influence of all these additions on the performance of the tower. The rectangular drawer made of galvanized steel with dimensions of 420 mm in width, 760 mm in depth and 280 mm in height. Six holes along the side of each (drawer) box were done to measure the water temperature, air dry bulb temperature and air relative humidity. The rain zone at height of 450 mm in the case of three boxes and it will be variable when lifting one ore tow packing's and increases as decreases the packing height.

Air from the atmosphere, enters the single stage centrifugal blower at a rate which is controlled by the butterfly valve. The fan discharges into the PVC pipe and entrance duct before entering the packed column. As the air flows through the packing and heat exchanger, its moisture content increases and the water in the heat exchanger are cooled. Hot water is pumped from the load tank through the control valve and water flow meter to the heat exchanger placed inside test section of tower. Plain tube heat exchanger was designed and manufactured for the present work. The tubes were fixed horizontally in test section inside supported frame of rectangular drawer .Cooling water moves through the tubes while the spray water and air moves over the tubes in perpendicular direction. The tubes are arrays in inline and staggered arrangement with (equilateral) tube pitch of $3D_o$ (pitch over diameter of 3) as shown in **Fig.2**.The specification of heat exchangers shows in **Table 1.**

The water distribution system in the cooling tower should distribute the water uniformly over the tube bundle and packing inside the tower, to be the most coefficient method of uniformly water distribution in counter flow wet-cooling tower a pressurized spray system used with different types of spray nozzles. The spray water passes through the spray nozzles and constantly distributed at upper part of the test section, controlled by means of flow control valve globe type located downstream of the spray water pump. In the spray frame a header distributes or divides the deluge water into several conduits or lateral branches. Spray water nozzles were fitted the end of each lateral branch.

2.2. Test Procedure

In order to evaluate the thermal performance of cooling tower, a series of experiments was carried out at different operational and conformational parameters. Operational parameters demonstrate: air flow rate of (0.12-0.3) kg/s, spray water flow rate of (20,25,30,35,40,45) l/min, cooling water flow rate of (10,15,20,25,30,35,40,45,50) l/min, inlet cooling water temperature of (35,40,45,50,55)˚C and inlet air wet bulb temperature of (7-24)˚C. Conformational parameters indicate: height of packing used (280 and 560) mm, location of packing (under Heat exchanger and above Heat exchanger) and arrangement of heat exchanger (staggered and inline).

Thermocouples type K insert before and after the cooler coil to measured cooling water temperature. To measure the spray water temperatures at intermediate locations inside test section, specially channels have been manufacturing to insert thermocouples type K through holes .These holes are closed by rubber stoppers through which thermocouples are inserted to measure the temperature profile. The variations of air dry bulb temperature and relative humidity along the test section as well as the inlet and outlet of the tower were measured by humidity meter, which combined temperature/humidity sensor. The humidity meter model TH-305 has a temperature and relative humidity measurement range from 0 to 60˚C and 20 to 95% respectively. The sensor probe handle is placed directly in the air stream and connected to display.

2.3. Performance Parameters

In viewpoint of energy analysis, the parameters used to determine the performance of cooling tower are:

1-Cooling range: is the temperature difference between the water inlet and exit states. Range can be measured by the temperature difference between the inlet and outlet from cooling tower:

$$CR = T_{cw,in} - T_{cw,out} \tag{1}$$

2- Thermal efficiency: The most important parameter of cooling tower performance is the thermal efficiency, which can be defined as the ratio of actual released of heat to the maximum theoretical heat from cooling tower. The thermal efficiency for the closed circuit cooling towers was defined as **Oliveira, and Facao, 2000 and Yingghan,et al., 2011**:

$$\eta = \frac{T_{cw,in} - T_{cw,out}}{T_{cw,in} - T_{awb,in}} \tag{2}$$

3-Cooling capacity is the heat rejected or heat dissipation, given product of mass flow rate of water, specific heat and temperature difference.

$$q = \dot{m}_{cw} C_{p,cw}\, CR \tag{3}$$

4-Mass transfer coefficient

The mass transfer coefficient obtained using enthalpy balance for an elementary transfer surface **Oliveira, and Facao, 2000**.

$$m_{air} dh_a = \alpha_m \, (i_i - i_{air}) \; dA \tag{4}$$

Which is known as the Merkel equation and integrated for the whole heat exchanger in tower gives:

$$\frac{\alpha_m A}{\dot{m}_a} = ln \frac{i_{masw} - i_{a,in}}{i_{masw} - i_{a,out}} \tag{5}$$

where, α_m is the mass transfer coefficient for water vapor between spray water film an air , A is the surface area of the heat exchanger and i_{masw} is the specific enthalpy of the saturated air at the mean spray water temperature .

The average of spray water temperatures was taken as the interface temperature according to **Zheng, et al., 2012** while the inlet and outlet air enthalpies were calculated from Psychometric chart according to the measured data. Outlet air enthalpy could be also calculated considering that all the heat goes from water to air **Oliveira, and Facao, 2008:**

$$\dot{m}_a \left(i_{a,out} - i_{a,in} \right) = \dot{m}_{cw} C_{p,cw} \, (T_{cw,in} - T_{cw,out} \;) \tag{6}$$

Then the outlet air enthalpy calculates as:

$$i_{a,out} = i_{a,in} + \frac{\dot{m}_{cw} C_{p,cw} \, (T_{cw,in} - T_{cw,out} \;)}{\dot{m}_a} \tag{7}$$

5-Heat transfer coefficient

Heat transfer from cooling water inside tubes to spray water and air through a water film .the rate of heat transfer from cooling water dq_c is given by **Hasan, and Sirén, 2002**:

$$dq_c = \dot{m}_{cw} C_{\mathrm{p},cw} dT_{cw} = -U_o \, (T_{cw} - T_{sw}) dA \tag{8}$$

Integrated Eq.8 from the inlet to outlet of cooling water, with constant spray water T_{sw}, gives.

$$\frac{U_o A_c}{C_{p,cw} m_{cw}} = ln \frac{T_{cw,in} - T_{sw,m}}{T_{cw,out} - T_{sw,m}} \tag{9}$$

where, U_o is the overall heat transfer coefficient between cooling water inside the tubes, tube wall and spray water on the outside .It is calculated by the following formula **Shim, et al., 2008 :**

$$\mathrm{U_o} = \left[\frac{R_o}{\mathrm{R}_i} \, \frac{1}{\alpha_c} + \frac{R_o}{\mathrm{k_t}} \ln \frac{R_o}{R_i} + \frac{1}{\alpha_s} \right]^{-1} \tag{10}$$

After the overall heat transfer coefficient was calculated from Eq.(9), it used to calculate, αs, tube to water film heat transfer coefficient (W/m^2 C).

$$\alpha_s = \left[\frac{1}{U_o} - \frac{R_o}{\mathrm{R}_i}\,\frac{1}{\alpha_c} - \frac{R_o}{\mathrm{k_{tube}}}\ln\frac{R_o}{R_i}\right]^{-1} \tag{11}$$

Where, α_c is the convection heat transfer coefficient of cooling water inside the tubes, it was calculated by the "**Dittuse-Boelter**" relation and **Incropera,et al.,2011**:

$$\alpha_c = 0.023\,\frac{k_{cw}}{D_i} Re^{0.8}\, Pr^{0.3} \tag{12}$$

Where, Reynolds number and Prandtl number were taken for the cooling water inside the tubes.
A MATLAB program was written to calculate the following parameters: water cooling range, tower approach, thermal efficiency, cooling capacity, heat transfer coefficient and mass transfer coefficient. The input data to this program is the measured parameters taken from the experimental runs.

3. RESULTS AND DESCUSSION

3.1. Verification of the Experimental Apparatus

To verify the reliability of the experimental apparatus, energy balance of the air and cooling water was adopted using eq. (8).As shown in **Fig.3**, the unbalance of the heat gained by the ambient air and the heat lost by the cooling water are within ±10%. The heat balance of the apparatus could be claimed to be satisfactory.

3.2. Effects of Operational Parameters

Figs. 4 to 6 indicate the effects of air flow rate, spray water flow rate, cooling water flow rate, inlet cooling water temperature and inlet AWBT (due to an atmospheric conditions) on the cooling water range for CWCT with (560 mm) packing height that located under heat exchanger with staggered tubes arrangement.

The effect of spray water flow rate on the cooling water rang for different values of the air flow rate is illustrated in **Fig.4**. For each value of spray flow rate , as the air flow rate increases , the cooling water range is increases. This can be explained by as the air flow rate increases, evaporated water per unit of air increases too. On the other hand, cooling water range is increasing exponentially while the spray water flow rate is increasing. The most important reason for increasing cooling rang with spray water flow rate is increasing in the amount of water exposed to air during the unit time and providing a largest contact surface for the heat and mass transfer between water and air.

The relationship between the cooling water range and cooling water flow rate with different spray water flow rates are illustrated in **Fig.5**. It can be noted that the cooling water range is inversely proportional to the cooling water flow rate when both air and spray water flow rates are constant. For constant heat load, at low flow rate of circulation cooling water inside the heat exchanger tube, the opportunity to be the largest in completion of heat exchange with spray water and air through the tube surface within the tower test section for same air flow rate caused an increasing in temperature difference of cooling water. If maximum cooling range is desired, the low flow rate of cooling water should be used. For the same manner in **Fig.4**, cooling water range for 40 l/min spray water flow rate approximately 14% higher than that 30 l/min.

The variation of cooling water range with inlet cooling water temperature for different values of spray water flow rate is illustrated in **Fig.6**. For each value of inlet cooling water temperature, as the spray water flow rate increased, the cooling water range is increased**.** It is apparent. that cooling water range increases .Which is due to the increasing in the air hold up as a result of a decreased viscosity of spray water that was caused by increased an inlet spray water temperature at the first stage of the tower. Therefore, at a higher inlet spray water temperature, the vapour pressure driving force is increased by operating cooling tower at a given inlet air condition, this conforms well to **Shim, et al., 2008.** What was observed from this figure is that the decrement of the cooling range at high inlet cooling water temperature is increased because of the increased in rate of heat and mass transfer.

Cooling range with respect to variable inlet AWBT for different inlet cooling water temperature has been shown in **Fig.7**.For each inlet cooling water temperature, cooling range decreases almost linearly with the increase of inlet AWBT and vice versa. This is because when the inlet AWBT increases, the amount of heat exchange between air and water by convection and evaporation decreases due to a decrease in temperature difference between the inlet air and cooling water temperatures. Also, it can be known for the same reason that when inlet cooling water increases for the same inlet AWBT, the cooling range increases.

3.3. Effect of Added Packing

The effect of added packing to CWCT on the cooling range is shown in **Fig.8**. Results clearly demonstrated that the water cooling range increases with an increase in packing height. This can be attributed to the decrease of spray water temperature due to the increasing in the mass transfer generated by intense adding packing that substantially increases the air-water contact area and the water resident time in the tower. It can be observed that the cooling range for added packing height of (280 mm) and (560 mm) approximately (6%) and (28%) higher than that conventional CWCT respectively**.** As can be seen from **Fig.9**, there is a significant variation in the cooling capacity of cooling tower with added packing on CWCT. The result indicated that the cooling capacity for added packing height of (280 mm) and (560 mm) approximately (6%) and (28%) higher than that conventional CWCT respectively.

3.4. Effect of Packing Location

From **Fig.10** it is observed that added packing to CWCT displays a higher cooling range when located the heat exchanger at the top of the tower than the lower location. It is believed due to the rate of evaporation will be at a maximum value at the top of the tower; therefore, a maximum rate of mass transfer will be found at this stage. The rate of mass transfer is decreased gradually from the top of tower to the bottom. If heat exchanger located at the top of the tower, spray water in the form of small droplets easily evaporate at the surface of heat exchanger .Whereas, if the heat exchanger located at the bottom of the tower, spray water outlet from packing will be big drops that may not cover all surface of heat exchanger. On the other hand, contact between warm spray water and cold air gives better heat and mass transfer for packing when located at the bottom It may be observed that the cooling range for CWCT with packing under heat exchanger and CWCT with packing above heat exchanger approximately (28%) and (16%) higher than that CWCT without packing respectively. **Fig.11** shows the cooling capacity comparing for different positions of packing. The result indicated that the cooling capacity for CWCT with packing under heat exchanger and CWCT with packing above heat exchanger approximately (28%) and (16%) higher than that CWCT without packing respectively.

3.5. Effect of Heat Exchanger Tubes Arrangement

To clarify the effect of heat exchanger tubes arrangements on tower performance, the performance analysis has been illustrated for CWCT with packing of 560 mm height located under heat exchanger for different types of tubes arrangement. **Figs .12 to 15** represent the comparison between cooling range, thermal efficiency and cooling capacity as a function of spray water flow rate for different tubes arrangement: staggered and inline.

Fig.12 presents the variation of cooling range with spray water flow rate for different air flow rate and different tubes arrangements. From this figure, in both arrangements, it can be observed that the cooling range increases with an increase in both air and spray water flow rates. However, the inline tubes arrangement had a higher cooling range than the staggered tubes arrangement. This could be due to air velocity through the minimum flow area; this area depends on the geometric of tube arrangement. Higher number of tubes per row in inline arrangement decreases minimum flow area normal to the flow then increase in air velocity. On the other hand, in spite of raised in the wakes of upstream tubes beyond the first row in inline arrangement, that causes a decrease in heat and mass transfer, the inline arrangement performs much better in case of widely space tube. The inline arrangement increasing cooling range more than (7.5%) compared to the staggered arrangement.

Fig .13 illustrates the variation of thermal efficiency with spray water flow rate for different air flow rates and different heat exchanger tubes arrangements. Results show that in both arrangements, it is indicated that the thermal efficiency increases with an increase in both air and spray water flow rates. However, the inline tubes arrangement had a higher thermal efficiency than the staggered tubes arrangement. The inline arrangement enhanced thermal efficiency more than (7%) compared to the staggered arrangement.

Variation of cooling capacity with spray water flow rate for different air flow rates and different heat exchanger tubes arrangements has been shown in **Fig .14**. It is stated that in both arrangements, it is indicated that the cooling capacity increases with an increase in both air and spray water flow rates. However, the inline tubes arrangement had a higher cooling capacity than the staggered tubes arrangement. The inline arrangement increases cooling capacity more than (5%) compared to the staggered arrangement.

Another e comparison between heat exchanger tubes arrangements are shown in **Fig.15**. In **Fig.15a**, the variation of cooling capacity with spray water flow rate for inline and staggered tubes arrangement are presented. As mentioned in **Fig.14**, the cooling capacity for inline tubes arrangement greater than the staggered tubes arrangement. On the other hand, the variation of cooling capacity per unit (heat exchanger) volume with spray water flow rate for inline and staggered tubes arrangement are presented in **Fig.15b**.Two heat exchangers do not have the same volumetric size, so it is expressed that cooling capacity which was divided by the volume of heat exchanger in this figure. Cooling capacity per unit volume for using staggered tubes arrangement has highest value than the inline tubes arrangement. This is because the staggered tubes arrangement has more compact comparing to the inline arrangement for similar tube dimensions. Generally, it is indicated that the inline arrangement gives higher cooling capacity in kW, whereas the staggered perform better for cooling capacity in kW/m^3.

Fig.16 shows a comparison of the impact of inlet cooling water temperature on the thermal efficiency of CWCT with packing under heat exchanger between the present work and test results of **Al-Tayyar, 2011**. Al-Tayyar studied the outline of a heat exchanger in a CWCT of 1 kW cooling capacity and an inline tubes arrangement of 8 mm outside tube diameter arranged in 6 rows and 12 columns .The thermal efficiency was increased with the increasing inlet cooling water temperature. The qualitative agreement in results between two studies is observed. The difference in the thermal efficiency between two studies is due to the distinction between the two experimental apparatus.

3.6. Correlations of Heat and Mass Transfer Coefficients

According to the results of the experiments of this work, for different operational parameters, correlations for heat and mass transfer coefficients were developed for cooling tower operates without packing for both inline and staggered arrangements. These correlations are:

1-Inline tubes arrangement

a-Mass transfer coefficient

$$\alpha_m = 0.00003\left(\dot{G}_{air}\right)^{0.4925}\left(\dot{G}_{sw}\right)^{0.527}(T_{cw})^{1.839} \tag{13}$$

b-Heat transfer coefficient

$$\alpha_s = 0.1872\left(\dot{G}_{sw}\right)^{0.6406}\left(\dot{G}_{cw}\right)^{0.4}(T_{cw})^{1.5089} \tag{14}$$

1-Staggared tubes arrangement

a-Mass transfer coefficient

$$\alpha_m = 0.000001\left(\dot{G}_{air}\right)^{0.5038}\left(\dot{G}_{sw}\right)^{0.7456}(T_{cw})^{2.4478} \tag{15}$$

b-Heat transfer coefficient

$$\alpha_s = 0.1349\left(\dot{G}_{sw}\right)^{0.3758}\left(\dot{G}_{cw}\right)^{0.2051}(T_{cw})^{1.7749} \tag{16}$$

The average roots square mean error between correlations and experimental data for mass and heat transfer was (0.9702), (0.9722) for inline tubes arrangement and (0.9666), (0.9424) for staggered tubes arrangement, respectively.

4. CONCLUSION

The inline tubes arrangement has a better thermal performance (higher cooling rang, thermal efficiency, cooling capacity heat and mass transfer coefficients and lower tower approach) than the staggered tubes arrangement. On the other hand, the inline arrangement gives higher cooling capacity in (kW), whereas the staggered perform better for cooling capacity per unit volume ($kW/m^{3)}$. The CWCT with packing has a better performance than without packing. Furthermore, it is noticed that the height of packing (560 mm) has a significant effect on tower performance in comparison with (280 mm) packing height. I t is found that the cooling capacity for added packing height of (280 mm) and (560 mm) approximately (6%) and (28%) higher than that CWCT respectively. Comparing CWCT with packing for both locations under and above heat exchanger, it has been observed that the best performance for the CWCT with packing under heat exchanger. Also, the result indicated that the cooling capacity for CWCT with packing under heat exchanger and CWCT with packing above heat exchanger approximately (28%) and (16%) higher than that CWCT without packing respectively.

REFERENCES

- Al Tayyar Mohammed Abd Al-Khaliq. A.,2011, *An Investigation into Thermal Performance of an Indirect Contact Closed Type Cooling Tower*, M. Sc. Thesis, University of Baghdad.

- Hasan A., and Sirén K.,2002, *Theoretical And Computational Analysis of Closed Wet Cooling Towers And Its Application In Cooling Of Buildings*, Energy And Buildings, Vol. 34, pp (477 - 486).

- Hasan A.and Sirén K, 2003, *Performance Investigation of Plain and Finned Tube Evaporatively Cooled Heat Exchangers*, Applied Thermal Engineering, Vol. 23, pp (325 – 340).

- Heyns J.A., and Kroger D.G.,2010, *Experimental Investigation into The Thermal-Flow Performance Characteristics of An Evaporative Cooler*, Applied Thermal Engineering, Vol. 30, pp (492-498).

- Incropera F.P , Dewitt D.P, Bergman T.L and Lavine A.S,2011, *Fundamentals of Heat and Mass Transfer*,seventh ed,John Wiley and Sons, New York.

- -Oliveira Armando, and Jorge Facao,2000, *Thermal Behavior of Closed Wet Cooling Towers for Use With Chilled Ceilings*, Applied Thermal Engineering, Vol. 20, pp (1225-1236).
- Oliveira Armando, and Jorge Facao,2008, *Heat and Mass Transfer in an Indirect Contact Cooling Tower: CFD Simulation and Experiment*, Numerical Heat Transfer, Part A,Vol. 54, pp (933-944).
- Shim Gyu-Jin, Serker M. M. A,Choon-Gun Moon,Ho-Saeng Lee,and Jung-In Yoon, ,2008,*Performance Characteristics of a Closed-Circuit Cooling Tower With Multi Path*, World Academy of Science, Engineering and Technology, Vol.2 pp(280-284).

- Shim Gyu-Jin, Serker M. M. A,Choon-Gun Moon,Ho-Saeng Lee,and Jung-In Yoon., ,2010,*Performance Characteristics of a Closed-Circuit Cooling Tower With Multiple Paths*, Heat Transfer Engineering , Vol.2 pp(992-997).
- Stabat Pascal, and Dominique Marchio, 2004, *Simplified Model for Indirect-Contact Evaporative Cooling-Tower Behavior*, Applied Energy, Vol. 78, pp (433-451).
- Yingghan Li, You Xinkui, Qiu Qi and Jiezhi Li, 2011,*The study on the Evaporation Cooling Efficiency and Effectiveness of Cooling Tower of Film Type*, Energy Conservation and Management, 52 pp (53-59).
- Zheng Wei-Ye, Dong-Sheng Zhu, Jin Song, Li-Ding Zeng and Hong-Jian Zhou,2012, *Experimental and Computational analysis of Thermal Performance of Oval Tube Closed Wet Cooling Tower*, Applied Thermal Engineering, 35 pp (223-239).

NOMENCLATURE

A=total heat transfer area, m^2
Cp=specific heat at constant pressure, kJ/kg ^oC
D=tube diameter, m
CR=cooling range, ^oC
G=mass flux , $kg/m^2.s$
i=specific enthalpy, kJ/kg
k=thermal conductivity, W/m ^oC
$\dot{m}$=mass flow rate, kg/s
q=cooling capacity, W
Q=volume flow rate, l/min
Pr=Prandtl number
R=tube radius, m
Re=Reynolds number
T=temperature , ^oC
U_o=overall heat transfer coefficient, $W/m^2\ ^oC$

GREEK SYMBOLS

α_m= mass transfer coefficient for water vapour, between spray water film and air, kg/m^2 s
α_s =heat transfer coefficient between tube external surface and spray water film, W/m^2 ^{o}C
α_c =heat transfer coefficient for water inside the tubes, W/m^2 ^{o}C
η = thermal efficiency,(%)

SUBSCRIPTS

a=air
cw=cooling water
in=inlet
m=mean
out=outlet
sw=spray water
t=tube

Table 1. Physical dimension of heat exchangers.

Heat exchanger configuration	value		Unit
	Inline	staggered	
Length	680	690	mm
Height	190	166	mm
Width	381	381	mm
Tubes for coil	32	30	-
Vertical tube spacing	47.64	24	mm
Horizontal tube spacing	47.64	80	mm
Tube per row	8	5	-
Outside tube diameter	15.88	15.88	mm
Tube thickness	0.81	0.81	mm
Total eat transfer area	1085573.57	1032691.77	mm^2
Minimum free flow area	175310	209148	mm^2

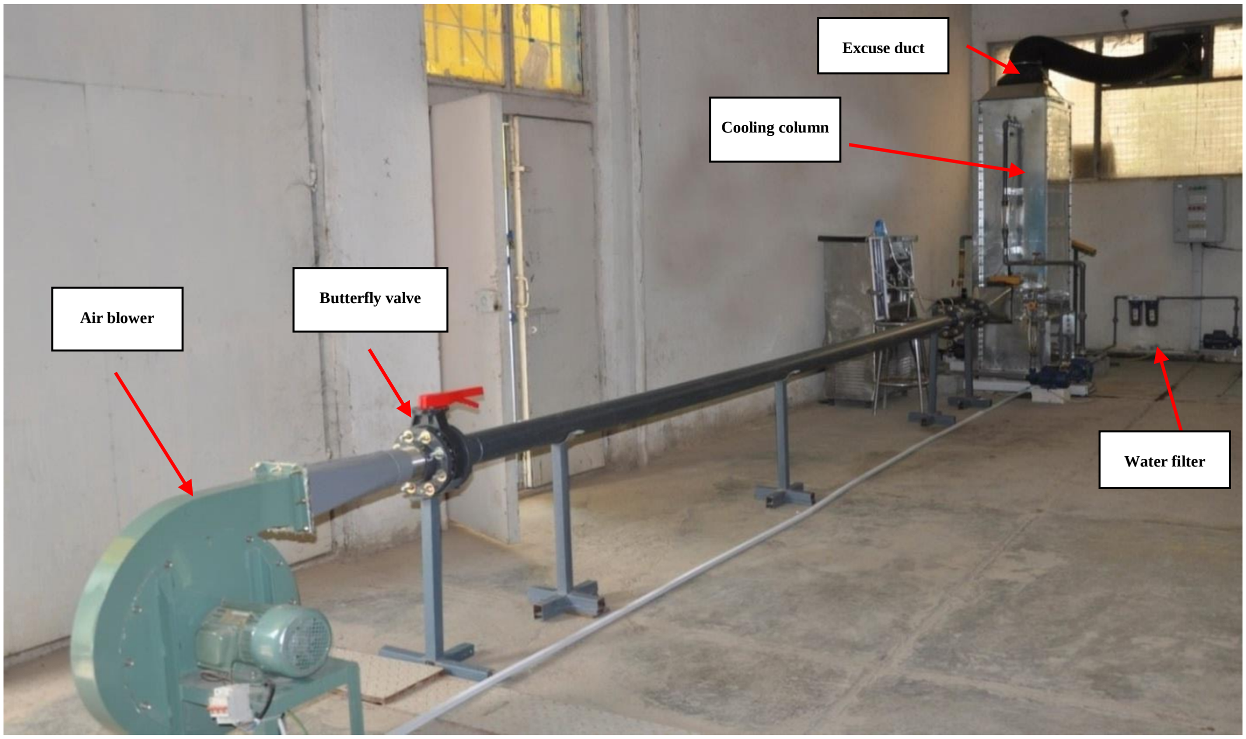

Figure 1a. Photographic picture for experimental apparatus (lateral view).

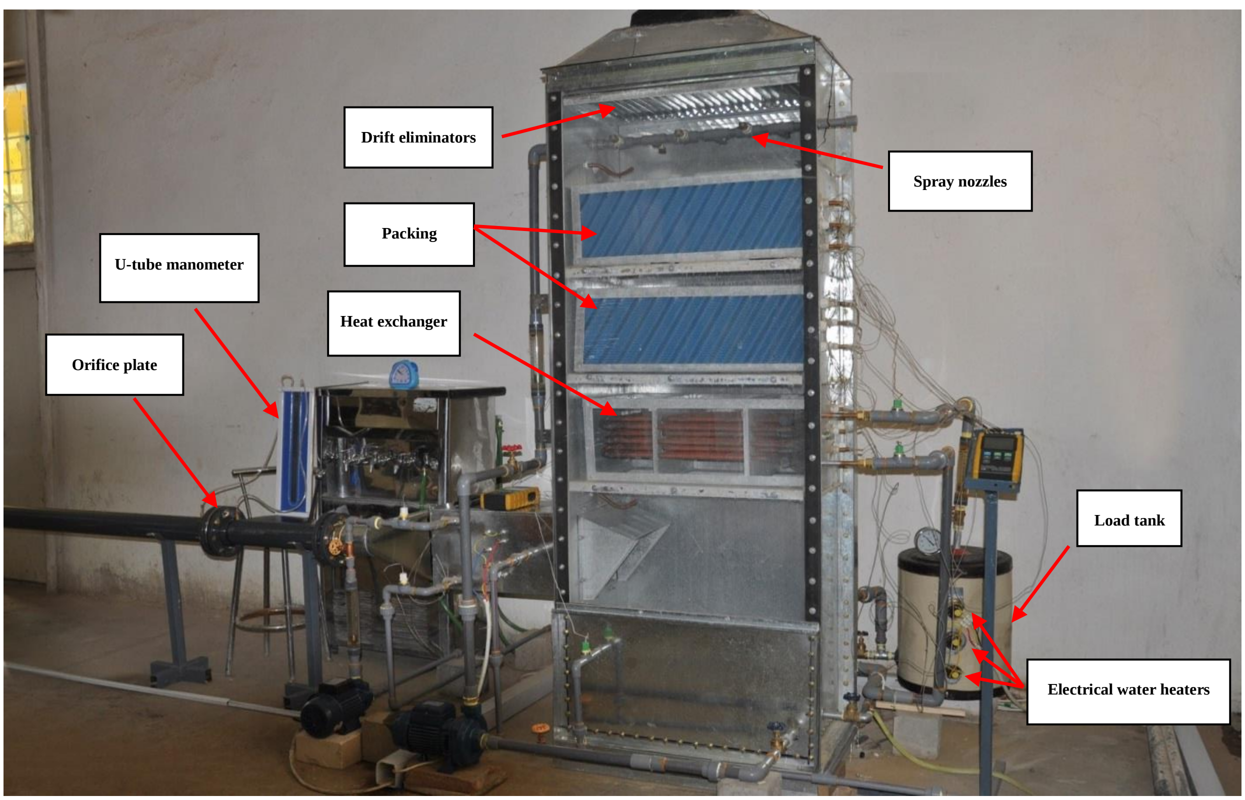

Figure 1a. Photographic picture for experimental apparatus (lateral view).

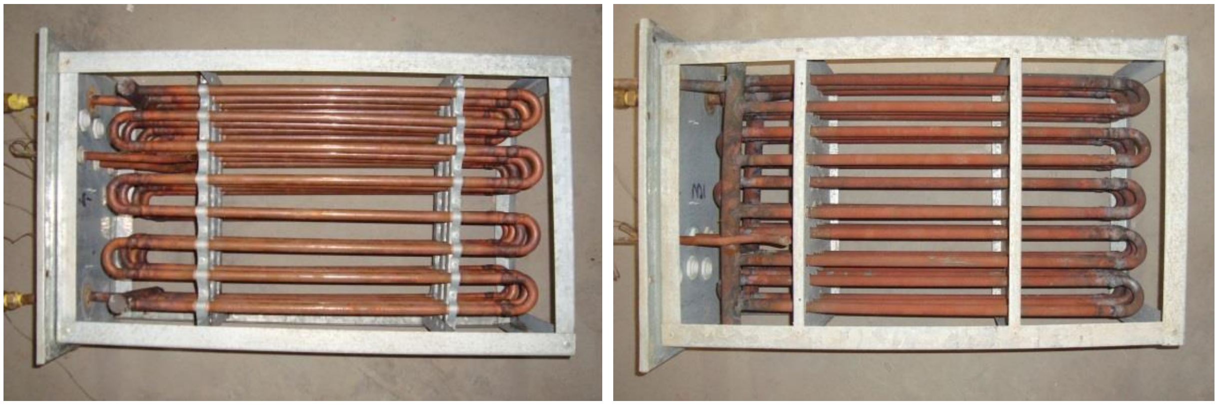

(a) (b)

Figure 2. Arrangement of tubes ;(a) inline arrangement, (b) staggered arrangement.

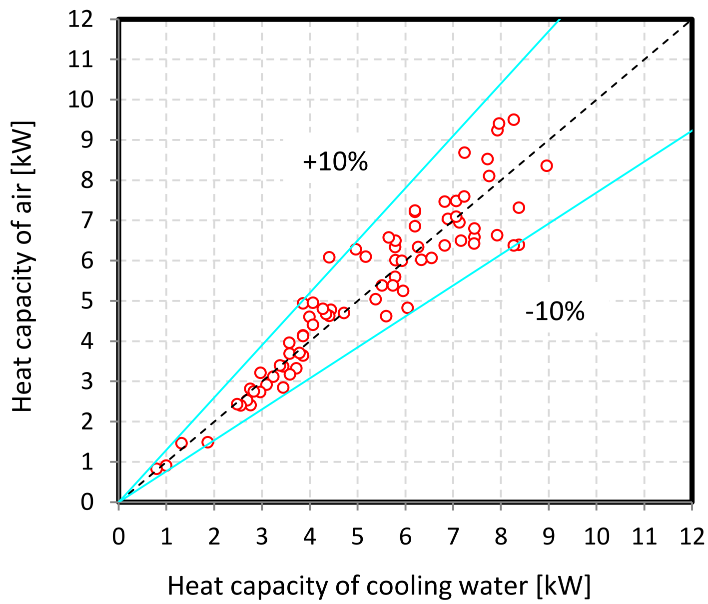

Figure 3. Energy balance of the experimental apparatus.

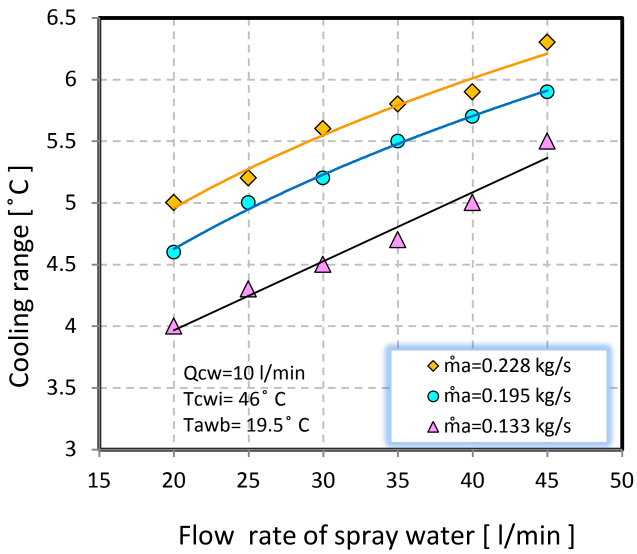

Figure 4. Variation of cooling range with spray water flow rate for different air flow rates.

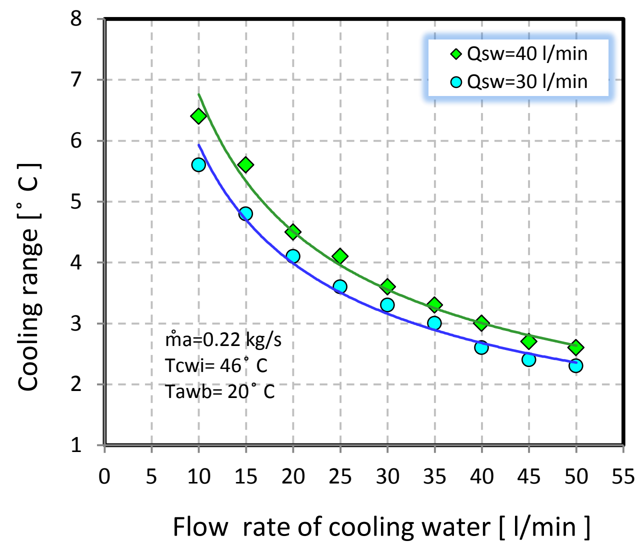

Figure 5. Variation of cooling range with cooling water flow rate for different spray water flow rates.

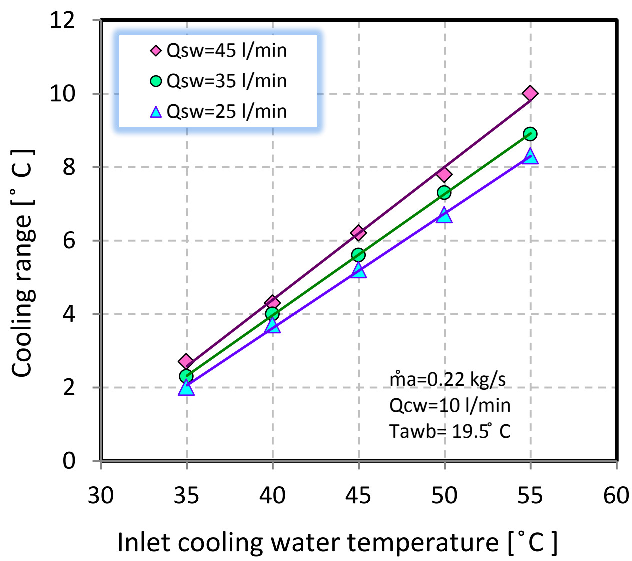

Figure 6. Variation of cooling range with inlet cooling water temperature for different spray water flow rates.

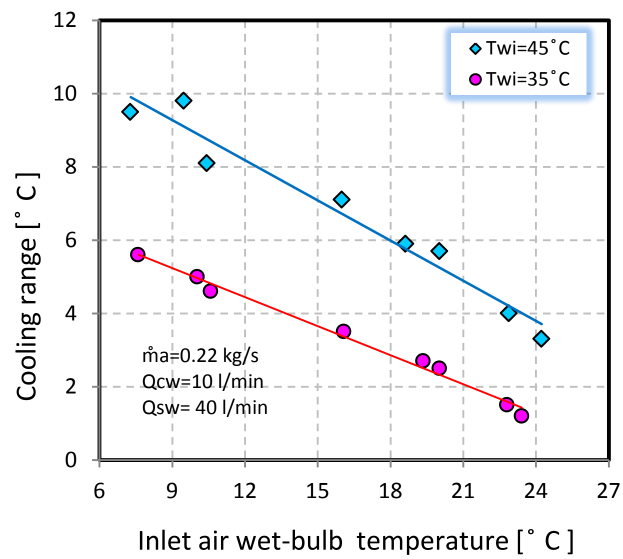

Figure 7. Variation of cooling range with inlet AWBT for different inlet water temperatures.

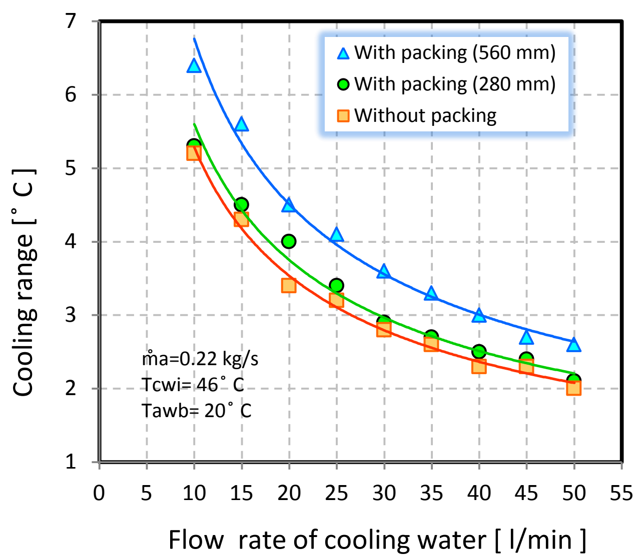

Figure 8. Variation of cooling range with cooling water flow rate for different heights of packing.

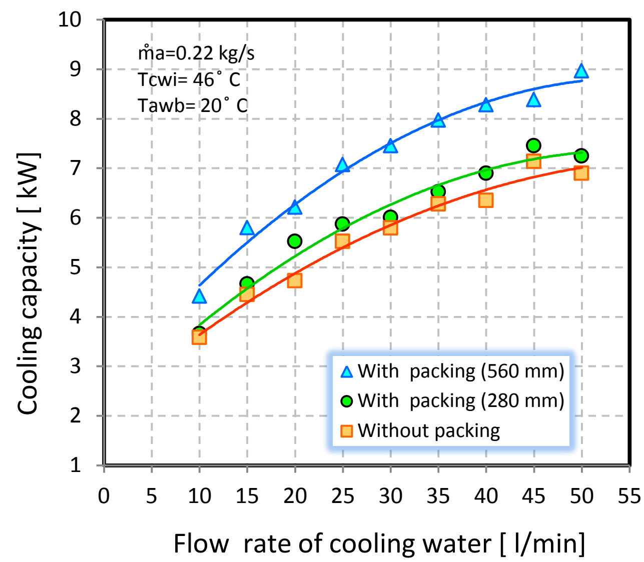

Figure 9. Variation of cooling capacity with cooling water flow rate for different heights of packing.

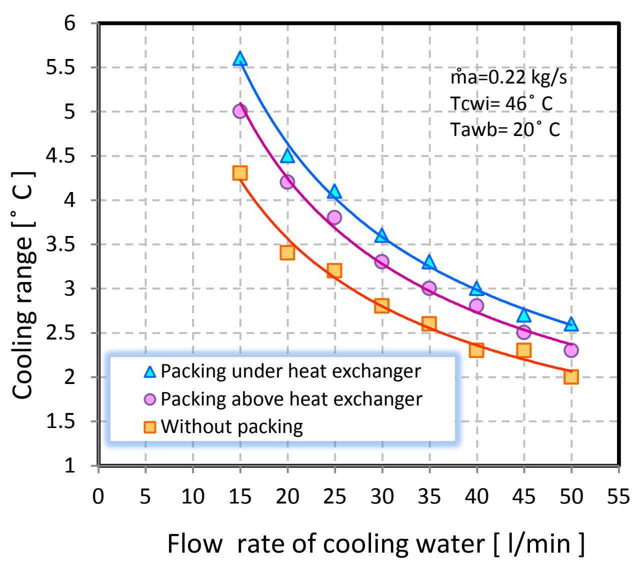

Figure 10. Variation of cooling range with cooling water flow rate for different locations of packing.

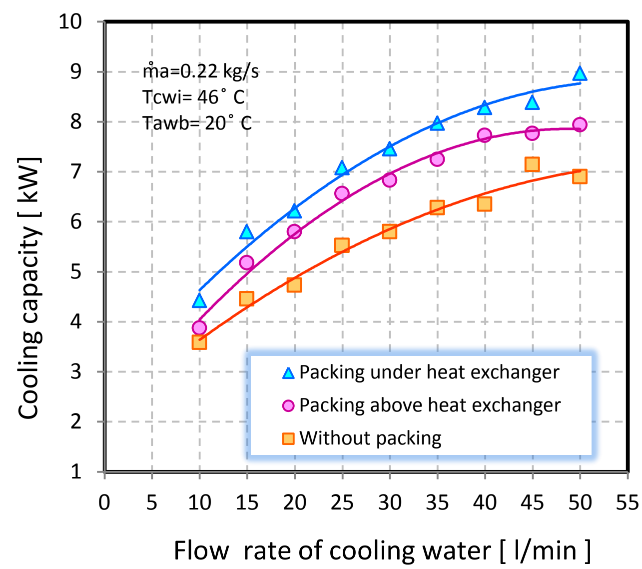

Figure 11. Variation of cooling capacity with cooling water flow rate for different locations of packing.

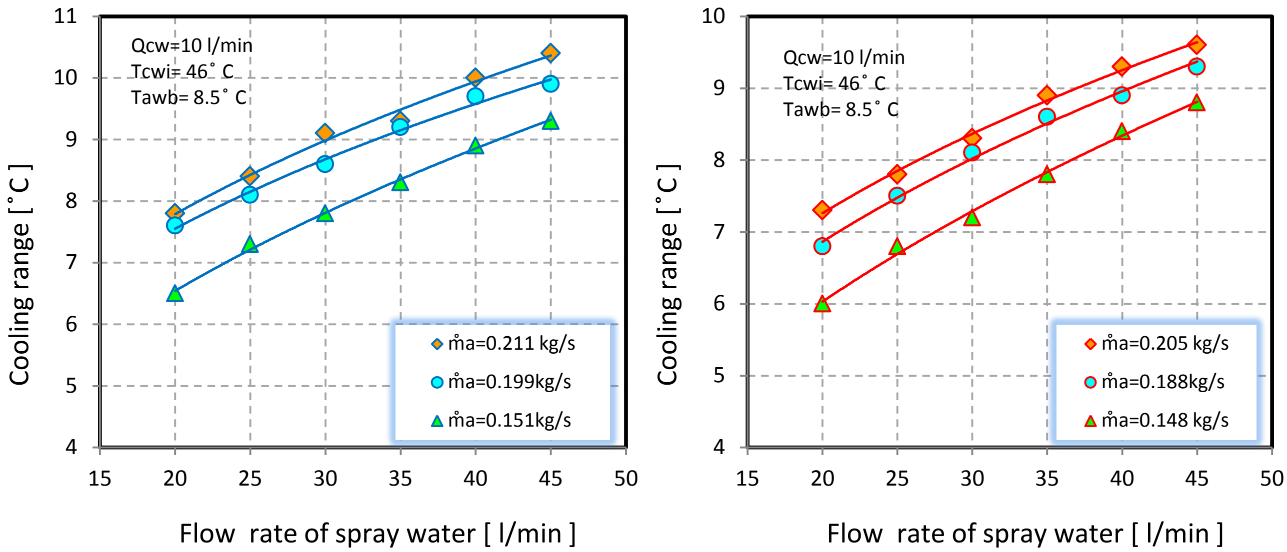

(a) (b)

Figure 12. Variation of cooling range with spray water flow rate for different air flow rates: (a) Inline arrangement, (b) Staggered arrangement .

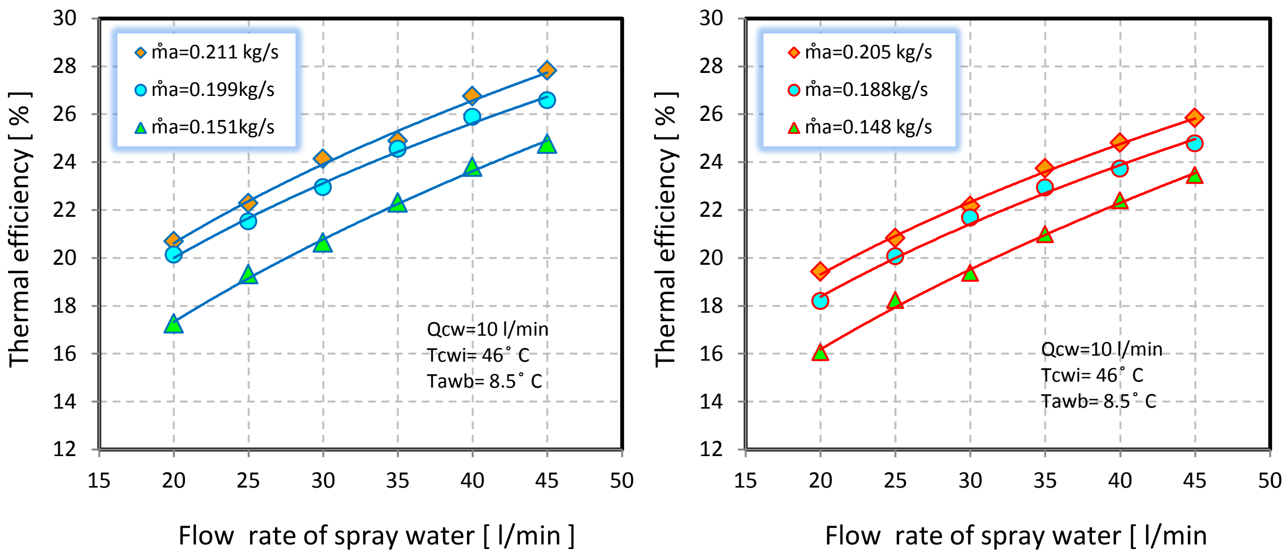

(a) (b)

Figure 13. Variation of thermal efficiency with spray water flow rate for different air flow rates: (a) Inline arrangement, (b) Staggered arrangement.

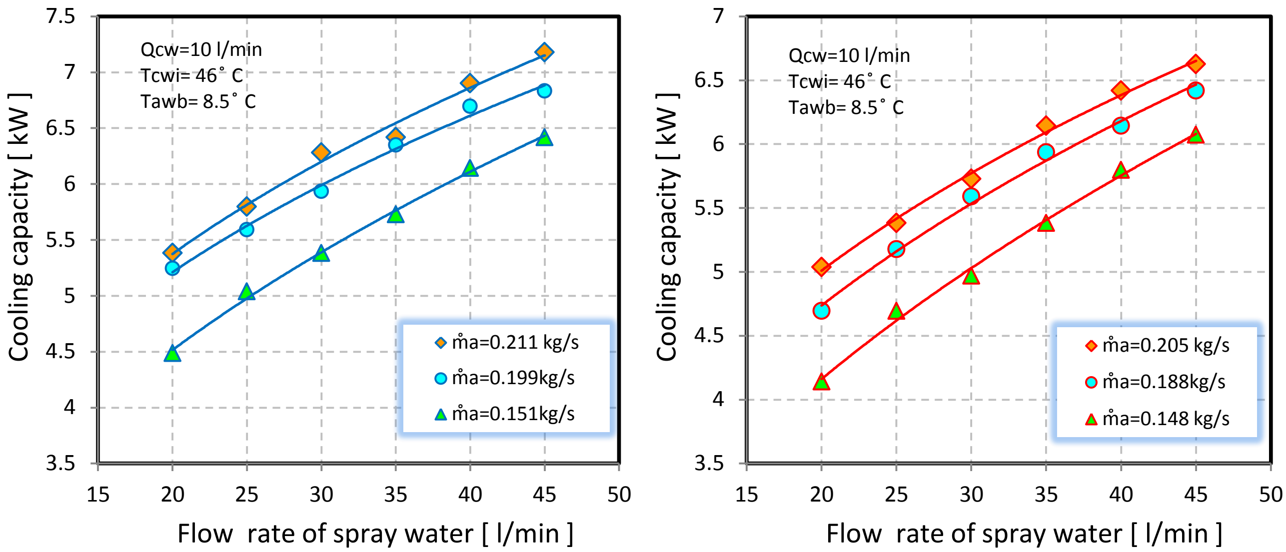

(a) (b)

Figure 14. Variation of cooling capacity with spray water flow rate for different air flow rates: (a) Inline arrangement, (b) Staggered arrangement.

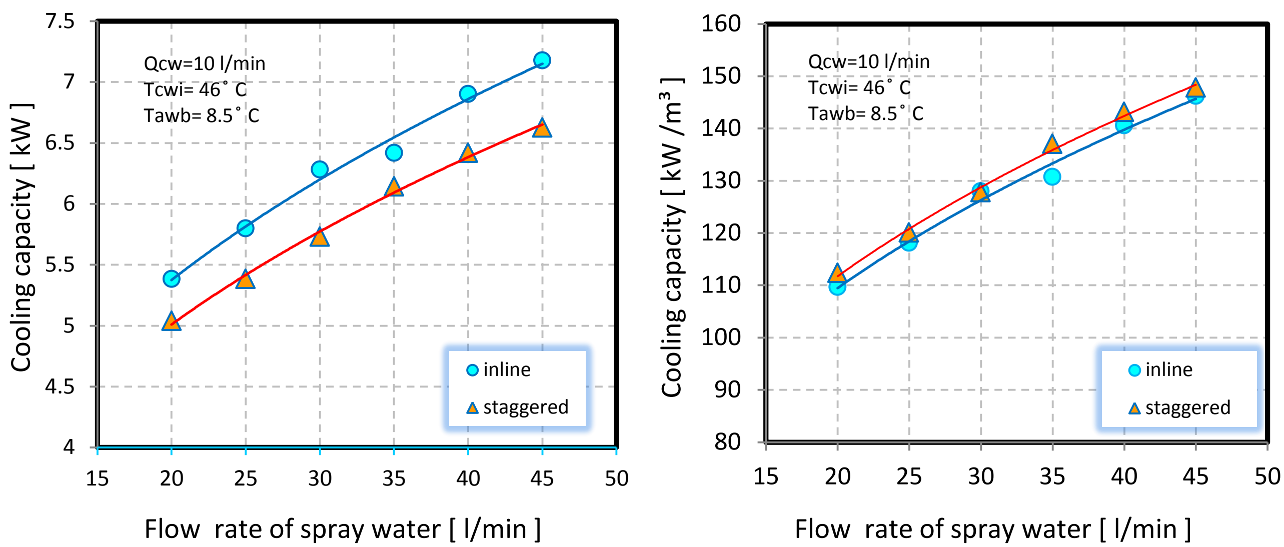

(a) (b)

Figure 15. Variation of cooling capacity with spray water flow rate for different tubes arrangements: (a) Cooling capacity in kW, (b) Cooling capacity per unit volume kW/m^3.

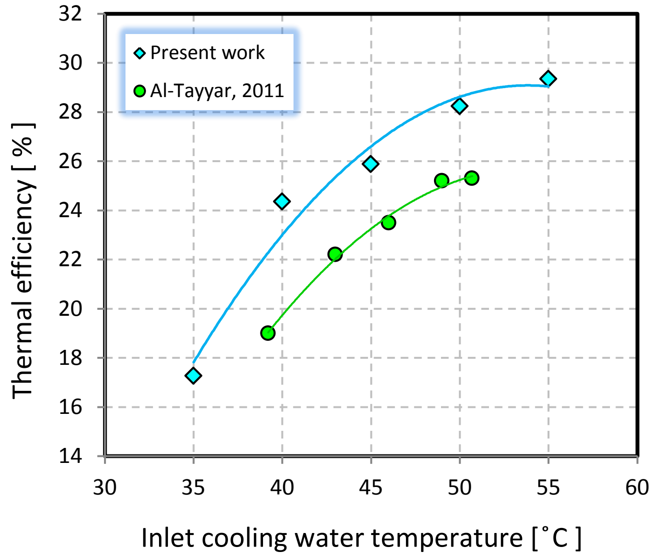

Figure 16. Comparison of the concluded effect of inlet cooling water temperature on thermal efficiency with other works.

The Effective of Pressure and Sintering Temperature for Hardness Characteristics of Shape Memory Alloy by Using Taguchi Technique

Asst prof. Ahmed Abdulrusool
Department of Mechanical Engineering
Collage of Engineering
University of Baghdad
Email:aa.alkhafaji@yahoo.com

Sarah Jalal Mosa
Department of Mechanical Engineering
Collage of Engineering
University of Baghdad
Email:sarah.aljaf92@yahoo.com

ABSTRACT

This paper presents the Taguchi approach for optimization of hardness for shape memory alloy (Cu-Al-Ni) . The influence of powder metallurgy parameters on hardness has been investigated. Taguchi technique and ANOVA were used for analysis. Nine experimental runs based on Taguchi's L9 orthogonal array were performed (OA),for two parameters was study (Pressure and sintering temperature) for three different levels (300 ,500 and 700) MPa ,(700 ,800 and 900)^{o}C respectively . Main effect, signal-to-noise (S/N) ratio was study, and analysis of variance (ANOVA) using to investigate the micro-hardness characteristics of the shape memory alloy .after application the result of study shown the height hardness at the level 2 of pressure and level 1 of temperature (A_2B_1) by taguchi technique at magnitude value 500MPa and 700 ºC. The best effective factor at ANOVA has pressure 36.39%. the interaction given the best pressure 500 MPa and Temperature 800 ºC.

Keywords :shape memory alloy , Cu-Al-Ni , taguchi method , optimization, powder metallurgy , hardness.

تأثير الضغط ودرجة حرارة التلبيد على الصلادة لسبيكة ذكية باستخدام تقنية تاكوشي

أ.م.د.أحمد عبد الرسول
قسم الهندسة الميكانيكية
كلية الهندسة /جامعة بغداد

سارة جلال موسى
قسم الهندسة الميكانيكية
كلية الهندسة /جامعة بغداد

الخلاصة:

هذا البحث بين استخدام طريقة تاكوشي للوقوف على امثلية الصلادة لسبيكة ذكية وتضمن المتغيرات المؤثرة على صلادة نماذج مصنعة بطريقة ميتالورجيا المساحيق.تقنية تاكوشي و تحليل التباين, استعملت في عملية تحليل تسع عينات تمت تصنيعها اعتمادا على خوارزمية تاكوشي لمتغيرين اساسين للدراسة (ضغط ودرجة حرارة التلبيد) لثلاث مستويات مختلفة (300,500and 700) Mpaودرجة حرارة التلبيد (700,800 and 900) ºC على التوالي تم دراسة تأثير العامل الرئيسي ونسبة الضوضاء وكذلك تمت تحليل التباين للصلادة المايكروية للسبيكة الذكية.نتائج الدراسة بينت بعد التطبيق ان اعلى صلادة كانت في (A_2B_1)اي عند المستوى الثاني للضغط والمستوى الاول للحرارة وكانت قيمة الضغط 500Mpaوحرارة التلبيد 700 ºC تحلل التباين بين ان افضل عامل مؤثر هو الضغط بنسبة 36.39 % .العامل المؤثر ضمن مستويات مختلفة(interaction) بينت ان افضل ضغط 500MPa ودرجة حرارة التلبيد 800 ºC.

الكلمات الرئيسية: سبائك ذكيةCu-Al-Ni, , طريقة تاكوشي, امثلية , ميتالورجيا المساحيق , الصلادة.

1. INTRODUCTION

During the past years, smart materials and structures have received increasing attention because of their great scientific and technological significance **,Wezz, et al.,1998.**Shape memory alloys are the most important branch from the smart and /or intelligence materials**,Noecker,2004 .**Smart materials and their technologies are still in the beginning stages of the implementation phase even though they have undergone extensive research, especially during the last two decades ,**Dunn, et al., 1999.** Shape memory materials (SMMs) are smart materials that "remember" their original shapes **, Huang, et al .,2010**.Some shape memory alloys (SMAs) when exposed to plastic deformation, it returns to their original shape when heated. These unusualeffects are called a thermal shape memory alloys and super elasticity (elastic shape memory). Both effects depend on the occurrence of aspecific type of phase change known as thermoelastic martensitic transformation **,Otsuka .,et al., 2002.**The shape memory alloys have two stable phases: the high–temperature phase, called austenite and the low–temperature phase, called martensite as shown in **Fig .1, Kneissl,et al.,2000.**The austenite phase is characterized by a cubic crystal structure ,while the martensite phase has a monoclinic (orthorhombic) crystal structure, shape memory applications as hydraulic couplings, force actuators as fire safety valves, proportional control as fluid flow control valve

2. THE TAGUCHI METHOD

In this work, analysis based on the Taguchi method is performed by utilizing the Minitab software to estimate the significant factors of the P/M process parameters on shape memory alloy . Taguchi’s orthogonal array is highly functional design, used to estimate main effects using few experimental tests only . These designs can investigate main effects when factors have more than two levels. In Taguchi method, the analysis of variation is performed using Signal – to – Noise ratio (S/N). There are three S/N ratio approaches of common interest for optimization **,Wen, ,2008.**

1. Smaller – the better (for making the system response as small as possible).
2. Larger – the better (for making the system response as large as possible).
3. Nominal – the best (for reducing variability around the target).

In this work, the objective is to maximize the P/M parameter. Therefore, the S/N ratio for each experiment of L9 calculated using larger- the better approach. The objective of using S/N ratio as a performance measurement is to develop a product and process insensitive to noise factor. In Taguchi method, the term “signal” represents the desirable value (mean) for the output characteristic, and the where *n* is the number of experiments in the orthogonal array andy_i the i^{th} value measured.term “noise” represents the undesirable value (square deviation) for the output characteristic . Therefore, the S/N ratio is the ratio of the mean to square deviation.
S/N ratio of the overcut can be calculated by **Taguchi, et al.,2000.**

$$S/N = -10\log\left[\frac{1}{n}\sum_{i=1}^{n}\frac{1}{y_i^2}\right] \quad (1)$$

Where: Yi: is the ith observed value of the response.
(n: number of observations).
S/N ratio is used to measure the quality characteristic deviating from the desired value.

3. EXPERIMENTAL PROCEDURE

The test samples are produced using powder metallurgy of Cu , Al , Ni powders , which consist of mixing , compacting and sintering processes . Copper powder with 99.9% purity (-325 mesh), nickel powder with 99.9% purity(-325 mesh) and aluminum powder with 99.9%purity (-325mesh)respectively were imported from Sky Spring Nanomaterials, Inc. USA used to prepare samples of the master alloy with a composition of (83% Cu weight 13%AL weight and 4% Ni weight as shown in **Table 1**. These powders were weighed accordingly and placed into cylindrical containers which were then mixed in a horizontal barrel mixer as shown in **Fig.2** . These elements were put into a glass cylindrical container which is 50% filled and 1% (acetone) was added in order to get better properties as lower friction at compaction and increase the segregation and prevent the separation of the components (since there is a difference in the densities) . Alumina balls for assisting the segregation has not been used in order to prevent the milling process and contamination of powder , the speed of rotating drum was set to 80 rpm and the time of mixing was 6 hour . Samples from powder were prepared in the same die with a cross section of 14 mm in diameter and approximately 5 mm length in average. The samples were pressed at (300MPa , 500MPa and 700MPa) in a 100 ton Hydraulic computerized press Machine as shown in **Table.2**. **Fig.3** shows samples from each composition after sintering in an electrical tube furnace supplied with a quartz tube and vacuum equipment as shown in **Fig.4** in order to get a fine samples without cracks or defect ,Two stage sintering has been implemented since there is difference in melting point of the alloy components and to prevent the appearance of liquid phase sintering. The first stage is to sinter the sample at 500ºC for 1 hour and followed by the second stage which is raising the temperature to (700 ºC) with soaking time of 5 hour then leaving the sintered sample to cool in furnace. A heating rate of 20ºC/min was maintained for the first stage and 20ºC/min for the second stage. The vacuum pressure was always allowed to reach $3x10^{\wedge -6}$ bar before sintering and during the whole sintering process and cooling. The dual stage vacuum pump is allowed to run for the entire sintering time to suck the harmful gases which will be produced during the diffusing of particles which might effect the sintering efficiency .After sintering , all sample have been quenched to get ß phase(shown the ß phase by X-Ray diffraction) which is AlCu3 (martensite) by heating the sintered sample to 800 ºC and holding it at this temperature for 1 hour then rapidly quenched into iced water . After the quenching process, an ageing heat treatment is implemented to stabilize the ß phase by heating the sample to 100ºC and holding at this temperature for 2 hour**.**The quenching and ageing process was also implemented in vacuum atmosphere to prevent the oxidation **.**Vickers micro hardness testing has been carried out on allsamples,the device shown in **Fig.5** . More than three values of hardness for each sample have been taken to get the mean value represents hardness.

4. RESULTS AND DISCUSSION

The results, in terms of average micro-hardness were obtained after conducting the hardness test for all nine sample . Each test sample , indeed represented one experiment in the orthogonal array **Table 3.** The experimental results for hardness test in **Table 4**. In the latter, the results were analyzed using main effects, ANOVA, and the signal-to noise ratio (S/N) analyses. **Fig. 6 (a ,b ,c)** shows four x-ray charts for samples with different sintering temperature(700 ,800,900)^{o}C samples respectively the result peaks was compared with the standard cards with the possible known phases which will be appear. All samples have shown the martensite phase after quenching which indicate no effect of pressure and sintering temperature to the martensite phase (AlCu3).

4.1 Main Effects

The average value of micro-hardness for each factor pressure and sintering temperature (A and B) at each level (level 1, level 2 and level 3) was obtained and the result is summarized in **Table 6**. It can be seen from **Fig.(7,8)** that the combination of parameters and their levels A_2B_1 yield the optimum quality characteristic. the other capability for ANOVA analysis its present to the effect of one parameter for any level (interaction). **Fig.9** shows that for the case under study the best parameter are (500 MPa and 800 ^oC). **Fig. 10** shows the Vickers micro hardness with different pressure and sintering temperature.

4.2 Signal-to-Noise Ratio (S/N Ratio)

The program (MINTAB 16.1) calculates the S/N ratio for each level of each variable by using Eq.(1). The results are shown in **Table 5.** According to **Figs.7 and 8,** second level of pressure (A), first level of sintering Temperature (B) are optimal levels in this test. They have highest S/N ratios.

4.3 Analysis of Variance (ANOVA)

The parameters which significantly affected the hardness were investigated using the analysis of variance (ANOVA). The contribution percentage of different parameters on Cu-Al-Ni as obtained by ANOVA are presented in **Table 7** and it can be seen from this Table that the pressure (A), and sintering temperature (B) affect hardness by 36.39% and 4.19% in the shape memory alloy respectively.

5. CONCLUTION

On the basis of the results obtained from the present case study the following points can be concluded:

- The combination of parameters and their levels for optimum micro-hardness and also for shape memory alloy Cu-Al-Ni is A_2B_1(pressure 500 MPa and temperature 700°C) .
- The contribution of pressure and temperature to hardness of shape memory alloy are 36.39% and 4.19% respectively.
- The value obtain from correlation between process parameters and hardness by using an optimum parameter combination (A_2B_1) was consistent with maximum hardness obtained by using the analysis of S/N ratios.
- The X-ray diffraction shown the AlCu3 (martensite) which indicate no effect of pressure and sintering temperature to the martensite phase
- from the ANOVA table ,pressure is the most significant parameter for minimum micro hardness
- This research gives how to use Taguchi's parameter design to obtain an optimum condition with lowest cost , therefore minimum number of experiments is required for industrial applications.

REFRNCES

- Dunn, Kerry A., McIntyre R. LouthanJr, Natraj C. Iyer, Victor Giurgiutiu, Michael F. Petrou, and Dorothy E. Laub. ,*Application of smart materials/technology at the Savannah River site.*, In 1999 Symposium on Smart Structures and Materials, pp. 64-75. International Society for Optics and Photonics, 1999.

- Huang, W. M., Z. Ding, C. C. Wang, J. Wei, Y. Zhao, and H. Purnawali.,*Shape memory materials,Materials today* 13, no. 7 (2010): 54-61.

- Kneissl A. C. , Unterweger E., and Bruncko M., , *Microstructure and Properties of NiTi And CuAlNi Shape Memory Alloys* , Association of Metallurgical , *Engineers of Serbia/ Metalurgija - Journal of Metallurgy/ 611.314:669,2000.*

- Otsuka, Kazuhiro, and TomoyukiKakeshita. ,*Science and technology of shape-memory alloys: new developments.,Mrs Bulletin* 27, no. 02 (2002): 91-100.

- Mel Schwartz ,2002 , *Encyclopedia of materials, parts and finishes*, second edition, ASM handbooks by CRC Press LLC.

- Noecker,R. , 2004, *Shape memory materials , martensitic structures, metallography and microstructure* , Vol.9,ASM Hand book , ASM international .

- -Taguchi G. and et al, “Robust engineering”, New York, McGraw – Hill, 2000.

- WEZ,Z.G.,Sandstrom ,R.andMiyazaki,S., 1998,*Review Shape memory materials and hybrid composites for smart systems*, J.Nat. Scie.33,pp.3743-3762.

- -Wen-Hsien Ho , *Adaptive network-based fuzzy interface system for prediction of surface roughness in end milling process using hybrid Taguchi-genetic learning algorithm*, Expert Systems with applications, 2008.

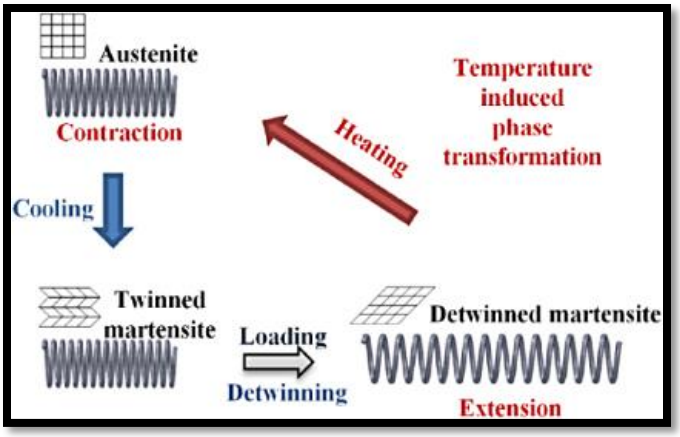

Figure 1. Phases of a shape memory alloy**, Mel Schwartz,2002.**

Figure 2. Horizontal barrel mixer.

Figure 3. Sintered samples after grinding and polishing

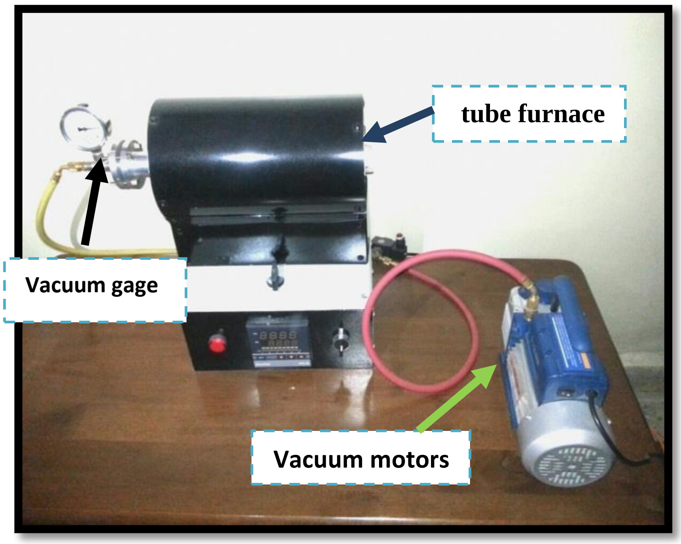

Figure 4. Electrical tube furnace.

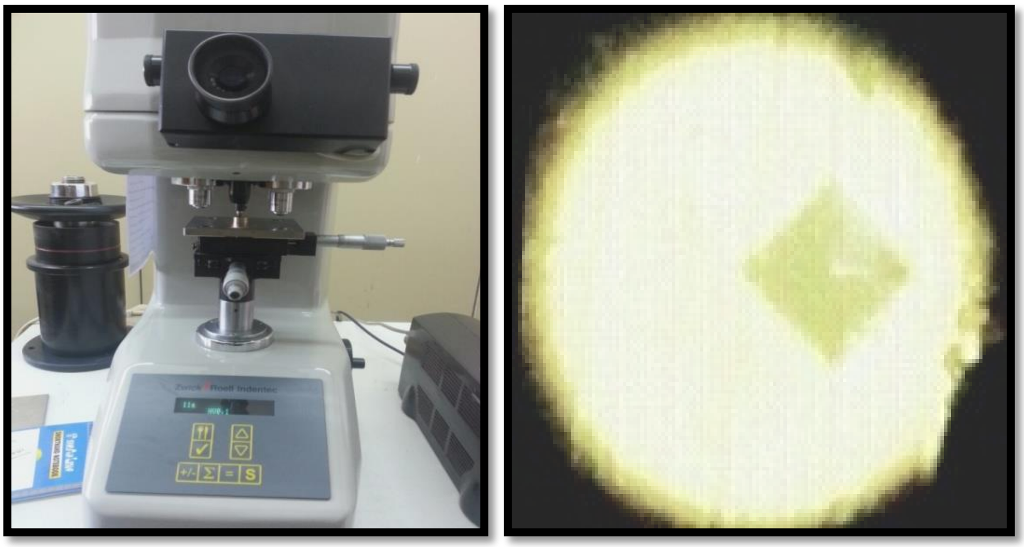

Figure 5. Micro-hardness device.

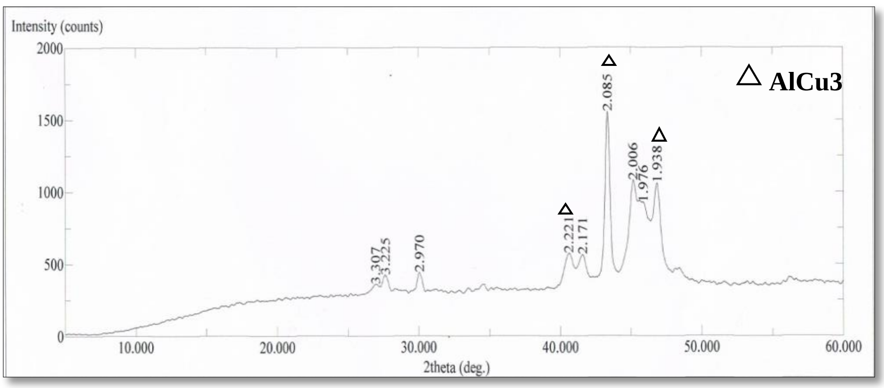

a

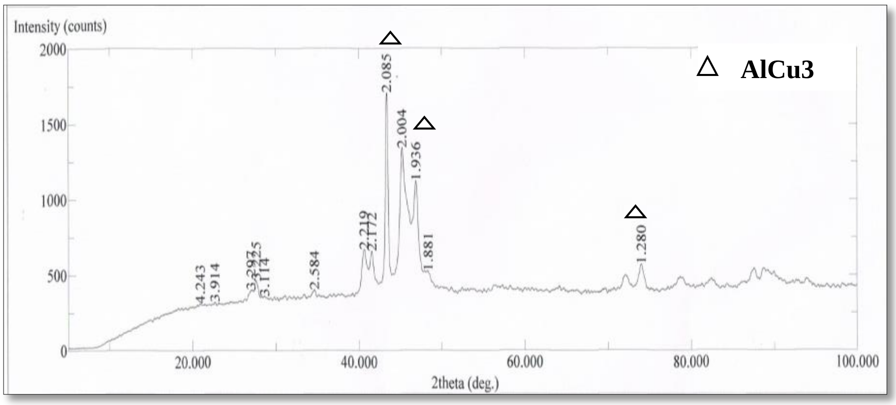

b

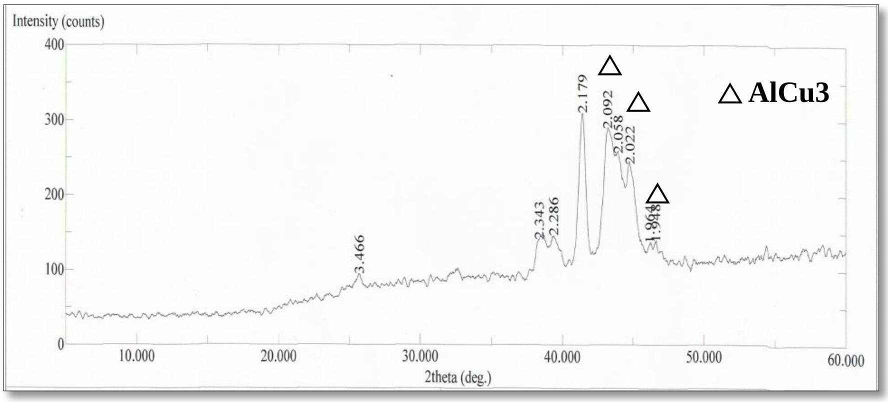

c

Figure 6. (a,b,c) X-ray diffractions.

Table 1. Notation for sample with alloying element.

Powder element	**Copper**	**Aluminum**	**Nickel**
Weight percentage	83%	13%	4%

Table 2 . Shape memory alloys parameters and their levels.

Factors	**Factors Code**	**Levels**		
		1	**2**	**3**
Pressure(MPa)	**A**	300	500	700
Temperature(˚C)	**B**	700	800	900

Table 3.Experimental plan using *L*9 orthogonal array.

Parameter / Level		
Experiment number	**Code No.for pressure (A)**	**Code No.for temperature (B)**
1	1	1
2	1	2
3	1	3
4	2	1
5	2	2
6	2	3
7	3	1
8	3	2
9	3	3

Where : A=Pressure(MPa),B=Temperature(^{o}C)

Table 4. Experimental results for micro-hardness test.

Exp. No	(A)	(B)	Average microhardness (HV)
1	300	700	137.66
2	300	800	114
3	300	900	116
4	500	700	135
5	500	800	166
6	500	900	133.66
7	700	700	148
8	700	800	123
9	700	900	148.33

Table 5. S/N ratio response for micro hardness test.

Experiment no.	Average Micro hardness (HV)	S/N ratio
1	137.66	42.77
2	114	41.13
3	116	41.28
4	135	42.60
5	166	44.40
6	133.66	42.52
7	148	43.40
8	123	41.79
9	148.33	43.42

Table 6. Levels average for main effects.

Average S/N Ratio					
Factors	**Level 1**	**Level 2**	**Level 3**	**Delta**	**Rank**
A	41.73	43.18	42.88	1.45	1
B	42.93	42.44	42.41	0.52	2

Where : A=pressure(MPa),B=temperature(^{o}C).

For Factor (A) for S/N ratio

(S/N) ratioA_1 = ((42.77+41.13+41.28)/3)

(S/N) ratioA_1 = (125.18/3) = 41.73

(S/N) ratioA_2= ((42.60+44.40+42.52)/3)

(S/N) ratioA_2 = (129.52/3) = 43.18

(S/N) ratioA_3= ((43.40+41.79+43.42)/3)

(S/N) ratioA_3 = (128.61/3) = 42.88

The same procedure for factor B
Delta =Max-Min

Delta=43.18-41.73=1.45 for factor A

Delta =42.93-42.41=0.52 for factor B

Table 7. Analysis of variance (ANOVA) table for the S/N ratio of hardness.

Where : A=pressure(MPa),B=temperature(^{o}C)

Source	Degree of freedom (DOF)	Sum of Squares (SS)	Mean Square (MS)	Model F-Value	Percentage Contribution, (%)
A	2	821.5	410.8	1.22	36.39%
B	2	94.5	47.3	0.14	4.19%
Error	4	1341.6	335.4		59.42%
Total	8	2257.6			

Total Degree of Freedom (DOF_T)= $n-1$

Where:n = *Number of experiments.*

Degree of Freedom of Factor A (DOF_A) = NO. of levels – 1

Degree of Freedom of Factor B (DOF_B) = NO. of levels – 1

Degrees of freedom of error($\mathbf{DOF}_e$)=DOF_T–DOF_A–DOF_B

Where: DOF_A=Degree of Freedom of factor pressure , DOF_B=Degree of Freedom of factor temperature

$$\hat{Y} = \sum_{i=1}^{n} \mathbf{Y_i} / \mathbf{n}$$

Where: $\hat{Y}$ = the average value of Yi.

$$SS_T = \sum_{i=1}^{n} (\mathbf{Y_i} - \hat{Y})^2$$

Where: SS_T = Total *sum of squares, Y_i = Sum of all results***,** n = *Experiment number ,*

$\hat{Y}$= the average value of Yi

SS any Factor = $N1(x1-X)^2 + N2(x2-X)^2 + N3(x3-X)^2$

Where: $X = (x1+ x2 + x3) / 3$ and x1,x2,x3 are mean of parameter as per level,

N1,N2,N3= number of experiments at level A1,A2andA3.

$SS_e = SS_T - SS_{(For\ all\ Factors)}$

Where:SSe = Sum of square of error.

$MS_A = SS_A/\mathbf{DOF}_A$

Where: MS_A = *Mean squares (variance)* **for** *one of factor* ***A,***DOF_y= Degree of freedom of any factor.

$MS_e = SS_e/\mathbf{DOF}_e$

Where:MS_e = Mean squares *of* error,SS_e = *Sum of square of error terms*

$MS_T = SS_T/\boldsymbol{DOF}_T$

Where: MS_T = Total mean squares.

$F = MS_A/MS_e$

*Where:*F = Variance or fisher ratio

P Percentage of contribution = SS/SS_T

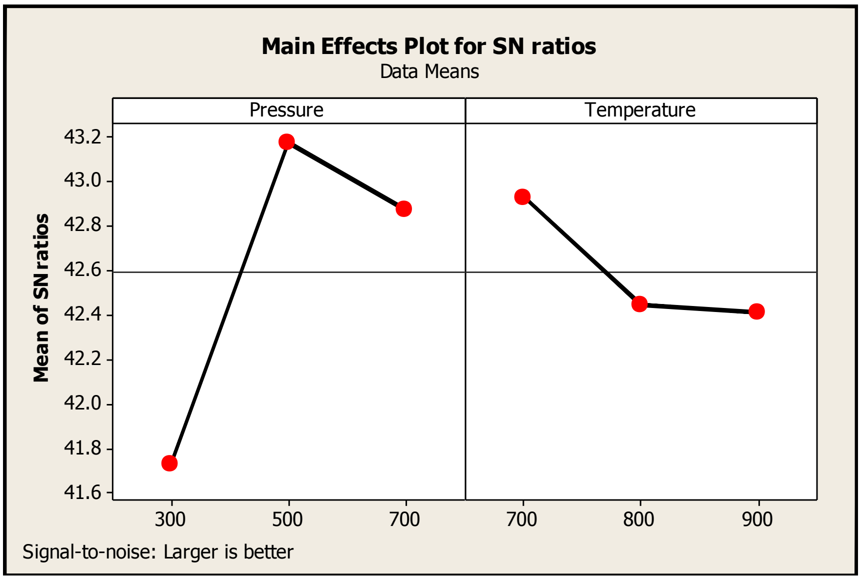

Figure 7. Main effects plot for S/N ratio.

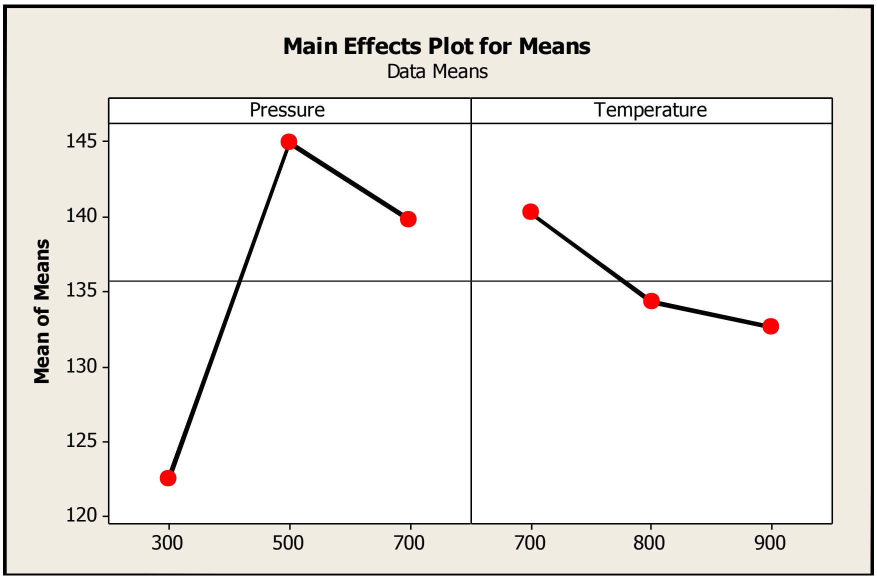

Figure 8. Main effects plot for means.

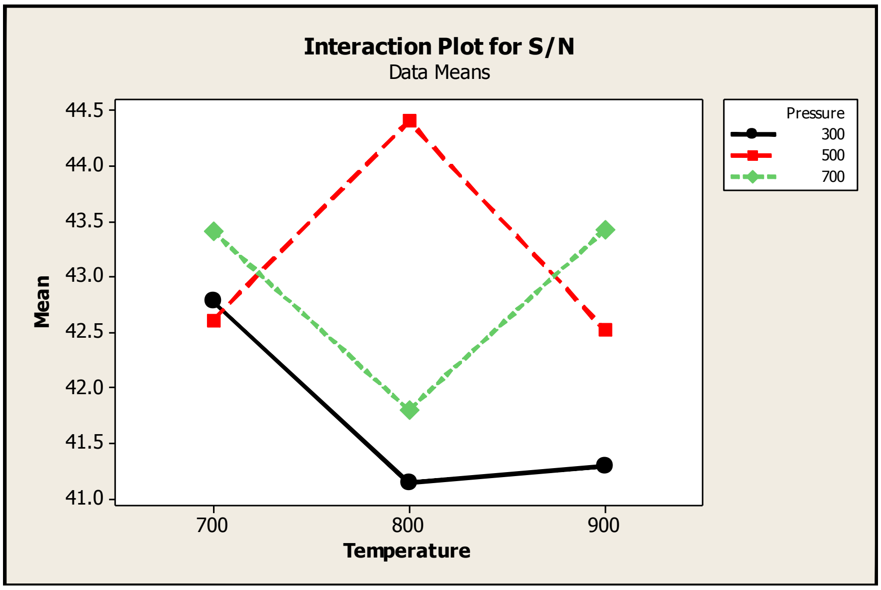

Figure 9. Interaction plot for S/N ratio (temperature and pressure).

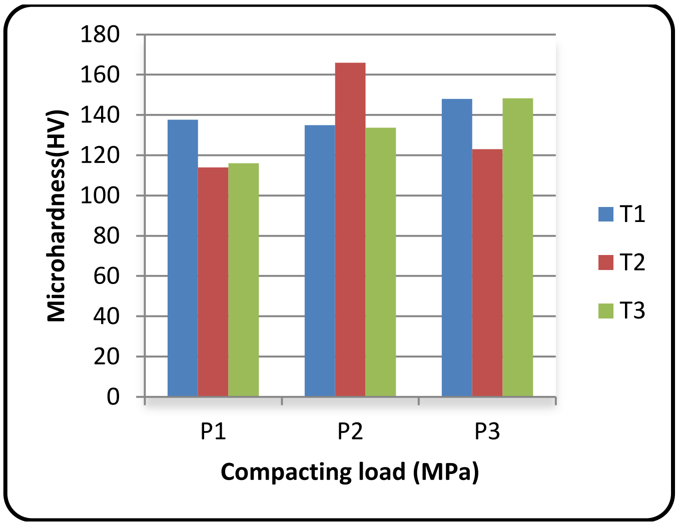

Figure 10. Vickers micro hardness.

Improve the Performance of PID Controller by Two Algorithms for Controlling the DC Servo Motor

Asst. Lect. Noor Safaa Abdul-Jaleel
Department of Electrical Engineering
College of Engineering
Al-Mustansyria University
E-mail: mail_ns1@yahoo.com

ABSTRACT

The paper uses the Direct Synthesis (DS) method for tuning the Proportional Integral Derivative (PID) controller for controlling the DC servo motor. Two algorithms are presented for enhancing the performance of the suggested PID controller. These algorithms are Back-Propagation Neural Network and Particle Swarm Optimization (PSO). The performance and characteristics of DC servo motor are explained. The simulation results that obtained by using Matlab program show that the steady state error is eliminated with shorter adjusted time when using these algorithms with PID controller. A comparative between the two algorithms are described in this paper to show their effectiveness, which is found that the PSO algorithm gives better results to improve the PID controller for controlling the DC servo motor compared to the neural network algorithm.

Keywords: - DC servo motor, direct synthesis, PID controller, neural network, particle swarm optimization (PSO).

تحسين اداء المسيطر التناسقي التكاملي التفاضلي باستخدام خوارزميتان للسيطرة على محرك تيار مستمر

م. م. نور صفاء عبد الجليل
قسم هندسة الكهرباء
كلية الهندسة / الجامعة المستنصرية

الخلاصة

يقدم هذا البحث طريقة (DS) في تحديد معاملات المسيطر التناسقي التكاملي التفاضلي للسيطرة على محرك تيار مستمر. حيث استخدمت خوارزميتين لتحسين اداء المسيطر التناسقي التكاملي التفاضلي هما: وحدة تحكم الشبكة العصبية وخوارزمية الحركة المثلى لاسراب الجسيمات. محرك التيار المستمر والخوارزميتان تم تمثيلهما باستخدام برنامج المحاكاة (Matlab), وقد تمت المقارنة بين الخوارزميتين لبيان تاثيرهم على المسيطر المقترح حيث اظهرت نتائج المحاكاة ان خوارزمية الحركة المثلى لاسراب الجسيمات اعطت نتائج افضل لتحسين اداء المسيطر المستخدم من حيث سرعة الاستجابة للسيطرة على محرك التيار المستمر بالمقارنة مع خوارزمية الشبكة العصبية.

• **الكلمات الرئيسية:** محرك تيار مستمر, التوليف المباشر, المسيطر التناسقي التكاملي التفاضلي, الشبكة العصبية, الحركة المثلى لاسراب الجسيمات.

1. INTRODUCTION

Direct current (DC) servo motor is essential in modern industries. Servo motors are not a specific group of motor, but the term servo motor is often used to refer to a motor suitable for use in a closed loop control system. Servo motors are used in different applications in industrial tools, control systems of computers, robotics, ect., **Dipraj**, and **Dr. A. K.**, **2012**. A lot of control methods are used with the servo motors, Akar, **et ai.**, **2012**, like Proportional Integral Derivative (PID) which is usually used in various systems because of their simple structure with high performance, **Akar,** and **Cankaya**, **2007**. So, to implement a PID controller, proportional gain (k_P), Integral gain (k_I) and Derivative gain (k_D) must be solved. Many approaches have been suggested to solve these parameters; **Kumar,** and **Babu**, **2014**, presents the PID tuning by Ziegler-Nichols (ZN) method to control the position of servo motor which is lead to satisfy the closed-loop response. **Bindu**, and **Namboothiripad**, **2013**, presents fast tuning method based on genetic algorithm to derive the parameters of PID controller for the desired system. **Venugopal**, **et al.**, **2013**, Applied the soft computing technique of the fuzzy logic for tuning the PID controller to get the best dynamic and static performance at the output. **Shalal**, **et al.**, **2013**, presents an optimal design of PID controllers based on the minimization of an integral standard; in this paper DS method is used to solve the parameter of the PID controller. Also, the study present the formal procedure to improve the PID controller for a DC servo motor, where the optimal parameter of the PID controller is determine by using DS method. PSO and neural network algorithms have been used to improve the PID controller to get the high quality response compared with the original system.

This paper organized as follows. Section (2) explains the mathematical model of DC servo motor. Section (3) describes the method of PID controller tuning by DS method. Section (4) describes the Neural Network and PSO algorithms respectively. Experimental results in section (5). Finally, conclusion is summarized in section (6).

2. MATHEMATICAL MODEL OF DC SERVO MOTOR

The Direct Current (DC) servo motor that has been used in this paper is shown in **Fig. 1** and **Fig. 2** represent the block diagram of DC servo motor, where this motor is a 25 V with no load speed of 4050 rpm.

The differential equations of the armature DC servo motor connection can be derived as the equations below, **Dipraj**, and **Dr. A. K.**, **2012**:

$$V_a\,(t) = R_a\ i_a\ + L_a \frac{di_a}{dt} + V_b \tag{1}$$

Where the equation of torque is:

$$T_m = J\frac{d\omega_m}{dt} + B\omega_m(t) \tag{2}$$

$$V_a = K_b.\omega_m(t) \tag{3}$$

Where K_b is constant. To create the block diagram of the system, the initial conditions and Laplace transform is implemented as the equations below:

$$V_a(s) = R_a i_a(s) + sL_a\ i_a(s)V_a(s) \quad (4)$$

$$T_m(s) = sJ\omega_m(s) + B\omega_m(s) \quad (5)$$

$$V_a = K_a\omega_m(s) \quad (6)$$

3. PID TUNING BY DIRECT SYNTHESIS METHOD

Direct Synthesis (DS) method is based on the required form for the system's response, and then finding controller parameters to get that response.

If we consider $\left(\frac{y}{r}\right)$ is the desired output response, *Gc* is the PID controller and *Gp* is a model of the process. The closed loop transfer function is:

$$\frac{y}{r} = \frac{G_c(s)G_p(s)}{1 + G_c(s)G_p(s)} \quad (7)$$

Rearranging and solving $G_c(s)$ to get the equation for the feedback controller:

$$G_c(\mathrm{s}) = \frac{1}{G_p(s)}\left[\frac{\left(\frac{y}{r}\right)}{1 - \left(\frac{y}{r}\right)}\right] \quad (8)$$

Let $\left(\frac{y}{r}\right) = \frac{1}{(\tau_c s+1)}$, Where τ_c is the time constant. Replacing the (y/r) by $\frac{1}{(\tau_c s+1)}$

The Eq. (9) becomes:

$$G_c(s) = \frac{1}{G_p(s)}\left[\frac{\frac{1}{(\tau_c s + 1)}}{1 - \frac{1}{(\tau_c s + 1)}}\right] \quad (9)$$

$$G_c(s) = \frac{1}{G_p(s)}\frac{1}{\tau_c s} \quad (10)$$

Let $G_p(s) = \frac{K_0}{(\tau_1 s+1)(\tau_2 s+1)}$

$$G_c(s) = \frac{(\tau_1 s+1)(\tau_2 s+1)}{K_0}\frac{1}{\tau_c s}$$

$$= \frac{(\tau_1 + \tau_2)}{K_0\tau_c}\left[1 + \frac{1}{(\tau_1 + \tau_2)s} + \frac{\tau_1\tau_2}{(\tau_1 + \tau_2)}s\right] \quad (11)$$

This is PID controller with:

$$K_p = \frac{(\tau_1 + \tau_2)}{K_0 \tau_c} \tag{12}$$

$$\tau_I = (\tau_1 + \tau_2) \tag{13}$$

$$\tau_D = \frac{\tau_1 \tau_2}{(\tau_1 + \tau_2)} \tag{14}$$

Fig. 3 show the block diagram of DC servo motor with PID controller

4. THE ALGORITHMS FOR IMPROVING THE PID CONTROLLER

Two algorithms are presented to improve the solution quality of the PID controller with finer tuning, Neural Network (NN) algorithm and Particle Swarm Optimization (PSO) algorithm. The two algorithms can be described as follows:

4.1 Neural Network Algorithm

The artificial neural network is a system of processing information and it has some features like biological neural network, **Kumar**, and **Singh**, **2013**. For a new control suggestion and the techniques in the control field, the artificial neural network as a new type of getting the information, characterization and processing which are the reason of process control interest. Intelligent control systems can design a method that can rating any signal for obtaining required response without assuming signal conduct, **Al-Ghasem**, and **Ussaleh**, **2012**. Also, neural network has ability to approximate the nonlinear function relation with more suitable learning techniques; therefore it can be applied on new complex process modeling, **Louren**, and **Jinling**, **2011**. Back propagation (BP) neural network considered as one of the forward feedback networks, and it's the most popular networks used. The neural network can classify by three sections:

1- The input layer: the input units which take the information to be generalized through the network, where the information from the input will be pass during the network and an output product.

2- The hidden units take the input from the input layer, where the hidden unit jointly from the hidden layer, every unit in the input layer is connected to every unit of the hidden layer.

3-The output layer: the output units which command the group assigned through the network. The output units form the output layer. Every unit in the hidden layer is connected to every unit in the output layer. The weighted sum of the output from the hidden units shapes the input to every output unit, **Al-Ghasem**, and **Ussaleh**, **2012**.

In this paper BP neural network is used to adjust the parameters of PID controller. **Fig. 4** explains the structure of BP neural network. From **Fig. 4**, BP neural network consist of three layers: one input layer, one hidden layer and one output layer with three input and three output variables. The input variables of the structure represented by: r(k) which is the reference response, y(k) is the output of the system, and the error between them represented by e(k). The input of the hidden neurons of the hidden layer can be written as:

$$net_j^2 = \sum_{n=0}^{x} w_{jn}^2 * I_n^1 \qquad (15)$$

$$net_i^2 = \sum_{n=0}^{x} w_{is}^2 * I_s^1 \qquad (16)$$

Where, net_j^2 and net_i^2 are the input of the hidden layer, when w_{jn}^2 and w_{is}^2 are the weights of the hidden layer, I_n^1 and I_s^1 is the output of the n^{th} and s^{th} input of the input layer, n and s represent the number of input layers. The output layer can be written as:

$$\begin{cases} o_1(k) = K_p \\ o_2(k) = K_i \\ o_3(k) = K_d \end{cases} \qquad (17)$$

4. 1. 2 Pid controller based on back propagation-neural network

Substitute the conventional PID controller by using BP-neural network PID controller to reduce the error between the output of the system and prospective values. **Fig. 5** shows that the controller has two parts: the ordinary PID controller and BP neural network, this structure called neural network-PID controller. PID controller controls the DC servo motor directly, so the parameters of PID controller: K_p, K_i and K_d are adjustable online; to obtain a good performance, the BP-neural network adjust the parameters of PID controller based on the operational situation of the system, that will make the adjustable parameters of the PID controller and the output of neurons are identical.

4.2 PSO Algorithm

The other algorithm is Particle Swarm Optimaization (PSO). PSO algorithm was improved by Kenndy and Eberhart, which is taken from a social behavior of bird and fish teaching, and has been established to be a robust in solving nonlinear optimaization problems, **Rastogi**, and **Tiwari**, **2013**. The advantage of PSO include the ease of implementation. It can be used to determine a various problems. PSO technique manage search using a population of a particles. Each one of this particle represents a elect solution to the problem, **Patel**, and **Parikh**, **2014**. In this system, these particles change their positions by flying toward a potential place in a several dimensions search space and shares public information between particles.

The number of the particles (n) is 30, and the number of the iterations (i) is 10 Let the n_{th} particle be represented by $x_n = (x_{n1}, x_{n2}, x_{n3}, \ldots x_{nj})$, where j is dimentional space = 3. The best previous position of the nth particle is $pbest_n$ = ($pbest_{n1}$, $pbest_{n2}$, ….$pbest_{nj}$), and $gbest_n$ is the global best position of tha swarm of these particles and the velocity of the particle n is v_n = (v_{n1}, v_{n2}, v_{n3}, ….v_{nj}). The velocity and position of each particle are updated as the following equations:

$$v_{nj}(i+1) = w*v_{nj}(i) + c1*rand*(pbest_{nj}-x_{nj}(i))+c2*rand*(gbest_n-x_{nj}(i)) \quad (18)$$

$$x_{nj}(i+1) = x_{nj}(i) + v_{nj}(k+1) \quad (19)$$

Where c1 and c2 are accelleration constants and w is weighting function. The fitness equation of the PSO algorithm is:

$$fitness = 0 * ones(n, bird\ step) \quad (20)$$

Where maximumm numbers of bird steps = 50. The procedure of PSO algorithm is as follows:

1- Create initial value of particles with random positions and velocities within dimensions search space.
2- Determine the value of the fitness function of each particle.
3- The fitness function of each particle was compared with local-best, if the solution is better than its local-best then the change its local-best by solution.
4- Compare the fitness of these particles with global-best, if the fitness of these particle is better than global-best then change its global-best by this solution.
5- Find the new position and velocity for all the swarm elements.
6- Iterate steps until a stopping criterion is done.

Fig. 6 describe the flow chart of the pso algorithm.

4. 2. 1 Pid controller based on PSO algorithm

The PSO algorithm was applied to obtain the parameters of PID controller (K_p, K_i and K_d) to acquire a good performance of the output response for the controller system. In this algorithm the search space of this particles has three dimentional space. **Fig. 7** shows the block diagram of the PSO-PID controller of the system, where the controller consist of two phases: the conventional PID controller and PSO. The parameters of PID controller are adjustable online to get the optimal values that achieved a better performance.

6. SIMULATIONS AND RESULTS

This section shows the output response of DC servo motor transfer function without and with (PID) controller in **Fig. 8,** and **Fig. 9** respectively. The PID controller is improved by two algorithms: Neural Network and PSO. To show the effectiveness of these algorithms, a comparison of them is made with basic control system. **Fig. 10**, and **Fig. 11**, and **Fig. 12** shows the comparison of control system with and without Neural Network method, the comparison of control system with and without PSO method and the comparison of control system without and with these methods respectively.

The results shows the output response with (PSO) and (NN) methods improve the quality solution of PID controller with zero overshoot but the method of PSO gives the better results and good performance compared with the neural network**.**

6. CONCLUSION

Two algorithms are presented for improving the PID controller. The response of the system with the controller is oscillatory with little overshoot, so to avoid this case back propagation neural network algorithm and PSO algorithm are designed to give the high quality for the required response. The two algorithms gives the fast and smooth output response compared with the present controller with zero overshoot, but PSO algorithm give the better performance compared to the neural network algorithm.

.

REFERENCES

- Akar, M., and Cankaya, I., 2007, *The Design of Real-Time PID Controller based on Lab view for DC Servo Motor*, National Technique Education Engineering and Education Science Young Researches Symposium in Turkish, pp. 76-179.

- Akar, M., and Hekim, M., and Temiz, I., and Dogan, Z., 2012, *The Speed and Torque Control of Direct Current Servo Motors by using Cascade Fuzzy PI Controller*, Electrical Review, ISSN 0033-2097, R. 88, NR. 5b.

- Al-Ghasem, A., and Ussaleh, N., 2012, *Air Conditioner Control using Neural Network and PID Controller*, IEEE 8th International Symposium on Mechatronics and its Applications (ISMA), pp. 1-5.

- Bindu, and Namboothiripad, M. K., 2013, *Tuning of PID Controller for DC Servo Motor using Genetic Algorithm*, International Journal of Emerging Technology and Advanced Engineering, vol. 2, Issue 3.

- Dipraj, and Pandey, Dr. A. K., 2012, *Speed Control of D. C. Servo Motor by Fuzzy Controller*, International Journal of Scientific and Technology Research, vol. 1, pp. 2277-8616.

- Kumar, P. R., and Babu, V. N., 2014, *Position Control of Servo Systems using PID Controller Tuning with Soft Computing Optimization Technique*, IEJT Journal of Process Control, vol. 3, Issue 11.

- Kumar, P., and Singh, K. P., 2013, *Comparative Analysis of Air Conditioning system using PID Controller and Neural Network Controller*, International Journal of Scientific and Research Publication, Vol. 3, Issue 8.

- Luoren, L., and Jinling, L., 2011, *Research of PID Control Algorithm Based on Neural Network*, Elsevier, vol. 13, pp. 6988-6993.

- Patel, A., and Parikh, K., 2014, *Speed Control of DC Motor using PSO Tuned PI Controller*, IOSR Journal of Electrical and Electronics Engineering, vol. 9, Issue 2, pp. 04-08.

- Rastogi, A., and Tiwari, P., 2013, *Optimal Tuning of Fractional Order PID Controller for DC Motor Speed Control using Particle Swarm Optimization*, International Journal and Soft Computer and Engineering (IJSCE), vol. 3, Issue 2.

- Shalal, A. H., and Rawaa, and Osama, 2013, *A Novel Method for Tuning PID Controller*, Diyala Journal of Engineering Science, vol. 6, No. 1.

- Venugopal, and Ajanta, and Priyanka, 2013, *Design of Tuning Methods of PID Controller using Fuzzy Logic*, International Journal of Emerging Trends in Engineering and Development, vol. 5, Issue 3.

NOMENCLATURE

B = viscous friction coefficient, mH.
i_a = armature current, Ampere.
J = moment of inertia, Kg.m^2.
K_0 = constant gain.
K_b = electromotive forces constant, V/rad/s.
K_D = derivative gain.
K_I = integral gain.
K_P = proportional gain.
K_t = tourque constant, N.m/rad/s.
L_a = armature inductance, mH.
R_a = armature resistance, ohm.
T_m = torque.
V_a = input voltage.
V_b = back voltage.
ω_m = motor angular velocity.
τ_1 = time constant.
τ_2 = time constant.
τ_D = derivative time constant.
τ_I = integral time constant.

Table 1. The parameters of DC servo motor, **Dipraj**, and **Pandey**, **2012**.

Parameter	Value	Units
L_a	29.79	mH
R_a	1	Ω
J	0.01	Kg.m^2
B	0.004	N.m/rad/s
K_t	0.052	N.m/rad/s
K_b	0.1	V/rad/s

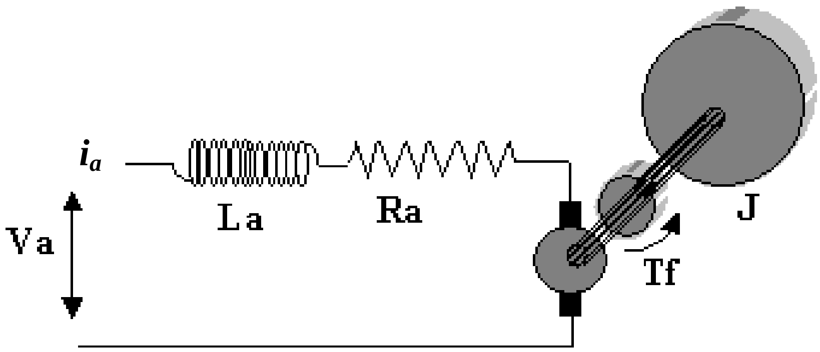

Figure 1. DC servo motor model.

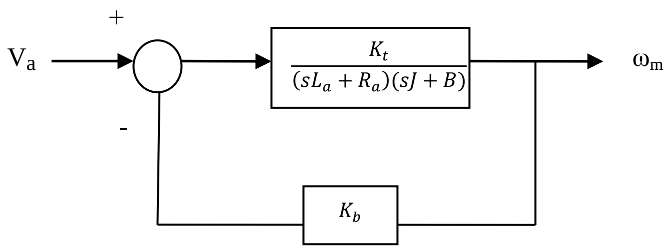

Figure 2. The block diagram of DC servo motor.

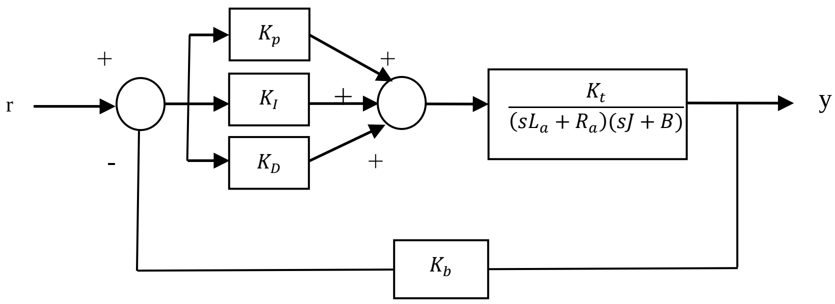

Figure 3. The block diagram of DC servo motor with PID controller.

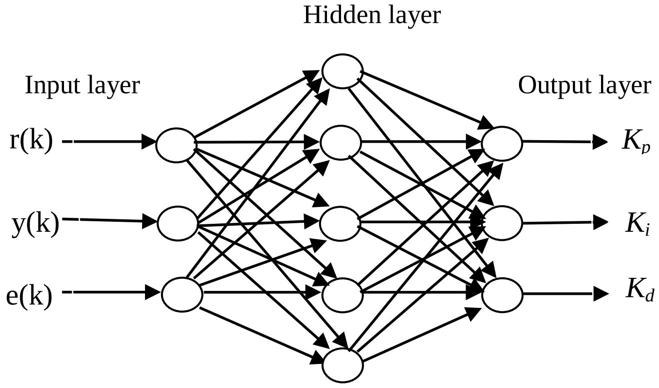

Figure 4. Structure of BP neural network

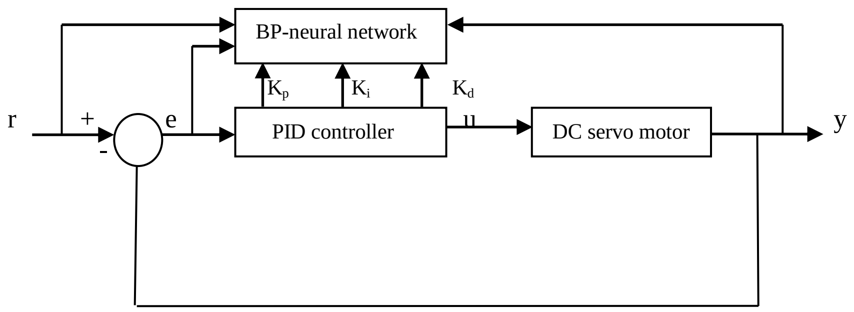

Figure 5. Block diagram of neural network-PID controller.

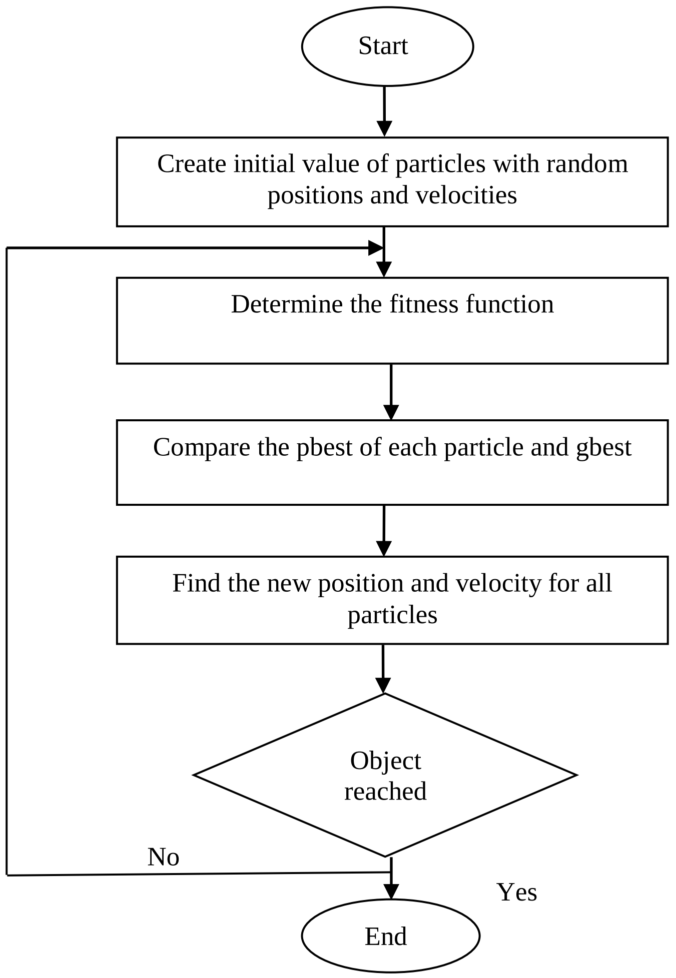

Figure 6. Flow chart of PSO algorithm tuning for DC servo motor.

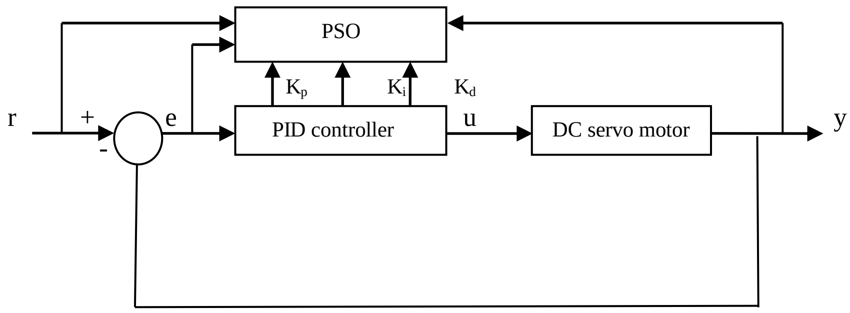

Figure 7. Block diagram of PSO-PID controller

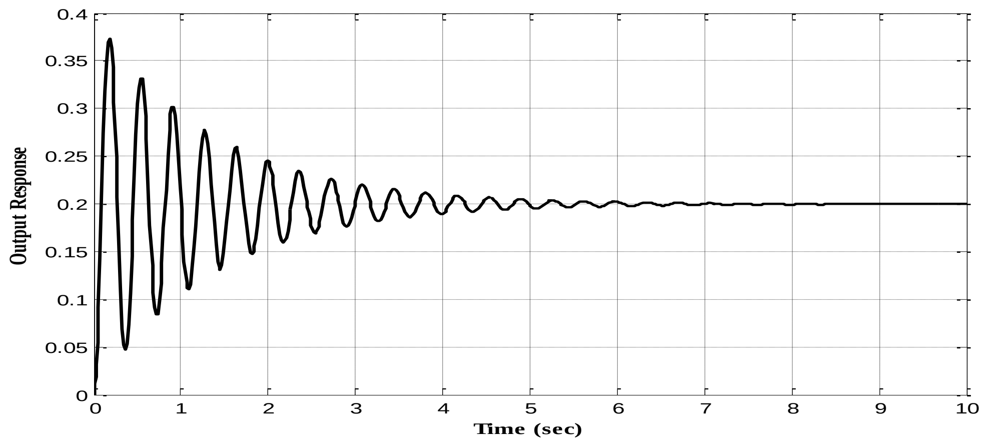

Figure 8. The closed loop transfer function for the DC servo motor without controller.

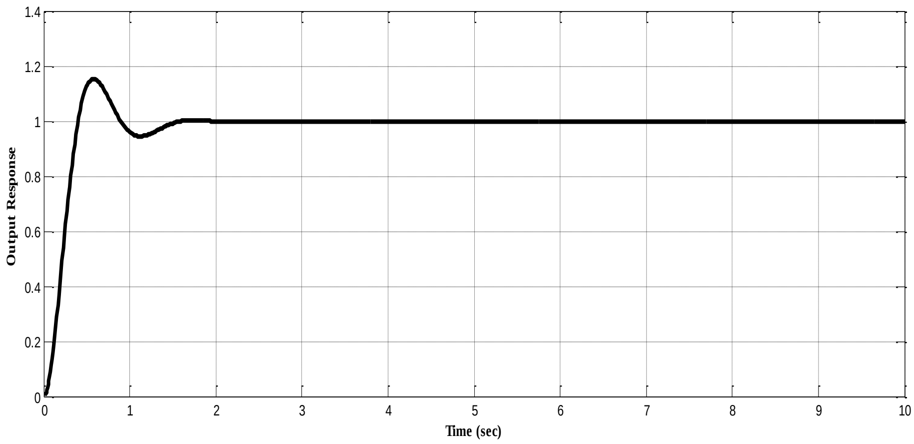

Figure 9. The DC servo motor transfer function with PID controller.

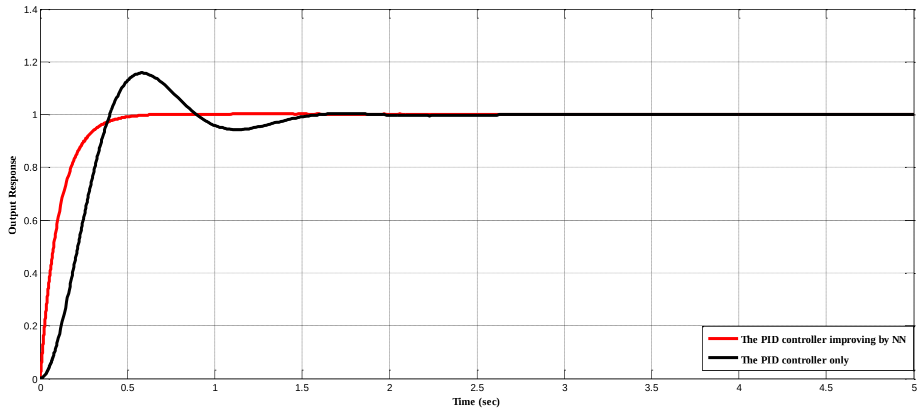

Figure 10. The comparison of PID controller with and without neural network method.

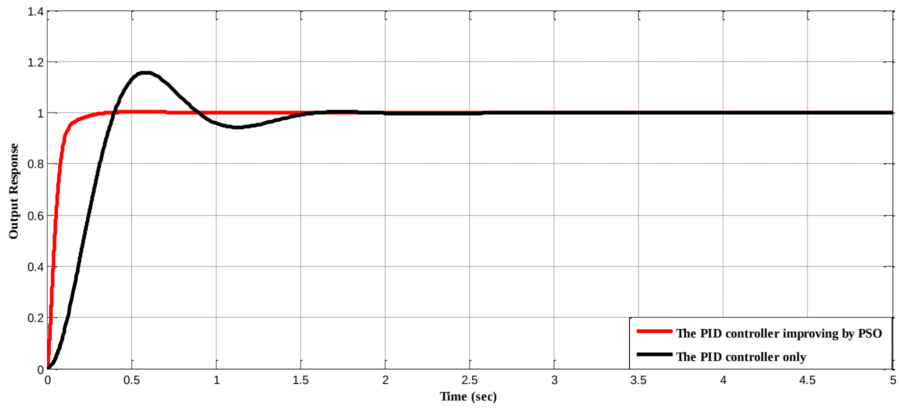

Figure 11. The comparison of PID controller with and without PSO Method.

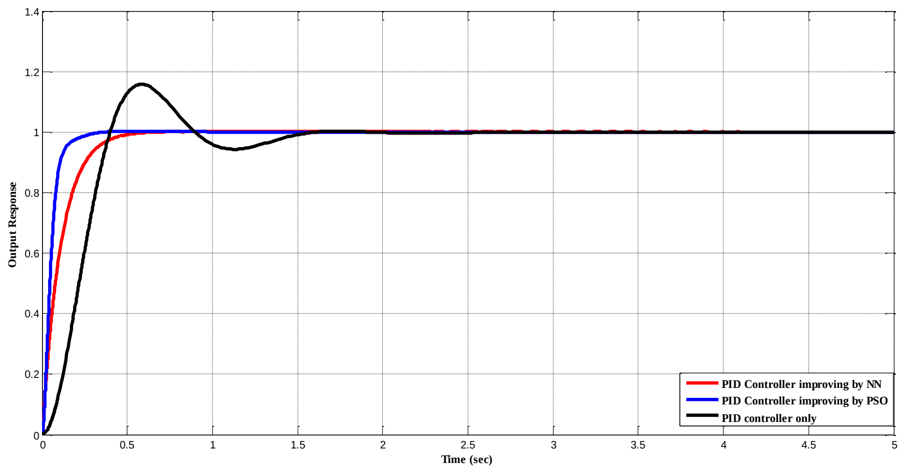

Figure 12. The comparison of controls with and without improving Methods.

Application of SWAT Model for Sediment Loads from Valleys Transmitted to Haditha Reservoir

Ayad Sleibi Mustafa
Assistant Professor
Engineering College-Anbar University
email:ayad_eng2001@yahoo.com

Sadeq Oleiwi Sulaiman
Assistant Professor
Engineering College-Anbar University
email:dr.sadiq1969@yahoo.com

Omar Manfi Hussein
Master Student
Engineering College-Anbar University
email:omar_manfy@yahoo.com

ABSTRACT

This study included the extraction properties of spatial and morphological basins studied using the Soil and Water Assessment Tool (SWAT) model linked to (GIS) to find the amount of sediment and rates of flow that flows into the Haditha reservoir . The aim of this study is determine the amount of sediment coming from the valleys and flowing into the Haditha Dam reservoir for 25 years ago for the period (1985-2010) and its impact on design lifetime of the Haditha Dam reservoir and to determine the best ways to reduce the sediment transport. The result indicated that total amount of sediment coming from all valleys about ($2.56 * 10^6$ ton). The maximum annual total sediment load was about ($488.22 * 10^3$ ton) in year 1988 due to the surface runoff about $167.79 * 10^6$ m^3, while the minimum annual total sediment load was about ($8.62 * 10^3$ ton) in year 2007. This due to the total runoff volume that was 5.67×10^6 m^3. Model calibration and verification were carry out using flow rate and sediment yield data observed at the study area and the results were satisfactory.

Key words: SWAT model, sediment load, runoff, Haditha Dam Reservoir

تطبيق نموذج SWAT لحساب الحمل الرسوبي المنقول من الوديان الى خزان سد حديثة

اياد صليبي مصطفى
استاذ مساعد
جامعة الانبار-كلية الهندسة

صادق عليوي سليمان
استاذ مساعد
جامعة الانبار-كلية الهندسة

عمر منفي حسين
طالب ماجستير
جامعة الانبار -كلية الهندسة

الخلاصة

تهدف الدراسة الى تحديد كمية الرسوبيات القادمة من الوديان وتصريفها الى خزان سد حديثه ل 25 سنة للفترة من 1985 لغاية 2010 وتأثيرها على العمر التصميمي لخزان سد حديثة وتحديد أفضل الطرق لتقليل الرسوبيات الواصلة إليه. شملت الدراسة استخراج الخواص المساحية والمورفولوجية للأحواض المائية المدروسة وتم تطبيق اداة النمذجة المعروف باسم Soil and Water Assessment Tool (SWAT) مرتبطة بنظم المعلومات الجغرافية Geographic Information System (GIS)لأيجاد كمية الرسوبيات ومعدلات الجريان التي تصب في خزان حديثة. اشارت النتائج الى ان الكمية الكلية للرسوبيات القادمة من جميع الادوية بلغت حولي ($2.56 * 10^6$ ton). وكانت أعظم كمية رسوبيات خلال الفترة 1985-2010في سنة 1988 وبلغت ($488.22 * 10^3$ ton) وكان حجم الجريان السطحي في هذه السنة ($167.79 * 10^6$ m^3)، بينما اقل كمية رسوبيات خلال هذه الفترة كانت سنة 2007 وبلغت ($8.62 * 10^3$ ton) وكان حجم الجريان السطحي في هذه السنة (5.67×10^6 m^3). خلصت الدراسة بمعايرة النموذج واختياره بالاعتماد على بيانات التصاريف والرسوبيات المقاسة حقليا في منطقة الدراسة وكذلك اشارت النتائج الى قدرة النموذج على تمثيل منطقة الدراسة.

الكلمات المفتاحية: نموذج سوات، الحمل الرسوبي، الجريان السطحي، خزان سد حديثة

1. INTRODUCTION

Many reservoirs can no longer perform their design functions because much of their original active storage volume has been fill by sediment. For hydropower projects and water supply schemes, any loss of storage increases the risk of failure to meet the design objectives in extreme dry periods **Ijam** and **Al-Mahamid, 2012**.

Several factors are effects on reservoir sedimentation, such as sediment transportation rate, mode of sediment deposition, sediment production, sediment type, reservoir operation, reservoir geometry, and stream flow variability. Sediment is transport as suspended and bed- loads by streams and rivers coming into the reservoir. Due to flow deceleration when rivers approach a reservoir, the sediment transport capacity decreases, and some of the incoming sediment was trapped and deposit in the reservoir. In addition, the deposited sediment may consolidate by their weight and the weight of overlying water through time. Predicting the sediment coming into a reservoir, its deposition and its accumulation throughout the years after construction of dam have been consider as important problems in hydraulic engineering.

There are several model types that can be used in prediction of sediment load ,**Arnold**, and **Fohrer**, **2005**; **Gassman, et al., 2007**; **Lin, et al., 2010**; **Neitsch, et al., 2005**.; **Sadeghi, et al., 2007**.; **Winchell, et al., 2010**.; **Wischmeir**, and **Smith**, **1978**.; **Zhu, et al., 2013**.

SWAT is a river basin scale model developed to quantify the impact of land management practices on water and sediment yields in large complex watersheds with varying soils, land use and management conditions over long periods. The main components of SWAT include weather, surface runoff, return flow, percolation, evapotranspiration, transmission losses, pond & reservoir storage, crop growth & irrigation, groundwater flow, reach routing, and water transfer.

Several studies were used SWAT model on sediment measurements that have been conducted to estimate the deposit of sedimentation in reservoirs. **Hao et al.,2003,** simulate the runoff and sediment yield in the upper basin of the Luohe River, a tributary of the Yellow River by using a GIS-based distributed Soil and Water Assessment Tool (SWAT) model, the simulated results demonstrate that the GIS-based SWAT model could be successfully used to simulate long-term runoff and sediment yield in large river basins . **Licciardello, et al., 2005,** have reported the results of a SWAT model for an experimental semi-arid watershed in Sicily, Italy. The watershed was discretized into 31 subbasins and 63 hydrologic response units to simulate different soil types and landuses. **Oeurng, et al., 2011**, used SWAT to simulate discharge and sediment transport at daily time steps within the intensively farmed. **Al-Madhhachi, A. T., 2014** was used Universal Soil Loss Equation (USLE) erosion model in order to quantify soil erosion risk in Little Washita River Watershed, Oklahoma. The objectives of his study were to quantify the average annual soil loss in Little Washita River Watershed using Geographic Information System (GIS) technique integrated with USLE model and compare the erosion risk in 2006 with those in 1992 for Little Washita River Watershed. Average annual soil losses were performed by USLE model show that the highest soil erosion risk values were 35.4 and 17.7 tons/ha/yr with mean value equal to 0.03 and 0.017 tons/ha/yr for 2006 and 1992, respectively.

The main objectives of this study are to estimate the runoff volume and the sediment load entering Haditha Dam reservoir from the main valleys using Soil and Water Assessment Tool (SWAT) model with GIS technique.

2. DESCRIPTION OF THE STUDY AREA

The study area **Fig. 1** was located in the desert of Anbar province between the longitudes (42°28'12") - (41°25'48") in the east, and the Latitudes (34°24'54") - (34°11'6") to the north. This desert contains many valleys, such as Al Akhdher, Al Fuhaimy, Al Qasir, Al Rihana, Al Skarh and Gedah, discharging to the Hadithah Dam reservoir. Some of them have broad and deep underway capacity that flows with the main stream that trends from south- west towards the north-east, producing a network of valleys with various configurations .The climate of study area is a dry weather when streams occurs in valleys at the winter season after heavy rainfall. The climate is hot and dry in summer with high diurnal changes in temperature and classified as a hyper arid.

3. THEORETICAL BACKGROUND OF SWAT MODEL

3.1 Estimation of Runoff

Precipitation-runoff relation affected by various storm and basin characteristics; therefore, accurate computation of runoff amount is difficult. Based on field experience and observations, the most commonly adopted methods to estimate runoff components, which are the runoff volume and the peak runoff rate, are the Curve Number (CN) method of the Soil Conservation Services of the USA (USSCS) for estimation of runoff volume, and the Rational method for the peak flow rate, along with several empirical relationships for estimation of flow rates (Das, 2000).

3.1.1 Curve number method

The US Soil Conservation Service (USSCS, 1972) developed the curve number method to transform daily rainfall to surface runoff using the following equation.

$$Q = \frac{(P_d - 0.2\,S)^2}{0.8S + P_d} \quad (1)$$

Where

Q : runoff (mm),

P_d: is the daily rainfall (mm), and

S : the potential maximum retention of rainfall at any time.

It can be predicted using the curve number (CN) by the following equation:

$$Q = \frac{25400}{254+S} \quad (2)$$

The CN depends upon basin characteristics, type of the cover, soil group and antecedent moisture conditions at the time of rainfall occurrence. It varies from zero for most permeable surface to 100 for impervious surface.

3.1.2 Rational method

The rational method is the most common procedure to predict the peak runoff rate, which considered as an indicator of the erosive power of storms and used to predict sediment loss (Chow et al, 1988).

$$Q_p = \frac{1}{3.6}\, C\, I\, A \quad (3)$$

Where,

Q_P : the peak runoff rate (m^3/sec),

A : the watershed area (km^2),

I : rainfall intensity (mm/hr) for storm duration ≥ the time of concentration (Tc),

C : the runoff coefficient, it ranges from 0 to 1.

The time of concentration is the time required for the effective rain falling on the furthest point of the basin to reach the outlet. There are several empirical relations to determine (Tc) in hour is:

$$T_c = \frac{1}{18}\left[\frac{L_s\, n_{ov}}{\sqrt{S_s}}\right] + 0.62\, L\left[\frac{n_{ch}}{\sqrt[4]{A_s}\;\;\sqrt{S_{ch}}}\right]^{0.75}$$
(4)

Where,
L_s : basin slope length (m),
n_{ov} : Manning's roughness coefficient for overland flow,
n_{ch} : Manning's roughness coefficient for channel flow,
S_s : the average slope in the basin (m/m),
A_s : basin area (km^2) and
S_{ch}: channel slope (m/m).

3.2 Soil Erosion Model

Many socio-economic and ecological factors caused and influenced in Soil erosion and sedimentation. The effects of some major factors on both soil erosion and sediment yield on catchment scale are Climate and rainfall, Soil type, Land use/cover, Catchment extent, and Geologic formation. There is a variety of predictive equations and models have been developed by several investigators in order to understand erosion occurrence and predict soil loss, the USLE has formulated the essence of many soil loss and sedimentation prediction models. It has achieved high degree of popularity and applicability for different regions of the whole world. **Williams, 1995** have introduced the updated formula for the (USLE) as:

$$E = 1.292\,.EI\,.K\,.LS\,.C\,.P\,.F_{cfrg} \tag{5}$$

Where,
E : the soil erosion on a given day (ton/ha),
EI : the rainfall erosion index (m.ton.cm/ (m^2 hr)),
K : the USLE soil erodibility factor (ton.m^2 hr/ (m^3- ton.cm)),
LS : the USLE topographic factor,
C : the USLE cover and management factor,
P : the USLE support practice factor and
F_{cfrg}: the coarse fragment factor.

4. MODEL SETUP AND INPUT DATA

4.1. Watershed Delineation

Watershed delineation is the first step in establishing a watershed simulation; it involves partitioning the watershed into smaller units (subbasins) and defining the spatial relationship of objects within these units, depending on the degree of complexity in topography and stream network. The watershed delineator is subdivide into four parts as follows:

A. Digital Elevation Model (DEM)

To delineate the watershed and subbasins and to determine drainage networks SWAT uses the digital representation of the topographic surface. The digital Elevation Model (DEM) of the study area watershed, **Fig. 2** take from the U.S. space agency (NASSA) with accurately 30 m resolution, where the data resides in the NASSA office site files format (HGT) where it has been converted to a formula (DEMs) through the program (Global Mapper).

B. Stream definition

SWAT starts to formulate the flow accumulation grid, based on the DEM, by counting the number of cells contributing to each cell in the grid. The stream branches were controlled by specifying a threshold on contributing a number of grid cells making up each branch (Di Luzio *et al*, 2002). The major streams are define and the downstream edge of each one is marked as its outlet; **Fig. 3** displays the stream definition for study area.

C. Main watershed outlet selection and definition

This is the last step in the delineation by which study area location is selected as the main outlet of the study area, hence, the upstream area which is the catchment is clipped and discretized into subbasins in a manner that a mainstream is associated with each subbasin; this forms the first level of subdivision. Study area catchment has been delineated into 188 subbasins as shown in **Fig. 4**. **Table 1** summarizes the calculated parameters for the study area streams and basins; respectively. The total area of all basins was (1725.181 km^2).

4.2 Land Use Map

Land use/cover data is assigned to SWAT in the form of separate GIS-layer (either vector or raster) reclassified using crops and landuse types that are defined within the model databases. The map has been loaded to the model interface, and clipped to the delineated 188 subbasins to produce **Fig. 5** shows study area basins with their respective land use cover, and the percentage of each category with respect to the catchment area.

4.3 Soil Map and Data

The upper layer soil characteristics in study area (about 25 cm depth) are estimate as follows:

1- During the field study of nine soil samples have been collected, at a depth 25 cm representing the study areas. **Fig. 6** shows the location of soil samples.
2- Soil texture: classified according to the USDA classification system.

4.4 Weather Data Definition

SWAT requires daily or sub-daily meteorological data. The meteorological data used was daily precipitation, daily maximum and minimum air temperature, daily solar radiation, wind speed, and relative humidity on a daily basis. **Table 2** shows Location of Weather stations.

4.5. Running the SWAT Model

After finalizing the set up of input, the SWAT model run by selecting the “Run SWAT” option in the SWAT Simulation menu. The simulation period used was from 1 December 1985 to 31 December 2010.

5. FIELD MEASUREMENTS

The rainfall depth for two daily rain storms were obtained from Ana hydrological weather station for data 25/11/2012 and 28/1/2013 which was 30.3 mm and 28 mm respectively. At the same data throughout the runoff flow time, the flow velocity was measured by a current meter at a cross-section on the outlet of valley perpendicular to the flow of water for the six catchments of the study area as shown in **Fig. 7.**

The flow velocity measurement was taken at 0.6 of the flow depth and the reading of depth at each point of measurement. The velocity – area method was used to estimate the discharge at each of six valleys at the specified time and the measurement of flow velocity and depth were repeated wherever there is significant variation in flow depth.

6. MODEL CALIBRATION AND VERIFICATION

Calibration is the process of adjusting model input parameters until the outputs satisfactorily match with field-observed values. The typical procedure for SWAT models calibration is to calibrate stream flow and sediment in succession. The current model calibrated by use the surface flow and sediment data at the outlet of study area. An initial simulation made for the period (1/11/2012 through 30/11/2012) because the data is only available for this period for the study area model setup and calibration.

Calibration of stream flow performed depending on observed flow measurements. Outflows from the whole catchment calculated by use SWAT Model and compared with the flow-measured from the study area valleys. The initial annual simulation has shown a general overestimation of flow values, thus the CN has been selected as a calibration parameter for its significant effect on flow computation, and the subbasins' CN values have been varied (mostly decreased) iteratively within a reasonable range during several calibration runs until satisfactory agreement has been reached between simulated and observed flow values.

The flow calibration results show that SWAT has simulated the hydrological processes of the study area watershed realistically, so calibration has proceeded to involve sedimentation results as well. Because of the shortage of direct measurements of sedimentation in the study area watershed, the required observed sediment loads acquired from the field measurement that was taken during November 2012. The USLE cover factor (C) and practice factor (P) have been adjusted to match observed and simulated sediment loads through several iterations, for which the previous model performance indicators and the context of relative errors have been applied, and accordingly, the best simulation has been selected by optimization. **Fig. 8** shows the procedure of calibration for SWAT model.

A good correspondence obtained between observed and calibrated monthly flow and sediment load for the period of calibration. Calibration for flow and sediment is acceptable and indicates that SWAT is able to simulate the study area and predict flows and sediment loads well.

Model verification is the approach by which parameters developed in calibration are tested and verified against independent observed data for the area of concern. Based on calibration results, the study area SWAT model verified using the calibrated parameters to check its capability of reproducing measured flows and the corresponding sediment loads at Valleys in the study area. The period of verification was selected on the basis of quality of the available observations, the record and of surface runoff and sediment concentration of storm rainfall at (28/1/2013) was selected to verify the study area model because it is the only available data records for the model verification in the study area. A good indication obtained between measured and calculated flow and sediment load for the period of verification, giving more support toward utilizing SWAT to model the six valleys watersheds in the study area and achieve the intended modeling objectives.

7. RESULTS ANALYSIS

The daily rainfall data, maximum and minimum temperature, sunshine, humidity, and wind speed of Haditha station was considered in this study. The data is use to estimate the annual runoff volume and sediment load that were delivered from the main valleys of the left bank on Haditha Dam reservoir for the period December/1985 - December/2010. The SWAT (soil and water assessment tool) was considered for monthly simulation for both runoff and sediment of the considered valleys. The total annual precipitation and surface runoff from period 1985 to

2010 where shown in **Fig. 9**. The maximum annual total runoff volume for the considered valleys was about 167.79 * 10^6 m^3 (97.26 mm) in 1988 , which was due the maximum total annual rainfall depth in that year (286.47 mm). The minimum total runoff volume was 5.67×10^6 m^3 (3.29 mm) for the year 2007, which had a minimum average annual rainfall depth of 51.86 mm.
The total sediment load for all years for period from 1985 to 2010 was about 1484 ton/km^2 (2.56 * 10^6 ton) .This was due to the total annual surface runoff volume about 1.0688*10^9 m^3 (619.55mm) , where the amount of sediment varies from year to year depending on the amount of precipitation and surface runoff. From **Fig. 10**, we can see the amount of the sediment load for 25 year ago. The maximum annual total sediment load in year 1988 is about 283 ton/km^2 (488.22 * 10^3 ton). This was due to the effect of high surface runoff in year 1988 that was 167.79 * 10^6 m^3 (97.26 mm) , which are due to the maximum total annual rainfall depth in that year (286.47 mm). The minimum total sediment load was in year 2007 about 5 ton/km^2 (8.62 * 10^3 ton), this is due to the total runoff volume which was 5.67×10^6 m^3(3.29 mm) for the year 2007 that had an average annual rainfall depth of 51.86 mm. it showed that the higher the amount of precipitation caused an increase of high surface runoff leading to erosion of large amount of soil and therefore this causes an increase of the amount of sediment yield from valleys. From Figures, SWAT shows a good performance in simulating the seasonal variation in flow as expected according to the climate of Iraq, where most precipitation occurs during the months (October to April).

8. CONCLUSION

Based on the results obtained from this study, the following conclusions can be drawn:

1- The SWAT model working under GIS (Geographical Information System) was applied to estimate the yearly runoff and sediment load carrying from the main valleys at the left bank of Haditha Dam reservoir .

2- The total sediment load for period from 1985 to 2010 was (2.56 * 106 ton); this was due to the total annual surface runoff volume about 1.0688*109 m^3.

3- The maximum annual total sediment load was in year 1988 about (488.22 * 10^3 ton), this was due to the effect of high surface runoff in year 1988 that was 167.79 * 10^6 m^3, while the minimum annual total sediment load was in year 2007 about 8.62 * 10^3 ton. This due to the total runoff volume is 5.67×10^6 m^3.

REFERENCES

- Al-Madhhachi, A. T., 2014. “*Quantifying Erosion Risk for Little Washita River Watershed Using GIS Technique Integrated with USLE Model*”. IJERT, Vol. 3(11) , ISSN: 2277-9655

- Arnold, J. and Fohrer, N., 2005. "*SWAT2000: Current Capabilities and Research Opportunities in Applied Watershed Modeling*". Hydrological Processes, No. 19: 563-572

- Di Luzio, M., R. Srinivasan, and J. G. Arnold. 2002. "*Integration of Watershed Tools and SWAT Model into BASINS*". J. American Water Resour. Assoc. 38(4): 1127-1141.

- Engel, B., D. Storm, M. White, J. Arnold, and M. Arabi. 2007. "*A Hydrologic/water Quality Model Application Protocol*". J. American Water Resour. Assoc. 43(5): 1223-1236.

- Gassman, P.W., M. R. Reyes, C. H. Green and J. G. Arnold, 2007. "*The Soil and Water Assessment Tool: Historical Development, Applications, and Future Research Directions*", Soil & Water Di-vision of ASABE 50(4), 1211-1250.

- Hao, F., Zhang, X., Cheng, H., Liu, C., and Yang, Z., 2003." *Runoff and Sediment Yield Simulation in a Large Basin Using GIS and a Distributed Hydrological Model*". GIS and Remote Sensing in Hydrology, Water Resources and Environment, IAHS Publ. 289.

- Ijam, A., and Al-Mahamid, M., 2012." *Predicting Sedimentation at Mujib Dam Reservoir in Jordan*". Jordan Journal of Civil Engineering, Volume 6, No. 4.

- Licciardello, F., Srinivasan, R. and Zimbone, S. M., 2005. "*Evaluation of the SWAT Model in a Small Experimental Mediterranean Basin*". Proceedings of 3rd International SWAT Conference, Zurich, Switzerland, No.27: 261-269.

- Lin, S., Jing, C., Chaplot, V., Yu, X., Zhang, Z., Moore, N. and Wu, J., 2010." *Effect of DEM Resolution on SWAT Outputs of Runoff, Sediment and Nutrients*". Hydrology and Earth System Sciences Discussions, 7, 4411–4435.

- Neitsch, S., Arnold, J., Kiniry, J. and Williams, J., 2005. "*Soil and Water Assessment Tool Theoretical Documentation*", Texas Water Resources Institute, USA.

- Oeurng, C., Sauvage, S., and Pérez, J., 2011." *Assessment of Hydrology, Sediment and Particulate Organic Carbon Yield in a Large Agricultural Catchment Using the SWAT Model*". Journal of Hydrology, vol. 401 (n°3-4). pp. 145-153. ISSN 0022-1694.

- Sadeghi, S., Mizuyam, T. and Vangah, B., 2007. "*Conformity of MUSLE Estimates and Erosion Plot Data for Storm-Wise Sediment Yield Estimation*". Terr. Atmos. Ocean. Sci., Vol. 18, No. 1, 117-128.

- U.S. Department of Interior, Bureau of Reclamation, 2006, "*Erosion and Sedimentation Manual"*, US Department of Interior, Bureau of Reclamation, Technical Service Center, Sedimentation and River Hydraulic Group, Denver, Colorado, pp. 508.

- Winchell, M., R. Srinivasan, M. Di Luzio, J. Arnold, 2010. "*ArcSWAT Interface for SWAT 2009*", User's Guide.

- Wischmeir, W.H. and Smith, D.D., 1978. "*Predicting Rainfall Erosion Losses-A Guide to Conservation Planning*". USDA Handbook No.537, Washington.

- Zhu, A.X., Wang, P., Zhu, T., Chen, L., Cai, Q. and Liu, H., 2013." *Modeling runoff and soil erosion in the Three-Gorge Reservoir drainage area of China using limited plot data*". Journal of Hydrology 492, 163–175.

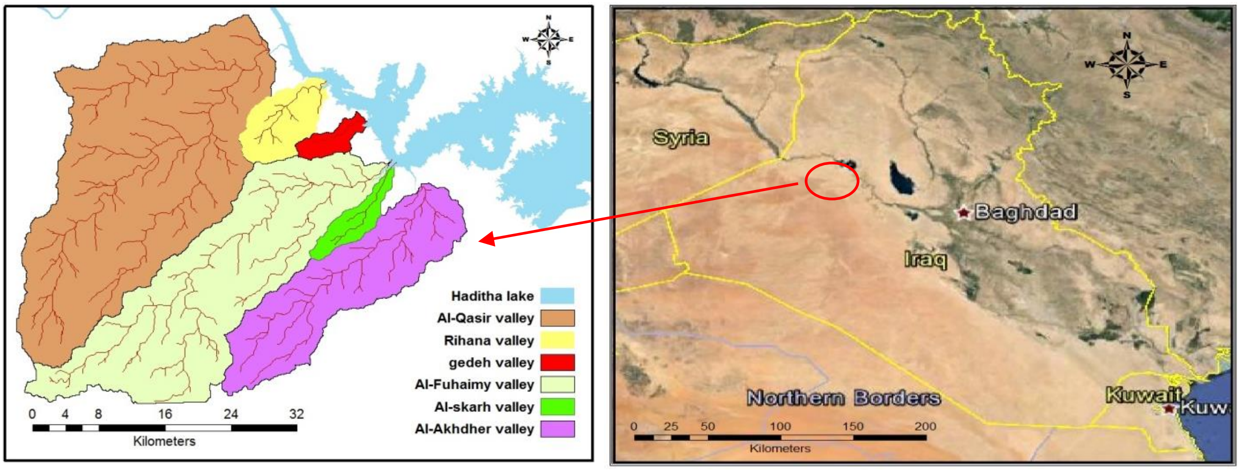

Figure 1. Location of the Haditha Dam Reservoir, and study area

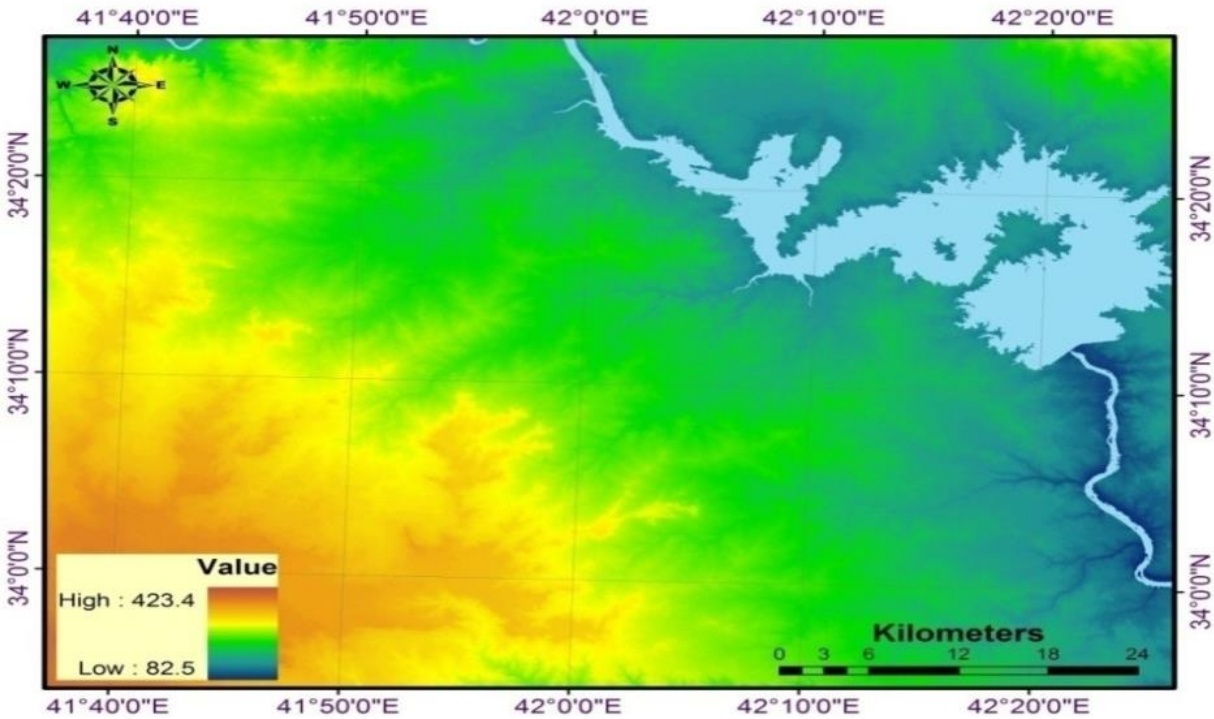

Figure 2. The digital elevation model of study area.

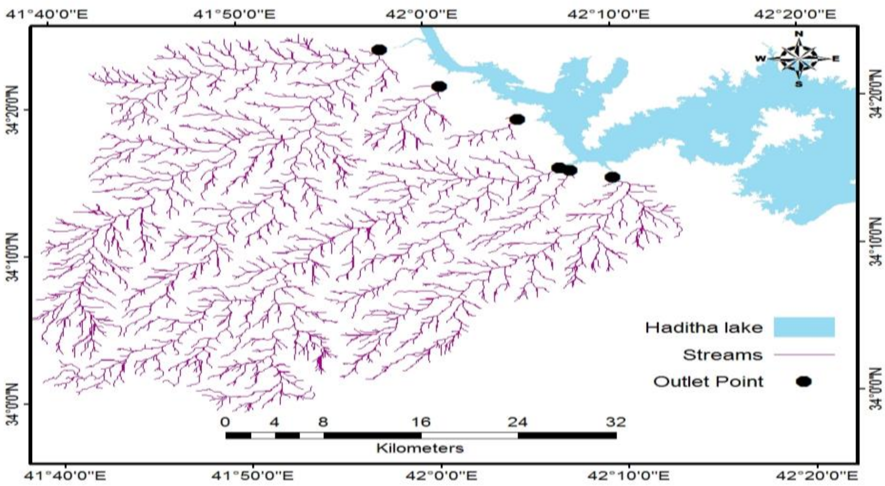

Figure 3. Study area watershed major streams and outlets.

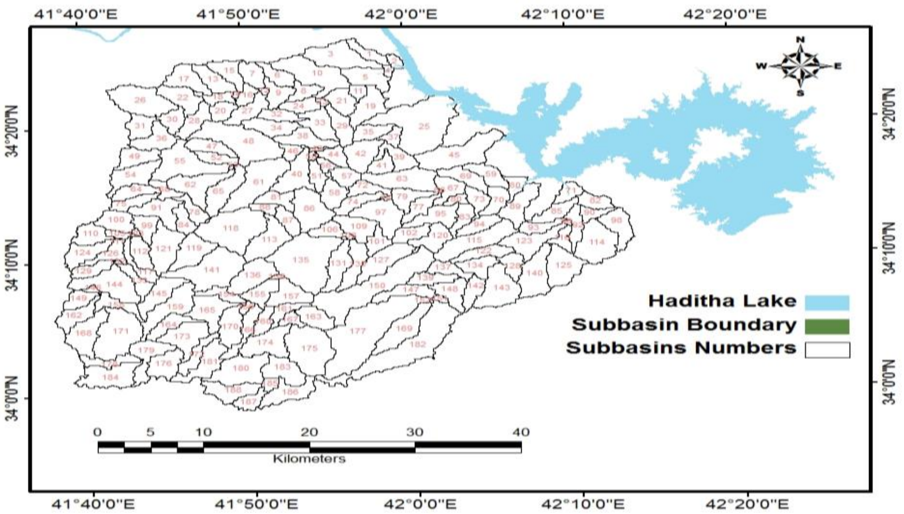

Figure 4. Catchment subbasins in study area as configured by SWAT.

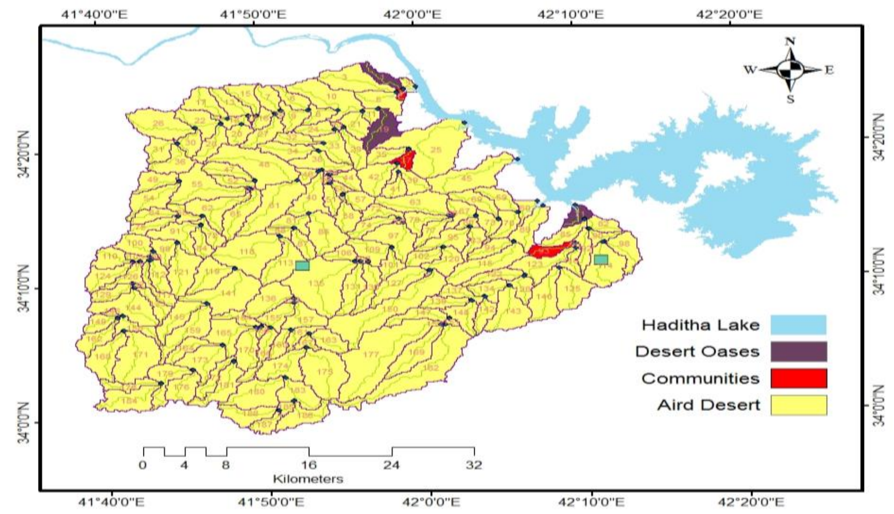

Figure 5. Landuse/cover map of study area catchment as defined by SWAT.

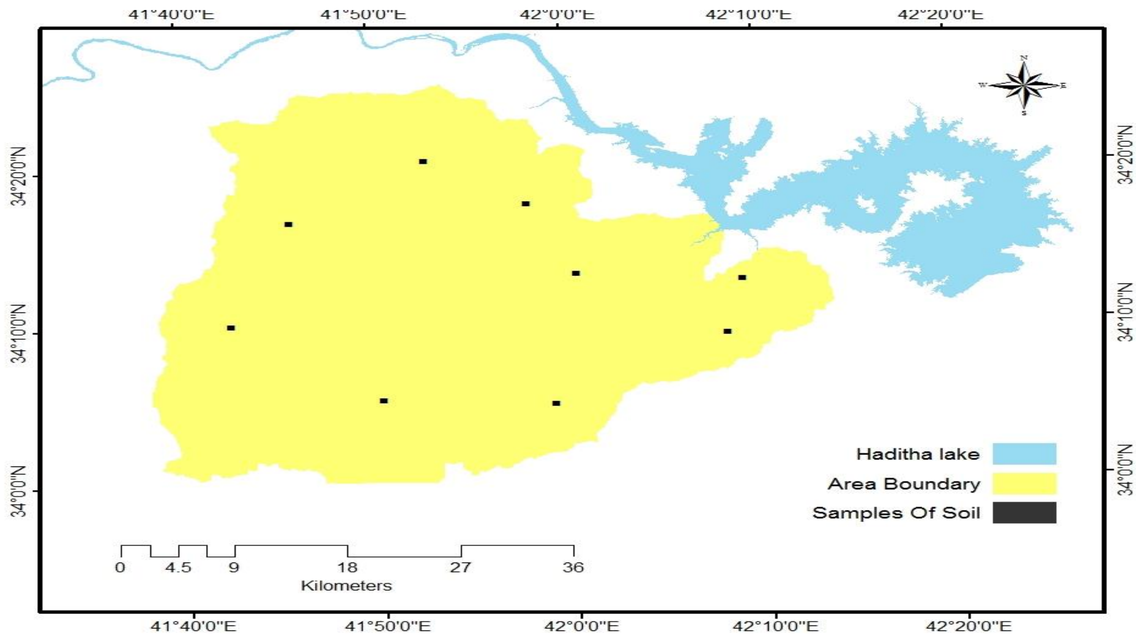

Figure 6. Location of soil samples.

Figure 7. Measurement velocity of valleys by current meter.

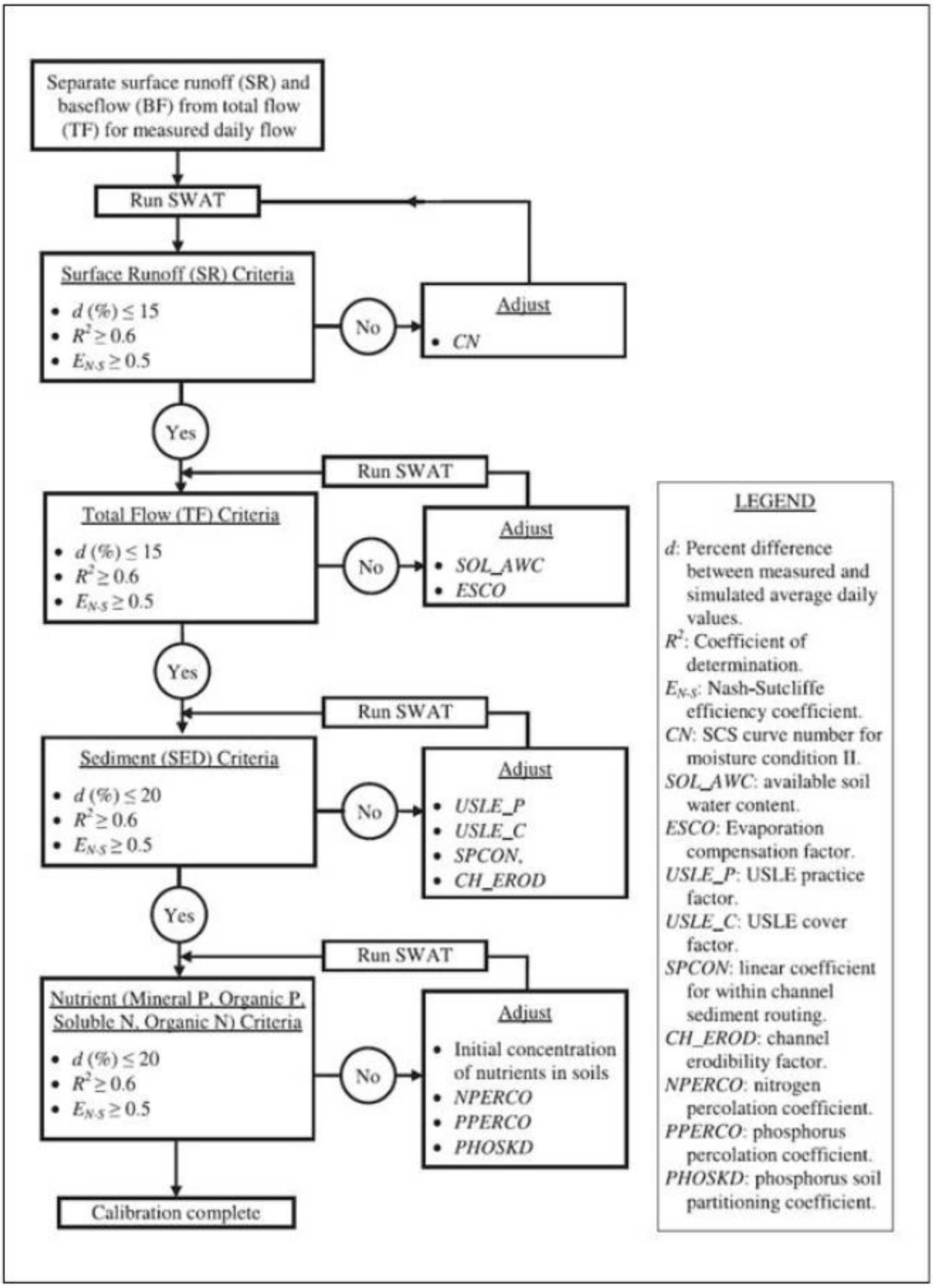

Figure 8. The procedure of calibration for SWAT model **(After Engel et al., 2007**).

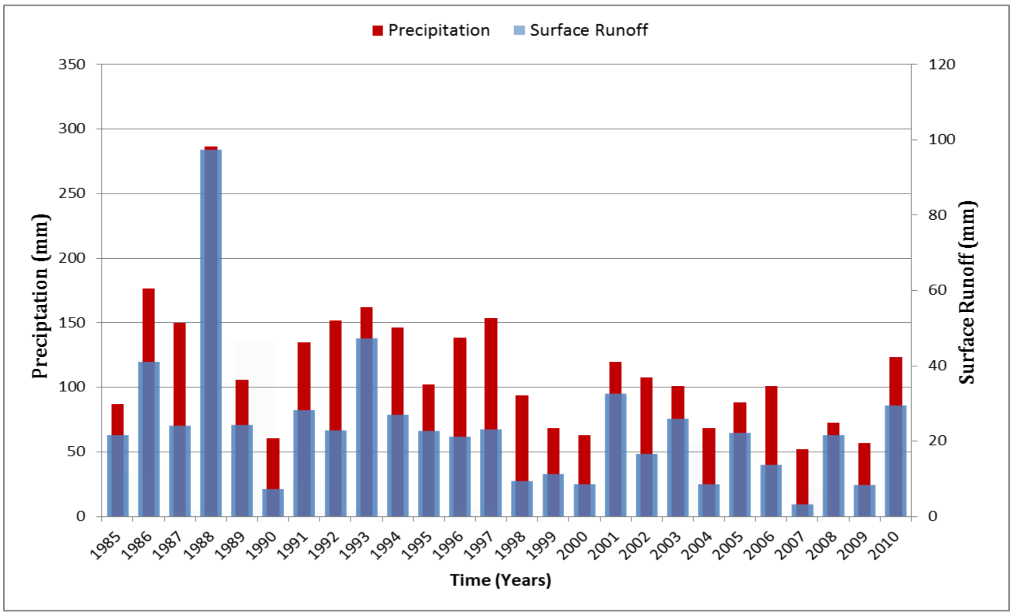

Figure 9. Annual precipitation and surface runoff simulated for the period (1985-2010).

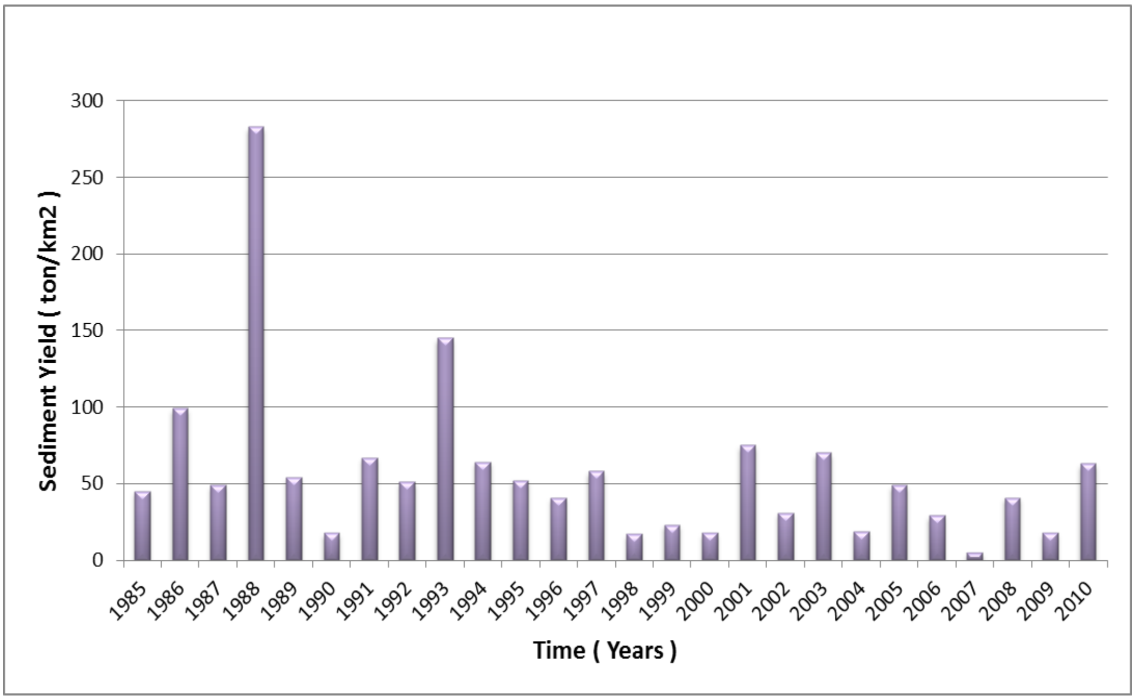

Figure 10. Annual total sediment yield simulated for the period (1985-2010).

Table 1. Study area basins parameters.

No.	Valley name	Area ($Km^{2)}$	Length of basin (m)	Slope %	Shape factor
1	Al-Qasir	769.55	48874.89	0.0120	3.10
2	Rihana	55.22	10777.24	0.0140	2.10
3	Gedeh	14.55	6209.32	0.0168	2.65
4	Al-Fuhaimy	531.21	50308.01	0.0129	4.76
5	Al-Skarh	33.36	12891.67	0.0135	4.98
6	Al-Akhdher	277.72	34560.19	0.0124	4.30

Table 2. Location of weather stations.

station	Latitude	Longitude	Elevatino
Haditha	34°08'41"	42°22'47"	120
Ana	34°22'14 "	41°50'07"	175

Theoretical and Experimental Stress Analysis of Cam With Simple Harmonic Motion

Aveen Ahmed Abdulkareem
Teaching Assistant
College of Engineering – University of Baghdad
email: av_mechanics@yahoo.com

ABSTRACT

Cams are considered as one of the most important mechanical components that depends the contact action to do its job and suffer a lot of with drawbacks to be predicted and overcame in the design process. this work aims to investigate the induced cam contact and the maximum shear stress energy or (von misses) stresses during the course of action analytically using Hertz contact stress equation and the principal stress formulations to find the maximum stress value and its position beneath the contacting surfaces. The experimental investigation adopted two dimensions photoelastic technique to analyze cam stresses under a plane polarized light. The problem has been numerically simulated using Ansys software version 15 as FE solver and depending on Lagrange and Penalty contact algorithm. The effect of cam geometry, characterized by some parameters such as follower radius, face width, rise and return angles, and modulus of elasticity on the contact stress is investigated aiming to minimize the induced stresses.

Key words: Cam modeling, contact stress, photoelastic experimental stress analysis

تحليل الإجهادات نظرياً وعملياً للحدبات ذات الحركة التناغمية البسيطة

أفين أحمد عبد الكريم
مدرس مساعد
كلية الهندسة - جامعة بغداد

الخلاصة

تعتبر الحدبات كواحدة من اهم العناصر الميكانيكية التي تعتمد فعل التلامس للقيام بوظيفتها وتعاني العديد من المعوقات التي يجب تنبأها والتغلب عليها في عمليات التصميم. يهدف هذا العمل لتحري اجهادات التلامس واجهادات طاقة القص العظمى خلال العمل نظريا باستعمال معادلة اجهادات التماس لهيرتز وعلاقات الاجهادات الاساسية لايجاد قيمة الاجهاد الاعظم وموقعة تحت سطوح التلامس . التحري العملي اعتمد تقنية المرونة الضوئية ثنائية البعد لفحص اجهادات الحدبة تحت الضوء مستوي الاستقطاب. تمت محاكات المشكلة عدديا باستخدام برنامج Ansys النسخة الخامسة عشر كمحلل عناصر محدد بأعتماد خوارزمية (Lagrange and penalty) . تم تحري تأثير شكل الحدبة , مميزا بمجموعة من العوامل كنصف قطر الحدبة وعرض الوجه وزوايا الصعود والنزول ومعامل المرونة , على إجهاد التماس بهدف تقليل الاجهادات المتولدة .

الكلمات الرئيسية : نمذجة الحدبة , اجهاد التماس ,تحليل الاجهاد ضوئيا .

1 .INTRODUCTION

Power and movement transmission are regarded as the principle of the mechanical engineering duties which contribute the modern life appearance. Gears, belts, sprockets and cams are the most common used mechanical elements for such purpose. In general the work of such elements is accompanied by some problems like power loss, heat generation, wear, fatigue, high induced contact and bending stresses. Cam may be defined as a machine element with a curved outline or a curved groove, which, by its oscillation or rotation motion, gives a predesigned motion to another element called the follower and has very important function especially in the printing presses, shoe machinery, textile machinery, gear-cutting machines, and screw machines. In any class of machinery in which automatic control and accurate timing are paramount, the cam is an indispensable part of mechanism **Anvoner, 1959.** This work will spot the light on the cam stresses affected by some geometrical parameters such as rise and return angles, face width. The role of modulus of elasticity will be taken into account in this study. Hertz contact stress equation for nonconforming bodies will be adopted as the analytical solution and examined how far the problem will obey Hertz equation. The interaction of the cam and its follower will be numerically simulated using Ansys software version 15 as a FE solver to investigate the different stresses values and distributions. The plane polarized light and photoelastic stress analysis technique will be used in order to compare the accuracy and the similarity between the assumed conditions, for the analytical and numerical, and the applied one on the experimental test and how amount of discrepancy will be produced.

2. Cam Mathematical Representation

The simplicity of cam manufacturing methods and its traditional use associated by the good performance, leads the researchers and the manufacturers to evolve cam shape and work and there are a lot of cam types which could be classified according to the follower motion relative to the cam rotational axis as:

1. Cylindrical cams.
2. Radial cams.

Another classification depends on the follower motion and divides cams into:

1. Uniform velocity.
2. Simple harmonic motion.
3. Uniform acceleration and retardation.
4. Cycloidal motion.

The precise geometrical representation is considered as the first step of any simulation or investigation to grantee the accurate and dependable results. The studied cam in this work is the harmonic displacement one and its profile characterized by the rising distance, base radius, and the different course angles where **Oberg, et al., 2000.**

$$r(\theta) = r_b + \frac{S}{2}\left(1 - cos\frac{\pi\theta}{\beta}\right) \tag{1}$$

While the follower velocity and acceleration is

$$v(\theta) = \frac{s\pi\omega}{2\beta}\sin\frac{\pi\theta}{\beta} \tag{2}$$

$$a(\theta) = \frac{s}{2}\left(\frac{\pi\omega}{\beta}\right)^2\cos\frac{\pi\theta}{\beta} \tag{3}$$

Where r is the cam profile radii, r_b is the cam base radius, S is the max. follower rise distance, $\boldsymbol{\beta}$ is the rising, dwell or falling angle as shown in **Fig. 4**, v is the follower velocity, and a is the acceleration.

Eq. (1) has been programmed using quick basic 64 to calculate the different profile radii and their angles. Each cam profile was presented by 180 points to ensure a realistic representation able to simulate the real cam shape. These points are feed to the FE solver as a key points and connected by a spline to construct the area and then the two dimensional model will be extruded to generate the 3 dimensional model.

3. THEORITICAL STRESS ANALYSIS

3. 1 Analytical Stress Analysis

The contact of the mechanical elements has the functional key role in their interaction, regarding power and movement transmission, and depends on the relative sliding and rolling action. Its relatively large contacting area and zero relative sliding movement makes the conforming contact cases works with low contact stress levels comparing to its counterpart cases i.e. the nonconforming contact problems. In the 19th century Heinrich Hertz proposed his famous equation to calculate the contact pressure of the nonconforming contacting surfaces and dealt with as the governing equation till now days. The most important assumptions that must be taken into account to ensure genuine results are that the two bodies are continuous of constant curvature radius and the contacting area is small compared to the other dimensions. The contact stress has been found as a function of the applied normal load, the face width of the contacting bodies, the two bodies radius of curvature, and the material properties **Hearn 2001**.

$$P_{max} = \sqrt{0.35\ \frac{F}{t} \times \frac{\left(\frac{1}{r_c}+\frac{1}{r_f}\right)}{\left(\frac{1}{E_c}+\frac{1}{E_f}\right)}} \tag{4}$$

Where σ_c is the contact stress, F is the applied load, t is the face width, r_c and r_f are the cam and the follower radius of curvature at the contact zone, E_c and E_f are the modulus of elasticity for the cam and follower

And the mating bodies contacting area characterized by a rectangular area with its length equal to the face width t, while the other dimension could be calculated by the following formula

$$b = 1.076\sqrt{\frac{F\times\left(\frac{1-{\nu_c}^2}{E_c}+\frac{1-{\nu_f}^2}{E_f}\right)}{t\times\left(\frac{1}{r_c}+\frac{1}{r_f}\right)}} \tag{5}$$

The previous equations assumed the contacting elements to be cylinders.

The principal contact stresses at the contacting zone could be evaluated as following **Johnson 2003**.

$$\sigma_1 = \sigma_y = -P_{max}\left[\sqrt{\frac{y^2}{b^2}+1}\right]^{-1} \tag{6}$$

$$\sigma_2 = \sigma_x = P_{max}\left[\left(2-\left(\frac{y^2}{b^2}+1\right)^{-1}\right)\times\sqrt{\frac{y^2}{b^2}+1}-2\left|\frac{y}{b}\right|\right] \tag{7}$$

$$\sigma_3 = \sigma_z = -2\nu P_{max}\left[\sqrt{\frac{y^2}{b^2}+1}-\left|\frac{y}{b}\right|\right] \tag{8}$$

While the shear stresses are

$$\tau_1 = \left|\frac{\sigma_2-\sigma_3}{2}\right| , \tau_2 = \left|\frac{\sigma_1-\sigma_3}{2}\right|, \tau_3 = \left|\frac{\sigma_1-\sigma_2}{2}\right| \quad (9)$$

Due to the applied load and material elastic behavior the contacting surfaces deformed elastically leading to minimize the center distance of the two bodies.

3. 2 Finite Element Approach

Unfortunately the most applicable differential equations governing the engineering and physical applications are complex, and have long term solutions so that the finite element approach has been adopted as a simple alternative way solving the most complex problems directly with a worthless error margin overcoming all the past time investigation techniques. The basic principle of the FEM is to discrete the general problem into a certain number of simple problems diminishing the time consume, efforts and cost. Dealing with FEM needs some experience and a well knowledge to the analytical background of the problem under concern because the results will come under any circumstances and it may be scattered or incorrect. The reliable and accurate results of the FEM depends on a lot of parameters such as the right simulation to the real working conditions like the applied load, the constraint, the working temperature and the right material properties such as the modulus of elasticity and poisson's ratio, as well as the accurate geometrical representation. The 3-D cam model has been built up in the FE environment, the material properties are setup as a structural of linear isotropic material with modulus of elasticity equal to 200 GN/m^2, 0.3 poisson's ratio, and density of 7830 Kg/m^3. The suitable element type and number have been chosen according to the convergence test. In general the larger element numbers the more accurate results but that leads to a long solution time so that the element number must be as small as possible to satisfy the solution. The applied load and constraint must be the same during the convergence test and by choosing a solid brick element 186 as the mesh element and by changing the element number and solve the problem again and again with different element numbers until there will be stabilized then this is the right element number. The best element type has been found to be solid brick element of 20 nodes and the adequate element number is 7555 including 450 contact surface elements and 375 contact target elements and the contact is frictionless **Akkamahdev 2015**. The target is chosen to be the follower while the contact surface is the cam and the applied load is 100 N distributed along the unity follower face width. The adopted contact algorithm approach is the Lagrange and penalty method.

4. Experimental Test

Almost engineering inventions and designs are part of the virtual world and haven't judged to engage the real working environment till it verified to be fully functional with comfortable safety especially for human related applications, high cost products, and mass production. Such critical decision couldn't be taken unless there is evidence support the claims of the vendor or designer, which is the experimental model.

The previous analysis of the cam contact and principal stresses are withdrawn analytically depending on Hertz equations which has some assumptions must be followed to ensure the results accuracy.

The experimental analysis will be conducted using the photoelastic technique to verify if the real cam induced stresses matches that of the analytical equations. The experimental cam model has been manufactured from the PSM-4 photoelastic sheet under a plane polarized light. The material properties such as modulus of elasticity and fringe value are investigated experimentally depending upon Euler's theory and bending test for a specimen cut from the same material **Helena Jin et.al. 2014** see **Fig.1**

$$EI\frac{\partial^2 y}{\partial x^2} = M \tag{10}$$

where

$$M = \left[\frac{wl}{2} + \frac{F}{2}\right]x - \frac{wx^2}{2} \tag{11}$$

Integrating the equation twice and applying the boundary condition's leads to

$$E = \frac{1}{I\delta}\left(-\frac{5}{384}\,wl^4 - \frac{1}{48}Fl^3\right) \tag{12}$$

Where w= 0.03 kg, l= 150 mm, h= 16 mm, t= 6 mm

By increasing the applied load gradually and measuring the resulting deflection using dial gauge and adopting these values (load and deflection) in Eq.(12) a set of the modulus of elasticity will be calculated and then averaged to get a reliable modulus value **, Table 1** illustrates the test results

The fringe value will be investigated using the four point test or the pure bending test **James and William 1991**. where

$$\sigma_1 - \sigma_2 = \frac{N\,f}{t} \tag{13}$$

For pure bending

$$\sigma_1 = \sigma_x = \frac{MY}{I} = \frac{6M}{t \times h^2}$$

$$\therefore 937.5 \frac{F}{N} = f \quad (14)$$

Where N is the fringe order, *f* is the fringe value. **Fig. 2** and **Fig. 3** show the specimen dimensions and position of the applied load as well as the resulting fringe pattern. The applied load and the resulting fringe order are listed in **Table 2**.

The resulting average modulus of elasticity is (4.1 MN/m^2), and the average fringe value is 230 N/ (m. fringe order).

The experimental cam model has been shown in **Fig. 4** which has 50 mm base radius, 25 mm stroke distance, 15 mm for the follower radius, and 6 mm thickness. The cam shape has been modeled depending on Eq. (1) with rise, return, and upper dwell angle equal to 60^o.

5 RESULTS AND DISCUSSION

The most important note to be mentioned at the first is that the applied load is 100 N, the base radius =50 mm, the follower radius is 15mm unless referred by other value, the face width is unity or clarified for different value, the modulus of elasticity is 200 GPa for cam and follower and showed for different values.

5.1 Analytical Results

According to the Hertz contact stress and area equations the results have been shown in **Fig. 5** and **Fig. 7**. It is clear that the contact stress decreased as a result of the increasing of the angular position and then return to its initial value while the contact area trends to behave in counter way and the cause behind such behavior is the variation of the radius of curvature as shown in **Fig. 6** which change from 50 mm at the base region to be 75 mm at the upper dwell region. It is evident that the follower of larger radii well enhances the contact stress values and that returned to the high contact area associated with the larger follower.

Fig. 8 implies the contact principal stresses distribution into the cam and how it decreases along the two contacting surfaces normal. The first and second max. principal stresses are equal to the max. contact stress at the contacting surfaces while the von mises equal to one sixth of the contact stress.

Fig. 9 shows the max. contact stress values for different cam face widths and for several follower radii. The increasing of the follower radius and cam face width increases the width and the length of the contact area respectively leading to decrease the max. induced stress.

Fig. 10 relates the effect of the cam and follower modulus of elasticity to the max. contact stress and clarify its increasing negative role for cam and follower, because the higher modulus means a lower deformation ability leading to lower contact area , where E_R is the ratio of the follower modulus of elasticity to that of the cam.

5.2 Numerical Results

The max principal stress in **Fig. 11** has max compressive value of 552 MPa and it is equal to the max. contact stress shown in **Fig. 12** , these results conform the results shown in **Fig. 5** and **Fig. 8**. The distribution of the von mises stress is shown in **Fig.13** with its max value equal to 408 MPa and equal to 0.7 of the max contact stress and that confirm the results in **Fig.8**. the distribution of the normal deformation within the cam and follower domain is shown in **Fig.14**

5.3 Experimental Results

The photoelastic pattern of stress analysis for three loaded cases are shown in **Fig.15**. The applied load are (a) 0.2, (b) 0.3, (c) 0.4 Kg and (d) is also 0.2 Kg but with scale 1:1, the resulting pattern are shown in the three figures. Depending upon Eq. (13) the left hand side could be gotten from Eq's. (6,7) by substituting the equivalent depth to the fringe order and find the difference between the 1^{st} and 2^{nd} principal stresses. **Table 3** summarized the experimental and theoretical results with the error percentage for the three cases.

The experimental principal stress differences have been measured depending on **Fig. 15** for the three loading cases by measuring the fringe orders and its y position. The N^{th} order will be substituted in Eq.(13) to find the experimental measurements as in fifth column in **Table 3** while the measured y values are substituted in Eq's. (6,7) to evaluate the theoretical first and second principal stresses (6^{th} and 7^{th} columns in **Table 3**) in terms of Eq's. (4,5) which in turn have been calculated for the same experimental loads of **Table 3**. The theoretical principal stress differences have been listed in 8^{th} column. The experimental and theoretical results percentage error have been shown in the last column.

The max percentage of error is 10% and justified by the manufacturing and calibration errors.

6. CONCLUATION

From the whole results there are some concluding remarks which can be withdrawn such.

Follower radius plays the key role in controlling the contact stress because of its smaller value and its variation will not affect the stroke. The low levels of modulus of elasticity minimize the chances of contact failure. The larger radius of curvature leads to smaller contact stress for both of the mating surfaces. Increasing the face width has a positive effect on the contact stress reduction. The max. principal stress at the contacting surfaces equal to the max. contact stress while von mises equal 0.6. The increasing of the applied load do not always leads to generate more photoelastic pattern but always shift them away of the contacting surfaces

REFRENCES

- Anvoner S. , 1959, *Theory of machines*, book.
- Akkamahdev G Chanagond., Raut L. B. 2015, *Finite Element Analysis of Roller Cam by Optimization of Surface Contact Area*, International Journal of Advanced Engineering Research and Studies.
- Hearn E. J, 2001, *Mechanics of Materials 2,*book, Third edition.
- Johnson, K, L, 2003, *Contact mechanics*, book
- James W. Dally, William F. Riley, 1991, *Experimental stress analysis*.
- Oberg Erik, Franklin D. Jones, Holbrook L. Horton, and Henry H. Ryffel, 2000, *Machinery's Handbook*, 26th Edition.
- Helena Jin, Cesar Sciammarella, Sanichiro Yoshida, Luciano Lamberti, 2014, *Advancement of Optical Methods in Experimental Mechanics*, Book, Volume 3.

NOMENCLATURE

b : contact zone half width (m).

E_c , E_f : cam and follower Modulus of elasticity , respectively (N/m^2).

F : applied load (N).

f : fringe value.

I : second moment of area (m^4).

L : length (m).

N : fringe order.

P_{max} : maximum contact pressure (N/m^2).

r_b : base radius of cam (m).

r_c , r_f : cam and Follower radius of curvature , respectively (m).

S : cam stroke (m).

t : face width (m).

v : follower velocity (N/m).

a : follower acceleration (m/s^2).

θ : angular position (degree).

σ_1 , σ_2, σ_3 : principal stress (N/m^2).

σ_c : contact stress (N/m^2).

v_f , v_c : poisson's rations.

τ_1 , τ_2 , τ_3 : principal shear stress(N/m^2).

δ: maximum beam deflection (m).

β : rising or falling angle (degree).

Table 1. Experimental modulus of elasticity

Mass(g)	100	200	300	400	500	600
δ (mm)	0.32	0.615	0.88	1.15	1.52	1.95
E (MN/m^2)	3.8981*10^6	4.0566*10^6	4.2525*10^6	4.3388*10^6	4.1033*10^6	3.8401*10^6

Table 2. Experimental fringe value

Load (F), N	Fringe Order (N)	Fringe Value (*f*)
0.245	1	229.68
0.49	1.9	241.77
0.74	3.1	222.27
0.981	4	229.68

Table 3. Experimental and theoretical cam stresses

P(Kg)	N	y'(scale depth) (mm)	y (real depth) (mm)	N*f/t (N/m^2)	σ_1 theoretical (N/m^2)	σ_2 theoretical (N/m^2)	(σ_1- σ_2) theoretical	Error %
0.2	1	14	4.375	38333.33	-43138.85	-1089.35	42049.5	8.8
	2	5	1.5625	76666.67	-93827.047	-14111.9	79715.179	3.97
0.3	1	25	7.8125	38333.33	-37195.462	-453.744	36741.718	4.3
	2	9	2.8125	76666.67	-89933.846	-7320.69	82613.157	7.1
	3	4.4	1.375	115000	-133969.77	-31610.7	102359.07	10
0.4	1	46	10.22	38333.33	-38112.201	-364.1857	38476.387	0.38
	2	21	4.6667	76666.67	-78091.454	-3342.614	81434.072	5.8
	3	13	2.889	115000	-112677.27	-11152.02	123829.28	7.1

Figure 1. Pure bending test specimen.

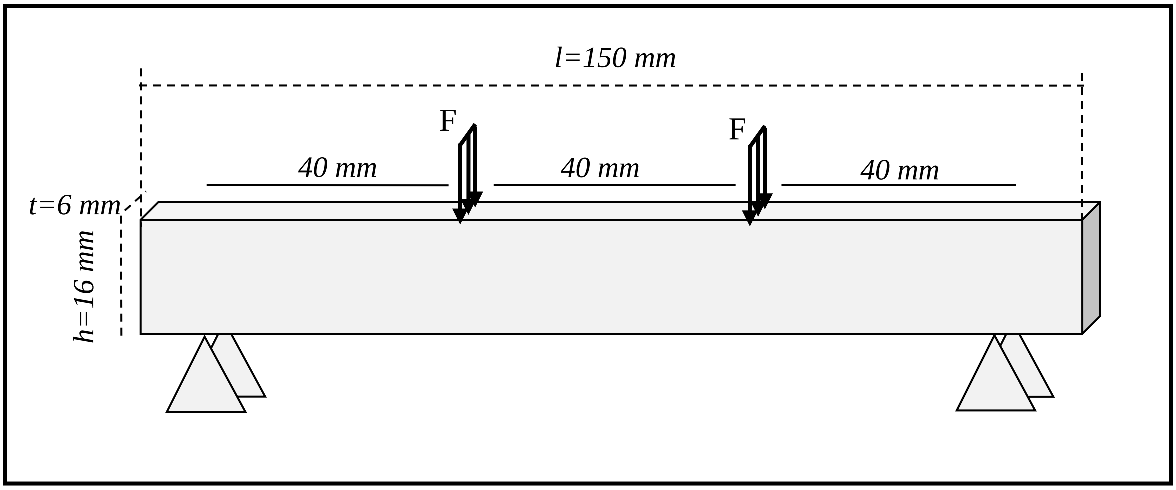

Figure 2. Dimension of pure test specimen with the position and value of the applied load

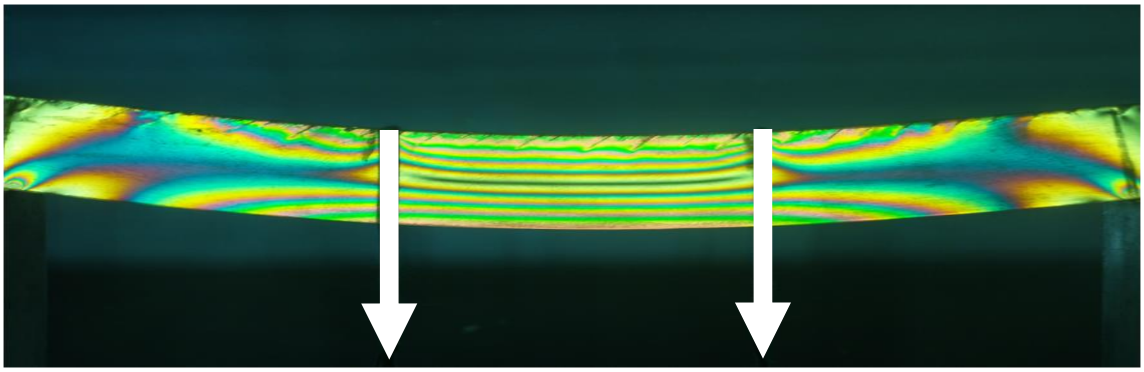

Figure 3. Photoelastic pure bending stress fring test

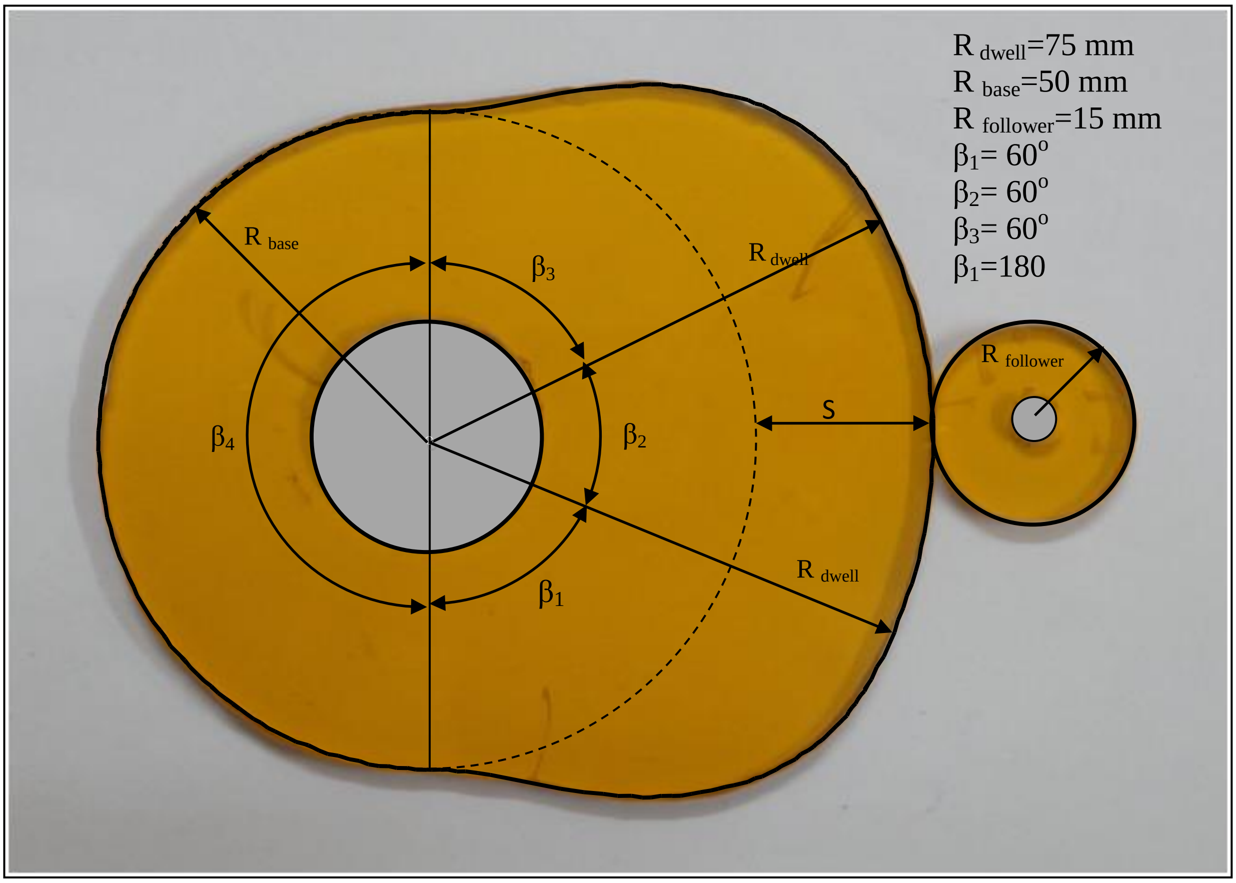

Figure 4. Experimental photoelastic cam and follower model

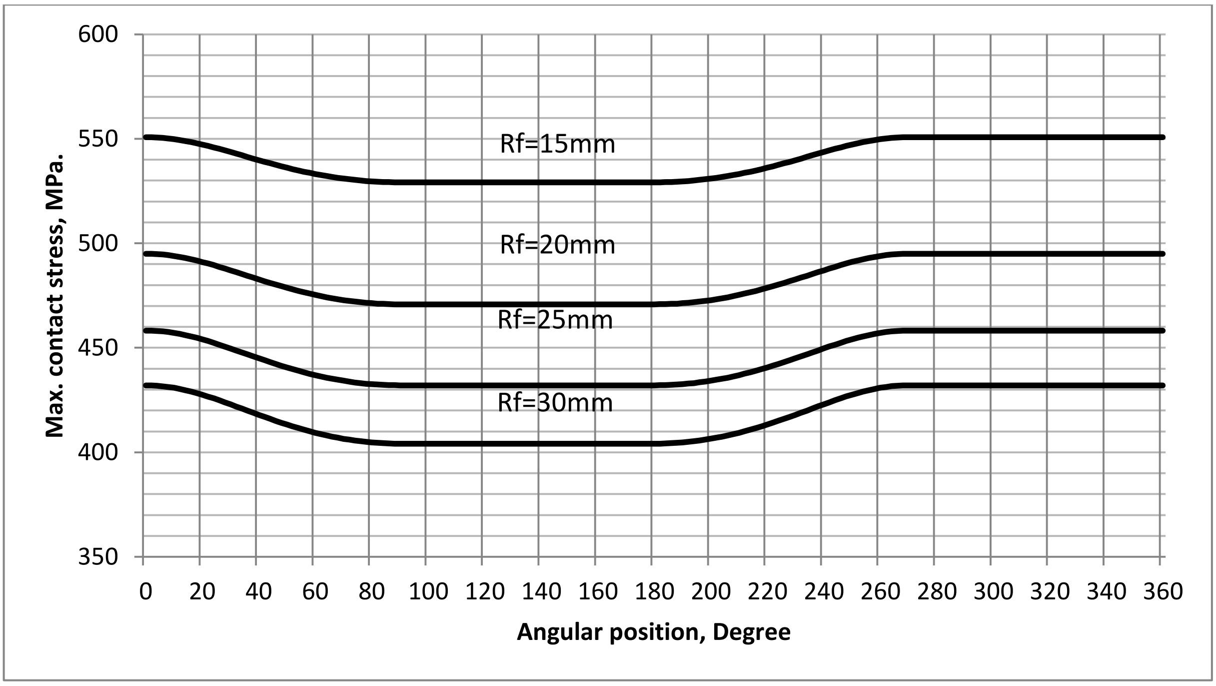

Figure 5. The variation of the contact stress with angular position for different follower radii

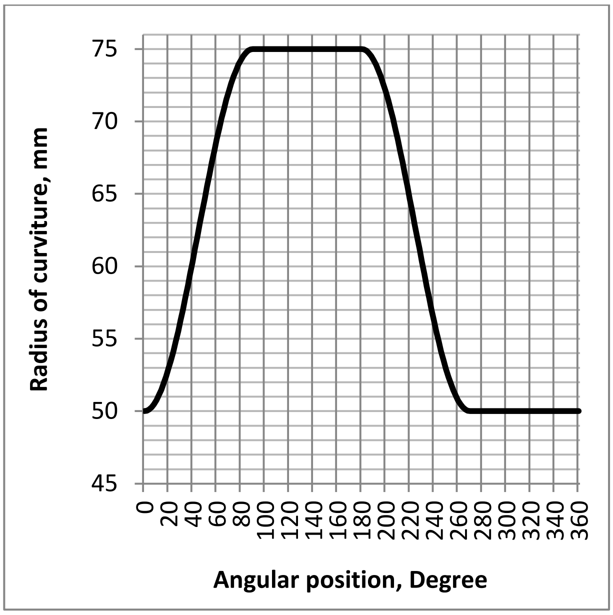

Figure 6. The variation of the cam radius with respect to the angular position

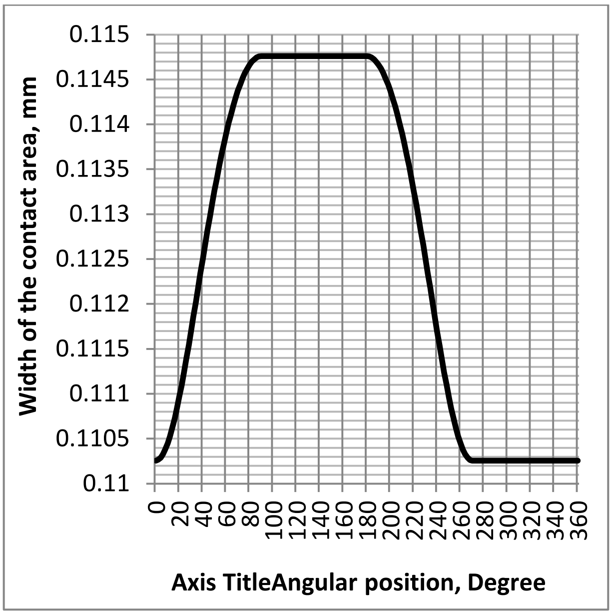

Figure 7. The contact zone half width dimension change with the angular position

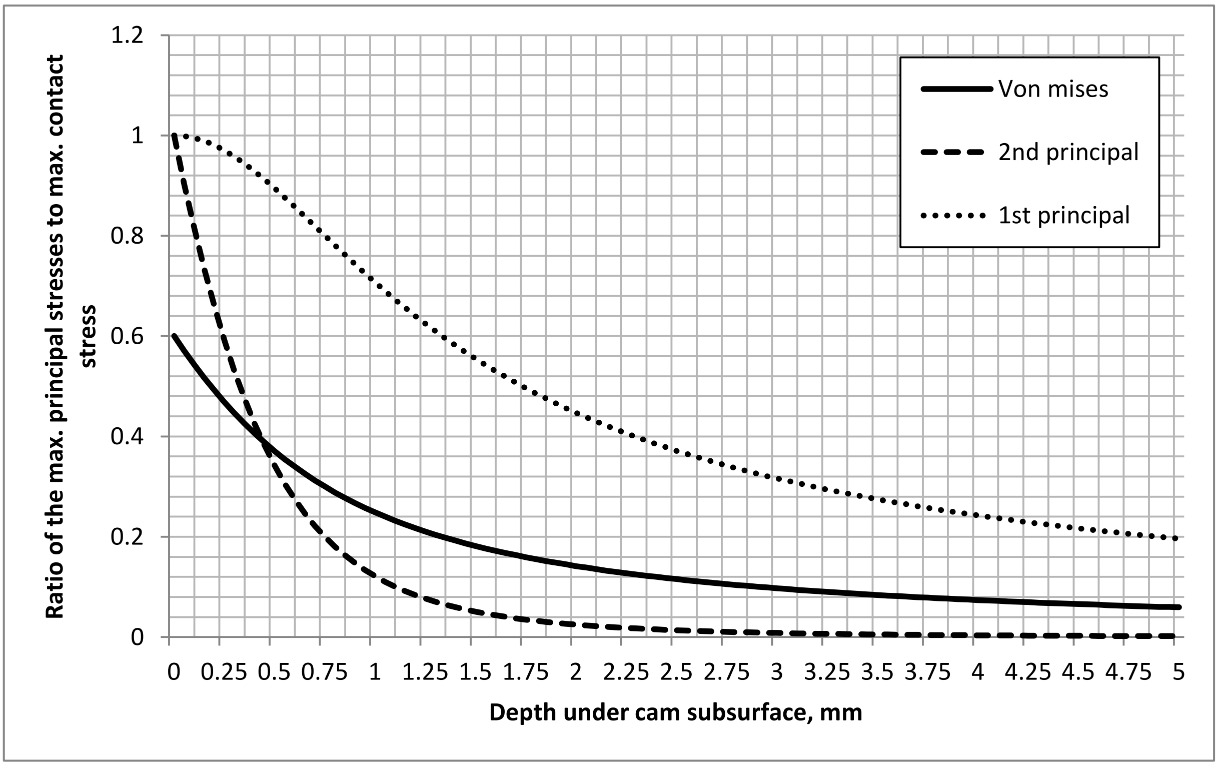

Figure 8. The ratio of the different principle stresses to the maximum contact pressure

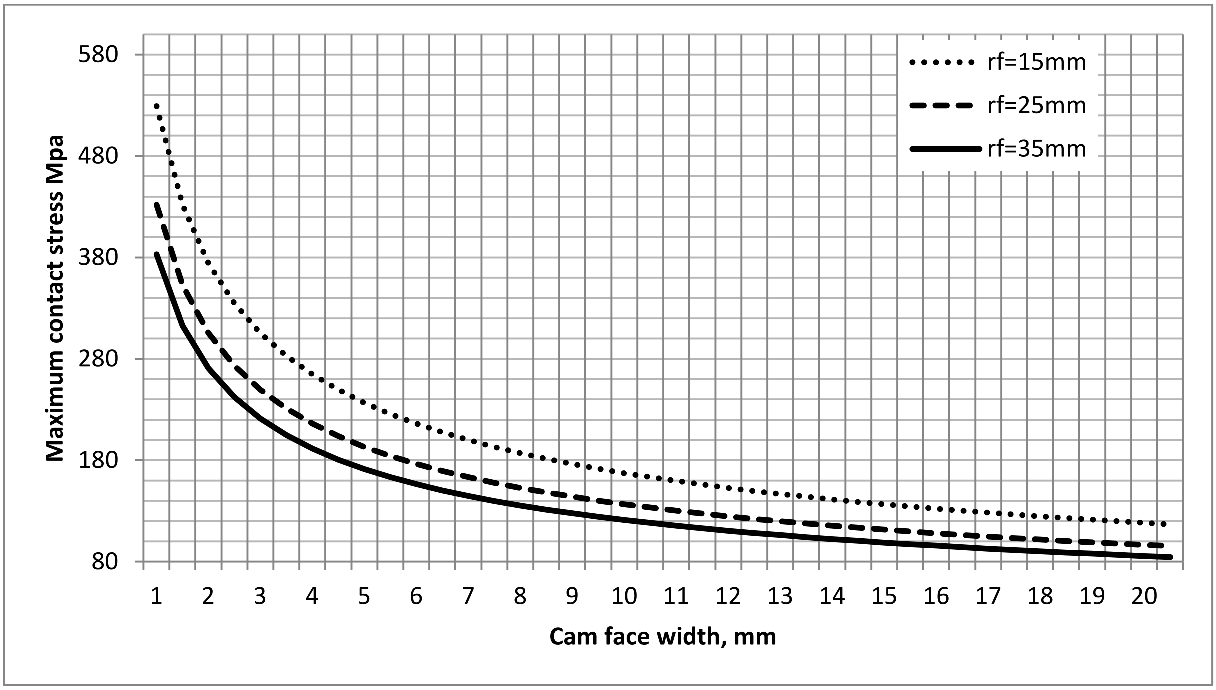

Figure 9. Trace the effect of the cam face width on the maximum contact stress

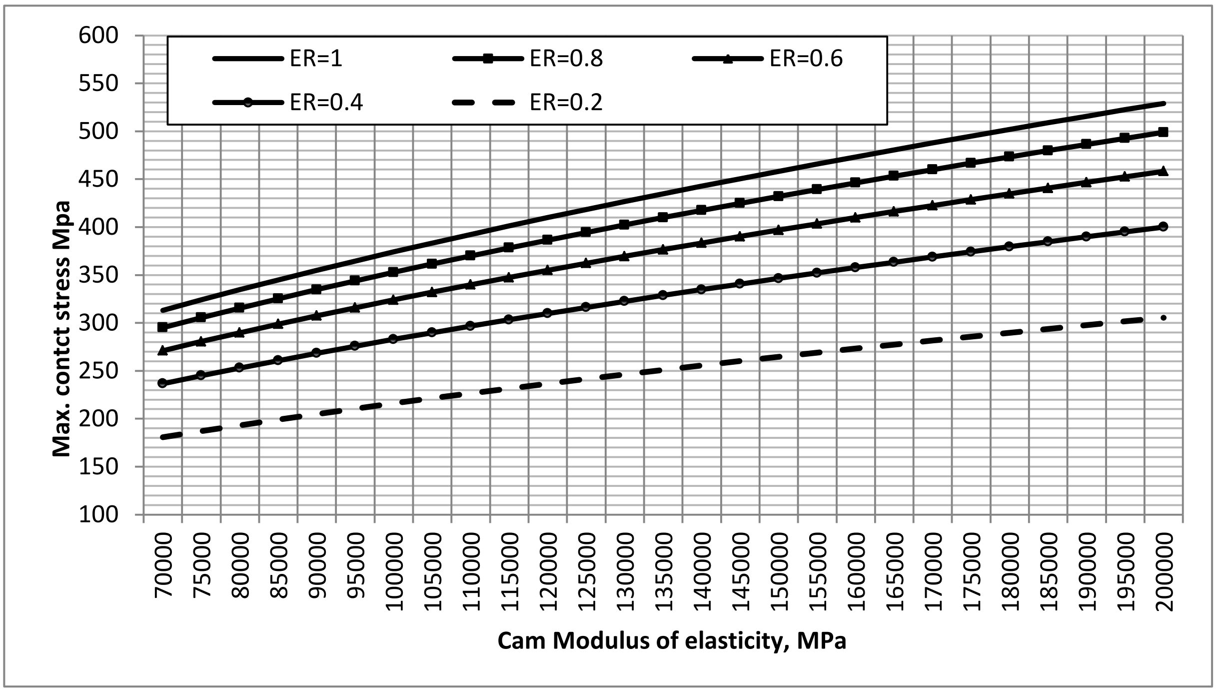

Figure 10. Variation of the maximum contact stress with the change of the modulus of elasticity

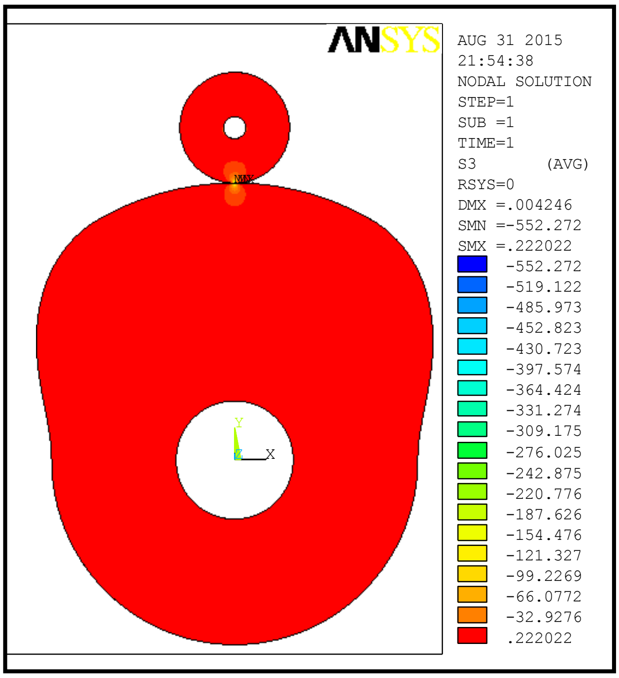

Figure 11. Maximum principal stress

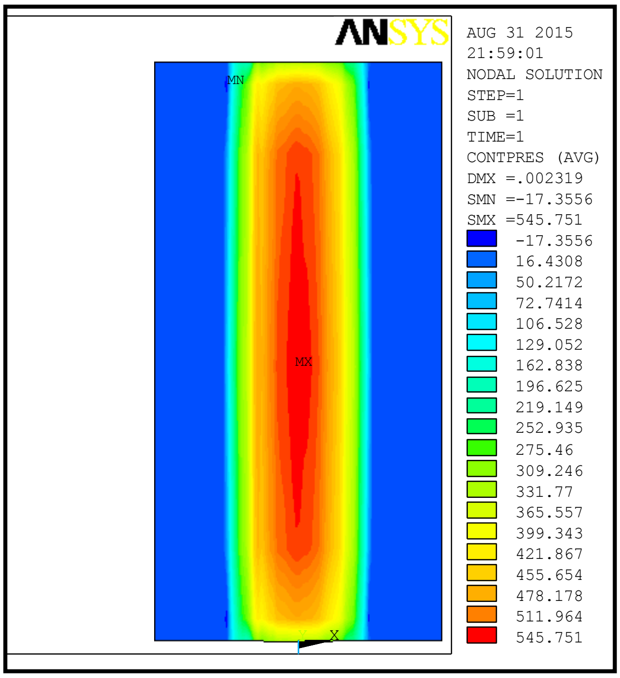

Figure 12. Contact area and contact stress distribution

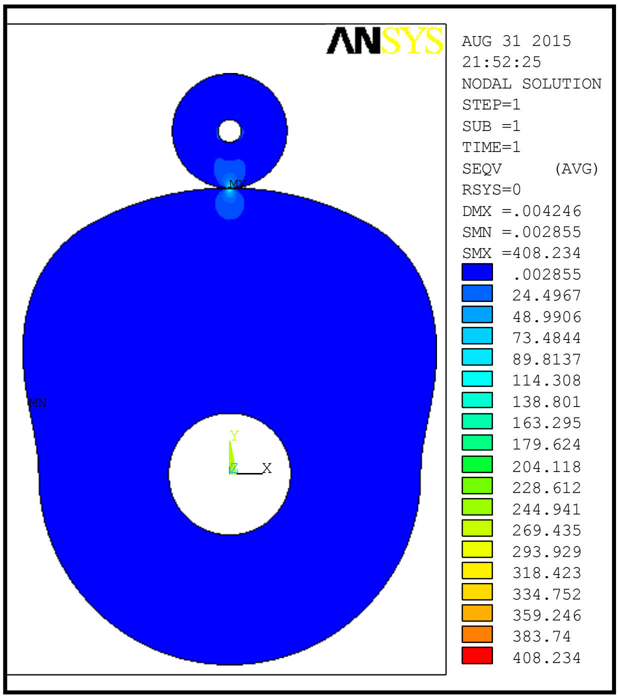

Figure 13. Von mises stress distribution

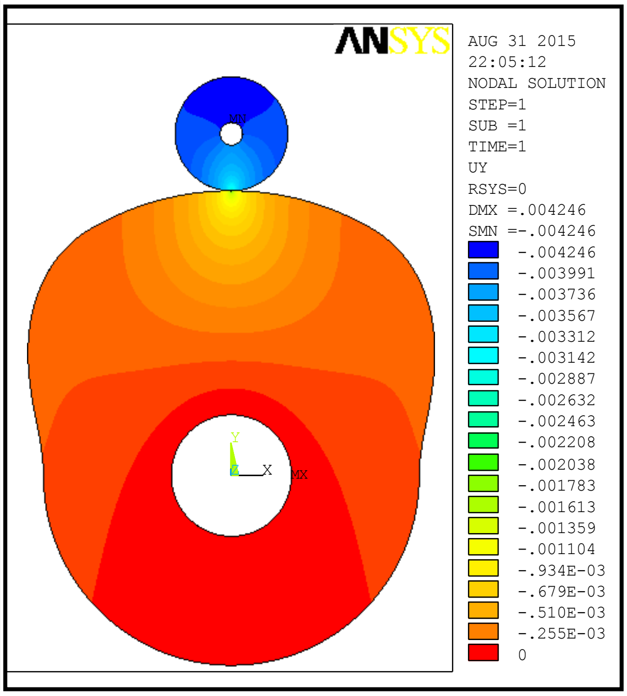

Figure 14. Y- component cam deformation

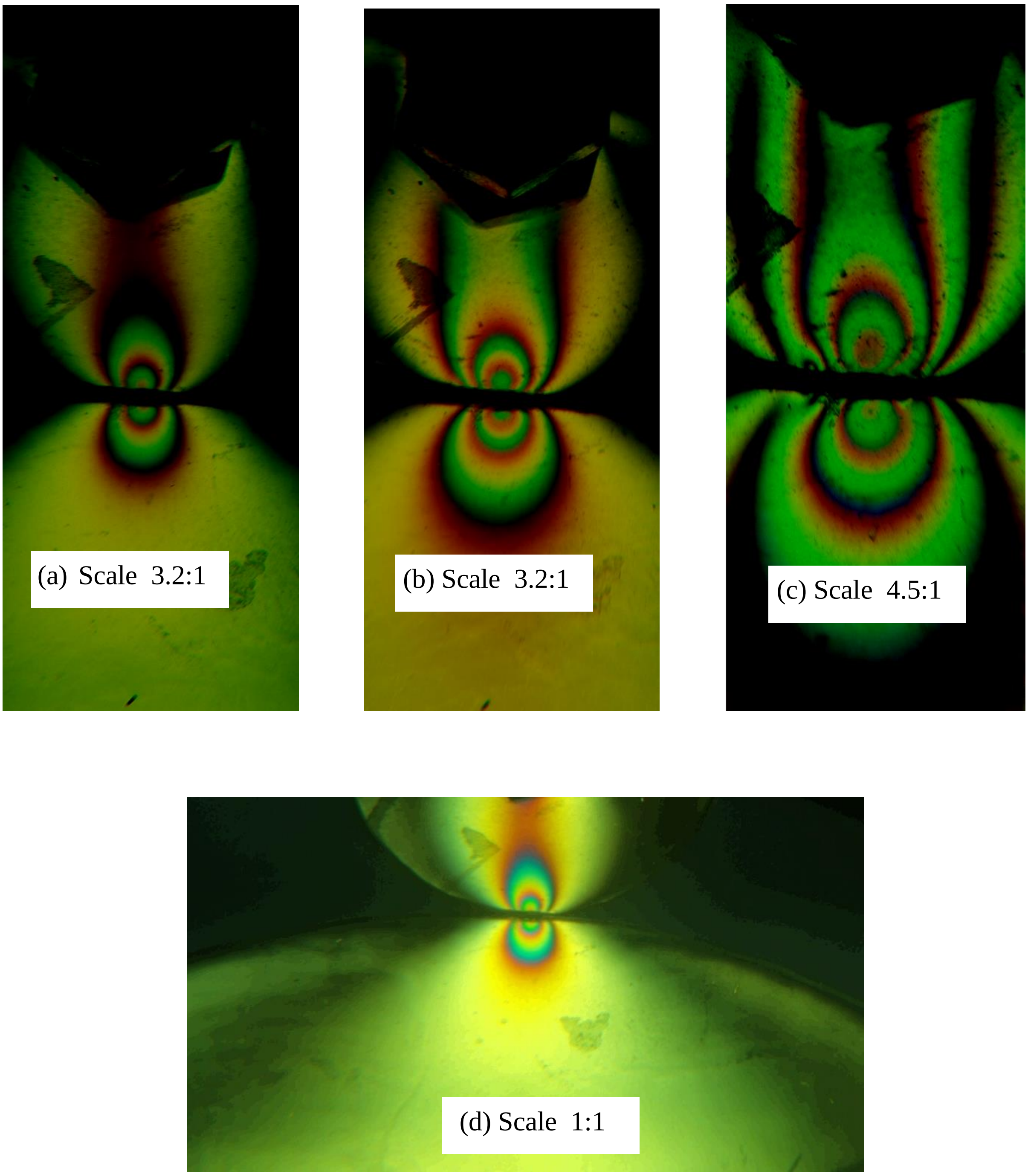

Figure 15. Photo elastic stress pattern when the load is
(a) 0.2 Kg , (b) 0.3 Kg , (c) 0.4 Kg, (d) 0.2 Kg with scale 1:1

Semantic Similarity Assessment of Volunteered Geographic Information

Dr. Maythm Al-Bakri
Lecturer
Department of Surveying
College of Engineering
University of Baghdad
Email: m.m.s.albakri@gmail.com

ABSTRACT

The recent development in communication technologies between individuals allows for the establishment of more informal collaborative map data projects which are called volunteered geographic information (VGI). These projects, such as OpenStreetMap (OSM) project, seek to create free alternative maps which let users add or input new materials to the data of others. The information of different VGI data sources is often not compliant to any standard and each organization is producing a dataset at various level of richness. In this research the assessment of semantic data quality provided by web sources, e.g. OSM will depend on a comparison with the information from standard sources. This will include the validity of semantic accuracy as one of the most important parameter of spatial data quality parameters. Semantic similarity testing covered feature classification, in effect comparing possible categories (legend classes) and actual attributes attached to features. This will be achieved by developing a tool, using Matlab programming language, for analysing and examining OSM semantic accuracy. To identify the strength of semantic accuracy assessment strategy, there are many factors should be considered. For instance, the confusion matrix of feature classifications can be assessed, and different statistical tests should be passed. The results revealed good semantic accuracy of OSM datasets.

Key words: OpenStreetMap; Semantic; Classification; Accuracy; Confusion Matrix

تقييم دقة تصنيفات عوارض الخرائط المُنتجة على الشبكة العنكبوتية

م.د. ميثم مطشر شرقي
قسم هندسة المساحة
كلية الهندسة / جامعة بغداد

الخلاصة

سمحت التطورات الأخيرة في تكنلوجيا جمع المعلومات والإتصالات بين الأفراد لتأسيس وإنتاج الخرائط التعاونية الغير رسمية على الشبكة العنكبوتية والتي تسمى بالمعلومات الجغرافية المنتجة من قبل المتطوعين. إن هذه المشاريع، مثل خارطة الشارع المفتوح (OSM) تسعى لانتاج خرائط مجانية بديلة للخرائط التي تنتج من المصادر الحكومية الرسمية. غالبا ما تكون البيانات المنتجة من المصادر المختلفة للبيانات المكانية المجانية غير متوافقة مع أي معيار وكل مجموعة من المتطوعين تنتج بيانات على مستويات مختلفة من الدقة والنوعية. يهدف هذا البحث إلى تقييم جودة التصنيفات الاسمية للعوارض المنتجة للخرائط على الشبكة العنكبوتية. لقد تم مقارنة البيانات الاسمية المنتجة من خارطة الشارع المفتوح (OSM) مع المعلومات من المصادر القياسية مثل المسح الحقلي. إن هذا الفحص يتضمن مقارنة تسميات العوارض الطبيعية والصناعية المعرفة ضمن مفتاح الخارطة او العناصر المرفقة كجداول مع البيانات الجغرافية. لإنجاز ذلك تم بناء برنامج متخصص باستخدام لغة الماتلاب لقياس وتحليل دقة البيانات

الاسمية لخارطة الشارع المفتوح (OSM) ، ولتحديد قوة استراتيجية الاسلوب المتبع في هذه الدراسة هناك عدة عناصر يجب أن تؤخذ بنظر الاعتبار مثل تكوين وتقييم مصفوفة التمييز الإسمي فضلاً عن إجراء فحوصات احصائية متعددة. لقد أظهرت نتائج البحث في هذه الدراسة إن دقة التصنيفات الإسمية لخارطة الشارع المفتوح جيدة الى حدٍ ما.

1. INTRODUCTION

Traditionally, professional surveyors seek to produce geospatial data through different methods such as plane surveying, remote sensing and photogrammetry. The data captured by these methods can usually ordered by users in digital or paper formats. However, recently by web developments, a free geospatial data based on volunteers' efforts have appeared on the Internet, **Esmaili, et al., 2013**. **Goodchild, 2007** termed this phenomenon as volunteered geographic information (VGI). Most VGI data are collected and distributed through the World Wide Web (www) by non-professionals users. Compared to authoritative datasets, the VGI data are freely and dynamically grown with the help of volunteers. The dynamic aspect of VGI service encouraged some mapping agencies and local authorities to utilize VGI to create new datasets and update their data. There are a broad categories of VGI sites are now available on the Internet. Such websites include Google Map, Flickr, Map share, Wikimapia and OpenStreetMap (OSM). The data from OSM project was investigated and analysed in this study because the OSM data can be downloaded easily and freely which makes it ideal for research.

The OSM project was founded in London UK in 2004. The OSM data are essentially collected using GPS receivers, and then transformed into map using online editing tools. After 2006, Yahoo started supplying free satellite images to OSM community; therefore mapping becomes achieved directly from the images, **Ma, et al., 2015**. The OSM is a collaborative mapping project which creates a free editable map for the whole world. The OSM project can be easily shared under its "Open Data Commons Open Database License (ODbL)", **Dorn, et al., 2015**. Despite the positive aspects of OSM data, the quality assurance of its data is still the major concern of geographical information (GI) users. In recent years, VGI quality has been interesting topic in GIS research. One of the first systematic attempts to assess OSM quality was conducted by **Haklay, 2010**. In addition to Haklay, a large and growing body of literature has investigated the quality of OSM project; see for example **Liu, et al., 2015**; **Sehra, et al., 2014; Koukoletsos et al., 2012**. Although these studies analysed the accuracy of OSM data compared to commercial or authoritative datasets, however the OSM data poses challenges regarding the heterogeneity of classifications or semantic data.

To date, several studies have begun to examine the semantic accuracy of OSM project. For instance, **Vandecasteele** and **Devillers, 2013** suggested a method for reducing the semantic inconsistency and improving the semantic data of OSM project. The method was implemented into a plugin for OSM and different examples illustrate how this plugin can be used to enhance the quality of VGI data. In another major study, **Ramos, et al., 2013** presented a procedure to measure the similarity between the correspondence features in OSM and official datasets. The proposed method was based on using ontologies for handling semantic heterogeneities. In a study conducted by **Ballatore, et al., 2013,** it was described a knowledge-based technique to identify the semantic similarity of lexical definitions. In the same view, **Girres,** and **Touya, 2010** assessed the semantic accuracy of 585 roads in OSM data compared to BD TOPO Large Scale Referential (RGE) from IGN as a reference data. The analysis showed that the percentages of correct classifications are varying for different classifications. For example motorways have 100% semantically correct, whereas the secondary roads have only 49% similarity.

The objective of this study is to evaluate the semantic accuracy of the OSM "tag" also called "features". The main idea is developing a methodological framework based on a confusion matrix approach to determine the classification accuracy using all of the information diversity of OSM project. The reminder of this article is structured as follows: section 2 describes the main characteristics of the features of OSM data. Section 3 presents the approaches for estimating classification accuracy. The discussion of the system prerequisites and code program will be introduced in section 4. In section 5, the results and findings are illustrated and analysed. The last section concludes with a discussion and provides an outlook on future research.

2. THE FEATURES OF OPENSTREETMAP DATA

The OpenStreetmap (OSM) is not the only source of feature classifications data that is available free of charge. Services such as Google Maps, Yahoo Maps, or the Microsoft offering Bing maps have very good mapping available for viewing via the Internet, and they do not require payment. In 2008, Google introduced "Map Maker", an edition that allows users to trace maps data from satellite or aerial imagery and upload it to Google servers. Google is using map maker primarily in countries, such as Iraq, where they cannot buy suitable map data from the traditional geodata supplier. All these offerings only very limited rights to the users for downloading maps with feature classifications. If users would like to add features to web maps, for example, these free

Internet sources are usually not usable. With OpenStreetMap, on the other hand, any form of reproduction or processing is allowed, and users do not have to ask anybody for permission.

The objects of OSM data may be classified into two most important types: nodes (also called points) and ways. A node consists of geographical coordinates (latitude and longitude), while a way consists of an ordered list of at least two nodes. Attributes assigned to these objects in order to describe what they represent are called tags. A tag consists of a key and a value and is usually written with an equals sign between both parts “key=value”. Both can be arbitrary strings of up to 255 characters. The most important tags from OSM map features may be divided into a number of groups such as roads and railways; forests, lakes, and rivers; coastline and islands; buildings and land use areas; villages, cities, and borders, **Ramm, et al., 2011**. An example of OSM tags or classifications can be seen in **Fig 1**.

The OSM data can be exported directly in a variety of data formats such as XML data or Mapnik image (e.g. PNG, JPEG, and PDF). The OSM raw data can be processed with suitable OSM software. This export has a size limit; users can only use it if they are looking at a reasonably small area of the map (approximately 10km x 10km), **Ramm, et al., 2011**. In this research the OSM data was exported as XML format, and it was imported using ArcGIS 9.3 software for processing and manipulating. In order to obtain the required features, a pre-processing (filter) step was adopted. This step was essentially applied for separating the undesired data from attribute table.

3. APPROACHES FOR ESTIMATING CLASSIFICATION ACCURACY

3.1 Confusion (Error) Matrix

An error or confusion matrix evaluates classification accuracy based on comparing actual or reference land class with map data. The matrix has tow dimension with the same number of rows and columns. The rows and columns express the labels of samples assigned to a particular category in one classification relative to the labels of samples assigned to a particular category in another classification **(Fig. 2)**. Each column is assumed to be correct and display the ground reference information, while each row of the matrix represents the map labels obtained from map classifications. The main diagonal of the matrix represents the correct feature classifications, **Congalton and Green, 2009**.

Confusion matrix can be considered one of the most effective ways to represent classification accuracy. This is because that error matrix can describe the accuracy of each map category based on omission and commission errors. The error of omission refers to the proportion of observed features excluded from map classes, whereas commission error arises when features on map are categorised incorrectly. Besides the omission and commission errors, the overall, producer's and user's accuracy can also be determined by confusion matrix, **Ismail** and **Jusoff, 2008.** The overall accuracy represents the summation of elements on the main diagonal of confusion matrix divided by the total number of samples of confusion matrix. The user's and producer's accuracies are simply the ways of computing individual accuracy rather than calculating overall accuracy, as will be discussed in the following section.

3.2 Mathematical Representation of the Error Matrix

Suppose that there is a square matrix with k^2 cells and n samples. Each sample represents one of k class in a map data, and one of the identical k class in the reference classifications, let n_{ij} symbolize the amount of samples classified into category i (where: i = 1,2,......, k) in the map data and category j (where: j = 1,2,....., k) in the reference classes , **Congalton and Green, 2009**, (as shown in **Fig. 2**).

Let:

$$n_{i+} = \sum_{j=1}^{k} n_{ij} \tag{1}$$

Be the number of samples classified into category i in the map classification, and

$$n_{+j} = \sum_{i=1}^{k} n_{ij} \tag{2}$$

Be the number of sampled classified into category j in the reference data set.

Overall accuracy between map classification and the reference data can be computed as follows:

$$overall\ accuracy = \frac{\sum_{i=1}^{k} n_{ij}}{n} \tag{3}$$

Producer's accuracy can be computed by:

$$producer's accuracy\ j = \frac{n_{jj}}{n_{+j}} \tag{4}$$

And the user's accuracy can be computed by:

$$user's accuracy = \frac{n_{ii}}{n_{i+}} \tag{5}$$

In addition to the above models, kappa coefficient can also be used as an index of classification accuracy, as follows:

$$\kappa = \frac{N\sum_{i=1}^{r} x_{ii} - \sum_{i=1}^{r} x_{i+}.x_{+i}}{N^2 - \sum_{i=1}^{r}\left(x_{i+}.x_{+i}\right)} \tag{6}$$

Where:

$r = number\ of\ rows\ in\ the\ error\ matrix.$

$x_{ii} = number\ of\ observations\ in\ row\ i\ and\ coloumn\ i\ (on\ the\ major\ diagonal).$

$x_{i+} = total\ of\ obsevations\ in\ row\ i\ (shown\ as\ marginal\ total\ to\ right\ of\ the\ matrix).$

$x_{+i} = total\ of\ observations\ in\ column\ i\ (shown\ as\ marginal\ total\ at\ bottom\ of\ the\ matrix).$

$N = total\ number\ of\ observations\ included\ in\ matrix.$

4. METHODOLOGY IMPLEMENTATON AND PROGRAM STRUCTURE

To achieve the main goal of this research, the classifications quality of OpenStreetMap (OSM) information must be checked carefully. It is indispensable because the information of different Volunteered Geographic Information (VGI) data sources are often not complaint to any standard and each organisation is producing a dataset at various level of richness. In this study the assessment of classifications quality of data provided by web sources will base on comparison with the information from other sources. In other words, utilizing the information from sources with known quality of data to evaluate the quality of data provided by sources with unknown quality of data. As **Thakkar, et al., 2007** observed in relation to VGI data sources and high quality sources, using this technique can produce the most accurate results. Assessment of attribute and feature based accuracy will be undertaken using statistical indices based on, for example, kappa coefficients (as described in previous section). It is proposed that the true or actual classifications by field surveying are to be used for geospatial data collecting of selected location (Baghdad / Iraq). The data set will consist of the self-generated field survey and the open access data from web-based VGI (e.g. OSM).

The intention is to compare classifications of these datasets. Initially this can be done with visual comparison of derived maps, to get a general picture but the methods indicated above will be applied to construct a quantitative approach, identifying the strength of accuracy assessment strategy. This exercise will help in developing methods of evaluating classification quality based on a rule set, coded into the data handling flowline. The result will be a set of operators which can measure data quality, allow for the preparation of datasets prior to successful integration, and actually undertake the integration of data. The proposed methodology was developed using Matlab 7.10.0 programming language, for academic and research purposes. In the first step the program inputs the features name or classifications through read a data file. Then, the input data will be employed to generate the confusion matrix by comparing the feature classes in reference and tested datasets. Subsequently, the program saved the completed confusion matrix and assessed the accuracy of classification data. The assessment processing based on determining the produce, user, an overall accuracy and kappa coefficient values. The report of final outcome can be exported and saved as text (.txt) or excel (.xlsx) format. **Fig. 3** presents the flowchart of the program that used in implementing the methodology of this study.

5. EXPERIMENT AND ANALYSIS

In this research, the obtained confusion matrix constructed from 543 features and 16 classes as shown in **Fig. 4**. In this matrix the x-axis represented the true (reference) class labels, whereas the y-axis listed the tested classes. The correct classifications lay on the main diagonal of the matrix, while the other elements of the matrix showed the misclassifications. The overall number of classifications can be seen in the bottom right cell. The accuracy measurements of confusion matrix have been achieved based on equations 3, 4, 5 and 6 as follows:

$$Overall\ accuracy = \frac{\sum_{i=1}^{k} n_{ij}}{n}$$

$$Overall\ accuracy = \frac{6+10+56+28+168+2+17+141+1+3+11+2+2+6+13+3}{543}$$

$$= \frac{469}{543} = 86\%$$

$$Producer's accuracy\ j = \frac{n_{jj}}{n_{+j}}$$

$$Producer's accuracy\ (Primary\ road) = \frac{6}{11} = 55\%$$

The procedure's accuracy of the primary road is one example for determining the procedures' accuracy in this article. Figure 5 shows the procedure's accuracy of other features.

$$User's accuracy = \frac{n_{ii}}{n_{i+}}$$

$$User's accuracy\ (Primary\ road) = \frac{6}{11} = 55\%$$

The user's accuracy of the primary road is one example for determining the users' accuracy in this article. Figure 6 shows the users' accuracy of other features.

To illustrate the computation of kappa coefficient (k) for the error matrix included in **Fig. 4**:

$$\sum_{i=1}^{r} x_{ii} = 6 + 10 + 56 + 28 + 168 + 2 + 17 + 141 + 1 + 3 + 11 + 2 + 2 + 6 + 13 + 3 = 469$$

$$\begin{aligned}\sum_{i=1}^{r}(x_{i+}.x_{+i}) = {} & (11 \times 11) + (19 \times 13) + (66 \times 77) + (29 \times 28) + (170 \times 181) + (3 \times 2) \\ & + (22 \times 18) + (164 \times 157) + (1 \times 2) + (3 \times 3) + (11 \times 13) + (2 \times 3) + (2 \times 2) \\ & + (19 \times 7) + (17 \times 22) + (4 \times 4) = 121 + 247 + 5082 + 812 + 30770 + 6 + 396 \\ & + 25748 + 2 + 9 + 143 + 6 + 4 + 133 + 374 + 16 = 63869\end{aligned}$$

$$k = \frac{543(469) - 63869}{(543)^2 - 63869} = \frac{190798}{230980} = 0.826$$

The accuracy assessment reports of OSM classifications from 543 reference data are illustrated in Figure 4, 5, and 6. The results showed that the overall accuracy of the tested data was 86%, where the lowest user and procedure accuracy were 32% and 50%, respectively, and the highest user and procedure accuracy were similar with 100%. The classification accuracy is vary and different from one class to another class. For instance, primary road has only 55% accuracy since it was confused with secondary road, service road, and path. The path has only 77% accuracy since it was confused with building. Another example of this is the building which has 90% accuracy since it was confused with secondary road, service road, parking and university. The most likely causes of diverse classification accuracy are because the wrong way for classifications of some of OSM datasets.

The kappa coefficient was also determined from the calculations of tested features and classes. This represents that the kappa statistics value of 0.826 which implies a credible 82% better accuracy than if a random unsupervised classification was adopted. According to **Landis** and **Koch, 1987**, the agreement scale of Kappa value as k>0.75 present excellent, 0.4<k<0.7 present good, and k<0.4 present poor. In another major study, **Monserud, 1990**, reported that the Kappa statistic is poor when k<0.4, fair when 0.40<k<0.55, good when 0.55<k<0.70, very good when 0.70<k<0.85, and excellent when k>0.85. In general, therefore, it seems that the kappa coefficient value of this study demonstrated an excellent to a very good agreement.

6. CONCLUSION

The OpenStreetMap (OSM) is one of the most popular projects of Volunteered Geographic Information (VGI) services. The OSM produced geospatial data by non professional volunteers of varying level of mapping experience. The OSM data does not follow any standard compared to authoritative or official datasets; therefore it's necessary to evaluate its quality continuously. The purpose of the current study was to present a method for assessing the quality of (OSM) semantic data. The methodology was implemented by designing a program using Matlab 7.10.0 programming language. The program was utilised in the assessment of classification accuracy of feature categories of OSM data. This was included the construction of confusion matrix and calculating the overall accuracy, users' accuracy, producers' accuracy and kappa coefficient.

The outcome of this investigation showed that the confusion matrix consisted of 543 elements, which is formed as 16 rows and 16 columns (as illustrated in Fig.4). The number of elements in each row and column are varying and different based on the number of features in each class. For instance there are eleven elements in the first column. These classified as six primary roads, three secondary roads, and two residential roads. Another example of what is meant by different elements of rows and columns of confusion matrix is the fifth row contains 170 elements. These distributed as two primary roads, and one hundred and sixty eight as residential roads. The research has also found that the overall accuracy was 86%; the users' accuracy was between 32% and 100%, while producers' accuracy was between 50% and 100%, and kappa statistics was 0.826. In general, therefore, it seems that the classification accuracy of OSM datasets is acceptable to some extent.

For future work, it is recommended that the further studies need to be carried out in order to apply this method with different data sources such as governmental agency data, Google map, and Wikimapia. Testing semantic accuracy of several geospatial data source can give an idea about the possibility of integrating different geospatial datasets to improve and enhance its quality. It is also suggested that the classification of OSM data can be investigated and assessed based on ontologies and definitions of online dictionary.

REFERENCES

- Ballatore, A., Wilson, D., and Bertolotto, M., 2013, *Computing the Semantic Similarity of Geographic Terms using Volunteered Lexical Definitions*, International Journal of Geographical Information Science, Vol. 27(10), PP. 2099–2118.

- Congalton, R. G. and Green, K., 2009, 'Thematic accuracy ', in *Assessing the Accuracy of Remotely Sensed Data:Priciples and Practices.* USA: CRC Press, PP. 55-59.

- Dorn, H., Törnros, T. and Zipf, A., 2015, *Quality Evaluation of VGI Using Authoritative Data—A Comparison with Land Use Data in Southern Germany*, ISPRS International Journal of Geo-Information, 4, PP. 1657-1671.

- Esmaili, R., Naseri, F., and Esmaili, A., 2013, *Quality Assessment of Volunteered Geographic Information*, American Journal of Geographic Information System, 2(2), PP. 19-26.

- Girres, J., and Touya, G., 2010, *Quality Assessment of the French OpenStreetMap Dataset*, Transactions in GIS, 14(4): PP. 435–459.

- Goodchild, M.F., 2007, *Citizens as Sensors: The World of Volunteered Geography*, Geojournal, 69 (4), PP. 211-221.

- Haklay, M., 2010, *How Good is Volunteered Geographical Information? A Comparative Study of OpenStreetMap and Ordnance Survey Datasets*, Environ. Plan. B Plan., 37, PP. 682–703.

- Ismail, M., H., and Jusoff, K., 2008, *Satellite Data Classification Accuracy Assessment Based from Reference Dataset*, International Journal of Computer and Information Science and Engineering, 2 (2). PP. 96-102.

- Koukoletsos, T., Haklay, M., Ellul, C., 2012, *Assessing Data Completeness of VGI through an Automated Matching Procedure for Linear Data*, Transactions in GIS, 16(4), PP. 477–498.

- Landis,J.R. and Koch,G.C., 1987, *The Measurement of Observer Agreement for Categorical Data*, Biometric, 33: PP. 159-179.

- Liu, C., Xiong, L., Hu, X., and Shan, J., 2015, *A Progressive Buffering Method for Road Map Update Using OpenStreetMap Data*, ISPRS International Journal of Geo-Information, 4, PP. 1246-1264.

- Ma, D., Sandberg, M., and Jiang, B., 2015, *Characterizing the Heterogeneity of the OpenStreetMap Data and Community*, ISPRS International Journal of Geo-Information, 4, PP. 535-550.

- Monserud,R.A., 1990, *Method for Comparing Global Vegetation Map*, WP- 90-40 II ASA,Laxenburg.

- OpenStreetMap, 2015, accessed on 27-12-2015, available at https://www.openstreetmap.org/note/new#map=15/33.2996/44.4606&layers=D

- Ramm, F., Topf, J. and Chilton, S., 2011, *OpenStreetMap - Using and Enhancing the Free Map of the World*, Cambridge, England: UIT Cambridge Ltd.

- Ramos J, M., Vandecasteele A., and Devilers, R., 2013, *Semantic Integration of Authoritative and Volunteered Geographic Information (VGI) using Ontologies*, Paper presented at 16th AGILE Conference on Geographic Information Science, 14–17 May.

- Sehra, S., Singh, J., and Rai, H., 2014, *A Systematic Study of OpenStreetMap Data Quality*
- *Assessment*, 11th International Conference on Information Technology: New Generations. PP. 377-381.

- Thakkar, S., K. Craig, and A. Jose , 2007, *Quality-Driven Geospatial Data Integration*, Proceeding of the 15th International Symposium on Advances in Geographic Information Systems.

- Vandecasteele, A., and Devillers, R., 2013, *Improving Volunteered Geographic Data Quality using Semantic Similarity Measurements*, International Archives of the Photogrammetry, Remote Sensing and Spatial Information Sciences, 8th International Symposium on Spatial Data Quality, Hong Kong, PP. 1-6

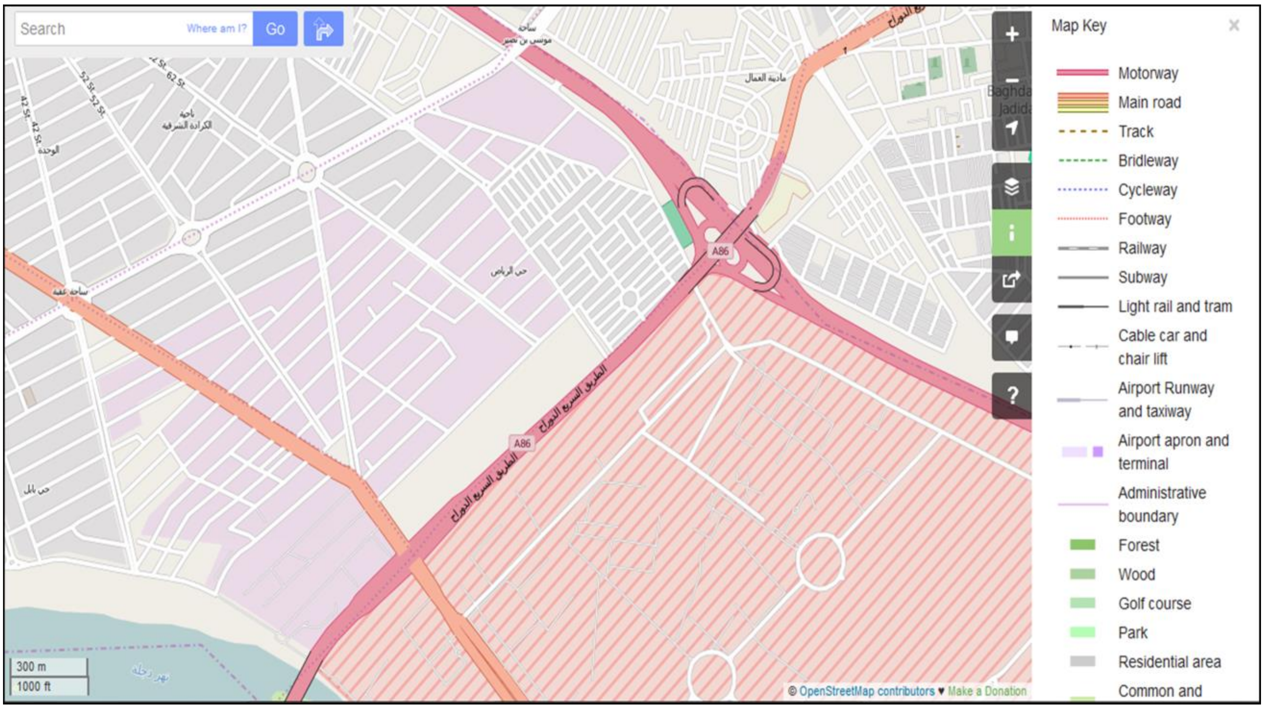

Figure 1. An example of feature classifications visualised on OSM project, **OpenStreetMap, 2015.**

		Reference Data			Row Total
		1	2	k	n_{i+}
Classified Data	1	n_{11}	n_{12}	n_{1k}	n_{1+}
	2	n_{21}	n_{22}	n_{2k}	n_{2+}
	k	n_{k1}	n_{k2}	n_{kk}	n_{k+}
Column Total	n_{+j}	n_{+1}	n_{+2}	n_{+k}	n

Figure 2. Example of Error Matrix.

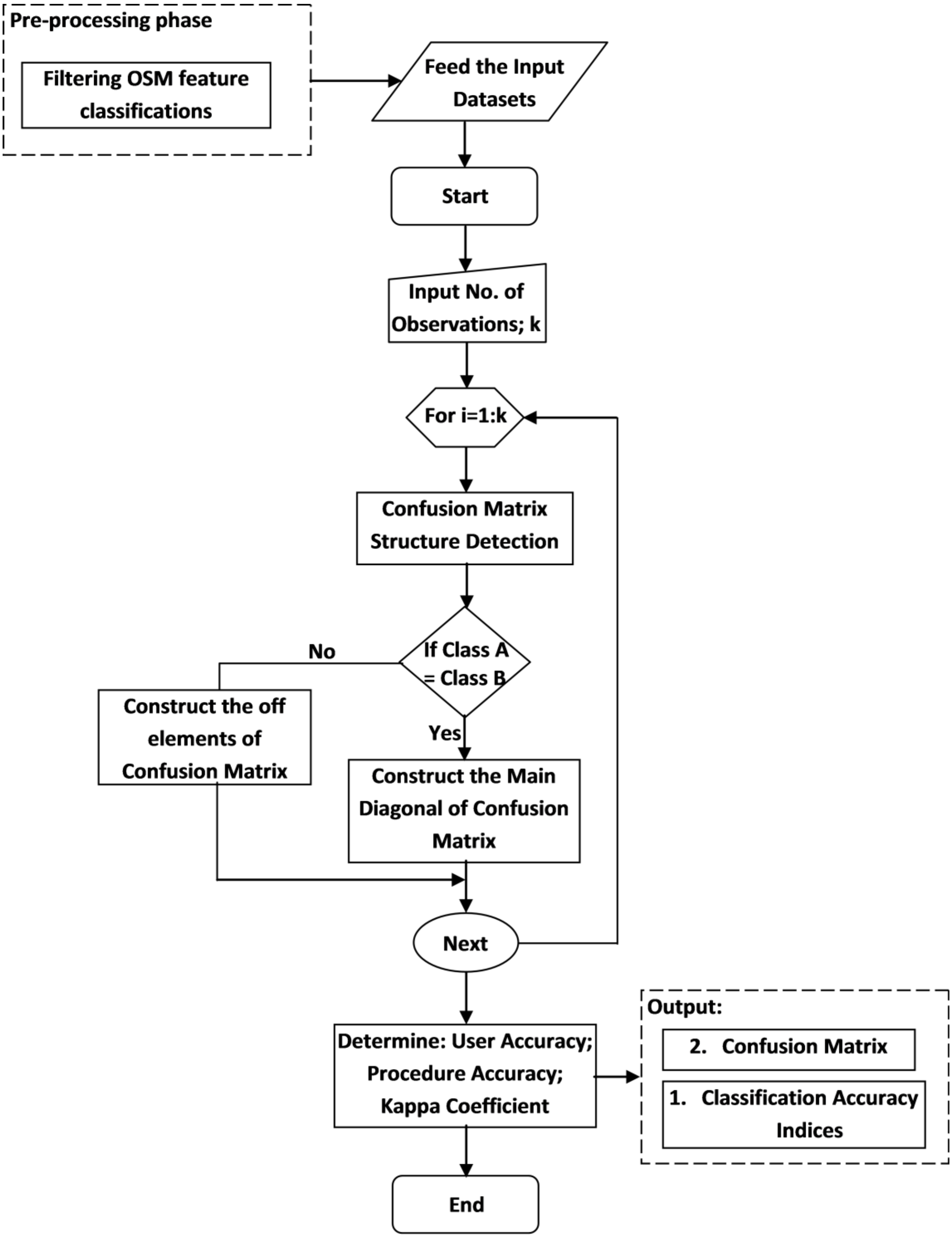

Figure 3. The Flowchart of the Designed Program.

	Reference Data																
OpenStreetMap Data	**Primary road**	**Secondary road**	**Service road**	**Track**	**Residential road**	**Bridge**	**Path**	**Building**	**River**	**Lake**	**Parking**	**Green area**	**Sports pitch**	**Residential area**	**University**	**Orchard**	**Row total**
Primary road	**6**	2	2	0	0	0	1	0	0	0	0	0	0	0	0	0	**11**
Secondary road	3	**10**	4	0	0	0	0	0	1	0	0	0	0	0	1	0	**19**
Service road	0	0	**56**	0	0	0	0	7	0	0	0	0	0	0	2	1	**66**
Track	0	0	0	**28**	0	0	0	0	0	0	0	1	0	0	0	0	**29**
Residential road	2	0	0	0	**168**	0	0	0	0	0	0	0	0	0	0	0	**170**
Bridge	0	0	1	0	0	**2**	0	0	0	0	0	0	0	0	0	0	**3**
Path	0	0	0	0	0	0	**17**	5	0	0	0	0	0	0	0	0	**22**
Building	0	1	14	0	0	0	0	**141**	0	0	2	0	0	0	6	0	**164**
River	0	0	0	0	0	0	0	0	**1**	0	0	0	0	0	0	0	**1**
Lake	0	0	0	0	0	0	0	0	0	**3**	0	0	0	0	0	0	**3**
Parking	0	0	0	0	0	0	0	0	0	0	**11**	0	0	0	0	0	**11**
Green area	0	0	0	0	0	0	0	0	0	0	0	**2**	0	0	0	0	**2**
Sports pitch	0	0	0	0	0	0	0	0	0	0	0	0	**2**	0	0	0	**2**
Residential area	0	0	0	0	13	0	0	0	0	0	0	0	0	**6**	0	0	**19**
University	0	0	0	0	0	0	0	4	0	0	0	0	0	0	**13**	0	**17**
Orchard	0	0	0	0	0	0	0	0	0	0	0	0	0	1	0	**3**	**4**
Column total	**11**	**13**	**77**	**28**	**181**	**2**	**18**	**157**	**2**	**3**	**13**	**3**	**2**	**7**	**22**	**4**	**543**

Figure 4. The Confusion Matrix.

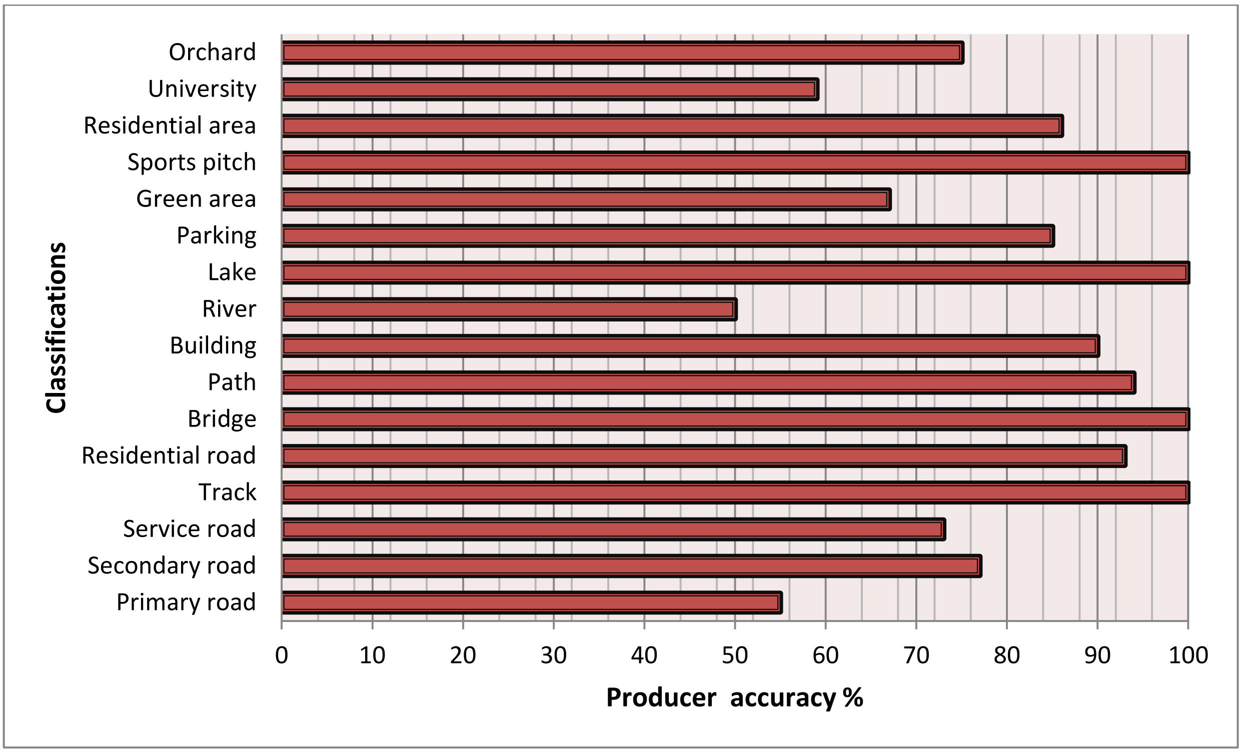

Figure 5. The Procedure Accuracy of OSM Classifications from 534 Reference Data.

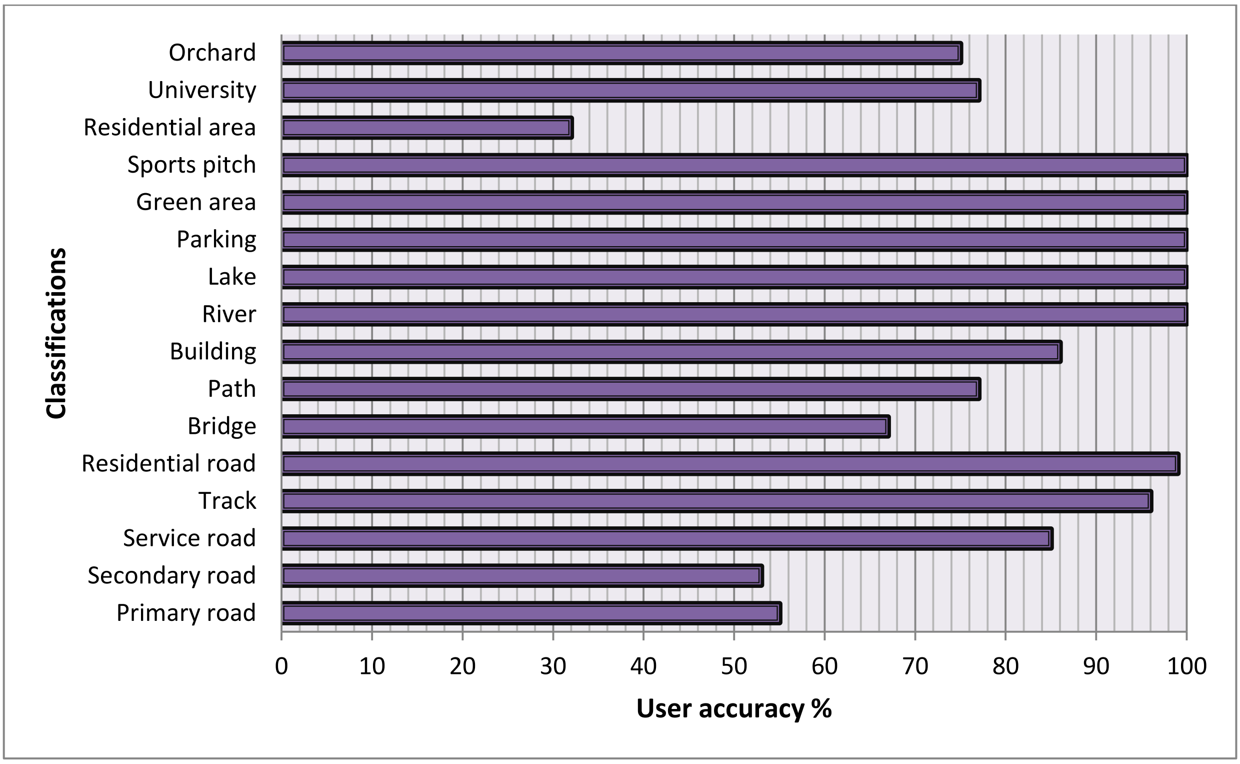

Figure 6. The User Accuracy of OSM Classifications from 534 Reference Data.